MCEER
EARTHQUAKE ENGINEERING TO EXTREME EVENTS

ISSN 1520-295X

Stress Wave Attenuation in Solids for Mitigating Impulsive Loadings

by
Reza Rafiee-Dehkharghani, Amjad Aref
and Gary Dargush

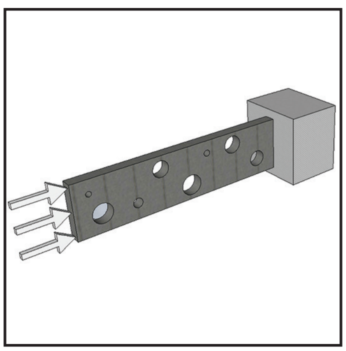

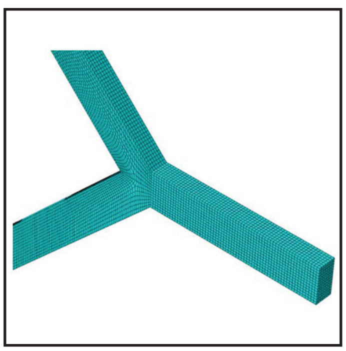

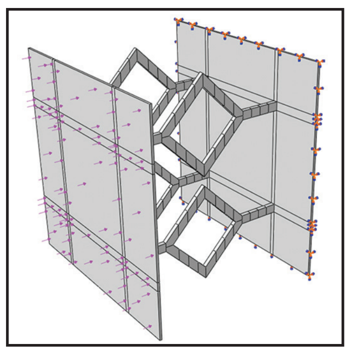

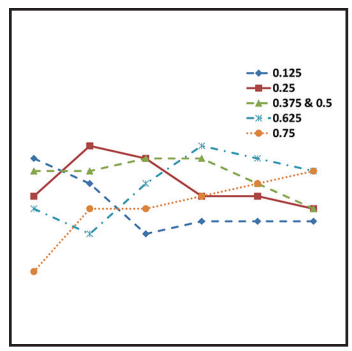

Technical Report MCEER-15-0003

August 15, 2015

This research was conducted at the University at Buffalo, State University of New York and was supported primarily by the George E. Brown, Jr. Network for Earthquake Engineering Simulation (NEES) Program of the National Science Foundation, NEESR award number CMMI-0900338.

NOTICE

This report was prepared by the University at Buffalo, State University of New York as a result of research supported primarily by the George E. Brown, Jr. Network for Earthquake Engineering Simulation (NEES) Program of the National Science Foundation, NEESR award number CMMI-0900338. Neither MCEER, associates of MCEER, its sponsors, the University at Buffalo, State University of New York, nor any person acting on their behalf:

a. makes any warranty, express or implied, with respect to the use of any information, apparatus, method, or process disclosed in this report or that such use may not infringe upon privately owned rights; or

b. assumes any liabilities of whatsoever kind with respect to the use of, or the damage resulting from the use of, any information, apparatus, method, or process disclosed in this report.

Any opinions, findings, and conclusions or recommendations expressed in this publication are those of the author(s) and do not necessarily reflect the views of MCEER, the National Science Foundation, or other sponsors.

Stress Wave Attenuation in Solids for Mitigating Impulsive Loadings

by

Reza Rafiee-Dehkharghani[1], Amjad Aref[2], and Gary Dargush[3]

Publication Date: August 15, 2015
Submittal Date: December 22, 2014

Technical Report MCEER-15-0003

NSF NEESR Award Number CMMI-0900338

1 Ph.D., Department of Civil,Structural and Environmental Engineering, University at Buffalo, State University of New York
2 Professor, Department of Civil, Structural and Environmental Engineering, University at Buffalo, State University of New York
3 Professor, Department of Mechanical and Aerospace Engineering, University at Buffalo, State University of New York

MCEER
University at Buffalo, State University of New York
212 Ketter Hall, Buffalo, NY 14260
E-mail: *mceer@buffalo.edu*; WWW Site: *http://mceer.buffalo.edu*

PREFACE

MCEER is a national center of excellence dedicated to the discovery and development of new knowledge, tools and technologies that equip communities to become more disaster resilient in the face of earthquakes and other extreme events. MCEER accomplishes this through a system of multidisciplinary, multi-hazard research, education and outreach initiatives.

Headquartered at the University at Buffalo, State University of New York, MCEER was originally established by the National Science Foundation (NSF) in 1986, as the first National Center for Earthquake Engineering Research (NCEER). In 1998, it became known as the Multidisciplinary Center for Earthquake Engineering Research (MCEER), from which the current name, MCEER, evolved.

Comprising a consortium of researchers and industry partners from numerous disciplines and institutions throughout the United States, MCEER's mission has expanded from its original focus on earthquake engineering to one which addresses the technical and socioeconomic impacts of a variety of hazards, both natural and man-made, on critical infrastructure, facilities, and society.

MCEER investigators derive support from the State of New York, National Science Foundation, Federal Highway Administration, National Institute of Standards and Technology, Department of Homeland Security/Federal Emergency Management Agency, other state governments, academic institutions, foreign governments and private industry.

This report investigates the effect of discontinuities on the wave propagation characteristics of structures and proposes new architectures for attenuating stress waves. The effects of different types of material and geometric discontinuities are thoroughly explored, and their attenuation capacity is investigated using explicit formulas. Based on these concepts, an optimal design problem is defined for finding the most effective structural configurations to attenuate the effects of impulsive loadings. Due to the highly nonlinear nature of the optimization problem combined with lack of gradient information about the objective function with respect to design variables, a genetic algorithm (GA) optimization procedure is used for the optimal design of the newly defined attenuating systems.

ABSTRACT

This report describes work aimed at investigating the effect of discontinuities on the wave propagation characteristics in structures and proposes new architectures for attenuating stress waves. Four types of stress wave attenuators are proposed in this report. These attenuators include: (i) layered collinear rod structures, (ii) layered diamond-shape beam structures, (iii) non-collinear beam structures, and (iv) porous plates. The layered stress wave attenuators have constant geometry while each material set-up is optimized during the design procedure. However, the non-collinear beam structures and porous plates are made of a single material, and the design procedure seeks to find the best geometry of these systems for mitigating the effects of impulsive loadings. In addition to the proposed stress wave attenuators, the problem of stress wave attenuation in bi-layered plates with a jagged interface profile is also studied in this research. Similar to the approach used in non-collinear systems and porous plates, the material properties of the bi-layered plates remains unchanged during the design procedure; however, the profile of the interface between the two materials changes for the objective of stress wave attenuation.

The results of this research show that with the aid of the developed optimization procedure, very efficient and practical stress wave attenuators can be deployed for protecting structural systems against impulsive loadings with consideration to broad frequency ranges.

ACKNOWLEDGEMENTS

We acknowledge the funding for this research, which was provided primarily by the US National Science Foundation under Grant No. CMMI-0900338, with additional support by the Multidisciplinary Center for Earthquake Engineering Research (MCEER).

TABLE OF CONTENTS

LIST OF FIGURES

LIST OF TABLES

SECTION 1

INTRODUCTION

1.1 Introduction

Wave propagation behavior in structures depends on the characteristics of their discontinuities. Discontinuities on the path of propagating waves can generally be categorized into two different groups—material and geometric. When a propagating wave encounters a discontinuity, new reflected and transmitted waves will be generated within the structure. For example, when a wave enters a new medium (material discontinuity) reflected and transmitted waves will be produced in the structure based on the impedance mismatch of the two media. Similarly, geometric discontinuities, such as angled joints in beam structures and interface profiles in layered plates can cause wave reflection and transmission, along with producing different types of wave modes. Considering these facts, the discontinuities within a structure can be organized in appropriate patterns for various objectives such as stress wave attenuation and amplification.

This report aims at developing new architectures for attenuating the effects of impulsive loadings. The proposed concepts in this report are based on harnessing the effects of reflection and transmission of waves at discontinuities. Hence, the characteristics of the discontinuities in different types of structures such as rods, beams, and plates are investigated. The results obtained from these investigations are then utilized to define optimal design problems for finding efficient structural configurations with high stress wave attenuation capacity. Due to the highly non-linear nature of the defined optimal design problems, a heuristic optimization procedure is exploited for designing the proposed architectures in this report.

1.2 Objectives

The primary objective of this report is developing efficient stress wave attenuators for mitigating the impulsive loadings with various frequency contents. To perform this task, it is necessary to have sufficient information about the characteristics of wave propagation at discontinuities within the structures. Furthermore, it is necessary to develop an appropriate methodology for optimal design of the stress wave attenuators.

The key objectives of the research documented in this report are:

- Investigate the effect of discontinuities in rods, beams, and plates
- Characterize the design parameters for stress wave attenuators

- Define different type of stress wave attenuators
- Develop an optimization methodology for designing the stress wave attenuators
- Explore the concept of material optimization in layered rods and beams
- Examine the concept of geometry optimization in beams and plates
- Analyze the attenuation capacity of the proposed stress wave attenuators for the impulsive loadings with various frequency contents

1.3 Report organization

This report contains 11 Sections. The outline of the report is:

- Section two presents a review of the literature about the wave propagation behavior of layered structures, the concept of topology optimization, and application of genetic algorithm in engineering problems.
- Section three explores the effect of discontinuities on the reflection and transmission of stress waves within rod structures.
- Section four reviews the flexural wave propagation in Timoshenko beams and investigates the effect of discontinuities in Timoshenko beam structures.
- Section five introduces the proposed stress wave attenuators and the optimization methodology for design.
- Section six represents the essential parameters that should be considered for designing the proposed stress wave attenuators.
- Section seven explores the optimal design of the layered collinear stress wave attenuators.
- Section eight studies the optimal design of the non-collinear stress wave attenuators. These structures include multi-layered and single-layered non-collinear systems.
- Section nine investigates the stress wave attenuation in two-dimensional structures with circular holes.
- Section ten examines the stress wave attenuation capacity of bi-layered plates with jagged interface profiles.
- Section eleven summarizes the findings of this report, gives the final conclusions, and proposes future work.

SECTION 2
BACKGROUND AND LITERATURE REVIEW

2.1 Introduction

Attenuation of stress wave amplitude in solid structures depends on the type and arrangement of discontinuities. Discontinuity is in fact a general term that can be attributed to any change in the material properties, geometry, or boundary condition of a structure that results in the scattering of the stress waves.

In order to design efficient stress wave attenuators, it is necessary to study the effects of different types of discontinuities on the wave propagation characteristics of a structure. Furthermore, it is necessary to explore different methods of optimization to find the most appropriate approaches for optimizing the stress wave attenuators. In this research, Genetic Algorithm (GA) is used for the optimal design of the stress wave attenuators. This method is utilized for material (layered structures) and geometry (shape and topology) optimization of the systems. Due to the importance of these concepts, a brief review of literature about layered structures, topology optimization, and GA is presented in this section.

2.2 Wave propagation in layered structures

The problem of wave propagation in layered media is of practical interest for many applications, such as impact attenuation, thermal insulation, seismology, and acoustics. As a stress wave attenuator, layered composite materials have been extensively used in applications involving mitigation of blast and ballistic loadings. For instance, a new generation of layered and sandwich composites are developed by using special types of materials, such as polyuria and ceramics that can mitigate the effect of blast and high velocity impact loadings.

Over the past decades a significant number of researchers have looked into wave propagation in layered structures. In one of the earliest works about this topic, Thomson (1950) derived analytical solutions for the propagation of plane elastic waves in stratified solid media consisting of parallel plates with different material properties and thickness. The solutions are derived by satisfying the continuity of particle velocity, normal stresses, and shear stresses at the interfaces of the layers using the matrix method. To provide general solutions, they assumed that the incident wave is oblique.

Lindholm and Doshi (1965) studied the wave propagation in a nonhomogeneous finite elastic free-free bar with varying modulus of elasticity which is subjected to a transient pressure pulse. They found analytical solutions for a bar with constant density while the elasticity modulus is continuously changing.

Anfinsen (1967) studied the optimal design of the one-dimensional elastic layered structures for attenuating and amplifying the amplitude of the stress waves. The results showed that the proper selection of materials can attenuate (or amplify) the amplitude of the stress waves more than 99 percent.

Maiboroda, Troyanovskii et al. (1992) derived the steady state solution for the wave propagation in two-dimensional two-layered structures with finite thickness. They studied the propagation of viscoelastic and elastic waves, and concluded that the damping characteristics of non-uniform viscoelastic systems can be controlled by changing the physical properties and geometric dimensions.

Konstanty and Santosa (1995) studied the optimal design of layered coatings subjected to incident pulses for minimization of the wave reflection. A regularization strategy is used for solving the problems and a computational scheme is proposed for designing the coatings. Their analyses showed that the optimal design problem is very dependent on the nature of the applied incident pulse and may be unstable for some pulses. The results that are obtained can be used for designing minimally reflective coatings in optics and acoustics.

Wang, Rostamian et al. (2000) developed theoretical algorithms for designing reflective or absorptive layered coatings. These algorithms are established for the acoustic waves in elastic systems; however, they can be applied for any problem that is governed by linear wave equation. The results showed that the designed coatings can completely reflect or transmit the waves at certain ranges of frequencies (frequency band).

Velo and Gazonas (2003) developed analytical solutions for the optimal design of two-layered elastic strips subjected to transient loadings. In their research, they used the method of characteristics and provided explicit formulas for the stresses in the layers. The results were used for validation of DYNA3D/GLO hybrid computational optimization software.

Naik, Goel et al. (2008) studied the micro-attenuation of stress waves in ceramic plates using a one-dimensional tracking algorithm. They validated the predictions with experimental results and concluded that the stress wave attenuation is a material property in ceramic plates with grains and grain boundaries.

Luo, Aref et al. (2009) investigated the stress wave attenuation in layered structures subjected to impulsive loadings. They derived a stress transfer function for the layered structures situated between free and fixed surfaces. It was observed that by proper selection of materials and layer dimensions, the amplitude of the stress pulse can be reduced, and the duration of the pulse can be elongated.

Wave propagation analysis of the finite layered structures subjected to transient loadings is very complex, and, generally, it is difficult to derive explicit analytical solutions for most practical applications. Hence, many researchers have developed numerical and experimental approaches for studying the wave propagation behavior of layered structures. Rizzi and Doyle (1992) developed an efficient matrix methodology for analysis of wave propagation in layered media. This methodology is similar to the finite element method and exactly models the mass distribution. Therefore, the exact frequency response of the layers can be obtained using this method. The results show that the proposed methodology is robust and accurate, and is at least four times more computationally efficient than the direct global matrix method.

Shim and Yap (1997) investigated the impact behavior of foam-plate sandwich systems consisting of polyurethane and mild steel plates. They did an extensive experimental study for this purpose and identified the effects of strain rate, system inertia, and stress wave interaction. The results showed that the behavior of polyurethane foam is rate-sensitive and the crushing force increases with the deformation rate. To validate the experimental data, the transient impact responses of the polyurethane-steel plates were analyzed using a one-dimensional mass-spring chain model with inertia and rate effects. It was observed that there is a good agreement between the experimental and numerical predictions.

Pandya, Dharmane et al. (2012) conducted an experimental study on the stress wave attenuation in polymer composite plates during a ballistic impact. They examined the strain profiles at certain distances from the impact, and found that the peak strains are reduced as the waves propagate away from the impact surface.

Alagappan, Rajagopal et al. (2014) studied the impact response of viscoelastic layered plates composed of Polymethylmethacrylate (PMMA) and Polycarbonate (PC) using a finite volume method (FVM). The plates were subjected to transient displacement at one end while the other end was clamped. They assumed that the behavior of PMMA and PC is nonlinearly rate dependent and studied the stress, velocity propagation, and their interactions at the interface for different material set-ups including pure PC, pure PMMA, bilayer PMMA/PC, bilayer PC/PMMA, trilayer PC/PMMA/PC, and trilayer PMMA/PC/PMMA. The results showed that the trilayer PMMA/PC/PMMA generates the lowest value of stress at the clamped wall.

2.3 Shape and topology optimization

Structural optimization is a multidisciplinary field that combines mechanics and mathematics to find optimal design of the structures in various applications such as aerospace, civil, and mechanical engineering (Kirsch 1989). The algorithms and techniques for optimal structural design have remarkably progressed during the past decades as a result of developments in numerical methods, optimization algorithms, and fast computation.

Structural optimization can be divided into three categories: size, shape, and topology optimization. A good explanation of the difference between these categories can be found in (Kirsch 1989). In size optimization problems, the geometry of the structure is fixed and the dimensions (size) of the components of the structure are varied to meet the design requirements. However, in shape and topology optimization problems, the layout of the structure is not fixed and it varies during the optimal design procedure. Although the layout of the structure is manipulated in shape and topology optimization problems, there is a slight difference between these two approaches. In shape optimization problems, the geometry of the structure is described using continuous variables while the design variables for topology optimization problems are characterized with the number of elements, joints, and supports along with the spatial sequence and the pattern of the connection of members.

The shape optimization of continuous structures can be performed by varying the integration limits, which can be very difficult in particular problems. Generally, numerical analysis such as FE is utilized for shape optimization of continuous structures. In these problems, it is required that the FE model be modified during the optimization process. Shape optimization can also be used for discrete structures if the design variables such as nodal coordinates are defined by continuous parameters.

Topological optimization algorithms are appropriate for discrete structures as the design parameters are discrete variables; however, these methods can be used for continuous structures such as surface-like systems if they are modeled with grid-like continuum space that consists of infinitesimal spacing (Kirsch 1989). Finite element models are also utilized in topological optimal designs. In these problems, new members are added or deleted to the structure and both the FE model and design variables change during the optimal design procedure. Therefore, optimal topological designs are among the most complicated structural optimization problems.

El-Sabbagh, Akl et al. (2008) used a topology optimization algorithm to widen the band gaps and maximize the natural frequency of periodic Mindlin plates (band gaps are the frequency bands in which the propagation of waves can be completely blocked). They developed an FE model for evaluating the natural frequencies of Mindlin plates and coupled it with a topology optimization algorithm which considers a unit cell of the plate as the design space and replicates the optimized topology of the unit cell over the whole structure. In this case, the optimization procedure is very efficient because the design space is limited to a local unit cell although the objective function is related to the global performance of the periodic assembly of the optimized local cell. They applied the developed approach to fixed-free and fixed-fixed aluminum plates. The results showed that the proposed topology optimization methodology can be successfully used to stop or confine undesirable disturbances.

During the past decades, various approaches and techniques are developed for shape and topology optimization of structures. Among the most common approaches we can name “ground structure method”, “homogenization method”, “evolutionary structural optimization (ESO)”, and “level set method (LSM)”.

Ground structure method is one of the simplest topology optimization approaches which is introduced by Dorn, Gomory et al. (1964) for topology optimization of trusses under static loading considering the stress and displacement constraints. In this method, a ground structure is formed by generating a truss with many members and including the nodes on which the supports (boundary conditions) and loads are applied. Then some unnecessary members will be removed from the ground structure based on the permissible stress (or displacement) constraints, and, after some iterations, the remaining members will form the optimal topology of the structure.

In homogenization methods, a porous medium is formed by introducing many micro-scale voids or holes within the design space, and the optimization algorithm seeks the optimal porosity of the generated porous medium with respect to the optimality criteria (Wang, Wang et al. (2003) and Suzuki and Kikuchi 1991). In this method, the internal voids in the structures are generated without any prior knowledge about their existence. This method generally produces porous structures with infinitesimal pores, which are difficult to build from a manufacturing point of view.

Evolutionary Structural Optimization (ESO) is based on the concept of removing the redundant materials gradually for obtaining the optimal designs. This method is proposed by Xie and Steven (1993) and Nha Chu, Xie et al. (1997). In considering ESO, a fixed model is used as the initial optimal design domain and the final topology of the structure is formed by removing the unwanted or low-stressed material. ESO was first developed for the problems with stress criteria and then extended for the problems with frequency optimization objectives and stiffness constraints (Nha Chu, Xie et al. (1997)). Generally, ESO is computationally expensive and it cannot ensure that the final optimal solution is not a local optimum. Querin, Steven et al. (1998) proposed a Bi-directional Evolutionary Structural Optimization (BESO) which is capable of searching the design space more thoroughly for finding the global minima. In BESO, it is possible to add the materials as well as removing them during the optimization procedure; therefore, the design space can be explored more efficiently.

Level set method (LSM) is another topology optimization approach which is introduced by Osher and Sethian (1988). This method relies on the theory of curve evolution in which the topology of the structure is altered by moving the boundaries. LSM has been successfully used for various problems such as multiphase fluid dynamical flows, image processing, and computer vision (Jia, Beom et al. 2011).

Yang, Xie et al. (1999) utilized ESO and BESO procedures for structural topology optimization with frequency constraints. They performed the optimization problems for three different objectives: maximizing a single frequency, maximizing multiple frequencies, and designing structures for a specified set of frequencies. They observed that there is a good agreement between the results of ESO and BESO; however, BESO is more computationally efficient in most of the cases.

Wang, Wang et al. (2003) presented a structural topology optimization methodology based on the LSM for optimizing linearly elastic structures with certain constraints and design objectives. In their proposed method, the structure is represented implicitly by a moving boundary which is defined by a scalar function with a higher dimensionality. The results of the 3D topology optimization with the proposed methodology showed that this method is very flexible in handling the topological changes compared to other topology optimization methods such as homogenization.

Jia, Beom et al. (2011) proposed a combined ESO-LSM structural topology optimization algorithm. This algorithm incorporates the advantages of these two methods and eliminates the weaknesses related to LSM. In traditional LSM algorithms, the optimization procedure requires an initial topology; however, this method requires no initial structure. It was observed that this method can explore the design space more thoroughly and it is computationally more effective than LSM. This method can be applied to different engineering problems with local stress constraints, eigenvalue optimization, and design of compliant mechanism.

2.4 Genetic algorithm

Genetic Algorithms (GAs) are bio-inspired evolutionary algorithms that are capable of finding optimum solutions for complex engineering problems with highly nonlinear relationships between the variables and objective function. This method can be efficiently used for the problems without gradient information or any other type of problem for which there is little information about the behavior of the objective function. GA is a very appropriate method for the problems studied in this research because there is not much information about the wave propagation behavior of the structures with multiple discontinuities.

There is an extensive amount of research about GA and its application in different fields of science and engineering. The initial concept of GA was introduced by Holland (1975). Later, Goldberg (1989) and Mitchell (1998) provided a detailed descriptions about GA in their textbooks. In the following, a brief review of literature is presented for the application of GA in civil engineering problems.

Hajela and Lee (1995) exploited GA for topology optimization of load-bearing trusses. Their proposed approach is a two-level GA based search in which the kinematic stability constraints are satisfied at the first level of optimization and followed by the treatment of response (member sizing) in the second level. The results showed that GA is a robust exploratory approach for topology optimization problems in discontinuous spaces.

Pezeshk, Camp et al. (2000) utilized a GA-based optimization procedure for the design of geometrically linear and nonlinear steel-framed structures. They used AISC-LRFD specifications for design of the steel frames and investigated the effect of P-Δ effects. For the GA procedure, they employed group selection scheme for reproduction and improved the adapting crossover operator for their problems. They also exploited a specific penalty function to transform their constrained problem to an unconstrained one, which is appropriate for GA optimization. The results showed that GA optimization can be very effective in finding the discrete nonlinear optimal or near optimal designs of the steel-framed structures.

Singh and Moreschi (2002) used GA for determining the optimal size and location of the viscous and viscoelastic dampers in the structures for reducing the seismic response. They found that GA can be used for any particular performance function of the structure as long as the functions can be presented numerically.

Camp, Pezeshk et al. (2003) used GA for the optimal design of the reinforced concrete (RC) frames considering the limitations and specifications of American Concrete Institute (ACI) Building code. The fitness function of their RC-GA procedure was evaluated by minimizing the material and construction costs of RC structural elements (such as simply-supported beams, uniaxial columns, and multi-story frames), while the limitations of ACI code (constraints of the optimization problem) were applied as penalty functions. The results showed that the reduction in the cost of the RC members that are designed by the RC-GA procedure is insignificant comparing to the total cost of the structure.

Yun and Kim (2005) incorporated a GA optimization procedure and a refined plastic hinge analysis into a program for optimum design of plane steel frames. The objective function of their program was minimizing the weight of the steel frames. The constraints of the optimization problem were the design criteria such as load-carrying capacity, serviceability, ductility, and constructability, which were applied through the appropriate penalty functions. Tournament selection method and micro-genetic algorithm were employed in their GA program. The analyses showed that the results of the optimal designs are satisfactory compared to the previous works in this area; however, their GA based optimization methodology requires a large number of generations for convergence.

Dargush and Sant (2005) proposed an evolutionary aseismic design methodology for discrete optimization of passively damped structural systems using GA. To determine robust designs, they included both the non-linearity of the structural systems and the uncertainty associated with the seismic environment. They applied the developed methodology to 5, 12, and 30 story buildings and configured the sizing and placement of passive dampers within the structures. In a similar work, Lavan and Dargush (2009) developed an advanced GA to solve the multi-objective evolutionary seismic design of the structures with passive energy dissipation systems.

Balling, Briggs et al. (2006) presented a GA methodology for simultaneous optimization of the size, shape, and topology of skeletal structures such as trusses and frames. The proposed algorithm is capable of finding multiple optimum and near-optimum topologies in a single run. They employed their algorithm for optimizing a bridge example and a plane frame, and found that the algorithm can generate either traditionally recognized or new (less familiar) topologies for the structures. The results showed that this algorithm provides the designer with more information than the algorithms that converge to a single solution; therefore, it can be used as a preprocessor to the human decision making.

Bel Hadj Ali, Sellami et al. (2009) developed a GA based multi-stage method for the cost optimization of the semi-rigid steel frame structures. This method can generate and evaluate the design alternatives concurrently in the early design stages, which helps the designer to make better decisions. Generally, the cost of the joints in steel frame structures is about 20% of the total cost of the structure, and the behavior of joints has a very important effect on the response of structural frames. The proposed method can optimize the structural members and the detailing of the joints to generate economical layouts. The results showed that the developed GA-based method can reduce the total cost of the structures as much as 10 to 25%.

Sun, Fang et al. (2010) combined a hybrid genetic algorithm (HGA) with an artificial neural networks (ANN) method to minimize the equivalent thermal conductivity (ETC) of the concrete hollow bricks with different rows of enclosure. They found that the combination of ANN and HGA is very efficient for improving the heat prevention properties of the bricks and the ETC of the bricks can be decreased as much as 21.69% for the given range of design parameters.

Dede, Bekiroğlu et al. (2011) studied the efficiency of the binary and value encoding for the discrete and continuous optimization of the weight of the truss structures using GA. Unlike the binary encoding, they observed that the fit chromosome will never be lost in value encoding. Moreover, they found that value encoding overcomes the effect of Hamming-cliff, while binary encoding requires a large number of changes in the genes if a small change is needed in the optimization parameter. In order to overcome the problem of a very large solution space for continuous optimization, they introduced a restricted range approach (RRA). The analyses showed that the continuous optimization of the trusses using RRA generates much lighter trusses.

Luo, Aref et al. (2011) investigated the optimal design of simple and bundled layered elastic stress wave attenuators using an adaptive real encoded GA. The developed GA optimization methodology is capable of optimizing the problems with mixed-float and integer type design parameters.

Kociecki and Adeli (2013) developed a two-phase GA methodology for minimizing the weight of the space-frame roof structures. It was observed that the proposed method is computationally efficient for optimizing the large real-life structures that contain discrete commercially sections.

2.5 Summary

In this section, a brief review of literature is presented for the wave propagation behavior of layered structures, topology optimization of structures, and application of GA in engineering problems. These concepts will be utilized in the following sections for designing efficient stress wave attenuators.

SECTION 3
WAVE REFLECTION AND TRANSMISSION IN RODS

3.1 Introduction

Analytical solutions of wave propagation in solid structures with physical boundary conditions that are subjected to real dynamic loads require complicated mathematical analyses. Longitudinal wave motion in thin rods is one of the simple problems that can be used for introducing the basic concepts of wave propagation in solids. Therefore, the problem of wave motion in rods is investigated in this section and the required relations for wave propagation analysis are introduced using this concept. In addition, the effect of discontinuities on the reflection and transmission of waves within rod structures is studied extensively in this section.

3.2 Wave propagation in thin rods

Rods are very important structural elements that can conduct longitudinal waves because of their axial load bearing capacity. The governing theory of an elastic thin rod can be found based on the exact equations of elasticity. In order to derive the governing equation of wave propagation in a thin rod, consider the straight prismatic rod that is shown in Figure 3-1.

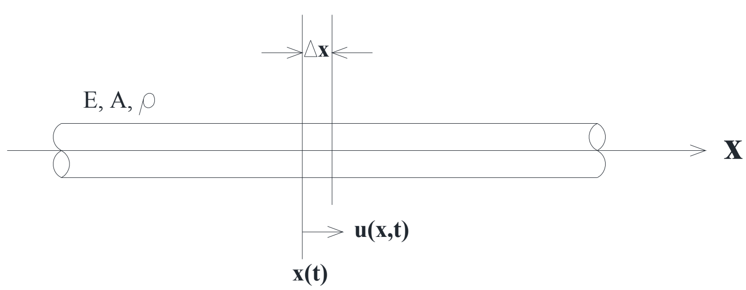

Figure 3-1 Straight prismatic thin rod with elastic properties

There are several theories for deriving the equation of motion of the rod structures such as Elementary rod theory and Mindlin-Herrmann rod theory (Doyle (1989)). For simplicity, elementary theory will be used in this section for deriving the governing wave equation. The following assumptions are made in the elementary theory (Doyle (1989)):

- The rod is long.
- The rod is slender.
- The rod supports only one-dimensional axial stress.
- The effect of Poisson's ratio is neglected.

On the contrary, in Mindlin-Herrmann rod theory, the effect of Poisson's ratio is considered; therefore, one-dimensional axial stress assumption will cease to be valid.

Figure 3-2 shows an element of a thin rod and the acting forces on this element. $q(x,t)$ is the externally applied body force per unit volume.

The equation of motion, or momentum balance, for this element is:

$$\sum F = m\ddot{u} \Rightarrow -F + (\mathrm{F} + \Delta F) + qA\Delta x - m\ddot{u} = 0 \tag{3.1}$$

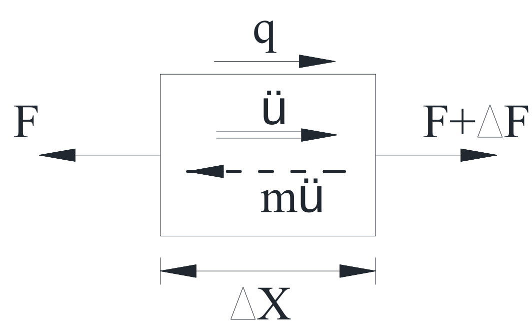

Figure 3-2 Forces acting on a small element of a thin rod

Therefore, in a differential form we can write:

$$\frac{\partial F}{\partial x} = \rho A \frac{\partial^2 u}{\partial t^2} - qA \tag{3.2}$$

In the above equation, the independent variable is *x* and *t*, and it is desirable to write the equation in terms of displacement. To do so, we should consider small deformation assumption of strain-displacement and stress-strain relations:

$$\varepsilon = \frac{\partial u}{\partial x} \tag{3.3}$$

$$\sigma = \frac{F}{A} = E\varepsilon \tag{3.4}$$

By combining the equations of (3.1) to (3.4), the longitudinal wave propagation equation can be written as:

$$\frac{\partial}{\partial x}\left\{EA\frac{\partial u}{\partial x}\right\} = \rho A\frac{\partial^2 u}{\partial t^2} - qA \tag{3.5}$$

In the absence of body force, for a prismatic rod with constant Young's modulus, we can write:

$$E\frac{\partial^2 u}{\partial x^2} = \rho\frac{\partial^2 u}{\partial t^2} \tag{3.6}$$

or

$$c_0^2\frac{\partial^2 u}{\partial x^2} = \frac{\partial^2 u}{\partial t^2} \quad , \quad c_0 = \sqrt{\frac{E}{\rho}} \tag{3.7}$$

Equation (3.7) is the familiar wave equation, and it has the general D'Alembert solution, given by:

$$u(x,t) = f(x - c_0 t) + g(x + c_0 t) \tag{3.8}$$

This solution is not used in the remainder of this section, but instead spectral analysis will be utilized as mentioned in Doyle (1989).

3.2.1 Spectral analysis

The key approach in spectral analysis of wave motion is to remove the time variable from the solution of the wave motion by using the spectral representation of the solution (Doyle (1989)).

We know that the independent variables of the wave equation are time and space. For particular points in space, the spectral representation of the wave motion is (Doyle (1989)):

$u(x_1, y_1, t) = f_1(t) = \sum C_{1n}e^{i\omega_n t}$

$u(x_2, y_2, t) = f_2(t) = \sum C_{2n}e^{i\omega_n t}$

$u(x_n, y_n, t) = f_n(t) = \sum C_{nn}e^{i\omega_n t}$

Therefore, for an arbitrary position we can write:

$$u(x,y,t) = \sum \hat{u}_n\,(x,y,\omega_n)e^{i\omega_n t} \tag{3.9}$$

where, $\hat{u}_n$ are the Fourier coefficients that are spatially dependent. It is obvious that the solution is a function of frequency and the number of independent variables is not reduced. Thus, using the spectral representation, the wave equation solution becomes dependent on the frequency instead of time:

$$u(x,y,t) \Rightarrow \hat{u}_n(x,y,\omega_n) \quad or \quad u(x,y,\omega) \tag{3.10}$$

The spectral representation of equation (3.6) is:

$$E\frac{\partial^2 \hat{u}}{\partial x^2} + \omega^2 \rho \hat{u} = 0 \tag{3.11}$$

This is an ordinary differential equation with the solution (Doyle (1989)):

$$\hat{u}(x) = Ae^{-ikx} + Be^{+ikx}\,, \;\; k = \omega\sqrt{\frac{\rho}{E}} \tag{3.12}$$

The complete solution can be derived by adding the time dependency of the response:

$$u(x,t) = \sum Ae^{-i(kx-\omega t)} + \sum Be^{+i(kx+\omega t)} \tag{3.13}$$

This means that the wave solution consists of forward moving (first term) and backward moving (second term) waves. The coefficients A, B, and k are frequency dependent.

3.3 Required relations in wave propagation analysis

The longitudinal wave solution in thin rods can be utilized for introducing the basic concepts and relations of wave propagation. To do so, the solution of a forward moving wave in one-dimensional space is considered. This solution can be written in the following forms:

$$\mathrm{u}(x,t) = \mathrm{A}e^{-i(\kappa x-\omega t)} = \mathrm{A}e^{-i\kappa(x-ct)} \tag{3.14}$$

where, A is the amplitude and it can be complex. Based on this solution, a summary of the wave relations is presented in Table 3-1.

Table 3-1 Summary of wave relations

Name	Symbol	Formula	Dimension
Amplitude	A	---	length
Phase	Φ	$(\kappa x - \omega t)$	Radians
Radial(angular) frequency	ω	kc	Radians/time
Cyclic frequency	f	$\omega/2\pi$	Hertz,1/time
Wavelength	λ	$2\pi/\kappa$	length
Wavenumber	κ	$2\pi/\lambda$	1/length
Phase speed	c	ω/κ	Length/time
Group speed	c_g	$d\omega/d\kappa$	Length/time
Period	T	$1/f$	Time

In addition to the relations that are presented in Table 3-1, there are two other important relations that are used in wave propagation analysis—namely, spectrum relation and dispersion relation. Spectrum relation is the relation between the wavenumber (κ) and radial frequency (ω). The spectrum relation for the longitudinal wave propagation in a thin rod is:

$$k = \pm\omega\sqrt{\frac{\rho}{E}} \tag{3.15}$$

The dispersion relation is the relation between the phase speed (c) and radial frequency (ω). The dispersion relation for the longitudinal wave motion can be expressed by:

$$c = \frac{\omega}{k} = \sqrt{\frac{E}{\rho}} = c_0 \tag{3.16}$$

Due to the importance of the concepts of the phase and group speed in wave propagation, a brief explanation about these concepts is provided herein.

3.3.1 Phase speed

In general, the wavenumber of a wave motion can have real and imaginary parts:

$$\kappa = \kappa_R + i\kappa_I \tag{3.17}$$

Therefore, the general solution of the one-dimensional wave propagation in rods can be written in the following form (Doyle (1989)):

$$u(x,t) = \sum \hat{F}_n e^{-k_I x} e^{-i(k_R x - \omega t)} \tag{3.18}$$

The wave motion in equation ((3.18) has three distinct parts:

$\hat{F}_n$: Amplitude spectrum

$e^{-k_I x}$: Spatially decaying term

$e^{-i(k_R x - \omega t)}$: Harmonic propagating waves

Each individual harmonic wave moves with a speed that is called "phase speed". To keep the harmonic waves moving with the phase speed, it is required to keep the phase of the harmonic waves constant as the time increases. Hence, the phase speed can be found as:

$$c = \frac{\omega}{\kappa_R} \tag{3.19}$$

3.3.2 Group Speed

Phase speed is the propagation speed of individual harmonics. The complete solution of a wave is the superposition of all the harmonic waves as a group. This group might have a different response than the individual response. Group speed is a parameter that can be used for analyzing the group behavior. It can be found using the following relationship (Doyle (1989)):

$$c_g = \frac{d\omega}{d\kappa} = c + \kappa \frac{dc}{d\kappa} \tag{3.20}$$

In general, the phase speed and group speed are not equal. The group speed of the longitudinal wave motion is:

$$c_g = \frac{d\omega}{dk} = \sqrt{\frac{E}{\rho}} = c_0 \tag{3.21}$$

The above equation shows that the phase and group speeds are equal, which means that the longitudinal wave in rods is non-dispersive and the shape of the wave will not change as it propagates.

The material properties and the wave speed of some of the commonly used materials are presented in Table 3-2. In this table, z is the impedance of each medium, which is the product of density and the wave velocity:

$$z = \rho c = \sqrt{\rho E} \tag{3.22}$$

Table 3-2 Properties of some materials for wave propagation analysis

Material	Density (kg/m^3)	Young's Modulus (GPa)	Wave speed (m/sec)	Impedance $(kg/m^2 . sec)$	Impedance Ratio (z_{steel}/z)
Aluminum	2700	72.7	5189	14.0E+06	2.8
Brass	8100	82.3	3188	25.8E+06	1.5
Cadmium	8650	50	2404	20.8E+06	1.9
Concrete	2400	27.4	3379	8.1E+06	4.9
Copper	8500	89.1	3238	27.5E+06	1.4
Epoxy	1000	3.4	1844	1.8E+06	21.5
Glass	2300	68.6	5461	12.6E+06	3.2
Gold	19300	79	2023	39.0E+06	1.0
Iron	7874	211	5177	40.8E+06	1.0
Lead	11340	16	1188	13.5E+06	2.9
Magnesium	1738	45	5088	8.8E+06	4.5
Nickel	8908	200	4738	42.2E+06	0.9
Rock	2500	30.1	3470	8.7E+06	4.6
Silver	10490	83	2813	29.5E+06	1.3
Steel	7850	200	5048	39.6E+06	1.0
Tin	7365	50	2606	19.2E+06	2.1
Tungsten	19250	411	4621	88.9E+06	0.4
Zinc	7140	108	3889	27.8E+06	1.4
Oak black Wood	669	11.53	4151	2.8E+06	14.1

3.3.3 Mechanical relations

Since we have the solution of wave motion, the mechanical relationships for a particular frequency can be easily derived. These relationships are listed in Table 3-3. The relations are shown separately for forward moving (designated with the index i) and backward moving (designated with the index r) waves. It is assumed that the deformations are small and material has an elastic behavior. It is worthwhile to note that the particle velocity and stress have the same profile; however, forward moving (tensile) stress causes backward movement in the particles (negative velocity) and vice versa (Doyle (1989)).

Table 3-3 Mechanical relationships for an elastic material with small deformations assumption

Parameter	Forward moving wave	Backward moving wave
Displacement	$u_i = Ae^{-i(kx-\omega t)}$	$u_r = Be^{i(kx+\omega t)}$
Strain	$\varepsilon_i = du_i/dx = -iku_i$	$\varepsilon_r = du_r/dx = iku_r$
Stress	$\sigma_i = E\varepsilon_i = -ikEu_i$	$\sigma_r = E\varepsilon_r = ikEu_r$
Force	$F_i = A\sigma_i = -ikEAu_i$	$F_r = A\sigma_r = ikEAu_r$
Particle Velocity	$v_i = du_i/dt = i\omega u_i = ikc_0u_i = -\frac{c_0}{E}\sigma_i$	$v_r = du_r/dt = i\omega u_r = ikc_0u_r = \frac{c_0}{E}\sigma_r$

3.4 Reflection and transmission at discontinuities of rod structures

In reality all of the structures have finite length, and the wave encounters different types of discontinuities as it passes through a physical medium. Discontinuity is a general term that can be attributed to any type of change in the material properties, geometry, and boundary conditions of a system, which results in the reflection and/or transmission of waves.

In this section, different types of discontinuities in rod structures are extensively investigated. These discontinuities include different types of end boundaries and changes in the material properties (impedance mismatch) along the wave path.

3.4.1 End boundaries in rods

As we know the wave solution in an infinite rod produces forward and backward moving waves (see equation ((3.13)):

$u(x,t) = \sum \alpha e^{-i(kx-\omega t)} + \sum \beta e^{+i(kx+\omega t)}$

For a finite rod, the incident wave produces a reflected wave at the boundary. These two waves are superposed at the boundary to satisfy the boundary conditions. The incident wave is the forward moving wave with the amplitude α which is known. Our problem is to find the unknown reflected wave with the amplitude β. The end boundary conditions are applied in terms of displacement (u), velocity ($\dot{u}$), and force ($EA\, du/dx$). Table 3-4 shows the properties of different types of boundary conditions in the time domain and spectral analysis format.

Table 3-4 Some boundary condition properties (Doyle (1989))

Type of Boundary	Time domain	Spectral Analysis
Fixed	$u(0,t) = 0$	$\hat{u} = 0$
Free	$EA\, \partial u(0,t)/\partial x = 0$	$EA\, d\hat{u}(0)/dx = 0$
Spring	$EA\, \partial u(0,t)/\partial x = -Ku(0,t)$	$EA\, d\hat{u}(0)/dx = -K\hat{u}(0)$
Dashpot	$EA\, \partial u(0,t)/\partial x = -\eta\, \partial u(0,t)/\partial t$	$EA\, d\hat{u}(0)/dx = \eta i\omega\hat{u}(0)$
Mass	$EA\, \partial u(0,t)/\partial x = -m\, \partial^2 u(0,t)/\partial t^2$	$EA\, d\hat{u}(0)/dx = m\omega^2\hat{u}(0)$

Fixed end

The displacement at the fixed end ($x = 0$) is zero; therefore we can write:

$\hat{u}(x) = \alpha e^{-ikx} + \beta e^{+ikx} \Rightarrow \hat{u}(0) = \alpha + \beta = 0$

Therefore:

$$\alpha = -\beta \tag{3.23}$$

This means that the reflected displacement wave is inverted at the fixed boundary. Now, the incident and reflected waves can be shown by:

Incident displacement = $u_i = \alpha e^{-ikx}$

Reflected displacement = $u_r = -\alpha e^{+ikx}$

The corresponding stresses are:

Incident stress: $\sigma_i = -ikE\alpha e^{-ikx}$

Reflected stress: $\sigma_r = -ikE\alpha e^{+ikx}$

Thus, the reflected stress wave is the same as the incident wave. Incident and reflected waves are superposed at the boundary. Therefore, at $x = 0$ we have:

$\sigma|_{x=0} = \sigma_i|_{x=0} + \sigma_r|_{x=0} = -2ikE\alpha = 2\sigma_i|_{x=0}$

This shows that a stress pulse is doubled at a fixed boundary; a classically known finding. The main characteristics of the fixed boundary are:

- Displacement pulse will be inverted after reflection from a fixed boundary.
- Stress pulse will remain the same after reflection from a fixed boundary.
- Incident stress pulse is doubled when it hits a fixed boundary.

Free end

To insure the zero stress condition at a free boundary, we have (it is assumed that the free boundary is at $x = 0$):

$\sigma(x) = E\left(-\alpha ike^{-ikx} + \beta ike^{+ikx}\right) \Rightarrow \sigma(0) = E(-\alpha ik + \beta ik) = 0$

Therefore:

$$\alpha = \beta \tag{3.24}$$

The incident and reflected stresses are:

Incident stress at a free boundary: $\sigma_i = -ikE\alpha e^{-ikx}$

Reflected stress at a free boundary: $\sigma_r = ikE\alpha e^{+ikx}$

This shows that stress will be inverted at a free boundary. For a displacement pulse at the free boundary we can write:

$u|_{x=0} = u_i|_{x=0} + u_r|_{x=0} = 2\alpha = 2u_i|_{x=0}$

This means that the displacement pulse will be doubled at the free boundary. The main characteristics of the free boundary are:

- Stress pulse will be inverted after reflection from a free boundary.
- Displacement pulse will remain the same after reflection from a free boundary.
- Incident displacement pulse is doubled when it hits a free boundary.

In Table 3-5, the reflection characteristics of fixed and free boundaries are compared.

Table 3-5 Comparison of the fixed and free boundary conditions in rods

Boundary	Reflected stress (σ_r)	Reflected Disp. (u_r)	Stress at boundary ($\sigma\|_{x=0}$)	Disp. at boundary ($u\|_{x=0}$)
Fixed	No change	Inverted	Doubled	Zero
Free	Inverted	No change	Zero	Doubled

Elastic boundaries

A typical elastic boundary condition (spring) is shown in Figure 3-3. The force condition at $x = 0$ requires:

$EA\,\partial u(0,t)/\partial x = -Ku(0,t) \Rightarrow EA(-ik\alpha + ik\beta) = -K(\alpha+\beta)$

Thus, the amplitude of reflected wave is (Doyle (1989)):

$$\beta = \frac{ikEA - K}{ikEA + K}\alpha \tag{3.25}$$

To check the accuracy of the derived equation, we can consider the limits on the stiffness of the spring. If the stiffness of the spring becomes zero ($K = 0$), it is similar to the free boundary and we have:

$\beta = \alpha$

Similarly, for a very stiff spring ($K = \infty$) we have the fixed end condition:

$\beta = -\alpha$

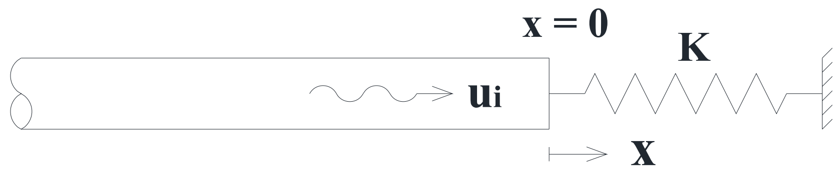

Figure 3-3 Elastic boundary condition (spring)

Equation ((3.25) can be written in terms of the frequency (ω), and the relation between the reflected and incident amplitudes can be expressed by the following transfer function:

$$G(\omega) = \frac{i\omega EA - Kc_0}{i\omega EA + Kc_0} \tag{3.26}$$

This transfer function can be expressed by real and imaginary parts:

$$G(\omega) = \frac{(\omega EA)^2 - (Kc_0)^2}{(\omega EA)^2 + (Kc_0)^2} + \frac{2EAKc_0\omega}{(\omega EA)^2 + (Kc_0)^2} i \tag{3.27}$$

$$(Re)_G = \frac{(\omega EA)^2 - (Kc_0)^2}{(\omega EA)^2 + (Kc_0)^2} \tag{3.28}$$

$$(Im)_G = \frac{2EAKc_0\omega}{(\omega EA)^2 + (Kc_0)^2} \tag{3.29}$$

$$Amplitude = \sqrt{{(Re)_G}^2 + {(Im)_G}^2} = 1 \tag{3.30}$$

Similar to the stiffness limits, the behavior of the spring can be investigated for the frequency limits. For very low frequencies ($\omega \to 0$), the transfer function is equal to -1, which means that the spring behaves as a rigid end condition for low frequency loadings. On the other hand, for very high frequencies ($\omega \to \infty$), the transfer is unity and the spring behaves as a free end. Considering equation ((3.26), we can say:

- The effect of elastic boundary condition is dependent to the frequency; therefore, each frequency component is affected differently. Consequently, for a pulse with a spectrum of frequencies the reflected signal will be distorted (Doyle (1989)).
- The propagated signal (longitudinal wave) is inherently non-dispersive; however, it becomes dispersive when it interacts with elastic boundary condition.

3.4.2 Impedance mismatch

When the material properties and/or cross section change along the path of a longitudinal wave, reflection and transmission will occur at the interface of the two media. This happens due to the impedance mismatch between the two sections. To study this phenomenon, three different types of problems are explored in this section: "lumped mass", "stepped rod", and "elastic joint". In all of the problems, the reflected and transmitted waves are defined by considering the continuity of force and displacement at the interface.

Lumped mass

Consider two similar rods that are connected by a mass (Figure 3-4). To satisfy the continuity of force and displacement at the interface we can write ((Doyle 1989)):

$$F_1 - F_2 = m_c \ddot{u}_c \tag{3.31}$$

$$u_1 = u_2 = u_c \tag{3.32}$$

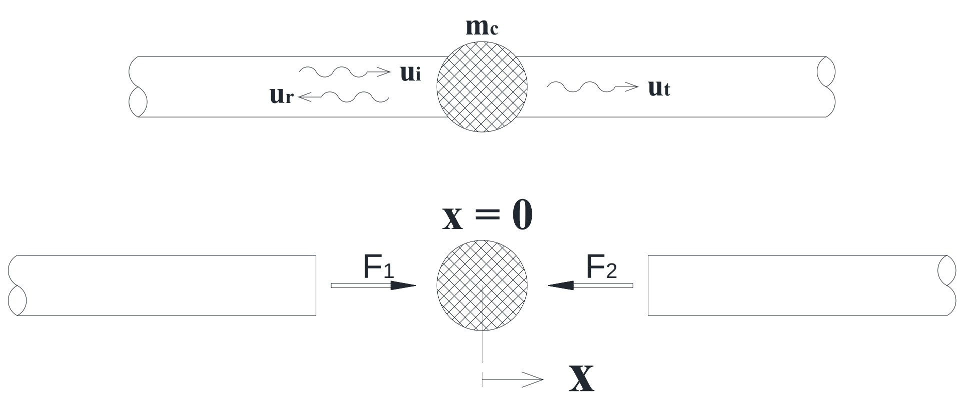

Figure 3-4 Effect of lumped mass on reflection and transmission of waves

If we assume that the amplitudes of incident, reflected, and transmitted waves are α_1, β_1, and α_2, respectively, we have (assuming that the cross section and material properties of the rods are similar):

$$u_1 = \left\{\alpha_1 e^{-ik_1 x} + \beta_1 e^{ik_1 x}\right\} e^{i\omega t} \tag{3.33}$$

$$u_2 = \{\alpha_2 e^{-ik_2 x}\} e^{i\omega t} \tag{3.34}$$

$$F_1 = EA\left\{-ik_1\alpha_1 e^{-ik_1x} + ik_1\beta_1 e^{ik_1x}\right\}e^{i\omega t} \tag{3.35}$$

$$F_2 = EA\{-ik_2\alpha_2 e^{-ik_2x}\}e^{i\omega t} \tag{3.36}$$

For simplicity, it is assumed that the center of the lumped mass is located at $x = 0$. Consequently, we can write:

$$EA\{-ik_1\alpha_1 + ik_1\beta_1\} - EA\{-ik_2\alpha_2\} = -m_c\alpha_2\omega^2 \tag{3.37}$$

$$\alpha_1 + \beta_1 = \alpha_2 \tag{3.38}$$

By solving equations ((3.37) and ((3.38) simultaneously, β_1 and α_2 can be found in term of α_1.

$$\beta_1 = \frac{-m_c\omega^2}{2ikEA + m_c\omega^2}\alpha_1 \tag{3.39}$$

$$\alpha_2 = \frac{2ikEA}{2ikEA + m_c\omega^2}\alpha_1 \tag{3.40}$$

Based on equations ((3.39) and ((3.40) following results can be concluded:

- The effect of lumped mass on the wave propagation is frequency dependent. This means that the wave can be distorted.
- At very small frequencies the mass has no effect on the propagating wave:
  $\omega \to 0 \Rightarrow \beta_1 = 0 \ \ and \ \ \alpha_2 = \alpha_1$
- At very high frequencies the mass behaves as a rigid boundary and wave cannot be transmitted:
  $\omega \to \infty \Rightarrow \beta_1 = -\alpha_1 \ \ and \ \ \alpha_2 = 0$
- The similar limit can be observed for the mass limits:
  $m_c \to 0 \Rightarrow \beta_1 = 0 \ \ and \ \ \alpha_2 = \alpha_1$
  $m_c \to \infty \Rightarrow \beta_1 = -\alpha_1 \ \ and \ \ \alpha_2 = 0$
- The summation of the magnitudes of the amplitude of the reflected and transmitted waves is always equal to unity ($|\beta_1| + |\alpha_2| = 1$).

Changing the material properties and/or cross section

When a wave enters a different medium with different material properties and/or cross section, reflection and transmission occurs at the intersection of the two media. Figure 3-5 shows two rods with different material and cross section properties that are attached at $x = 0$.

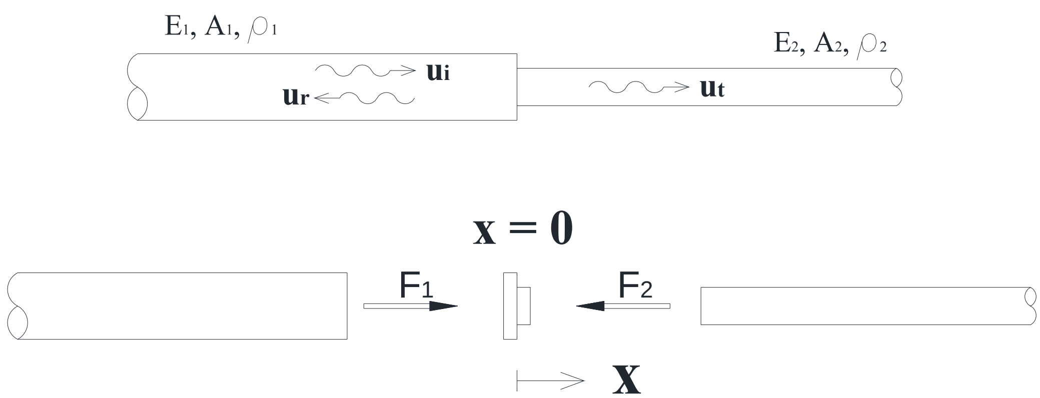

Figure 3-5 Effect of changing material properties and cross section

According to the continuity of force and displacement at the interface ($x = 0$), we have:

$$F_1 = F_2; \quad u_1 = u_2 \tag{3.41}$$

Therefore,

$$EA\{-ik_1\alpha_1 + ik_1\beta_1\} = EA\{-ik_2\alpha_2\} \tag{3.42}$$

$$\alpha_1 + \beta_1 = \alpha_2 \tag{3.43}$$

Solving equations ((3.42) and ((3.43) gives:

$$\beta_1 = \frac{1 - \sqrt{\frac{E_2}{E_1}\frac{\rho_2}{\rho_1}\left(\frac{A_2}{A_1}\right)^2}}{1 + \sqrt{\frac{E_2}{E_1}\frac{\rho_2}{\rho_1}\left(\frac{A_2}{A_1}\right)^2}}\alpha_1 = \frac{1 - \frac{z_2 A_2}{z_1 A_1}}{1 + \frac{z_2 A_2}{z_1 A_1}}\alpha_1 \tag{3.44}$$

$$\alpha_2 = \frac{2}{1+\sqrt{\frac{E_2}{E_1}\frac{\rho_2}{\rho_1}\left(\frac{A_2}{A_1}\right)^2}}\alpha_1 = \frac{2}{1+\frac{z_2 A_2}{z_1 A_1}}\alpha_1 \tag{3.45}$$

where, z is the impedance of each medium (equation (3.22).

Equations ((3.44) and ((3.45) show that the response is independent of frequency. For the static loads, changing the material properties and cross section is exactly similar to the problem of an elastic spring. However, since we have distributed mass in the stepped rod problem the response is completely independent of frequency while in the elastic spring the results are frequency dependent.

Since the reflected and transmitted amplitudes are known, the reflected and transmitted stresses can be found as:

$$\sigma_{\mathrm{r}} = \frac{-\beta_1}{\alpha_1}\sigma_{\mathrm{i}} = \frac{\frac{z_2 A_2}{z_1 A_1} - 1}{\frac{z_2 A_2}{z_1 A_1} + 1}\sigma_{\mathrm{i}} \tag{3.46}$$

$$\sigma_{\mathrm{t}} = \frac{E_2}{E_1}\frac{k_2}{k_1}\frac{\alpha_2}{\alpha_1}\sigma_{\mathrm{i}} = \frac{E_2}{E_1}\frac{c_1}{c_2}\frac{\alpha_2}{\alpha_1}\sigma_{\mathrm{i}} = \frac{z_2}{z_1}\frac{\alpha_2}{\alpha_1}\sigma_{\mathrm{i}} = \frac{2\frac{z_2}{z_1}}{1+\frac{z_2 A_2}{z_1 A_1}}\sigma_{\mathrm{i}} \tag{3.47}$$

If the second medium has very small impedance ($z_2 \to 0$), it is similar to the free end condition ($\sigma_{\mathrm{r}} = -\sigma_{\mathrm{i}}$ and $\sigma_{\mathrm{t}} = 0$).

If the second medium has very large impedance ($z_2 \to \infty$), it is similar to the fixed end condition ($\sigma_{\mathrm{r}} = \sigma_{\mathrm{i}}$ and $\sigma_{\mathrm{t}} = 2\frac{A_1}{A_2}\sigma_{\mathrm{i}}$). Therefore, if the cross section of the two rods are equal ($A_1 = A_2$), the transmitted amplitude will be doubled when the second rod has very large impedance.

Effect of a finite elastic rod between two long bars

Consider an elastic finite bar that is implanted between two long elastic rods. If the material properties of the two long bars are the same, the problem would be very similar to a Split Hopkinson test.

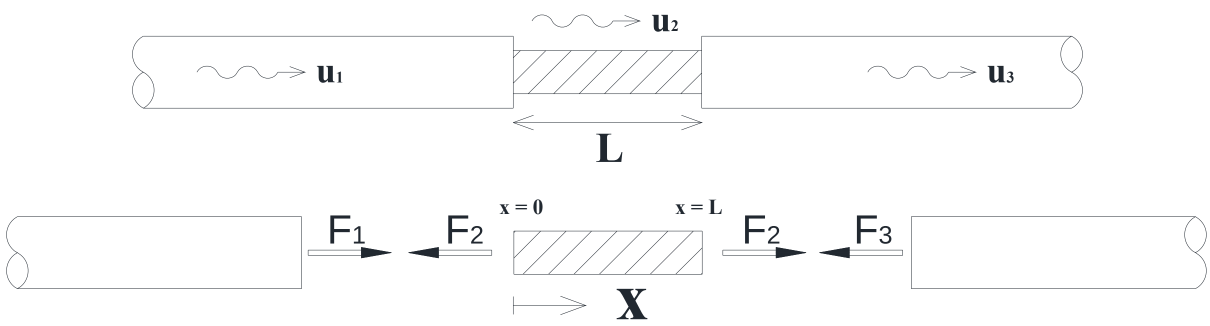

Figure 3-6 Effect of a finite rod between two long bars on wave propagation

Figure 3-6 shows the displacements and forces of the three bars. According to the continuity of displacement and stress at the two sides of the finite rod, we can write:

$$at\ x = 0, \quad u_1 = u_2 \quad and \quad F_1 = F_2 \tag{3.48}$$

$$at\ x = L, \quad u_2 = u_3 \quad and \quad F_2 = F_3 \tag{3.49}$$

where,

$$u_1 = \alpha_1 e^{-ik_1x} + \beta_1 e^{ik_1x} \quad and \quad F_1 = (EA)_1\left\{-ik_1\alpha_1 e^{-ik_1x} + ik_1\beta_1 e^{ik_1x}\right\} \tag{3.50}$$

$$u_2 = \alpha_2 e^{-ik_2x} + \beta_2 e^{ik_2x} \quad and \quad F_2 = (EA)_2\left\{-ik_2\alpha_2 e^{-ik_2x} + ik_2\beta_2 e^{ik_2x}\right\} \tag{3.51}$$

$$u_3 = \alpha_3 e^{-ik_3x} \qquad and \quad F_3 = (EA)_3\left\{-ik_3\alpha_3 e^{-ik_3x}\right\} \tag{3.52}$$

By substituting equations ((3.50) to ((3.52) in equations ((3.48) and ((3.49), we can write the reflected and transmitted amplitudes in the following matrix form ((Doyle 1989)):

$$\begin{bmatrix} -1 & 1 & 1 & 0 \\ (kEA)_1 & (kEA)_2 & -(kEA)_2 & 0 \\ 0 & e^{-ik_2L} & e^{ik_2L} & -e^{-ik_3L} \\ 0 & -(kEA)_2 e^{-ik_2L} & (kEA)_2 e^{ik_2L} & (kEA)_3 e^{-ik_3L} \end{bmatrix} \begin{Bmatrix} \beta_1 \\ \alpha_2 \\ \beta_2 \\ \alpha_3 \end{Bmatrix} = \begin{Bmatrix} 1 \\ (kEA)_1 \\ 0 \\ 0 \end{Bmatrix} \alpha_1 \tag{3.53}$$

The general solution of equation ((3.53) is very long. In the following the solution is given for a special case when rods one and three have the same material properties ($E_1 = E_2 = E$ and $k_1 = k_2 = k$) and the cross section of all of the rods are equal ($A_1 = A_2 = A_3 = A$). Please note that the results are presented in terms of frequency (ω).

$$\beta_1 = \frac{Ec_2\left(E_2c - Ec_2 + E_2ce^{\left(\frac{2iLw}{c_2}\right)} + Ec_2e^{\left(\frac{2iLw}{c_2}\right)}\right) - \left(E_2^2c^2e^{\left(\frac{2iLw}{c_2}\right)} - E_2^2c^2 + E_2Ecc_2 + E_2Ecc_2e^{\left(\frac{2iLw}{c_2}\right)}\right)}{E_2^2c^2e^{\left(\frac{2iLw}{c_2}\right)} - E^2c_2^2 - E_2^2c^2 + E^2c_2^2e^{\left(\frac{2iLw}{c_2}\right)} + 2E_2Ecc_2 + 2E_2Ecc_2e^{\left(\frac{2iLw}{c_2}\right)}} \tag{3.54}$$

$$\alpha_2 = \frac{2Ec_2e^{\left(\frac{iLw}{c_2}\right)}\left(E_2ce^{\left(\frac{iLw}{c_2}\right)} + Ec_2e^{\left(\frac{iLw}{c_2}\right)}\right)}{E_2^2c^2e^{\left(\frac{2iLw}{c_2}\right)} - E^2c_2^2 - E_2^2c^2 + E^2c_2^2e^{\left(\frac{2iLw}{c_2}\right)} + 2E_2Ecc_2 + 2E_2Ecc_2e^{\left(\frac{2iLw}{c_2}\right)}} \tag{3.55}$$

$$\beta_2 = \frac{2Ec_2(E_2c - Ec_2)}{E_2^2c^2e^{\left(\frac{2iLw}{c_2}\right)} - E^2c_2^2 - E_2^2c^2 + E^2c_2^2e^{\left(\frac{2iLw}{c_2}\right)} + 2E_2Ecc_2 + 2E_2Ecc_2e^{\left(\frac{2iLw}{c_2}\right)}} \tag{3.56}$$

$$\alpha_3 = \frac{4E_2Ecc_2e^{\left(\frac{iLw}{c}\right)}e^{\left(\frac{2iLw}{c_2}\right)}}{E_2^2c^2e^{\left(\frac{2iLw}{c_2}\right)} - E^2c_2^2 - E_2^2c^2 + E^2c_2^2e^{\left(\frac{2iLw}{c_2}\right)} + 2E_2Ecc_2 + 2E_2Ecc_2e^{\left(\frac{2iLw}{c_2}\right)}} \tag{3.57}$$

3.5 Summary

In this section, the solution of wave propagation in thin rods is reviewed extensively, and basic concepts and relations of wave propagation in solids are introduced based on this solution. In addition, a review of the wave reflection and transmission characteristics at different types of discontinuities in rod structures is presented in this section. These discontinuities include various types of end boundary conditions and changes in the material and cross section properties. The analyses show that the reflection and transmission properties are very different for various types of discontinuities. Some discontinuities such as lumped mass and elastic boundaries can disperse the waves although the propagating signal is inherently non-dispersive, while some others such as stepped rods induce no dispersion.

SECTION 4
WAVE REFLECTION AND TRANSMISSION IN BEAMS

4.1 Introduction

Beams are one of the major structural components that can carry lateral loads. Because of the lateral loading, the displacement of a beam is transverse to the centerline, and therefore, under dynamic loadings flexural waves will be generated in the beam structures.

There are significant differences between the wave propagation in rods and beams. Beams have higher order differential equations in comparison to the rods and there is no D'Alembert solution available. Flexural waves in beams are dispersive, and due to the inherent higher order differential equations, they have two fundamental modes—propagating and evanescent (near field).

There are different types of formulations that describe the kinematic relations of beams such as Euler-Bernoulli, Rayleigh, and Timoshenko. Based on the assumptions for calculating the lateral deformation of each beam formulation, the associated dynamic behavior is different. Euler-Bernoulli formulation is appropriate for analysis of beams under low frequency excitations as it predicts unrealistic speed of waves at high frequencies due to neglecting the effect of rotary inertia. Timoshenko formulation for beams, on the other hand, considers the effect of shear deformation and rotary inertia. Therefore, more accurate results can be achieved for either low or high frequency excitations. Due to these facts, this section only focuses on the behavior of Timoshenko structures.

In this section, the flexural wave propagation formulation in Timoshenko beams and the effect of different types of discontinuities on the wave reflection and transmission in these structures are investigated extensively.

4.2 Wave propagation in Timoshenko beams

As mentioned in the previous section, the Euler-Bernoulli model is not appropriate for analyzing the beams under very high frequency loads. Rayleigh (1926) considered the effect of rotary inertia in the wave propagation formulation of beams. Timoshenko (1921) and (1922) extended Rayleigh's assumption and introduced the effect of shear deformation in addition to the rotary inertia.

4.2.1 Governing differential equation of Timoshenko beams

To derive the governing differential equation, consider a Timoshenko beam in Figure 4-1 which is under positive bending moment and shear force. The positive directions of moment and shear forces are shown on an element of the beam. The equation of motion (momentum balance) for this element in the vertical direction can be written as:

$$\sum F_y = m\ddot{y} \Rightarrow -V + \left(V + \frac{\partial V}{\partial x}\Delta x\right) + q\Delta x - \rho A \Delta x \frac{\partial^2 y}{\partial t^2} = 0$$

or

$$\frac{\partial V}{\partial x} + q = \rho A \frac{\partial^2 y}{\partial t^2} \tag{4.1}$$

Similarly, the equation of motion can be written for the moments for an axis which is perpendicular to x-y plane and passes through the center of the element:

$$\sum M = J\ddot{\psi} \Rightarrow -M + \left(M + \frac{\partial M}{\partial x}\Delta x\right) + V\Delta x - J\frac{\partial^2 \psi}{\partial t^2} = 0$$

where, J is the polar moment of inertia about the perpendicular axis to x-y plane and can be written as:

$$J = \int \rho y^2 dV = \int \rho y^2 \Delta x dA = \rho \Delta x I$$

where, I is the second moment of area of the cross section of the beam about the axis of perpendicular to x-y plane. Consequently, the moment equilibrium equation can be written as:

$$\frac{\partial M}{\partial x} + V = \rho I \frac{\partial^2 \psi}{\partial t^2} \tag{4.2}$$

According to Figure 4-1, the displacements of the beam can be written as:

$$u_x = -y\psi(x,t); \quad u_y = y(x,t); \quad u_z = 0 \tag{4.3}$$

For small deformations the strain-displacement relations are:

$$\varepsilon_{xx} = \frac{\partial u_x}{\partial x} = -y\frac{\partial \psi}{\partial x}; \quad \varepsilon_{xy} = \frac{1}{2}\left(\frac{\partial u_x}{\partial y} + \frac{\partial u_y}{\partial x}\right) = \frac{1}{2}\left(-\psi + \frac{\partial y}{\partial x}\right) \tag{4.4}$$

where, ψ is the rotation angle of the normal to the cross section and $\frac{\partial y}{\partial x}$ is the slope of the midline. The difference between these two angles is the shearing angle γ_0 which is shown in Figure 4-1.

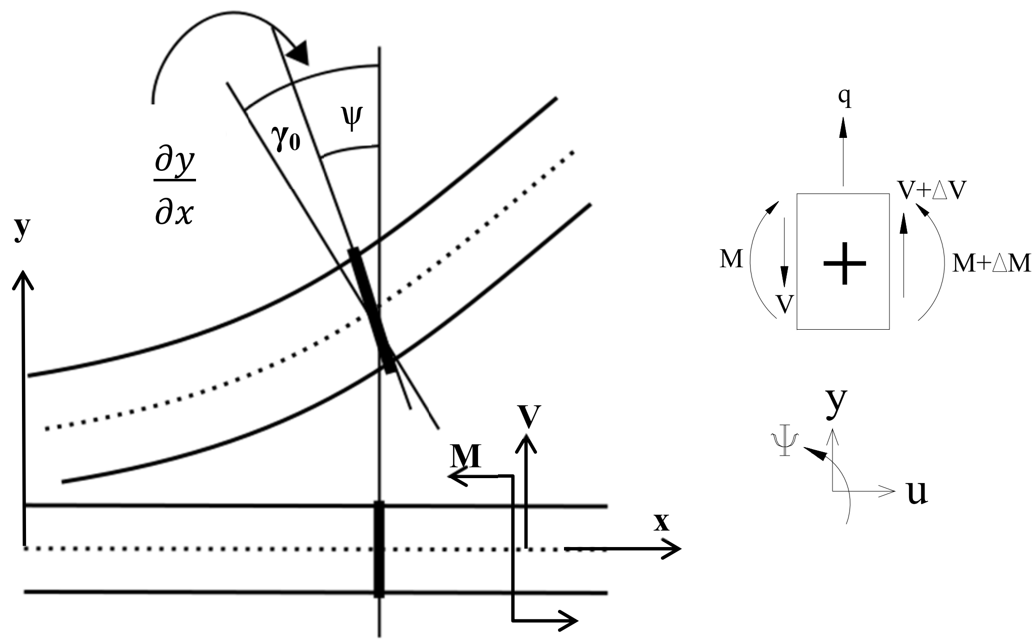

Figure 4-1 Kinematics of Timoshenko beam under flexure

The actual shear is not constant over the cross section. Therefore, a correction factor should be used for ε_{xy}:

$$\varepsilon_{xy} = \frac{1}{2}\kappa\left(-\psi + \frac{\partial y}{\partial x}\right) \tag{4.5}$$

Based on the sign of the positive moment and shear force in Figure 4-1 we can write:

$$M(x) = -\int y\sigma_{xx} dA = -\int yE\varepsilon_{xx} dA = \int y^2 E\frac{\partial \psi}{\partial x} dA = EI\frac{\partial \psi}{\partial x} \tag{4.6}$$

$$V(x) = \int \sigma_{xy} dA = \int 2G\varepsilon_{xy} dA = \int \kappa G\left(-\psi + \frac{\partial y}{\partial x}\right) dA = \kappa AG\left(-\psi + \frac{\partial y}{\partial x}\right) \tag{4.7}$$

By substituting equations (4.6) and (4.7) into equations (4.1) and (4.2), the equations of motion can be written in terms of the rotation angle $\psi(x,t)$ and the transverse deflection $y(x,t)$ of the beam as follows

$$\kappa AG\left(\frac{\partial\psi}{\partial x}-\frac{\partial^2 y}{\partial x^2}\right)+\rho A\frac{\partial^2 y}{\partial t^2}=q(x,t) \tag{4.8}$$

$$\kappa AG\left(\frac{\partial y}{\partial x}-\psi\right)+EI\frac{\partial^2\psi}{\partial x^2}=\rho I\frac{\partial^2\psi}{\partial t^2} \tag{4.9}$$

When no external force is applied, the free vibration equation of the beam can be found by eliminating ψ from equations (4.8) and (4.9):

$$\frac{EI}{\rho A}\frac{\partial^4 y}{\partial x^4}-\frac{I}{A}\left(1+\frac{E}{G\kappa}\right)\frac{\partial^4 y}{\partial x^2\partial t^2}+\frac{\partial^2 y}{\partial t^2}+\frac{\rho I}{\kappa AG}\frac{\partial^4 y}{\partial t^4}=0 \tag{4.10}$$

The solution for the above equation can be written as:

$$y(x,t)=\ \alpha e^{-ikx}e^{i\omega t} \tag{4.11}$$

For convenience, we can define the following parameters for solving equation (4.10):

$$C_b=\sqrt{\frac{EI}{\rho A}};\quad C_s=\sqrt{\frac{GA\kappa}{\rho A}};\quad C_r=\sqrt{\frac{\rho I}{\rho A}} \tag{4.12}$$

C_b, C_s, and C_r represent bending, shear, and rotational stiffness of the beam. By substituting equation (4.11) into equation (4.10), and using the stiffness parameters the following fourth-order equation can be written in terms of the wavelength (κ) and frequency (ω):

$$\kappa^4-\left[\left(\frac{1}{C_s}\right)^2+\left(\frac{C_r}{C_b}\right)^2\right]\omega^2\kappa^2-\left(\frac{1}{C_b}\right)^2\omega^2+\left(\frac{C_r}{C_bC_s}\right)^2\omega^4=0 \tag{4.13}$$

This equation is the dispersion equation of the beam and its solution takes the following form:

$$k = \pm\left\{\frac{1}{2}\left[\left(\frac{1}{C_s}\right)^2 + \left(\frac{C_r}{C_b}\right)^2\right]\omega^2 \pm \sqrt{\left(\frac{\omega}{C_b}\right)^2 + \frac{1}{4}\left[\left(\frac{1}{C_s}\right)^2 - \left(\frac{C_r}{C_b}\right)^2\right]^2 \omega^4}\right\}^{\frac{1}{2}} \tag{4.14}$$

Since there is no linear relationship between the wavelength and frequency, the flexural waves in Timoshenko beams are dispersive. There are two $\pm$ signs in the above equation. The first sign indicates that the waves are moving in positive and negative directions, while the second sign (in the middle of bracket) relates to the existence of two different pairs of wavenumbers (two different modes). The first pair is always a real number, and its corresponding wave is a propagating wave because e^{-ikx} will have an imaginary term. The type of the corresponding wave of the second pair depends on the frequency of the applied load. Based on the material and geometrical properties of the beam, there is a cutoff frequency (ω_c). This frequency is defined as:

$$\omega_c = \frac{C_s}{C_r} \tag{4.15}$$

If $\omega < \omega_c$, the second pair of the wave numbers is imaginary, which means that the second mode of the wave is a decaying or evanescent wave. This is the most common situation because the value of the cutoff frequency is usually high.

If $\omega > \omega_c$, the second pair of the wave numbers is real; therefore, the second mode will also be a propagating wave. This condition happens in applications when the frequency of the applied load is very high such as audio-frequency applications, Mei and Mace (2005).

The spectral solution for equation (4.10) can be written by suppressing the time dependence $e^{i\omega t}$ as follows (Mei (2012)):

$$y(x) = a_1^+ e^{-ik_1 x} + a_2^+ e^{-k_2 x} + a_1^- e^{ik_1 x} + a_2^- e^{k_2 x} \tag{4.16}$$

A similar equation can be written for the angle of rotation:

$$\psi(x) = \overline{a_1^+} e^{-ik_1 x} + \overline{a_2^+} e^{-k_2 x} + \overline{a_1^-} e^{ik_1 x} + \overline{a_2^-} e^{k_2 x} \tag{4.17}$$

where, k_1 and k_2 are the propagating and evanescent wavenumbers:

$$k_1 = \left\{ \frac{1}{2}\left[\left(\frac{1}{C_s}\right)^2 + \left(\frac{C_r}{C_b}\right)^2\right]\omega^2 + \sqrt{\left(\frac{\omega}{C_b}\right)^2 + \frac{1}{4}\left[\left(\frac{1}{C_s}\right)^2 - \left(\frac{C_r}{C_b}\right)^2\right]^2 \omega^4} \right\}^{\frac{1}{2}} \tag{4.18}$$

$$\begin{aligned} k_2 &= \left\{ \left| \frac{1}{2}\left[\left(\frac{1}{C_s}\right)^2 + \left(\frac{C_r}{C_b}\right)^2\right]\omega^2 - \sqrt{\left(\frac{\omega}{C_b}\right)^2 + \frac{1}{4}\left[\left(\frac{1}{C_s}\right)^2 - \left(\frac{C_r}{C_b}\right)^2\right]^2 \omega^4} \right| \right\}^{\frac{1}{2}} \quad if\ \omega < \omega_c \\ k_2 &= i\left\{ \left| \frac{1}{2}\left[\left(\frac{1}{C_s}\right)^2 + \left(\frac{C_r}{C_b}\right)^2\right]\omega^2 - \sqrt{\left(\frac{\omega}{C_b}\right)^2 + \frac{1}{4}\left[\left(\frac{1}{C_s}\right)^2 - \left(\frac{C_r}{C_b}\right)^2\right]^2 \omega^4} \right| \right\}^{\frac{1}{2}} \quad if\ \omega > \omega_c \end{aligned} \tag{4.19}$$

The amplitudes of the transverse deflection y and the angle of rotation ψ can be found by considering equations (4.8) and (4.9), with $q = 0$. Since there are two dependent variables and the coefficients of the equations are constant, the solution for both of the variables is in the form of equation (4.11):

$$y(x,t) = B_1 e^{-ikx} e^{i\omega t}, \quad \psi(x,t) = B_2 e^{-ikx} e^{i\omega t} \tag{4.20}$$

By substituting the above equations in equations (4.8) and (4.9) we can find:

$$\begin{bmatrix} \kappa AGk^2 - \rho A\omega^2 & -i\kappa AGk \\ i\kappa AGk & \kappa AG + EIk^2 - \rho I\omega^2 \end{bmatrix} \begin{bmatrix} B_1 \\ B_2 \end{bmatrix} = 0 \tag{4.21}$$

Thus,

$$\frac{B_2}{B_1} = i\frac{\rho A\omega^2 - \kappa AGk^2}{\kappa AGk} = -ik\left(1 - \frac{\omega^2}{C_s^2 k^2}\right) \tag{4.22}$$

Therefore, the relations between the coefficients of the spectral solutions in equations (4.16) and (4.17) can be expressed by:

$$\frac{\overline{a_1^+}}{a_1^+} = -iP, \quad \frac{\overline{a_1^-}}{a_1^-} = iP, \quad \frac{\overline{a_2^+}}{a_2^+} = -N, \quad \frac{\overline{a_2^-}}{a_2^-} = N \tag{4.23}$$

where

$$P = k_1\left(1 - \frac{\omega^2}{{k_1}^2{C_s}^2}\right), \;\; N = k_2\left(1 + \frac{\omega^2}{{k_2}^2{C_s}^2}\right) \tag{4.24}$$

4.3 Reflection and transmission at discontinuities of Timoshenko beam structures

In this section, different types of discontinuities in Timoshenko beam structures are extensively investigated. These discontinuities include various types of end boundaries, stepped beams, and angled joints.

4.3.1 End boundaries in Timoshenko beams

The boundary conditions and their properties for three different types of end boundaries are presented in Figure 4-2 and **Table 4-**1. For simplicity, it is assumed that the end boundaries are located at $x = 0$.

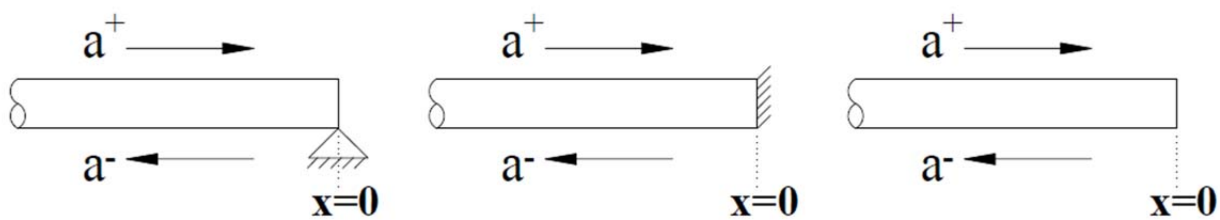

Figure 4-2 Pin, clamped, and free boundary conditions

In Figure 4-2, a^+ and a^- represent the incident and reflected flexural wave amplitudes, respectively. These amplitudes are related to each other using a reflection matrix, r, as follows:

$$a^- = ra^+ \tag{4.25}$$

where

$$a^+ = \begin{bmatrix} a_1^+ \\ a_2^+ \end{bmatrix}, \;\; a^- = \begin{bmatrix} a_1^- \\ a_2^- \end{bmatrix}, \;\; r = \begin{bmatrix} r_{11} & r_{12} \\ r_{21} & r_{22} \end{bmatrix} \tag{4.26}$$

The moment and shear force of the beam can be found using equations (4.6), (4.7), (4.16), and (4.17):

$$M(x) = \mathrm{EI}\{-\mathrm{P}k_1 a_1^+ e^{-ik_1x} + \mathrm{N}k_2 a_2^+ e^{-k_2x} - \mathrm{P}k_1 a_1^- e^{ik_1x} + \mathrm{N}k_2 a_2^- e^{k_2x}\} \quad (4.27)$$

$$V(x) = \kappa\mathrm{AG}\{i(\mathrm{P} - k_1)a_1^+ e^{-ik_1x} + (\mathrm{N} - k_2)a_2^+ e^{-k_2x} + i(-\mathrm{P} + k_1)a_1^- e^{ik_1x} + (-\mathrm{N} + k_2)a_2^- e^{k_2x}\} \quad (4.28)$$

Table 4-1 End boundary condition properties for Timoshenko beams

Type of Boundary	Boundary conditions
Clamped	$y(0) = 0,\ \psi(0) = 0$
Free	$V = \kappa AG\left(\frac{\partial y(0)}{\partial x} - \psi(0)\right) = 0,\ M = EI\, d\psi(0)/dx = 0$
Pin	$y(0) = 0,\ M = EI\, d\psi(0)/dx = 0$

By applying the boundary conditions for each end boundary, a two-by-two system of equations can be obtained. The reflection matrices for pinned (r_p), clamped (r_c), and free (r_f) boundaries can be found by solving these equations Mei (2012):

$$r_p = \begin{bmatrix} -1 & 0 \\ 0 & -1 \end{bmatrix}$$

$$r_c = \begin{bmatrix} \frac{P - iN}{P + iN} & \frac{-2iN}{P + iN} \\ \frac{-2P}{P + iN} & -\frac{P - iN}{P + iN} \end{bmatrix} \quad (4.29)$$

$$r_f = \begin{bmatrix} \frac{-Pk_1(-N + k_2) + ik_2N(k_1 - P)}{Pk_1(-N + k_2) + ik_2N(k_1 - P)} & \frac{2Nk_2(-N + k_2)}{Pk_1(-N + k_2) + ik_2N(k_1 - P)} \\ \frac{2iPk_1(-P + k_1)}{Pk_1(-N + k_2) + ik_2N(k_1 - P)} & \frac{Pk_1(-N + k_2) - ik_2N(k_1 - P)}{Pk_1(-N + k_2) + ik_2N(k_1 - P)} \end{bmatrix}$$

Consider a beam with $E = 190GPa$, $G = 77.5GPa$, $\vartheta = 0.29$, $\rho = 7680\, kg/m^3$, $b = 0.6m$, $h = 0.4m$, and $L = 2m$, where, b, h, and L are representing the width, height, and length, respectively. The moment and shear ratio at the end of the beam for clamped, free, and pinned boundary conditions are shown in Figure 4-3 and Figure 4-4.

Figure 4-3 shows the results when the propagating flexural wave (a_1^+) is the incident wave, while Figure 4-4 depicts the results for evanescent flexural wave (a_2^+) as the incident wave. The moment and shear ratios can be defined as follows:

$$R_M = abs\left(\frac{M|_{x=0}}{M_i|_{x=0}}\right) = \text{abs}\left(\frac{M_i + M_r}{M_i}\right) \tag{4.30}$$

$$R_V = abs\left(\frac{V|_{x=0}}{V_i|_{x=0}}\right) = \text{abs}\left(\frac{V_i + V_r}{V_i}\right) \tag{4.31}$$

where,

$$M_i = EI\{-Pk_1 a_1^+ + Nk_2 a_2^+\} \tag{4.32}$$

$$M_r = EI\{-Pk_1(r_{11}a_1^+ + r_{12}a_2^+) + Nk_2(r_{21}a_1^+ + r_{22}a_2^+)\} \tag{4.33}$$

$$V_i = GA\kappa\{i(P - k_1)a_1^+ + (N - k_2)a_2^+\} \tag{4.34}$$

$$V_r = GA\kappa\{i(-P + k_1)(r_{11}a_1^+ + r_{12}a_2^+) + (-N + k_2)(r_{21}a_1^+ + r_{22}a_2^+)\} \tag{4.35}$$

According to Figure 4-3 and Figure 4-4, it can be observed that the moment and shear ratios are zero for the free boundary which proves the accuracy of the derivation of the reflection matrices. Moreover, the results show that these ratios are dependent on the frequency of the loading for the clamped boundary while there is no such dependency for the pinned support. For a clamped boundary, the trend of changing of R_M with respect to the frequency when a_1^+ is the incident wave is similar to R_V when a_2^+ hits the boundary and vice versa. For a pinned boundary R_V is equal to 2 at all frequencies for both a_1^+ and a_2^+ incident waves.

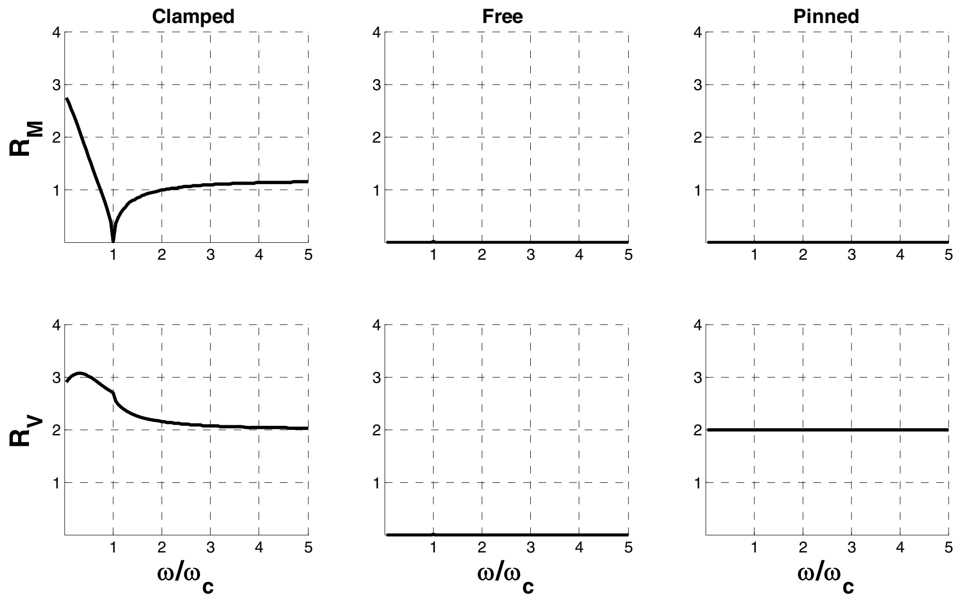

Figure 4-3 Moments and shear forces at boundaries when a_1^+ is the incident amplitude

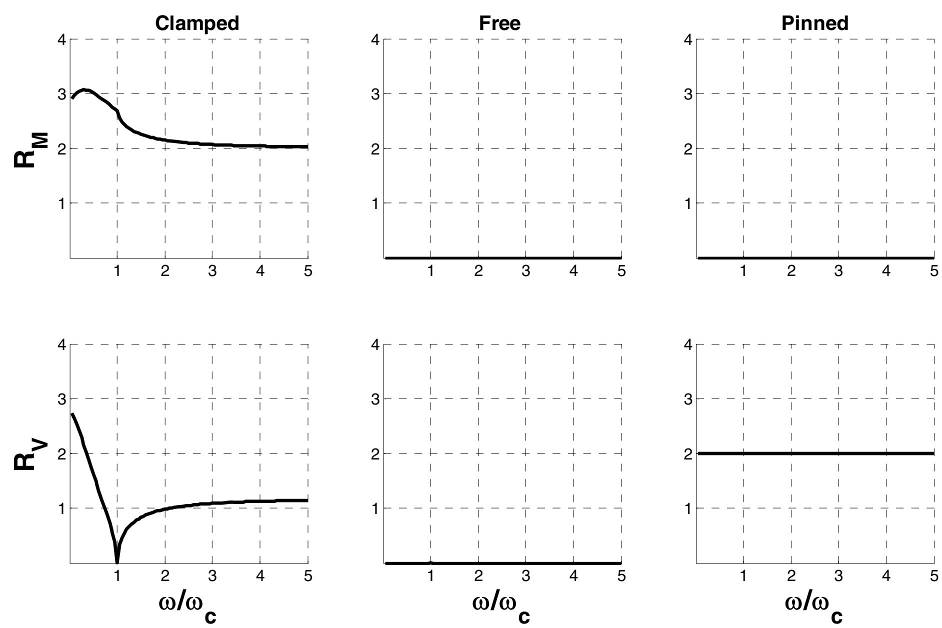

Figure 4-4 Moments and shear forces at boundaries when a_2^+ is the incident amplitude

4.3.2 Lumped mass at the end of a Timoshenko beam

Mei (2012) found the reflection matrix for the problem of a Timoshenko beam with a lumped end mass (Figure 4-5). The reflection matrix for this problem (r_m) can be found by satisfying the compatibility and equilibrium equations at the end of the beam.

Based on the positive directions for the forces and displacements in Figure 4-5, the equations of motion (equilibrium equations) for the lumped mass are:

$$-V = m\ddot{y}_m, \quad -M + V\frac{h}{2} = J_m\ddot{\psi}_m \tag{4.36}$$

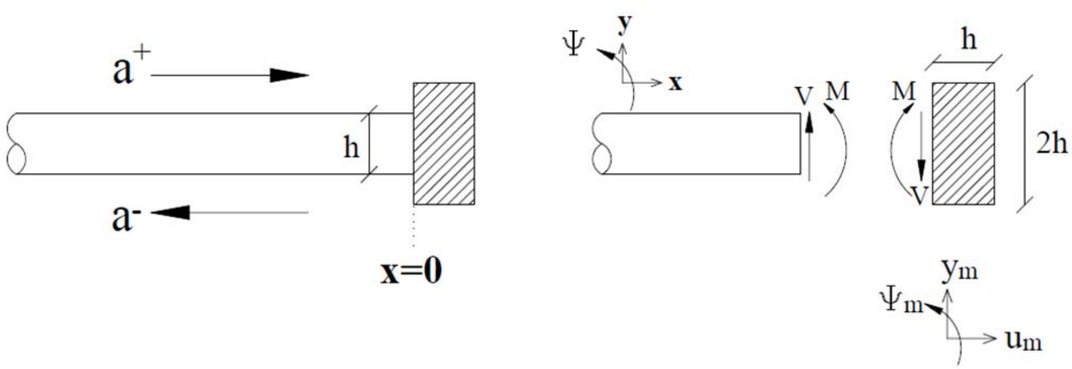

Figure 4-5 Lumped mass at the end of a Timoshenko beam

Here, y_m and ψ_m can be related to the transverse deflection and rotation angle of the end of the beam using the compatibility equations:

$$y_m = y + \frac{h}{2}\psi, \quad \psi_m = \psi \tag{4.37}$$

By combining the compatibility and equilibrium equations, the reflection matrix for a lumped mass can be found as:

$$a^- = r_m a^+; \quad r_m = M_1^{-1}M_2 \tag{4.38}$$

where,

$$M_1 = \begin{bmatrix} -iP\kappa AG + ik_1\kappa AG - m\omega^2 - iPm\omega^2\dfrac{h}{2} & -N\kappa AG + k_2\kappa AG - m\omega^2 - Nm\omega^2\dfrac{h}{2} \\ Pk_1EI - iP\kappa AG\dfrac{h}{2} + ik_1\kappa AG\dfrac{h}{2} + iPJ_m\omega^2 & -Nk_2EI + NJ_m\omega^2 - N\kappa AG\dfrac{h}{2} + k_2\kappa AG\dfrac{h}{2} \end{bmatrix} \quad (4.39)$$

$$M_2 = \begin{bmatrix} -iP\kappa AG + ik_1\kappa AG + m\omega^2 - iPm\omega^2\dfrac{h}{2} & -N\kappa AG + k_2\kappa AG + m\omega^2 - Nm\omega^2\dfrac{h}{2} \\ -Pk_1EI - iP\kappa AG\dfrac{h}{2} + ik_1\kappa AG\dfrac{h}{2} + iPJ_m\omega^2 & Nk_2EI + NJ_m\omega^2 - N\kappa AG\dfrac{h}{2} + k_2\kappa AG\dfrac{h}{2} \end{bmatrix} \quad (4.40)$$

Figure 4-6 and Figure 4-7 show the moment and shear ratios for a beam with a lumped end mass. The beam properties are exactly the same as the beam in the previous section. It is assumed that the lumped mass dimensions are h, $2h$, and b as shown in Figure 4-5, where h and b are the height and width of the beam, respectively. The mass ratios in Figure 4-6 and Figure 4-7 are representing the ratio of the mass of the lumped end mass to the mass of the beam. The results show that the beam behaves as a free end structure when the mass ratio is zero, which proves the accuracy of the derivation. For mass ratios larger than 5 the moment (R_M) and shear ratios (R_V) are very similar to the clamped boundary.

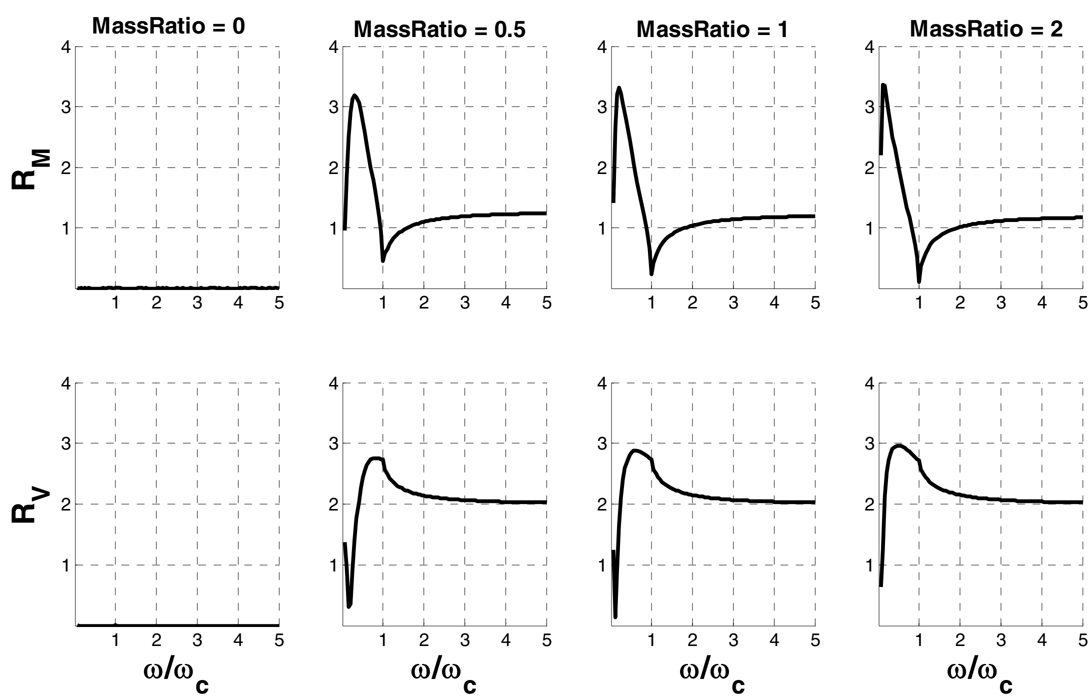

Figure 4-6 Effect of lumped end mass, mass ratios 0, 0.5,1, and 2

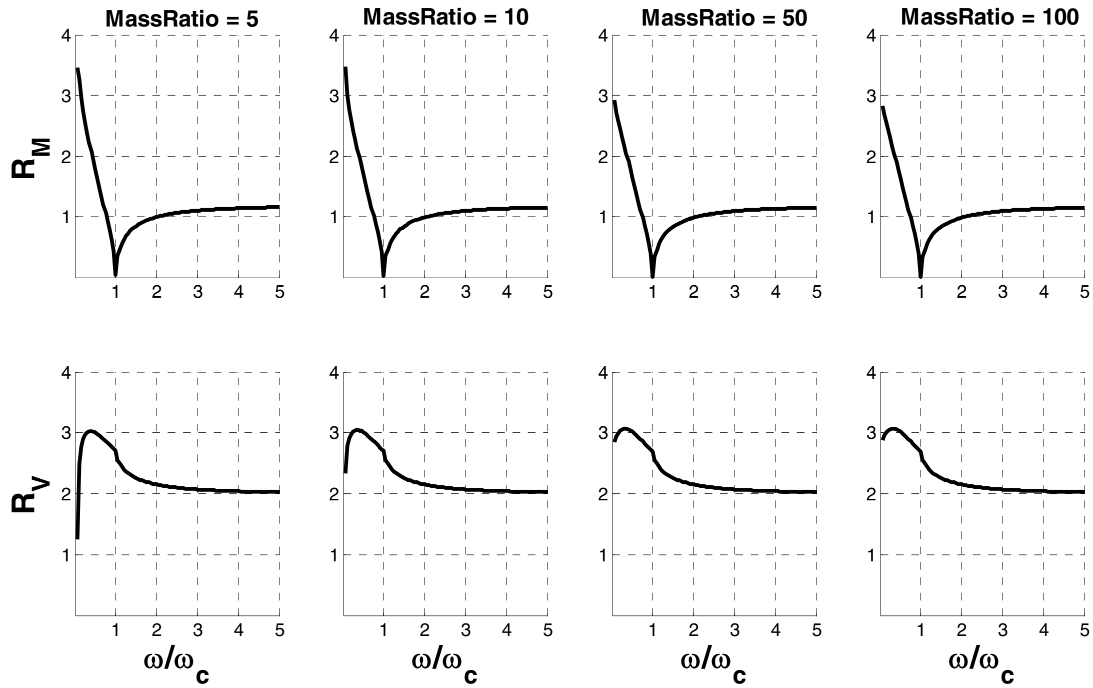

Figure 4-7 Effect of lumped end mass, mass ratios 5, 10, 50, and 100

4.3.3 Stepped Timoshenko beam

The flexural waves are reflected and transmitted when they encounter a change in the material properties and/or cross section dimensions along the beam. The beams with different material or cross section properties are called stepped beams. The reflection and transmission matrices for a stepped Timoshenko beam has been found by Mei and Mace (2005).

Figure 4-8 shows a stepped Timoshenko beam with the shear forces and moments at the point where the material or cross section properties are changing. Similar to the lumped end mass, the equilibrium and compatibility equations should be satisfied for finding the reflection and transmission matrices.

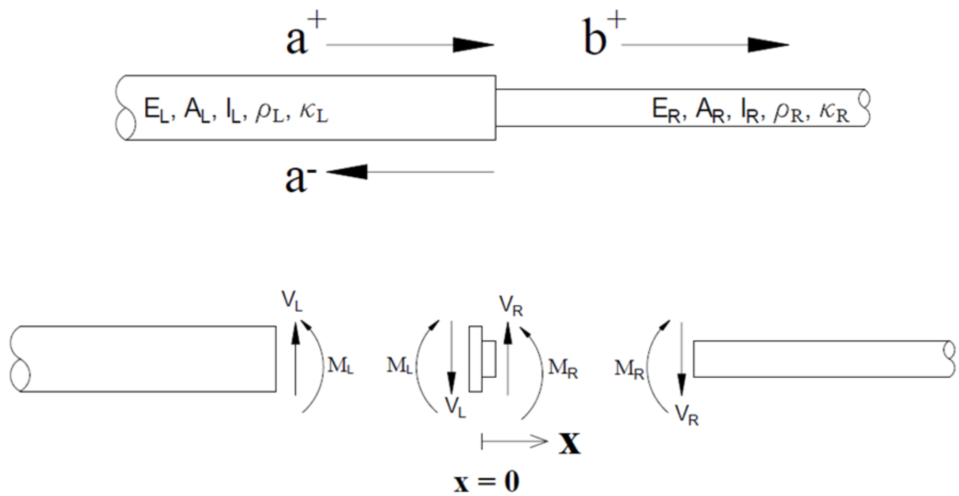

Figure 4-8 Stepped Timoshenko beam

The reflection and transmission matrices can be defined as follows:

$$b^+ = ta^+, \;\; a^- = ra^+ \tag{4.41}$$

where,

$$r = \begin{bmatrix} r_{11} & r_{12} \\ r_{21} & r_{22} \end{bmatrix}, \;\; t = \begin{bmatrix} t_{11} & t_{12} \\ t_{21} & t_{22} \end{bmatrix}, \;\; a^+ = \begin{bmatrix} a_1^+ \\ a_2^+ \end{bmatrix}, \;\; a^- = \begin{bmatrix} a_1^- \\ a_2^- \end{bmatrix}, \;\; b^+ = \begin{bmatrix} b_1^+ \\ b_2^+ \end{bmatrix} \tag{4.42}$$

The transverse deflection and rotation angle of the beam at the left and right hand side of the stepped beam are:

$$\begin{gathered} y_L = \; a_1^+ e^{-ik_{\mathrm{L}1}x} + a_2^+ e^{-k_{\mathrm{L}2}x} + a_1^- e^{ik_{\mathrm{L}1}x} + a_2^- e^{k_{\mathrm{L}2}x} \\ y_R = \; b_1^+ e^{-ik_{\mathrm{R}1}x} + b_2^+ e^{-k_{\mathrm{R}2}x} \\ \psi_L = -iP_L a_1^+ e^{-ik_{L1}x} - N_L a_2^+ e^{-k_{L2}x} + iP_L a_1^- e^{ik_{L1}x} + N_L a_2^- e^{k_{L2}x} \\ \psi_R = -iP_R b_1^+ e^{-ik_{R1}x} - N_R b_2^+ e^{-k_{R2}x} \end{gathered} \tag{4.43}$$

The compatibility and the equilibrium equations can be written as:

$$y_L = y_R, \;\; \psi_L = \psi_R \tag{4.44}$$

$$M_L = M_R, \;\; V_L = V_R \tag{4.45}$$

By combining the above equations, the final system of equations for finding the reflected and transmitted coefficients is:

$$AX = B \tag{4.46}$$

where,

$$A = \begin{bmatrix} 1 & 0 & 1 & 0 & -1 & 0 & -1 & 0 \\ 0 & 1 & 0 & 1 & 0 & -1 & 0 & -1 \\ iP_L & 0 & N_L & 0 & iP_R & 0 & N_R & 0 \\ 0 & iP_L & 0 & N_L & 0 & iP_R & 0 & N_R \\ P_L k_{L1} & 0 & -N_L k_{L2} & 0 & -\beta_{RL} P_R k_{R1} & 0 & \beta_{RL} N_R k_{R2} & 0 \\ 0 & P_L k_{L1} & 0 & -N_L k_{L2} & 0 & -\beta_{RL} P_R k_{R1} & 0 & \beta_{RL} N_R k_{R2} \\ i(-P_L + k_{L1}) & 0 & (-N_L + k_{L2}) & 0 & i\gamma_{RL}(-P_R + k_{R1}) & 0 & \gamma_{RL}(-N_R + k_{R2}) & 0 \\ 0 & i(-P_L + k_{L1}) & 0 & (-N_L + k_{L2}) & 0 & i\gamma_{RL}(-P_R + k_{R1}) & 0 & \gamma_{RL}(-N_R + k_{R2}) \end{bmatrix}$$

$$X = \begin{bmatrix} r_{11} \\ r_{12} \\ r_{21} \\ r_{22} \\ t_{11} \\ t_{12} \\ t_{21} \\ t_{22} \end{bmatrix}, \quad B = \begin{bmatrix} -1 \\ -1 \\ iP_L \\ N_L \\ -P_L k_{L1} \\ N_L k_{L2} \\ i(-P_L + k_{L1}) \\ (-N_L + k_{L2}) \end{bmatrix}, \quad \beta_{RL} = (EI)_R/(EI)_L, \quad \gamma_{RL} = (GA\kappa)_R/(GA\kappa)_L \tag{4.47}$$

Figure 4-9 and Figure 4-10 show the absolute value of the ratio of the reflected and transmitted moment and shear forces to the corresponding incident values in a stepped Timoshenko beam which is made of Aluminum and Steel. It is assumed that the incident wave has a propagating flexural component (a_1^+), and it hits the stepped part of the beam from left hand side (see Figure 4-8). The dimensions of the beam are similar to the beam in the previous section, and the material properties of Steel and Aluminum are as follows:

$E_{Steel} = 200\ GPa$; $E_{Al} = 68.9\ GPa$;

$\rho_{Steel} = 7850\ kg/m^3$; $\rho_{AL} = 2700\ kg/m^3$

$\vartheta_{Steel} = 0.3$; $\vartheta_{AL} = 0.33$

The incident, reflected, and transmitted moment and shear forces are determined as:

$$M_i = (EI)_L\{-P_L k_{1L} a_1^+ + N_L k_{2L} a_2^+\} \tag{4.48}$$

$$M_r = (EI)_L\{-P_L k_{1L}(r_{11}a_1^+ + r_{12}a_2^+) + N_L k_{2L}(r_{21}a_1^+ + r_{22}a_2^+)\} \tag{4.49}$$

$$M_t = (EI)_R\{-P_R k_{1R}(t_{11}a_1^+ + t_{12}a_2^+) + N_R k_{2R}(t_{21}a_1^+ + t_{22}a_2^+)\} \tag{4.50}$$

$$V_i = (GA\kappa)_L\{i(P_L - k_{1L})a_1^+ + (N_L - k_{2L})a_2^+\} \tag{4.51}$$

$$V_r = (GA\kappa)_L\{i(-P_L + k_{1L})(r_{11}a_1^+ + r_{12}a_2^+) + (-N_L + k_{2L})(r_{21}a_1^+ + r_{22}a_2^+)\} \tag{4.52}$$

$$V_t = (GA\kappa)_R\{i(P_R - k_{1R})(t_{11}a_1^+ + t_{12}a_2^+) + (N_R - k_{2R})(t_{21}a_1^+ + t_{22}a_2^+)\} \tag{4.53}$$

where, the subscripts L and R refer to the left and right sections, respectively. The critical frequency (ω_c) in Figure 4-9 and Figure 4-10 is the critical frequency of the left part of the beam.

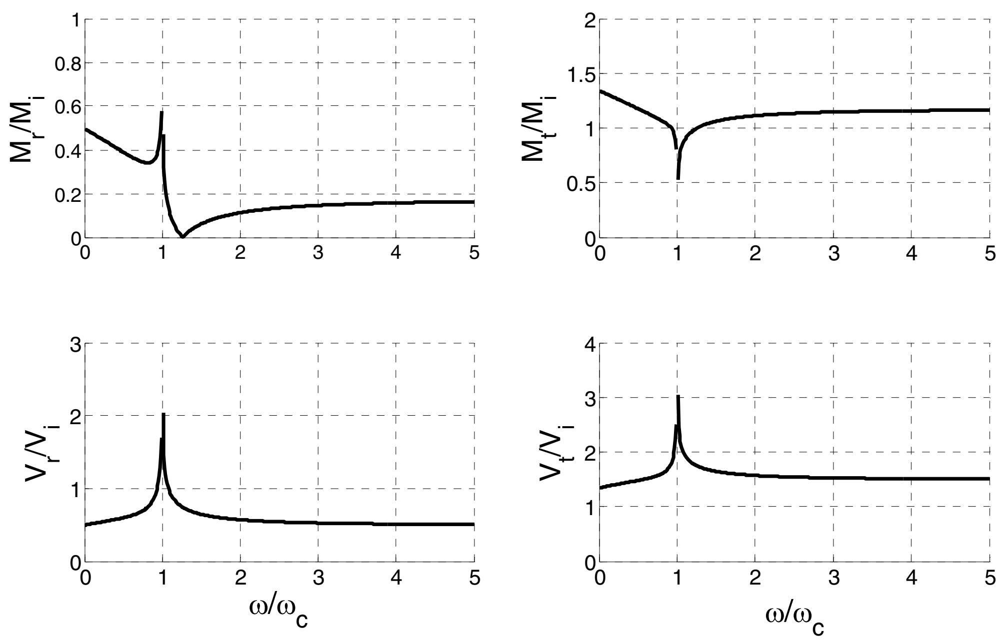

Figure 4-9 Changing of moment and shear when the wave enters from Aluminum to Steel

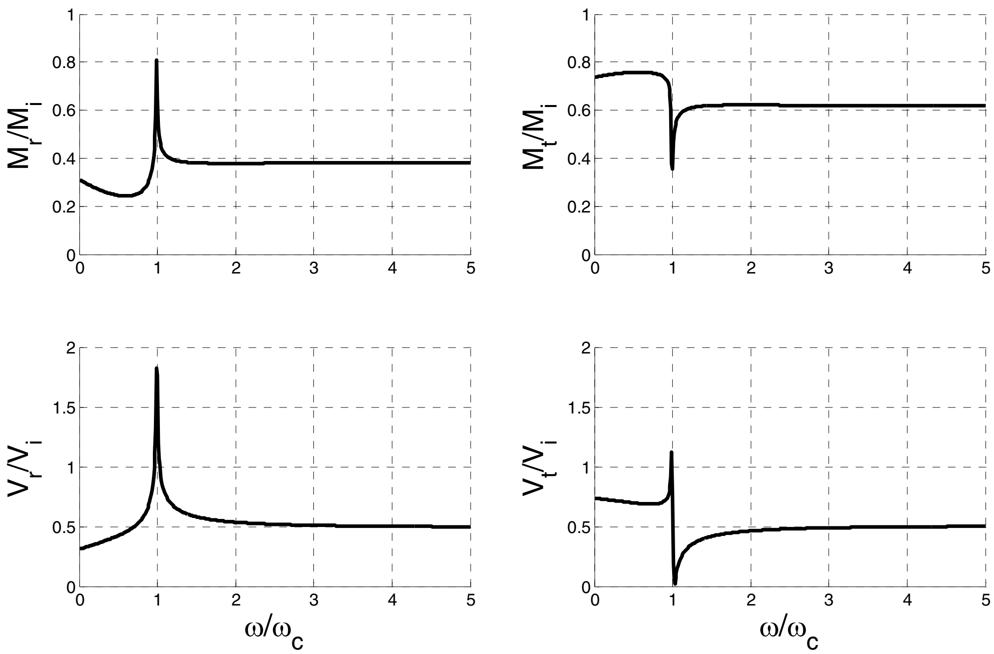

Figure 4-10 Changing of moment and shear when the wave enters from Steel to Aluminum

The results show that the amount of the transmitted moment (M_t/M_i) and shear (V_t/V_i) ratios are larger when the wave passes from Aluminum to Steel (Figure 4-9), which is similar to the behavior of the stepped rods (the transmitted stress amplifies when the wave passes from a soft to hard medium).

4.3.4 Angled joints in Timoshenko beams

In this section, the wave propagation behavior of arbitrary "L" and "T" shaped angled joints in Timoshenko beams is investigated.

Wave reflection and transmission in an arbitrary "L" joint

Figure 4-11 shows a schematic of an arbitrary "L" joint of two Timoshenko beams. It is assumed that the joint is a rigid member with physical values for mass and polar moment of inertia. The reflection and transmission matrices for this joint can be found by satisfying the equations of motion and compatibility. The detailed geometry of the "L" joint is depicted in Figure 4-12, and its required dimensions are extracted in Rafiee-Dehkharghani (2014). The equations of motion for the joint can be written as:

$$-F_1 - V_2 \sin\theta + F_2 \cos\theta = m\ddot{u}_J \tag{4.54}$$

$$F_2 \sin\theta - V_1 + V_2 \cos\theta = m\ddot{y}_J \tag{4.55}$$

$$-M_1 + M_2 + V_1 x_G + V_2 \overline{BG} - F_1(y_G - h/2) - F_2 \overline{BC} = J\ddot{\psi}_J \tag{4.56}$$

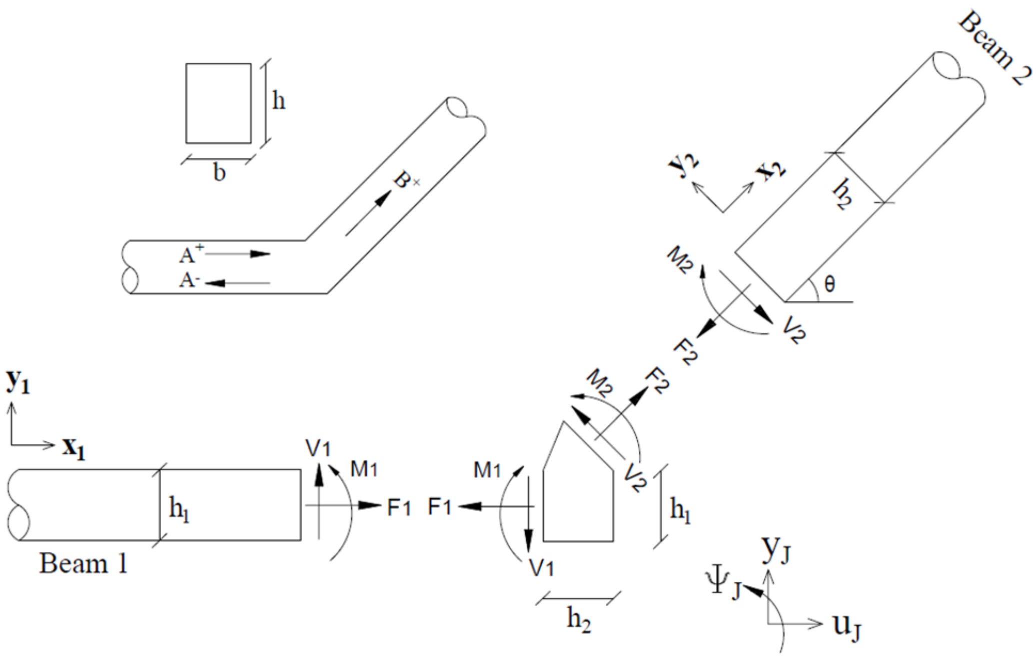

Figure 4-11 Two beams jointed at an arbitrary "L" joint

And, the compatibility equations are:

$$u_1 = u_J + L_1\psi_J \sin\alpha \tag{4.57}$$

$$u_2 = u_J \cos\theta + y_J \sin\theta - L_2\psi_J \sin\beta \tag{4.58}$$

$$y_1 = y_J - L_1\psi_J \cos\alpha \tag{4.59}$$

$$y_2 = -u_J \sin\theta + y_J \cos\theta + L_2\psi_J \cos\beta \tag{4.60}$$

$$\psi_1 = \psi_J \tag{4.61}$$

$$\psi_2 = \psi_J \tag{4.62}$$

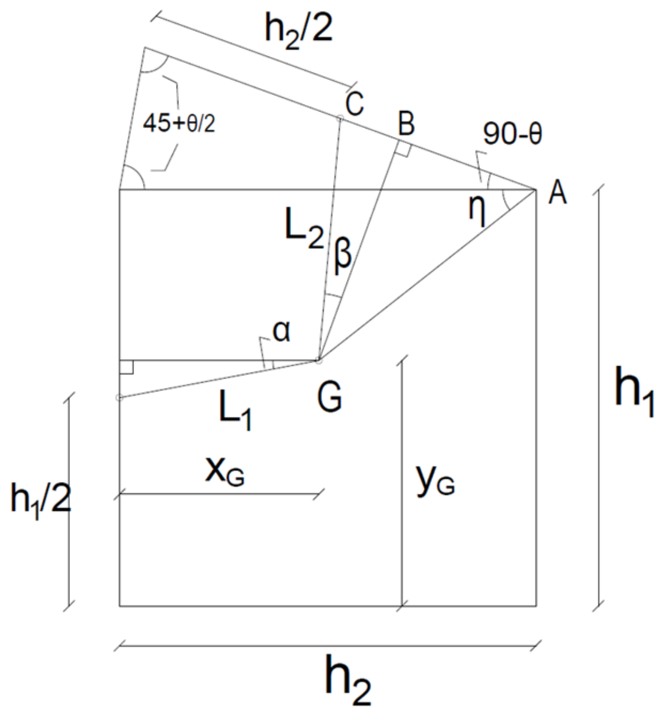

Figure 4-12 Geometry of the "L" joint

It is assumed that positive waves with the amplitude vector of A^+ are the incident waves at the angled joint. These waves generate transmitted and reflected waves in beam 2 and beam 1, respectively. The relation between the amplitudes of the transmitted and reflected waves with the incident waves can be expressed using the transmission (t) and reflection (r) matrices as follows:

$$B^+ = tA^+, \quad A^- = rA^+ \tag{4.63}$$

where,

$$A^+ = \begin{Bmatrix} a^+ \\ a_N^+ \\ c^+ \end{Bmatrix}, \quad A^- = \begin{Bmatrix} a^- \\ a_N^- \\ c^- \end{Bmatrix}, \quad B^+ = \begin{Bmatrix} b^+ \\ b_N^+ \\ d^+ \end{Bmatrix} \tag{4.64}$$

Six equations are required for finding the six unknown reflected and transmitted amplitudes. These equations are derived in Rafiee-Dehkharghani (2014).

Figure 4-13 to Figure 4-18 show the reflected and transmitted amplitudes for an “L” joint with 90°, 45°, and 15° angles. It is assumed that both beams have similar material properties and dimensions as indicated in section 4.3.1.

Figure 4-13, Figure 4-15, and Figure 4-17 represent the amplitudes when the incident wave is a longitudinal wave (c^+), while Figure 4-14, Figure 4-16, and Figure 4-18 show the results for the case when the incident wave is a propagating flexural wave (a^+).

For a longitudinal incident wave, the results show that the reflected longitudinal amplitude (c^-) approaches to unity by increasing the frequency of the loading. This is in accordance with the results that are obtained in Section 3 for a rod with a lumped end mass. It was observed that a lumped end mass behaves as a rigid boundary at high frequencies and the reflected amplitude is unity. In lower frequencies, it can be observed that the reflected longitudinal amplitude is decreasing by decreasing the angle of the joint. A reversed trend can be seen in the behavior of the transmitted longitudinal amplitude (d^+), which is conceivable since more longitudinal waves should be transferred in small angles.

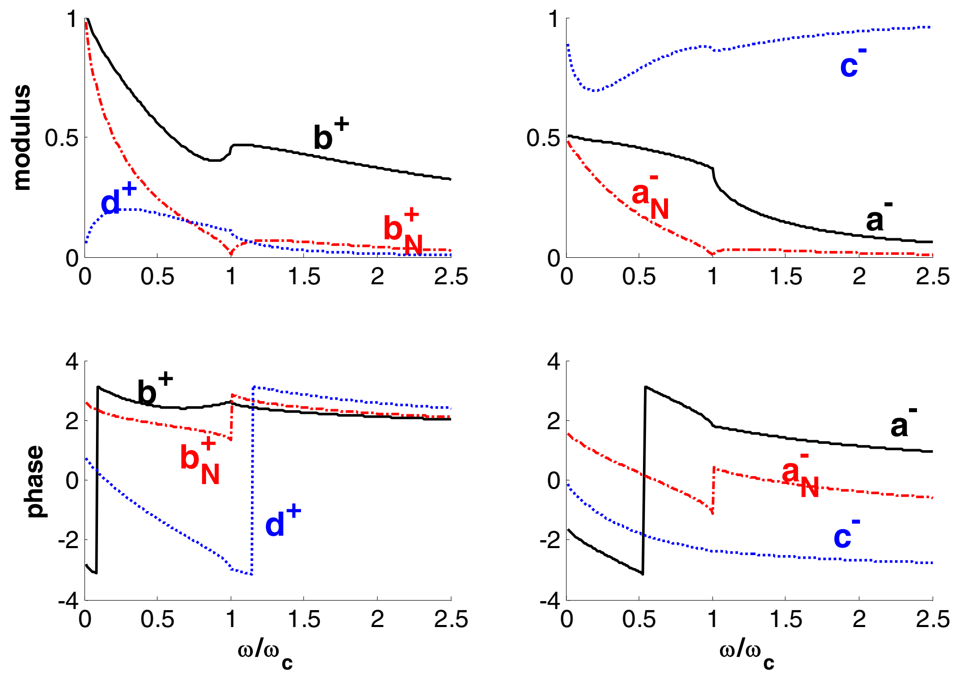

Figure 4-13 Longitudinal incident (c^+), $\theta = 90°$, "L" joint

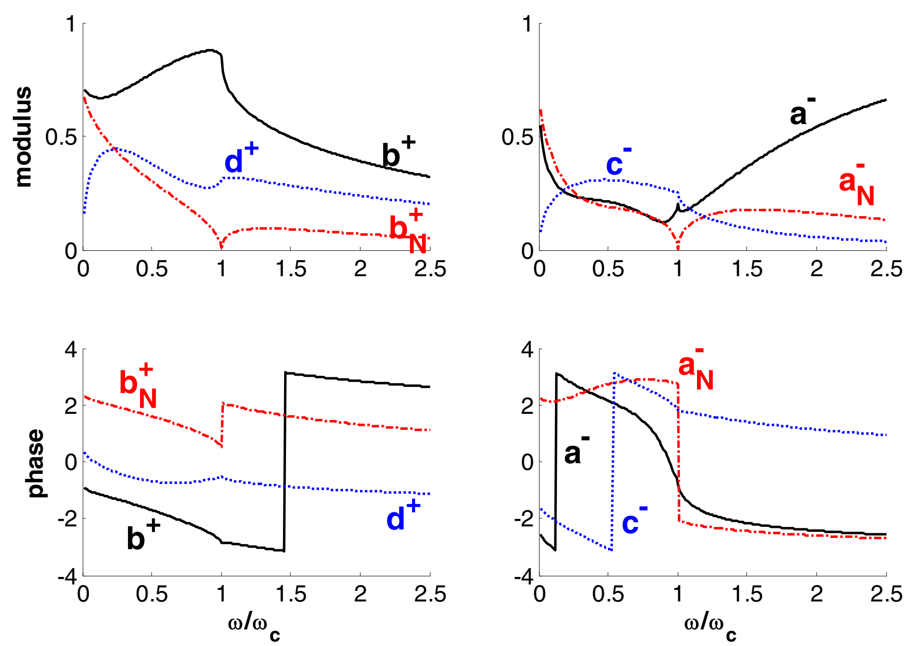

Figure 4-14 Propagating flexural incident (a^+), $\theta = 90°$, "L" joint

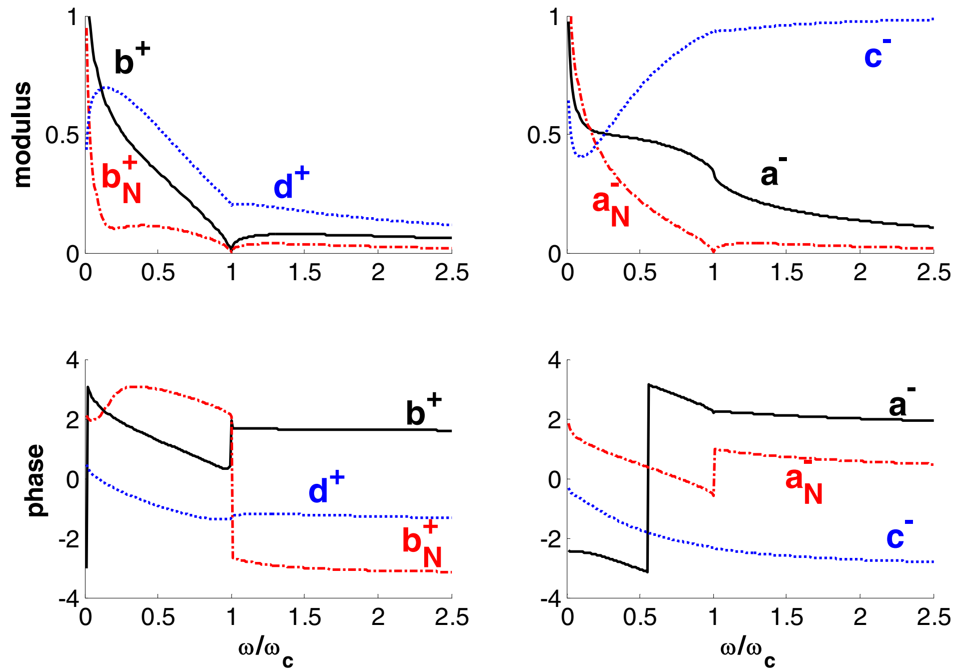

Figure 4-15 Longitudinal incident (c^{+}), $\boldsymbol{\theta} = 45°$, "L" joint

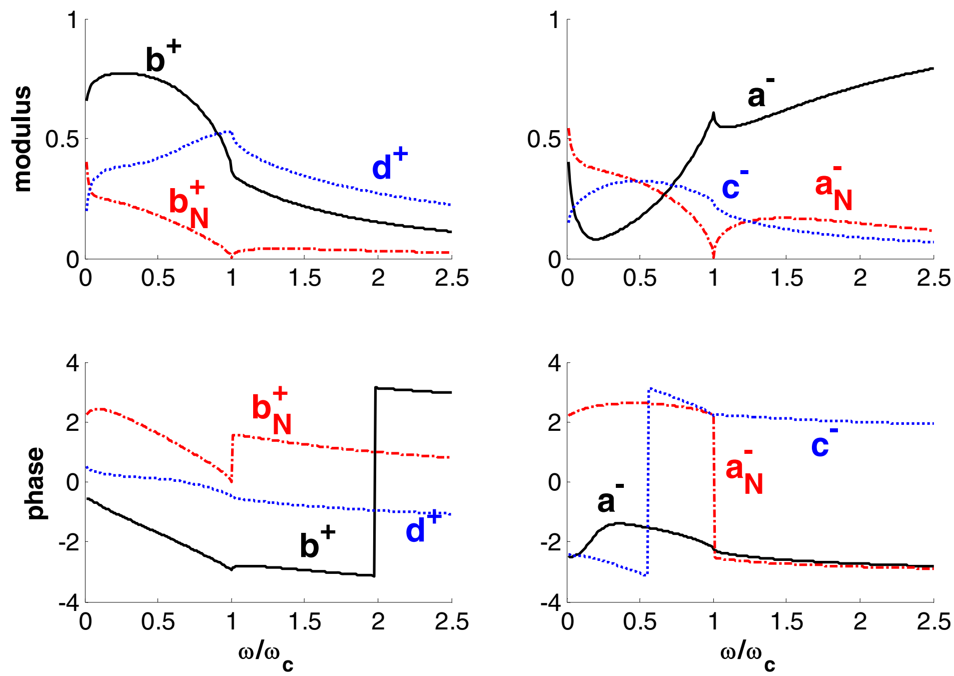

Figure 4-16 Propagating flexural incident (a^{+}), $\boldsymbol{\theta} = 45°$, "L" joint

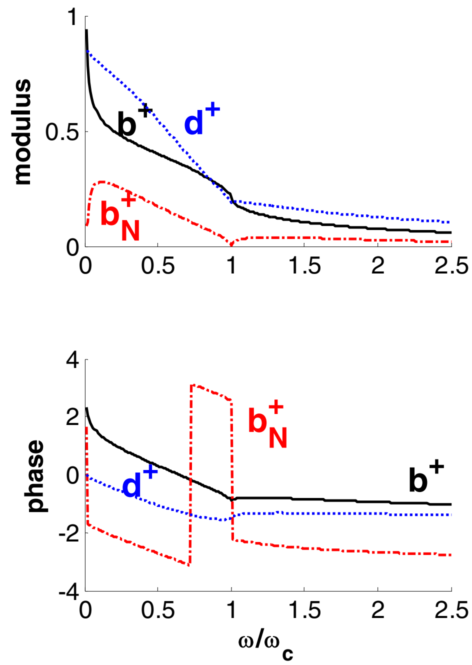

Figure 4-17 Longitudinal incident (c^{+}), $\theta = 15°$, "L" joint

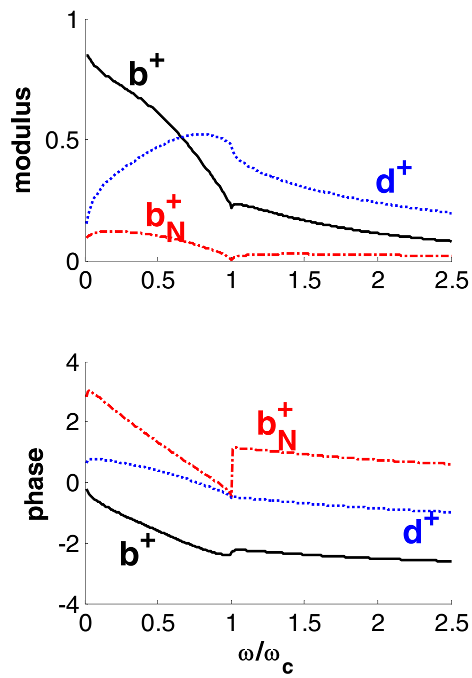

Figure 4-18 Propagating flexural incident (a^{+}), $\theta = 15°$, "L" joint

Wave reflection and transmission in an arbitrary "T" joint

Figure 4-19 shows a schematic of an arbitrary "T" joint of three Timoshenko beams. Similar to the "L" joint, it is assumed that the "T" joint is rigid with physical values for mass and polar moment of inertia. A closer view of the "T" joint is depicted in Figure 4-20, and the details of its geometric characteristics can be found in Rafiee-Dehkharghani (2014).

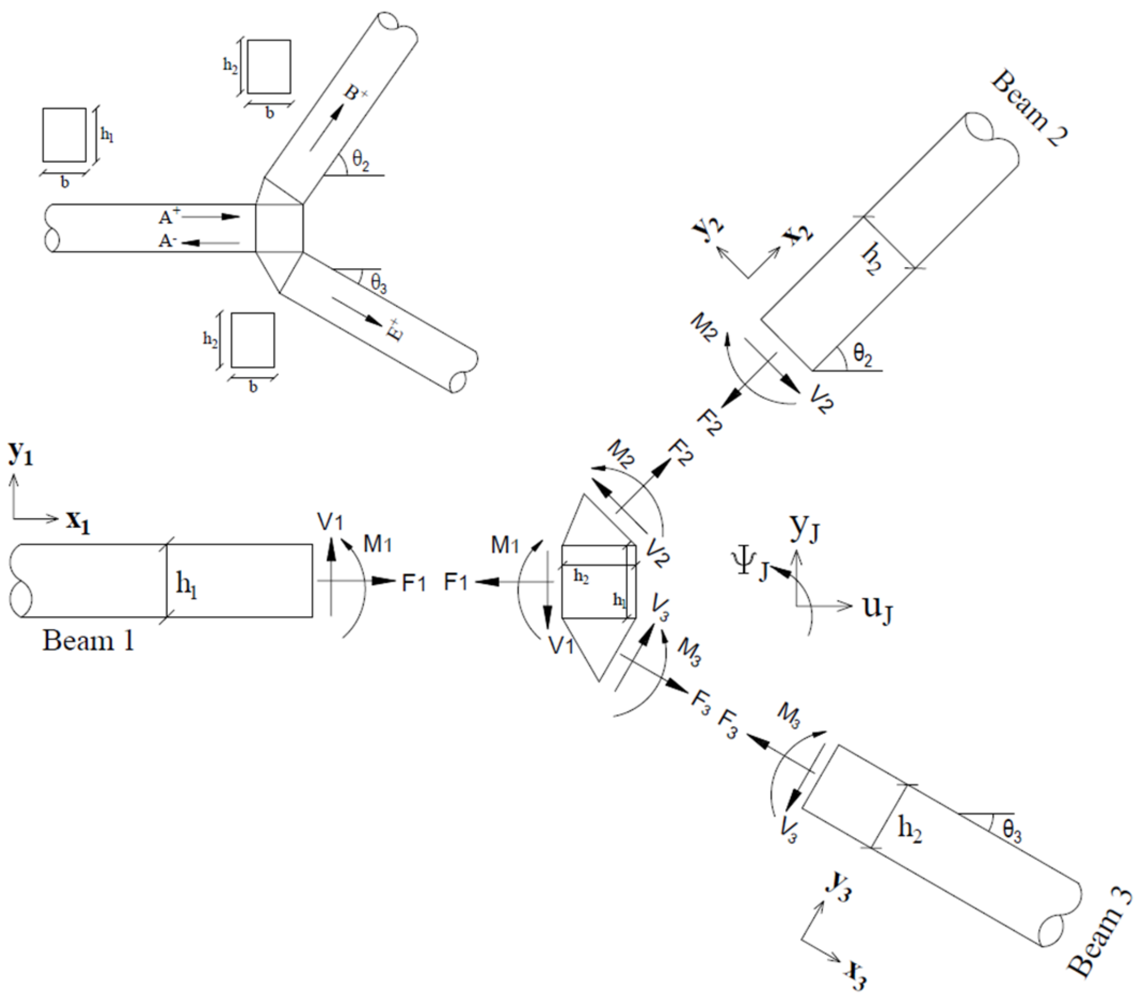

Figure 4-19 Three beams jointed at an arbitrary "T" joint

The equations of motion for the "T" joint can be written as:

$$-F_1 - V_2 \sin\theta_2 + F_2 \cos\theta_2 + V_3 \sin\theta_3 + F_3 \cos\theta_3 = m\ddot{u}_J \tag{4.65}$$

$$-V_1 + F_2 \sin\theta_2 + V_2 \cos\theta_2 - F_3 \sin\theta_3 + V_3 \cos\theta_3 = m\ddot{y}_J \tag{4.66}$$

$$-M_1 + M_2 + M_3 + V_1 x_G + V_2\overline{BG} + V_3\overline{EG} - F_1(y_G - h_1/2) - F_2\overline{BC} + F_3\overline{EF} = J\ddot{\psi}_J \tag{4.67}$$

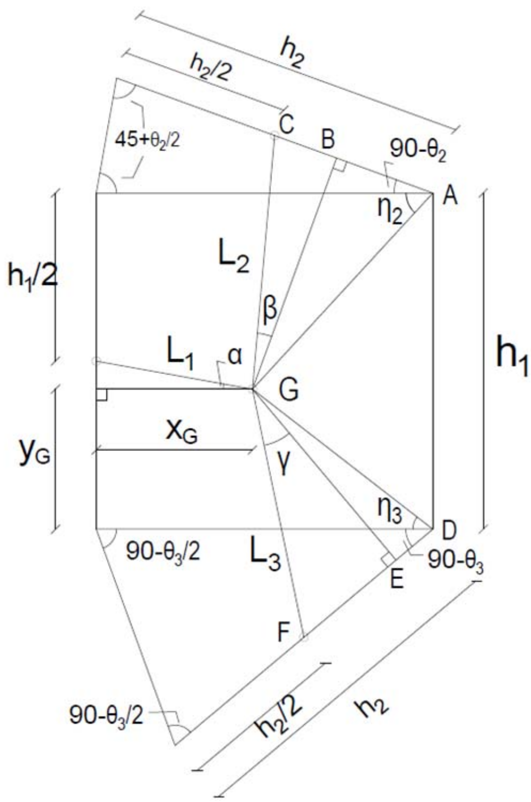

Figure 4-20 Geometry of the "T" joint

And, the compatibility equations are:

$$u_1 = u_J + L_1\psi_J \sin\alpha \tag{4.68}$$

$$u_2 = u_J \cos\theta_2 + y_J \sin\theta_2 - L_2\psi_J \sin\beta \tag{4.69}$$

$$u_3 = u_J \cos\theta_3 - y_J \sin\theta_3 + L_3\psi_J \sin\gamma \tag{4.70}$$

$$y_1 = y_J - L_1\psi_J \cos\alpha \tag{4.71}$$

$$y_2 = -u_J \sin\theta_2 + y_J \cos\theta_2 + L_2\psi_J \cos\beta \tag{4.72}$$

$$y_3 = u_J \sin\theta_3 + y_J \cos\theta_3 + L_3\psi_J \cos\gamma \tag{4.73}$$

$$\psi_1 = \psi_J \tag{4.74}$$

$$\psi_2 = \psi_J \tag{4.75}$$

$$\psi_3 = \psi_J \tag{4.76}$$

It is assumed that positive going waves with the amplitude vector of A^+ are the incident waves at the angled joint. These waves generate transmitted waves in beams 2 and 3 and reflected waves in beam 1. The relations between the amplitudes of the transmitted and reflected waves with the incident waves can be expressed using the transmission (t_{13} and t_{12}) and reflection (r_{11}) matrices as follows:

$$E^+ = t_{13}A^+, \quad B^+ = t_{12}A^+, \quad A^- = r_{11}A^+ \tag{4.77}$$

where,

$$A^+ = \begin{Bmatrix} a^+ \\ a_N^+ \\ c^+ \end{Bmatrix}, \quad A^- = \begin{Bmatrix} a^- \\ a_N^- \\ c^- \end{Bmatrix}, \quad B^+ = \begin{Bmatrix} b^+ \\ b_N^+ \\ d^+ \end{Bmatrix}, \quad E^+ = \begin{Bmatrix} e^+ \\ e_N^+ \\ g^+ \end{Bmatrix} \tag{4.78}$$

Nine equations are required for finding the nine unknown reflected and transmitted amplitudes. These equations are derived in Rafiee-Dehkharghani (2014).

Figure 4-21 to Figure 4-26 show the reflected and transmitted amplitudes for a "T" joint with three different combinations for angles θ_2 and θ_3. These combinations include $\theta_2 = \theta_3 = 90°$, $\theta_2 = \theta_3 = 45°$, and $\theta_2 = 15°,\ \theta_3 = 60°$.

It is assumed that all of the beams have similar material properties and dimensions as indicated in section 4.3.1.

Figure 4-21, Figure 4-23, and Figure 4-25 represent the amplitudes when the incident wave is a longitudinal wave (c^+), while Figure 4-22, Figure 4-24, and Figure 4-26 show the results for the case when the incident wave is a propagating flexural wave (a^+).

For a longitudinal incident wave (c^+), the longitudinal transmitted components (d^+) and (g^+) for the joint with $\theta_2 = \theta_3 = 90°$ are zero. Moreover, the reflected flexural components (a_1^-) and (a_2^-) are zero, and the transmitted flexural components in beams 2 and 3 are equal due to the symmetry of the joint. For the joint with, $\theta_2 = \theta_3 = 45°$, the transmitted longitudinal components are not zero, and their moduli are equal due to the symmetry; however, the reflected flexural components are still zero. For the joint with $\theta_2 = 15°$ and $\theta_3 = 60°$ the transmitted longitudinal amplitude in beam 2, d^+, is larger than the amplitude in beam 3, g^+, since more waves can be transmitted to beam 2 because of having a small angle with respect to the horizontal line. Since the joint with $\theta_2 = 15°$ and $\theta_3 = 60°$ is not symmetric, the reflected flexural components are not zero.

When the incident wave has a flexural propagating component (a_1^+), the reflected longitudinal amplitude (c^-) is zero for the joints with $\theta_2 = \theta_3 = 90°$ and $\theta_2 = \theta_3 = 45°$. Similar to the longitudinal incident, the transmitted amplitudes are equal for symmetric joints. The transmitted flexural amplitudes for the joint with $\theta_2 = 15°$ and $\theta_3 = 60°$ are larger in beam 3 because of the larger angle of this beam with respect to the horizontal line.

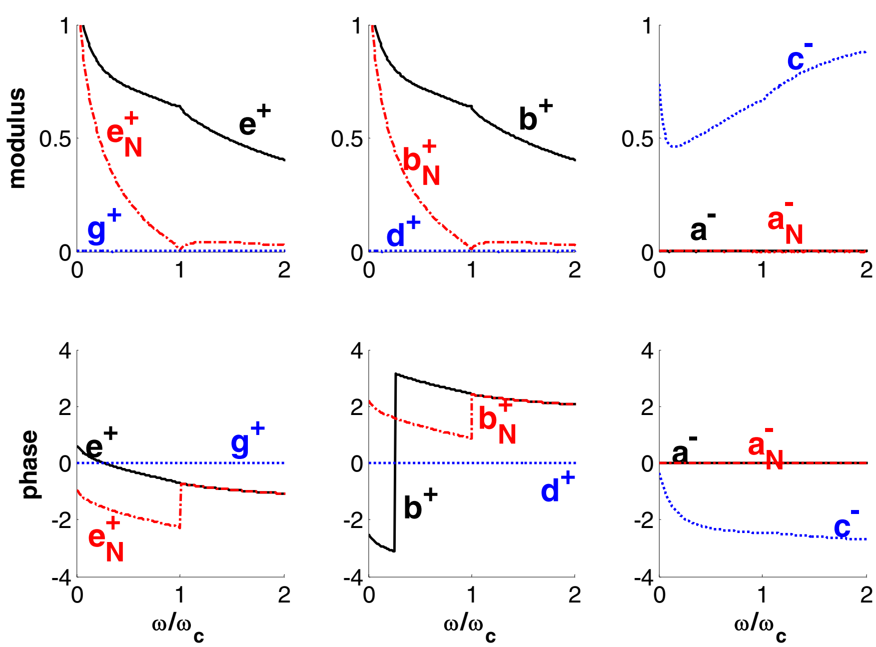

Figure 4-21 Longitudinal incident (c^+), $\theta_2 = \theta_3 = 90°$, "T" joint

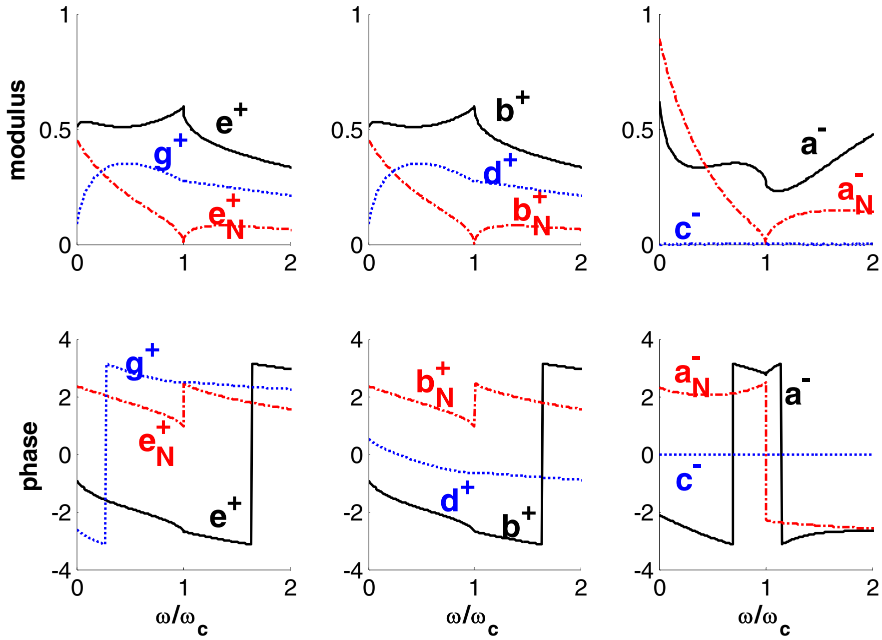

Figure 4-22 Propagating flexural incident (a^{+}), $\theta_2 = \theta_3 = 90°$, "T" joint

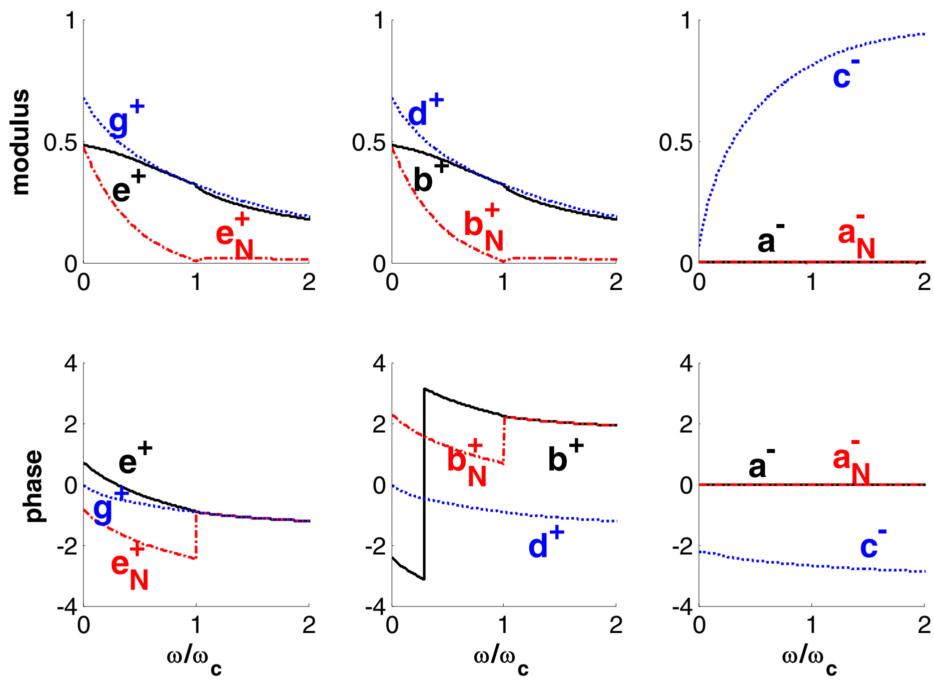

Figure 4-23 Longitudinal incident (c^{+}), $\theta_2 = \theta_3 = 45°$, "T" joint

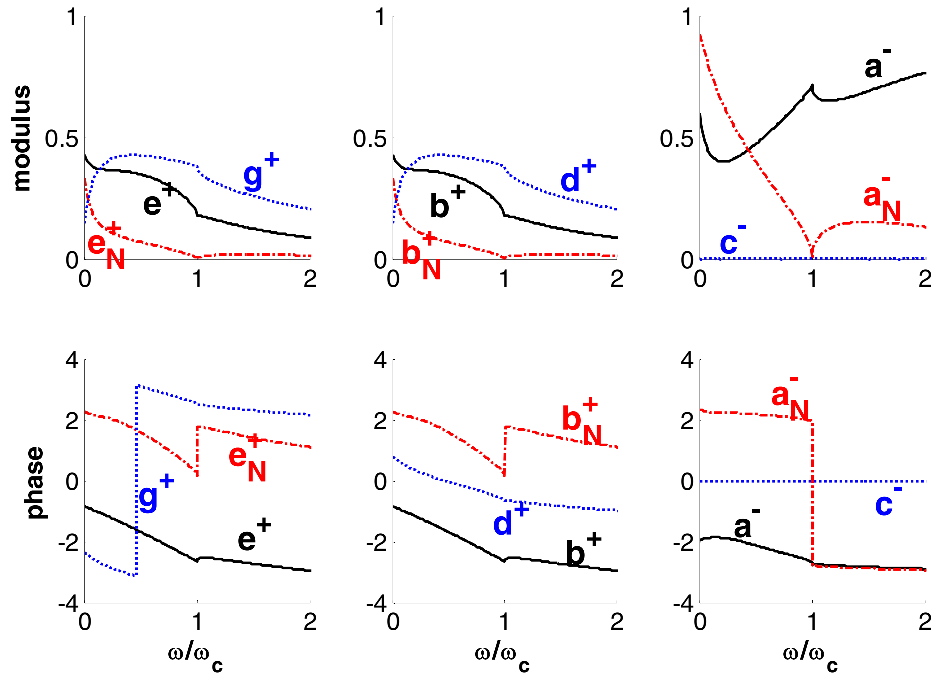

Figure 4-24 Propagating flexural incident (a^+), $\theta_2 = \theta_3 = 45°$, "T" joint

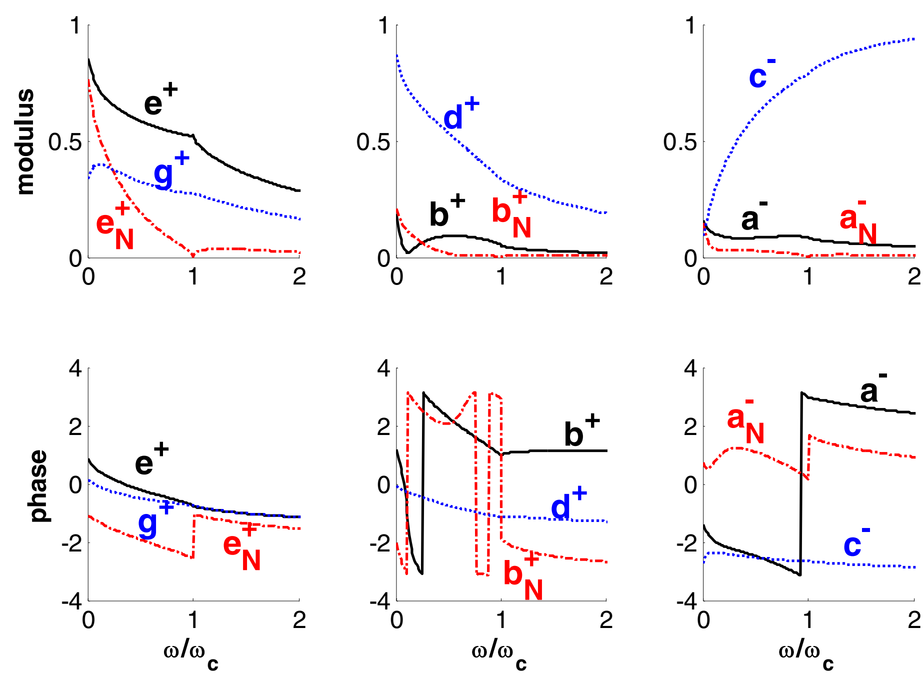

Figure 4-25 Longitudinal incident (c^+), $\theta_2 = 15°, \theta_3 = 60°$, "T" joint

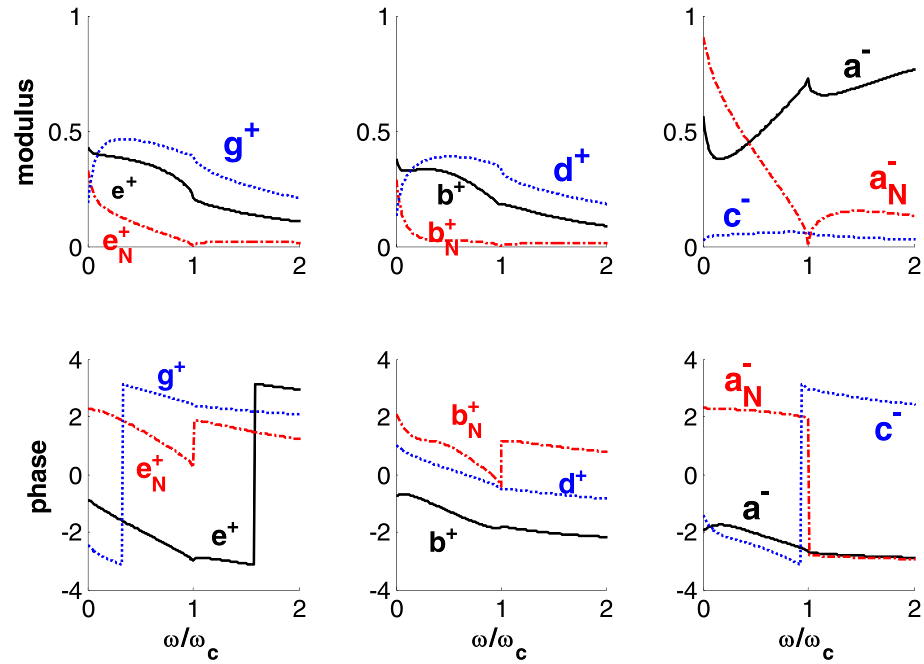

Figure 4-26 Propagating flexural incident (a^{+}), $\theta_2 = 15°, \theta_3 = 60°$, "T" joint

4.4 Summary

In this section, the flexural wave propagation in Timoshenko beams is studied, and the effect of different types of discontinuities on the reflection and transmission of the waves in Timoshenko structures is reviewed broadly. These discontinuities include different types of end boundaries, lumped mass, and stepped beam. In addition, the reflection and transmission matrices at arbitrary "L" and "T" shaped angled joints are developed in this section. The results show that the reflection and transmission phenomena in Timoshenko beams are much more complex than rods due to the dispersive nature of the flexural waves, and reflection and transmission matrices are completely dependent of the material properties, geometry of the cross section, and frequency of loading.

SECTION 5
OPTIMIZATION METHODOLOGY FOR DESIGNING STRESS WAVE ATTENUATORS

5.1 Introduction

The effect of discontinuities on the wave propagation through rods and beams was extensively studied in Sections 3 and 4, and it was observed that the discontinuities can alter the wave properties significantly. In real structures the waves will definitely encounter such discontinuities along their path since any real system has finite dimensions and boundaries. The simplest real systems are homogenous systems in which the waves interact, merely, with the boundaries and geometric discontinuities. More complex systems such as composite and layered structures include more discontinuities as the waves travel in different media within the structure. The common characteristic for the problem of wave propagation in real systems is the changing of the wave behavior due to the existence of discontinuities. This concept can be exploited in designing the systems that can attenuate or amplify the effect of stress waves.

This section introduces different types of protective systems for mitigating the effects of impulsive loadings, and describes an optimization methodology for designing these systems. The basic concept of designing these systems is centered on exploiting a variety of discontinuities within the structure for attenuating the effects of stress waves.

5.2 Elastic stress wave attenuators

The main purpose of this research is designing elastic systems for stress wave attenuation. These systems are called "Elastic Stress Wave Attenuators." For designing the stress wave attenuators, a design procedure is introduced which aims at optimizing the type, location, and size of discontinuities for finding the most effective mitigating structure. This can be illustrated with a simple example.

Consider an eight-layered structure shown in Figure 5-1 that can be used as a stress wave attenuator. The structure has a constant cross section and its length is long enough for one-dimensional wave propagation analysis. For each individual layer, we may select from an array of eight materials, each supporting equal wave speeds, but having different impedances separated by a factor of two ($z_8 = 2z_7 = 4z_6 = \cdots = 128z_1$). Based on the analytical solutions for the stepped rods in Section 3 (Equation 3.47), the transmitted stress amplitude at each point between the loading face and boundary can be found using the following equation:

$$\sigma_{\mathrm{i}+1} = \left(\frac{2 \frac{Z_{\mathrm{i}+1}}{Z_{\mathrm{i}}}}{1 + \frac{Z_{\mathrm{i}+1}}{Z_{\mathrm{i}}}} \right) \sigma_{\mathrm{i}} \quad , \quad i = 1,2,3, \ldots ,7 \tag{5.1}$$

Then, due to the stress doubling phenomenon at the clamped boundary, we have:

$$\sigma_9 = 2\sigma_8 \tag{5.2}$$

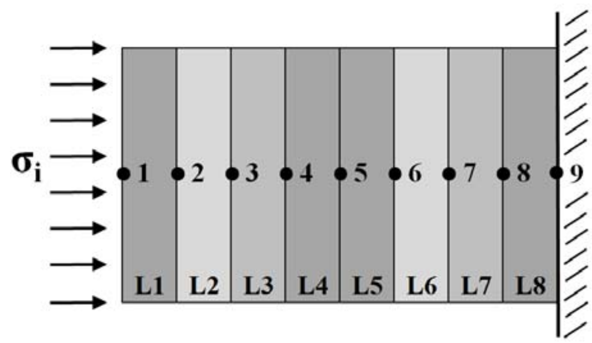

Figure 5-1 Eight layered structure

Therefore, an optimization problem can be defined for finding the best material setup of the layered structure which can attenuate the first arriving pulse to the boundary. Since the structure has eight layers and eight different materials are available, the minimum value of the stress at the boundary can be found by solving Equations (5.1) and (5.2), for every single combination of materials, which means solving these equations 8^8=16,777,216 times. By searching all of the possible combinations, it was observed that the best material string for attenuating the amplitude of the first arriving pulse to the boundary is "81818181", which reduces the amplitude by 99.9999 percent. Clearly, this type of exhaustive search for finding the best solution is very time consuming, and is more challenging for real complex systems as the optimization function becomes more sophisticated.

The computational cost of the problem at hand can be significantly reduced by utilizing an optimization method, such as Genetic Algorithms (GA). In the next section, it will be explained how GA can be used as a robust optimization tool for designing such classes of optimization problems. For the simple problem at hand, the GA optimization method can give very good results such as "81818161" or "81718181" in a very small amount of computing time compared to the exhaustive search, which shows the efficiency of this approach.

In real problems, the stress wave attenuators should be designed for attenuating the transient stress waves over a larger period of time compared to the time of the first arriving pulse. Therefore, to solve a problem analytically, the analytical solutions should be used numerously, since the number of reflected and transmitted waves increases by extending the analysis time. This becomes cumbersome as the number of layers increases, and, from the practical point of view, it is required to use some other techniques, such as finite element (FE) method for solving these problems. In Figure 5-2, the time history of the stress at the boundary of the layered structure in Figure 5-1 is plotted for three different material strings over the time period, which is taken to be 20 times the duration of the transient loading. According to this figure, it is obvious that although the structure with the material string “81818181” is the best solution for mitigating the amplitude of the first arriving pulse, it is not the desired stress wave attenuator over a larger period of time, because there are some other solutions, such as the structure with the graded impedance, i.e. “87654321” or “88816121” that can provide larger attenuation capacities.

The problem of designing the stress wave attenuators using the analytical solutions becomes even more challenging, if the structure has non-straight parts or more than one dimension. For non-straight structures, the dispersive nature of the flexural waves and the complexity of the behavior of the discontinuities make the analytical analysis more difficult. Similarly, in two-dimensional and three-dimensional structures, finding the closed form solutions for the structures with finite dimensions and multiple types of discontinuities is not feasible. Therefore, for a realistic problem, it is required to use a numerical method, such as FE analysis, to track the stress history within the structure. However, the analytical relations that are obtained in the previous sections can be very useful in selecting the appropriate design parameters. For example, based on the formulas for the reflected and transmitted waves in the stepped rods and beams, it can be concluded that a set of materials with a wide range of impedance values is required for designing effective stress wave attenuators.

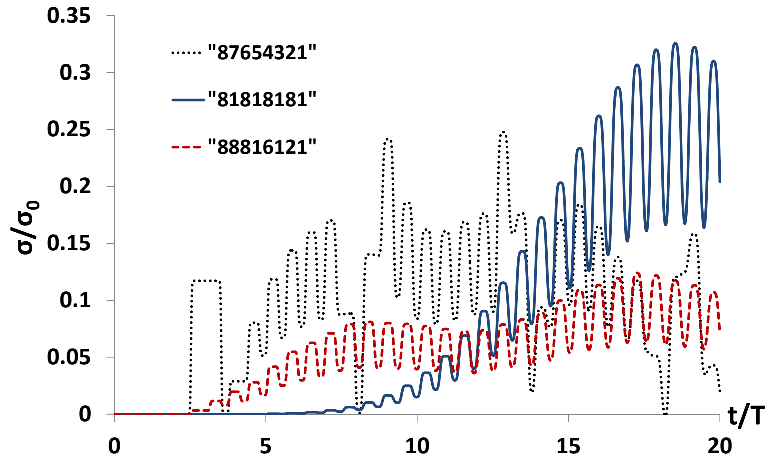

Figure 5-2 Stress history at the boundary of the structure in Figure 5-1 for three different setups

Due to the facts that are mentioned above, it is obvious that a robust optimization technique should be utilized for optimal design of the stress wave attenuators. The optimization methodology should be based on a heuristic and evolutionary procedure (such as GA) since there is no gradient information of the optimization function in designing the real stress wave attenuators. Furthermore, since it is not possible to find the closed-form solutions for wave propagation in complex systems, it is required that the optimization methodology be coupled with robust numerical methods such as FE analysis.

In this research, a coupled GA-FE optimization tool will be introduced for designing the stress wave attenuators using the concepts that exploit the effects of discontinuities. A brief explanation of GA is provided in the next section. Various types of stress wave attenuators and the coupled GA-FE optimization methodology for optimal design of these structures are described in sections 5.4 and 5.5.

5.3 Genetic algorithms

Genetic algorithms (GA) are stochastic methods of optimization that are inspired by Darwin's theory of evolution. In comparison to the traditional methods of optimization, GA have certain advantages in optimizing complicated problems. One of the main advantages of this method, which is very useful for the optimal design of the stress wave attenuators, is its capability in handling discontinuities and non-convex regions. Consequently, there is no need to have gradient information for optimizing a problem.

Genetic algorithms differ from the classical optimization procedures in two ways. The first difference is that the classical optimization methods generate a single solution at each iteration which approaches the best solution, while GA generate a population of solutions at each iteration, and the better solutions among this population advance toward the optimal solution. The second difference relates to the selection of the next optimization point. Classical methods select the next point based on the deterministic procedures; however, GA selects the next generation of solutions using some random number generators (MATLAB (2012)).

Extensive research has appeared on GA development and application in the literature, and a review of this topic is presented in Section 2. A brief description about utilizing this method (along with GA parameters) will be provided in this section. A typical GA procedure follows the steps below:

- **Generating initial population**: In this step, a random population of candidate solutions is generated based on the population size. Each candidate solution has a set of characteristics (chromosomes or genotypes) which can be evolved according to the biological rules such as crossover and mutation.
- **Evaluating the optimization function**: In this step, the optimization function (fitness function) is calculated for each solution in the population.
- **Creating new generation**: The GA problem evolves by creating a new generation by repeating the following steps until the stopping criteria is satisfied. These steps are:

  Selection: During this step, a proportion of candidate solutions will be selected to breed the new generation. The selected solutions are called parents. The parents are selected based on their fitness value (the better fitness, the bigger chance to be selected). It is better to carry over some of the best solutions of the current generation to the next generation without altering them. This strategy is called ***elitism***, which is very efficient in preserving the best solution that can be generated within the whole optimization procedure.

  Crossover: In this step, two parents are combined to form a new offspring (children). This is performed using a crossover function.

  Mutation: In this step, small random changes will be made on the new solutions using an appropriate mutation function. Mutation provides genetic diversity and helps the GA to search a broader solution space.

  Evaluating the fitness value of the new generation and checking the stopping criteria: In this step, the fitness value of the new generation is calculated, and the stopping criteria are examined to find whether the GA should be terminated or continued. Stopping criteria can be determined based on the nature of the optimization problem. Some of the most common stopping criteria include: reaching a maximum number of generations, maximum analysis time, fitness limit, and function tolerance.

There are different methods and functions for generating the populations, and performing selection, crossover, and mutation. More information about these methods and their relevance to biological evolution can be found in Holland (1975), Goldberg (1989), and Mitchell (1998).

5.4 Proposed stress wave attenuators

Four different types of stress wave attenuators are introduced in this research. These attenuators include: layered collinear rod structures, layered diamond-shape beam structures, non-collinear beam structures, and porous plates. These structures are shown schematically in Figure 5-3 to Figure 5-6.

Layered collinear rod structures and layered diamond-shape beam structures have constant geometry. These systems are divided into a specific number of layers in the horizontal direction and the optimization algorithm aims to find the best material setup for attenuation of a stress pulse when it reaches the boundary. This procedure is called “Material Optimization” as the geometry of the structure remains unchanged and the only variable parameter, during the optimal design, is the material setup.

Non-collinear beam structures and porous plates are made of a single material, and the optimization method tries to find the best geometry of the structure for mitigating the effects of a stress pulse. Therefore, this procedure is called “Geometry Optimization” as the structure is made of a single material and its geometric characteristics are the variables that are changing during the optimization procedure.

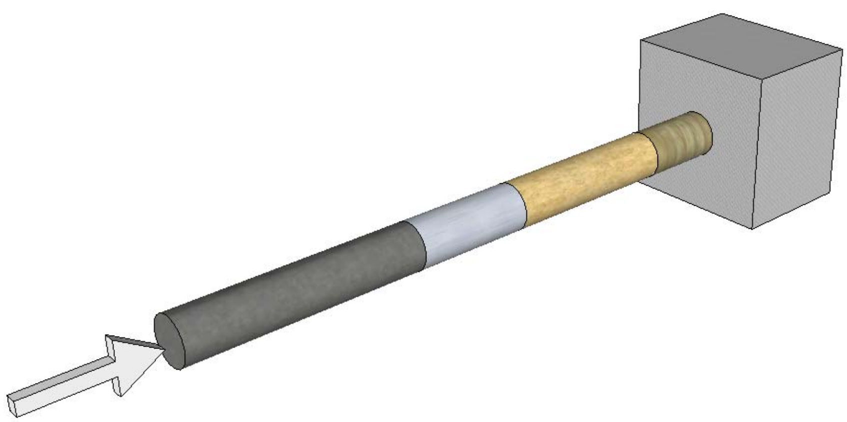

Figure 5-3 Layered collinear stress wave attenuator

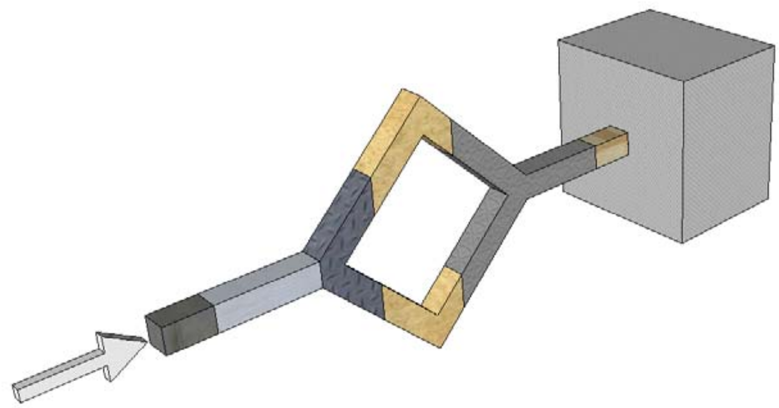

Figure 5-4 Layered diamond-shape stress wave attenuator

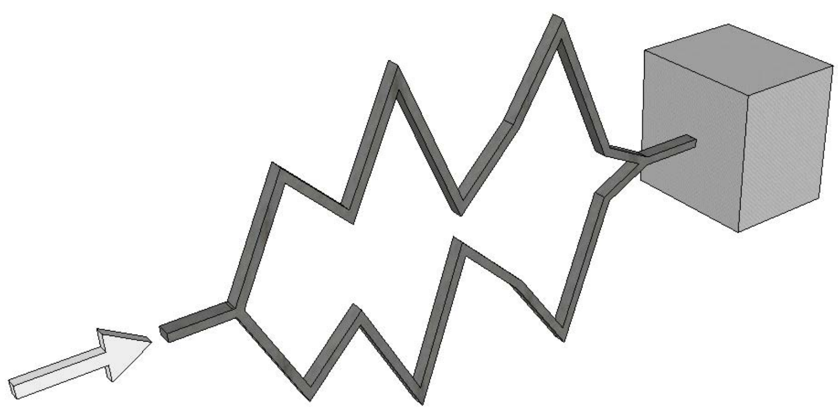

Figure 5-5 Non-collinear stress wave attenuator

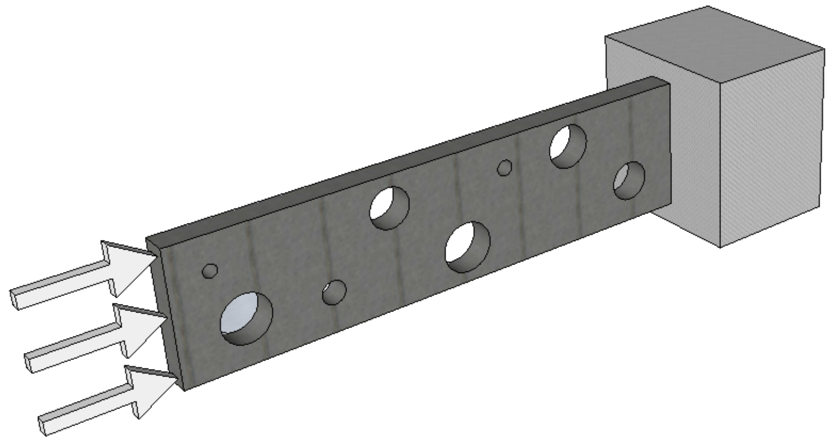

Figure 5-6 Two-dimensional porous stress wave attenuator

5.5 Design of stress wave attenuators using GA and FE

The general design procedure of the stress wave attenuators can be explained with a simple example. Consider the layered collinear structures in Figure 5-7 which is subjected to a transient loading at point A. The structure has n layers with a total length of L in the horizontal direction, and the material of each layer can be selected from a group of m materials. It is assumed that the objective of the optimization problem is minimizing the peak amplitude of the force history at the clamped boundary of the layered structure. This can be accomplished by selecting an appropriate material and tuning the length for each layer. In the mathematical form, the GA optimization problem can be defined as:

$$\begin{cases} Find\ minimum\ value\ of\ force\ at\ the\ boundary\ while: \\ X_1 + X_2 + \cdots X_{\mathrm{i}} + \cdots + X_n = L \\ 0 < X_1, X_2, \dots, X_{\mathrm{i}}, \dots, X_n < L \\ 1 \leq mat_1, mat_2, \dots, mat_{\mathrm{i}}, \dots mat_n \leq m \end{cases} \tag{5.3}$$

where X_{i} and mat_{i} denote the length and material number of each layer, respectively. This is a multiple-variable constrained optimization problem since there are a number of design parameters (material and length of each layer) and there is a constraint condition for the summation of the length of the layers. These types of problems can be easily optimized using GA; however, there are some practical limitations if we consider the computational cost of the optimization procedure. For example, when the optimization problem contains a constrained condition (such as the finite length of the structure), some specific functions should be used for the GA operators such as crossover and mutation. Therefore, to obtain appropriate results, the population size should be increased and the problem should be run for multiple times to avoid premature convergence. To avoid these practical problems, attempts are made to remove the constraint conditions of the problems in this research. This will be explained with more details in the next sections.

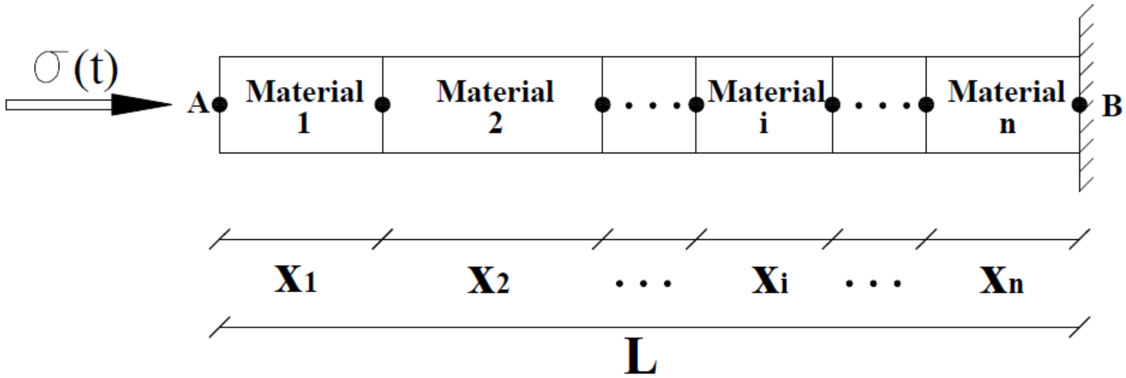

Figure 5-7 Schematic of a layered stress wave attenuator

In this research, the Genetic Algorithm Optimization Solver of MATLAB (2012) is used for all of the optimization problems. This solver is one of the solvers of Optimization Toolbox 6.2. For optimal design of the stress wave attenuators, this toolbox is coupled with Abaqus 6.12 commercial software (Simulia (2012)) for finding the fitness function. This procedure is explained below.

5.5.1 Calculating fitness function

The GA optimization fitness function for optimal design of the stress wave attenuators is minimizing the maximum amplitude of the force history at the boundary:

$$Fitness\ Function = min\big(max(F_b)\big) \tag{5.4}$$

where, F_b is the force history at the boundary. As mentioned before, for real complex structures it is very difficult to find closed form solutions for finding F_b. Therefore, to calculate the fitness function for each design within a GA run, the force history at the boundary of the stress wave attenuator is derived using FE analysis and its minimum value is calculated. In the present work, this process is performed using Abaqus 6.12 (Simulia (2012)). Since the material or geometric properties of the structures are changing for each design within each run of the GA, it is required to change the Abaqus model at each step. This is done using the Abaqus Scripting Interface. By using this interface, a new Abaqus model can be created for each fitness evaluation within GA using Python scripts. The scripts are generated based on the values of the optimization variables at each step. In summary, the following general tasks are performed by each script:

- Creating the components of the Abaqus model such as parts, materials, and sections, based on the material and geometric characteristics of the stress wave attenuators
- Assembling the model, defining the required surfaces and requesting the history output parameters
- Creating the load amplitude based on the input wavelength
- Estimating the size of the mesh and partitioning the model for generating an appropriate mesh
- Initiating the Abaqus transient dynamic analysis
- Reading the force history at the boundary from the Abaqus output database
- Calculating the peak value of the force history at the boundary

The details of the above steps are different for various types of the structures. These details will be explained separately for each category of the stress wave attenuators in the next sections.

5.6 Summary

In this section, various types of stress wave attenuators are introduced, and the optimization methodology for designing these structures is explained. It is observed that a heuristic or evolutionary optimization methodology such as GA should be used for optimal design of the stress wave attenuators as there is no gradient information about the optimization function. Furthermore, it is recognized that GA should be coupled with a robust numerical method such as FE for calculating the fitness function due to the complexity of the closed form solutions for real stress wave attenuators with multiple number of discontinuities. Therefore, a coupled GA-FE optimization methodology is introduced, which will be used in the next sections for designing the mitigating systems.

SECTION 6
DESIGN PARAMETERS FOR STRESS WAVE ATTENUATORS

6.1 Introduction

There are many parameters that should be considered for designing the stress wave attenuators. These parameters relate to the material setup and geometry of the stress wave attenuators and the nature of the dynamic loading. This section presents the essential parameters that should be considered for designing the proposed stress wave attenuators in this research. A general two-dimensional stress wave attenuator is used for this purpose since all of the parameters can be defined using this general example. Based on the type of the structure, one or a few of these parameters should be considered for the optimal design of the proposed stress wave attenuators in the following sections.

6.2 Design parameters

To define the parameters for designing the stress wave attenuators, consider the structure in Figure 6-1. This structure is a two-layered plate with the length L and the height h. A half-sine transient loading with the duration of $T/2$ is applied to the left hand side of the plate, and the plate is attached to a block on the right hand side, which is called the "host structure". The main purpose of designing the stress wave attenuators in this research is reducing the effect of the transient loading when it reaches to the host structure. For simplicity, it is assumed that the plate has two layers with the length of L_1 and L_2. The mechanical impedance of the layers and the host structure are Z_{L1}, Z_{L2}, and Z_H, respectively.

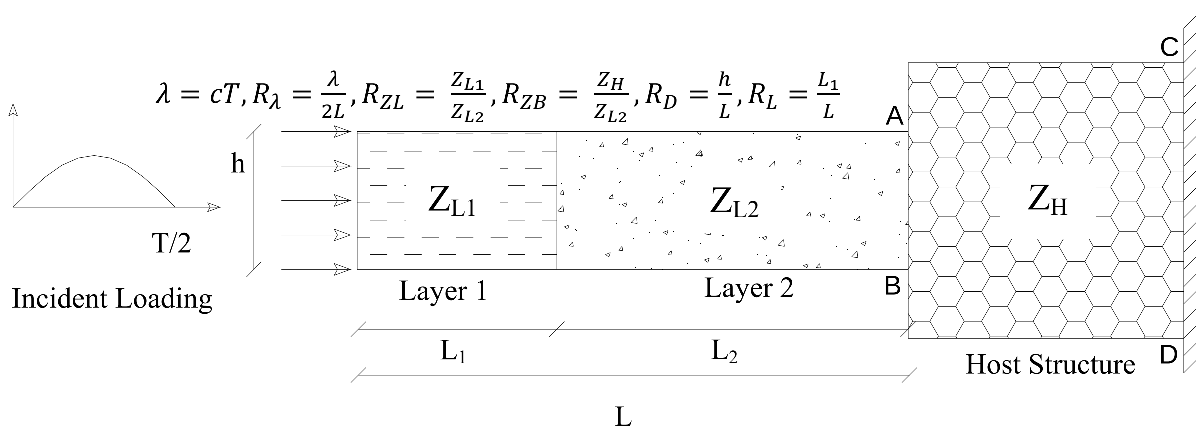

Figure 6-1 Schematic of a stress wave attenuator and the design parameters

Generally, the following five parameters can be defined for designing the stress wave attenuators:

- **Relative length of the layers:** The relative length is the ratio of the length of each layer to the total length of the structure, $R_{Li} = \frac{L_i}{L}$. For an n-layered structure, there are "$n - 1$" relative length ratios as the relative length ratio of the last layer can be defined by knowing the length ratio of the other layers. For the two-layered structures in Figure 6-1, the relative length ratio is defined as $R_L = \frac{L_1}{L}$.
- **Rigidity of the host structure:** This parameter shows the impedance mismatch between the host structure and the last layer of the stress wave attenuator (here the second layer), which can be defined as $R_{ZB} = \frac{Z_H}{Z_{L2}}$.
- **Wavelength ratio:** In this research, it is assumed that the incident pulse to all of the stress wave attenuators is a half-sine transient loading with the duration of $T/2$. The ratio of the wavelength associated with this pulse to the horizontal length of the structure is called wavelength ratio and can be designated as $R_\lambda = \frac{\lambda}{2L}$, where λ is the wavelength which is the product of the minimum wave speed within in the structure (c) and the duration of a complete sine pulse T. The minimum wave speed in the collinear and non-collinear stress wave attenuators relates to minimum longitudinal and flexural wave speed of the materials within the structure, respectively. For plate structures, the minimum wave speed refers to the minimum shear speed of the materials.
- **Impedance mismatch ratio:** For each layer in a layered structure, the impedance mismatch ratio (R_{ZL}) is the ratio between the impedance of the corresponding layer to the minimum impedance of the materials available for the optimal design. For the two-layered plate in Figure 6-1, this parameter can be defined as $R_{ZL} = \frac{Z_{L1}}{Z_{L2}}$ (assuming that the first layer has larger impedance).
- **In-plane and out-of-plane dimensions:** These parameters are only applicable to the two-dimensional stress wave attenuators. The in-plane dimension parameter is the ratio of the height over the length of the plate. For the structure in Figure 6-1, this parameter can be defined as $R_D = \frac{h}{L}$. The out-of-plane parameter relates to the thickness of the structure. Thin structures should be analyzed using plane stress (PS) analysis, while thick structures should be analyzed using the plane strain (PE) formulations.

In the following sections the effect of each of these parameters on the behavior of the two-layered stress wave attenuator, depicted in Figure 6-1, will be investigated. It should be noted that this structure is a representative of a general stress wave attenuator, which can be utilized for defining the design parameters. This means that there is no need to examine the effect of all of these parameters in designing the stress wave attenuators, and, only, a few (or one) of these parameters should be changed for the optimal design of the proposed stress wave attenuators in Section 5.

6.3 Effect of relative length of each layer (R_L)

To study the effect of the relative length of each layer R_L, a parametric study is performed on thin layered stress wave attenuators for different values of R_{ZL} (the impedance mismatch between layers), and incident wave frequencies R_λ. The rigidity of the host structure R_{ZB} and the in-plane dimensions ratio R_D are kept constant to infinity and 0.5, respectively. The value of $R_L = \frac{L_1}{L}$ is varied from $\frac{1}{8}$ to $\frac{7}{8}$. The ratio of the maximum amplitude of the force history at the boundary to the amplitude of the loading ($F_{Boundary}/F_{Load}$) is plotted versus R_L in Figure 6-2. This figure shows that R_L is an important design parameter for layered stress wave attenuators as the maximum force amplitude at the boundary is changing significantly for all values of R_λ and R_{ZL} (except for R_{ZL}=1, which refers to a structure that is made of a single material). For the two-layered structure in Figure 6-1, the maximum attenuation of the force happens for $R_L = \frac{3}{8}$ to $\frac{5}{8}$. This ratio can be different for different types of the structures based on their geometries and the material properties of the layers.

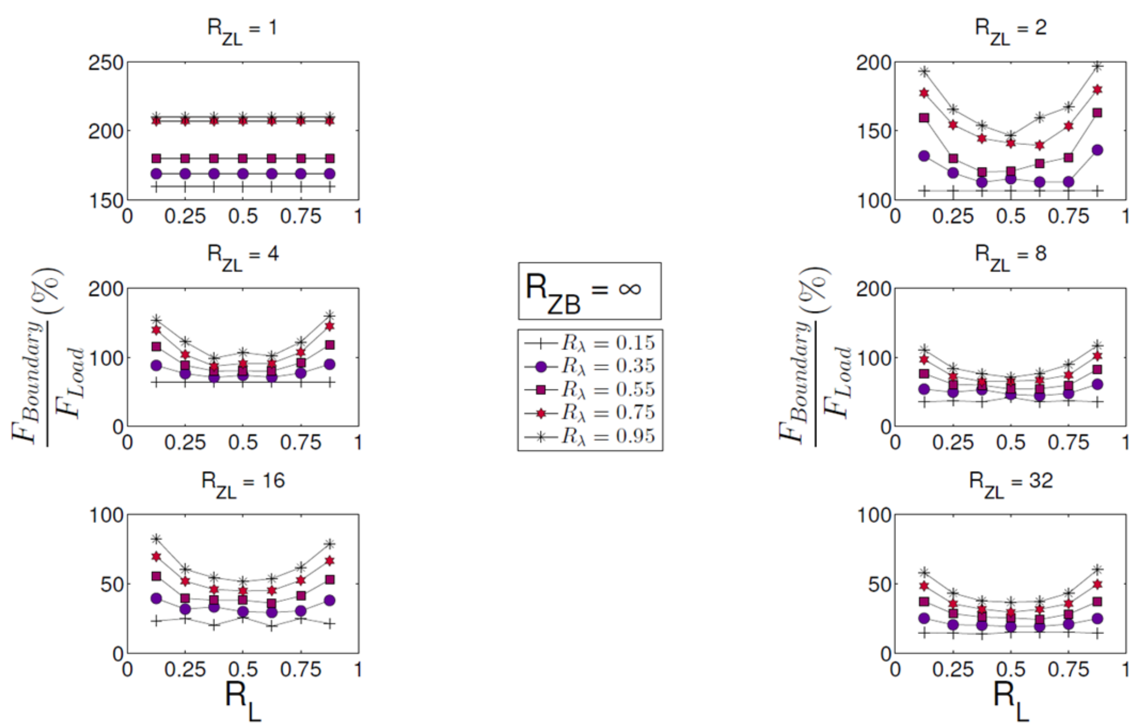

Figure 6-2 Effect of R_L on the peak force at the boundary of a thin stress wave attenuator with $R_D = 0.50$

Since the maximum attenuation for this type of stress wave attenuator happens when $R_L = \frac{3}{8}$ to $\frac{5}{8}$, in the following sections a constant value of $1/2$ is used for R_L, and consequently the effects of the other design parameters are investigated for a stress wave attenuator with a constant $R_L = 1/2$.

To investigate the effect of R_{ZL}, R_λ, R_{ZB}, R_D, and out-of-plane dimensions, the ratio of the maximum force amplitude at the boundary over the amplitude of the loading are plotted in Figure 6-3 to Figure 6-8 for different values of these parameters. Considering these figures the effect of each parameter is explained in the following sub-sections.

6.4 Effect of the impedance mismatch ratio (R_{ZL})

Efficiency of a stress wave attenuator increases as R_{ZL} increases. For both thin and thick layered structures, the stress wave attenuation capacity is heavily dependent on R_{ZL}. As the value of this parameter increases from 1 to 32, the efficiency of the stress wave attenuators goes up by approximately 90% for all cases. The larger impedance mismatch between two layers leads to higher attenuation of stress wave amplitude, and thus provides better efficiency. This trend is consistent across all parameters.

6.5 Effect of the wavelength ratio (R_λ)

Efficiency of a stress wave attenuator decreases as R_λ increases. This is due to the fact that when the length of a stress wave attenuator is long compared to the incident wavelength, the incident pulse will be reflected and transmitted many times within the system, and thus, will attenuate to a larger extent. This trend is also consistent across all parameters.

6.6 Effect of the rigidity of the host structure (R_{ZB})

Efficiency of a stress wave attenuator decreases as R_{ZB} increases. The larger impedance mismatch between the host structure and the last layer results in greater reflection at the boundary as compared to the transmission of incident waves through the host structure; consequently, the wave attenuation efficiency is reduced. Again, this trend is also consistent across all parameters.

6.7 Effect of the in-plane dimension parameter (R_D)

Efficiency dependence on in-plane dimension parameter R_D cannot be generalized across all parameters. For smaller wavelength parameter R_λ, lower values of R_D provides better efficiency, while for larger R_λ, higher values are superior. This trend is largely applicable for $R_{ZL} \leq 4$, and has minimal observable effect on efficiency for $R_{ZL} > 4$; however, we do not see any influence of R_{ZB}, and attenuator thickness on this trend. We expected that larger width to incident wavelength ratio will lead to reflection and transmission of waves for a large number of times (for small value of R_λ), and will provide better attenuation efficiency; however, the results seem to indicate that smaller width is desirable for smaller R_λ. This implies that the selection of in-plane dimension parameter R_D is important, and must be tuned to incident loading wavelength for $R_{ZL} \leq 4$, as the effect of tuning the R_D in relation to R_λ can lead to an efficiency gain as large as 25% and 15% for thick and thin layered stress wave attenuators, respectively.

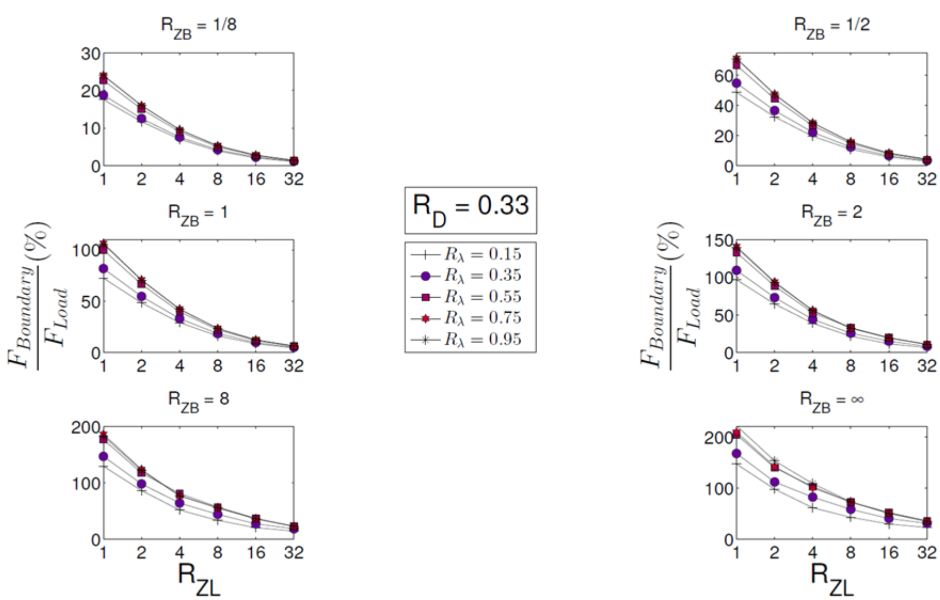

Figure 6-3 Effect of R_{ZL}, R_λ, and R_{ZB} on the peak force at the boundary of a thin stress wave attenuator with $R_D = 0.33$

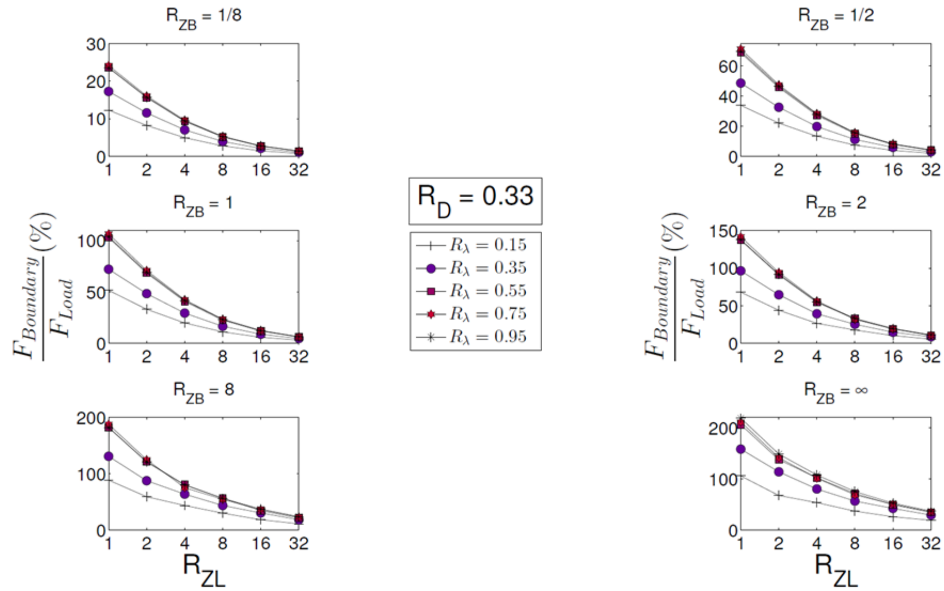

Figure 6-4 Effect of R_{ZL}, R_λ, and R_{ZB} on the peak force at the boundary of a thick stress wave attenuator with $R_D = 0.33$

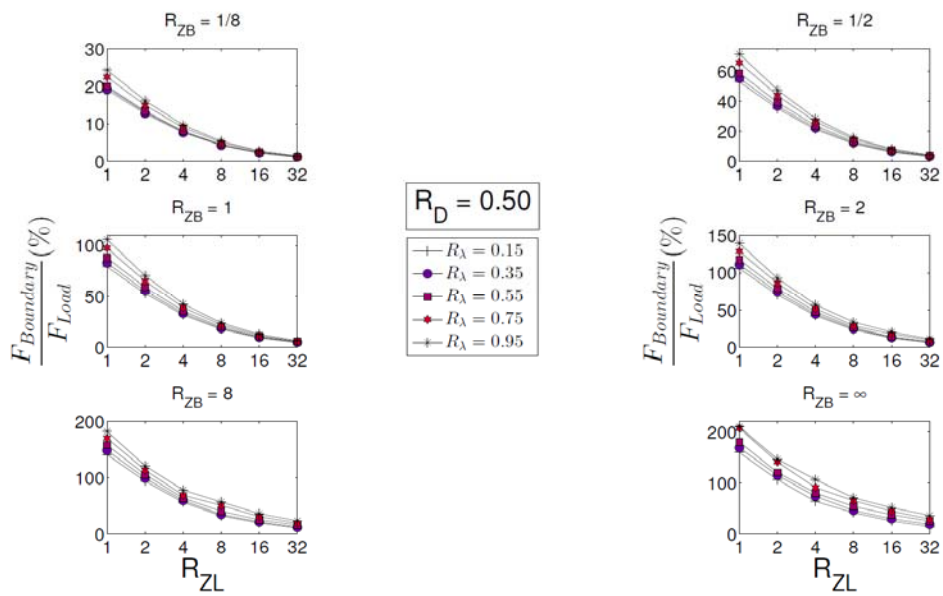

Figure 6-5 Effect of R_{ZL}, R_λ, and R_{ZB} on the peak force at the boundary of a thin stress wave attenuator with $R_D = 0.5$

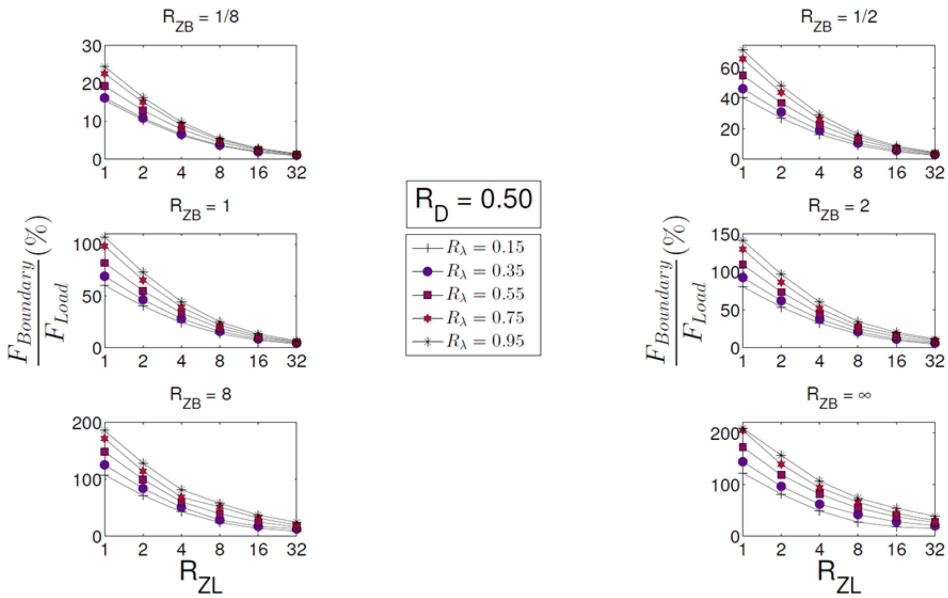

Figure 6-6 Effect of R_{ZL}, R_λ, and R_{ZB} on the peak force at the boundary of a thick stress wave attenuator with $R_D = 0.5$

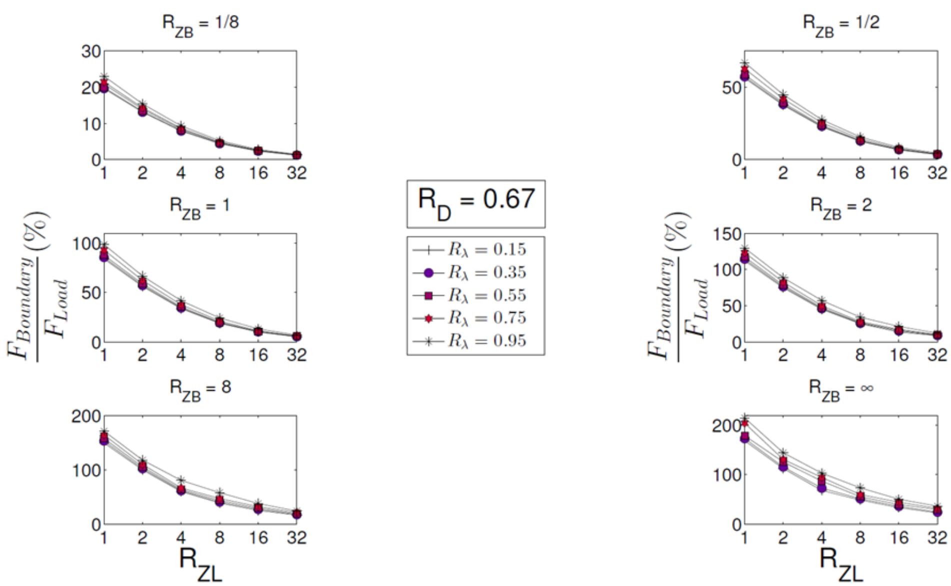

Figure 6-7 Effect of R_{ZL}, R_λ, and R_{ZB} on the peak force at the boundary of a thin stress wave attenuator with $R_D = 0.67$

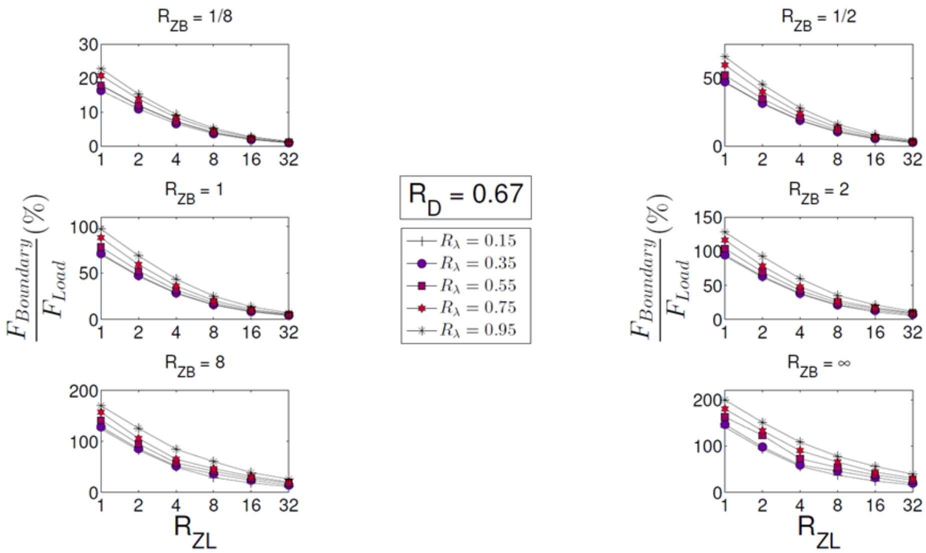

Figure 6-8 Effect of R_{ZL}, R_λ, and R_{ZB} on the peak force at the boundary of a thick stress wave attenuator with $R_D = 0.67$

6.8 Effect of the out-of-plane dimension (PS & PE)

Again, dependency of efficiency on out-of-plane dimension (thin and thick layered structures) cannot be generalized across all parameters. For smaller wavelength parameter, R_λ, thick layered stress wave attenuators have better efficiency, while for larger R_λ values, there is no clear difference between the efficiency of the thin and thick layered stress wave attenuators. This trend is more noticeable for $R_{ZL} \leq 8$; however, the trend is true for larger values of R_{ZL} as well. For smaller R_λ values, the efficiency gain with thick structures is as high as 20% compared to the thin layered structures.

Figure 6-3 to Figure 6-8 can be used as the design charts for analyzing the general plate structure in this section. In the next section, the application of these design charts will be illustrated using two examples.

6.9 Examples for elastic stress wave attenuator design

Example 6-1

This example provides the details for designing a stress wave attenuator with a concrete host structure, which is subjected to an incident pulse shown in Figure 6-9. The frequency content of the incident wave is assumed to be in the range from 15 KHz to 60 KHz. For the design calculations, the length of the stress wave attenuator is fixed to be $L = 0.25m$. The schematic of the design is shown in Figure 6-10. Table 6-1 presents the various design combinations that are explored in this example. The impedance mismatch ratio in 2D analyses with normal incident wave (plane stress and plane strain) is given by Sauren, Claessens et al. (1994) as: $Z_{L2}/Z_{L1} = c_1\lambda_2/c_2\lambda_1$, where $c = (\lambda + 2\mu)/\rho$ is the longitudinal wave speed in the material, λ and μ are Lame's constants, and ρ is the density of the material. Thus, as we look in Table 6-1, the impedance mismatch ratios are different for plane stress and plane strain analyses because Lame's constant λ is different for each case. Since, the frequency content of the incident wave is calculated to be in the range from 15 KHz to 60 KHz, the range of R_λ in Table 6-1 has been calculated using $\frac{c_s}{Lf_{max}} < R_\lambda < \frac{c_s}{Lf_{min}}$, where f_{min} and f_{max} are the minimum and maximum values of the given frequency content, and c_s is the minimum shear wave velocity of the two layers. It should be noted that the minimum shear wave velocity of the two layers is chosen, as it provides the minimum wavelength, which can be used to tune the finite element mesh size (mesh size = $\lambda_{min}/20$) and minimum range of R_λ. Table 6-1 also provides the stress wave attenuation efficiency for three different values of the in-plane parameter R_D. Design requirements and cost constraints can determine the most suitable design.

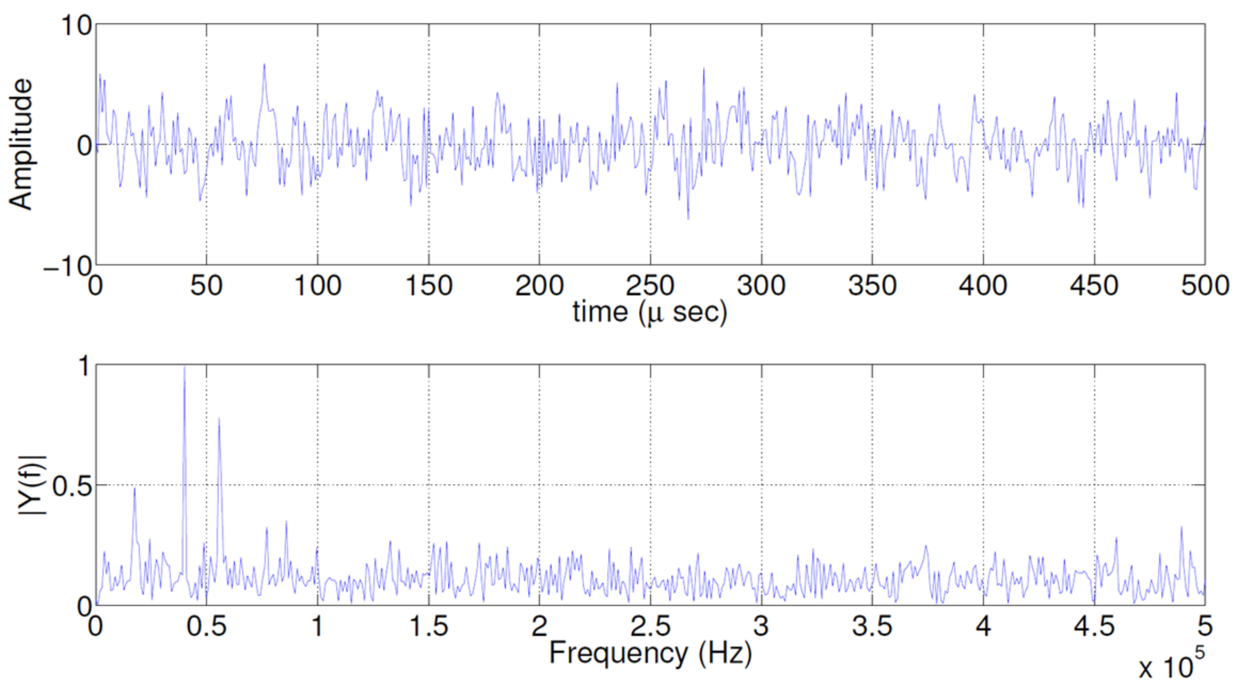

Figure 6-9 Incident pulse time history and its frequency content for the stress wave attenuator design in Example 6-1

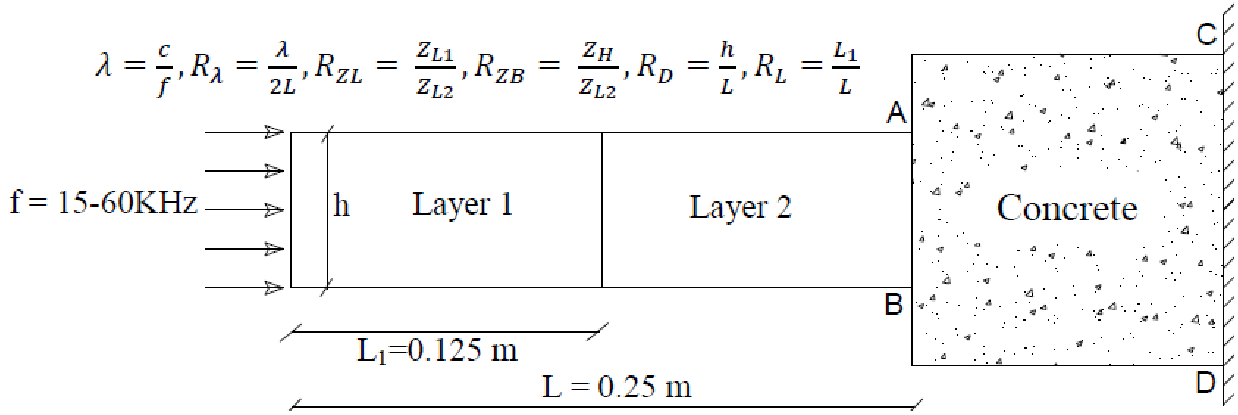

Figure 6-10 Schematic of the stress wave attenuator in Example 6-1

Table 6-1 Peak force at the boundary of the structure in Example 6.1, PS = Plane Stress & PE = Plane Strain

Layer 1	Layer 2	R_λ	R_D	R_{ZL}		R_{ZB}		$\frac{F_{Boundary}}{F_{Load}}\%$	
				PS	PE	PS	PE	PS	PE
Steel	Aluminum	0.20-0.85	0.33	2.5	2.3	0.3	0.2	30	25
Steel	Concrete	0.15-0.60	0.33	8.4	10.6	1.0	1.0	22	22
Steel	Oak Wood, Black	0.15-0.65	0.33	9.0	4.6	1.1	0.4	22	22
Steel	Epoxy	0.07-0.30	0.33	17.6	14.9	2.1	1.4	15	12
Concrete	Epoxy	0.07-0.30	0.33	2.1	1.4	2.1	1.4	75	68
Concrete	Oak Wood, Black	0.15-0.60	0.33	1.1	0.4	1.1	0.4	100	---
Steel	Aluminum	0.20-0.85	0.50	2.5	2.3	0.3	0.2	35	32
Steel	Concrete	0.15-0.60	0.50	8.4	10.6	1.0	1.0	20	17
Steel	Oak Wood, Black	0.15-0.65	0.50	9.0	4.6	1.1	0.4	20	20
Steel	Epoxy	0.07-0.30	0.50	17.6	14.9	2.1	1.4	13	10
Concrete	Epoxy	0.07-0.30	0.50	2.1	1.4	2.1	1.4	74	68
Concrete	Oak Wood, Black	0.15-0.60	0.50	1.1	0.4	1.1	0.4	90	---
Steel	Aluminum	0.20-0.85	0.67	2.5	2.3	0.3	0.2	30	20
Steel	Concrete	0.15-0.60	0. 67	8.4	10.6	1.0	1.0	20	18
Steel	Oak Wood, Black	0.15-0.65	0. 67	9.0	4.6	1.1	0.4	20	20
Steel	Epoxy	0.07-0.30	0. 67	17.6	14.9	2.1	1.4	15	11
Concrete	Epoxy	0.07-0.30	0. 67	2.1	1.4	2.1	1.4	75	68
Concrete	Oak Wood, Black	0.15-0.60	0. 67	1.1	0.4	1.1	0.4	88	---

Example 6-2

This example is similar to Example 6.1, except the host structure is made of black oak wood, and the incident pulse time history has frequency content ranging from 25 KHz to 50 KHz as shown in Figure 6-11. The length of the wave attenuator has been fixed to $L = 0.15m$. The various design possibilities providing different stress wave attenuation efficiency are listed in Table 6-2, while the schematic of the designed structure is shown in Figure 6-12. The design calculations, parameters, and notations are the same as Example 6.1.

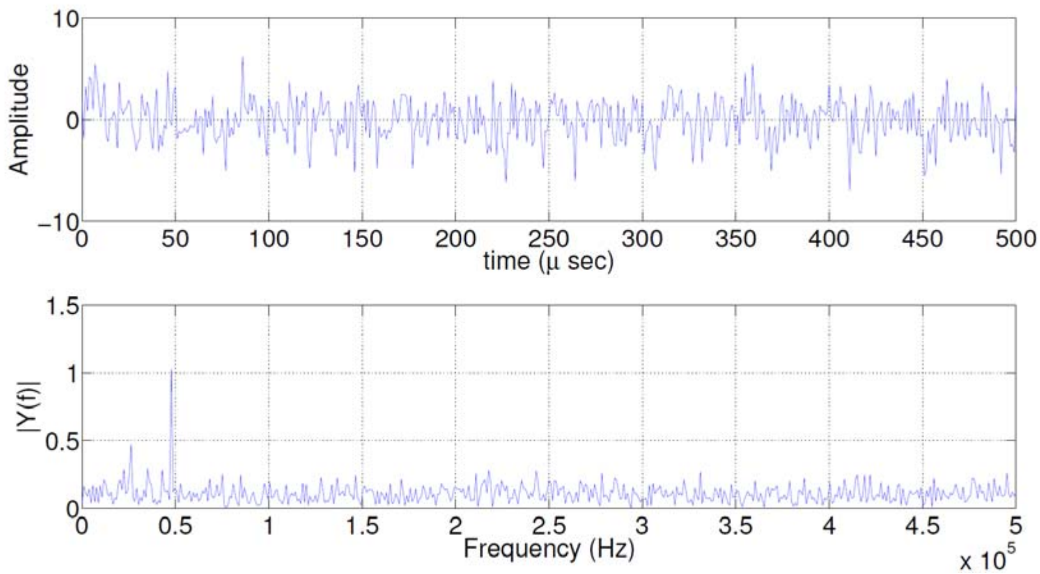

Figure 6-11 Incident pulse time history and its frequency content for the stress wave attenuator design in Example 6-2

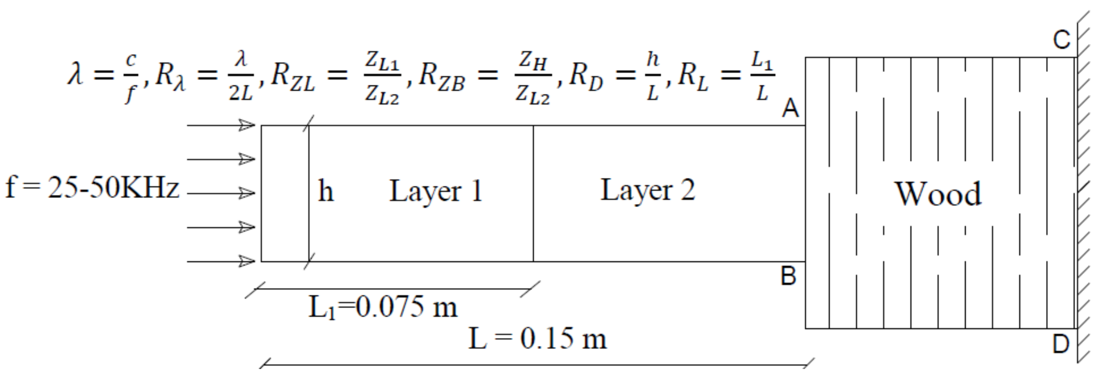

Figure 6-12 Schematic of the stress wave attenuator in Example 6-2

Table 6-2 Peak force at the boundary of the structure in Example 6-2

Layer 1	Layer 2	R_λ	R_D	R_{ZL}		R_{ZB}		$\frac{F_{Boundary}}{F_{Load}}\%$	
				PS	PE	PS	PE	PS	PE
Steel	Aluminum	0.40-0.85	0.33	2.5	2.3	0.3	0.5	30	48
Steel	Concrete	0.30-0.60	0.33	8.4	10.6	0.9	2.3	22	32
Steel	Oak Wood, Black	0.30-0.65	0.33	9.0	4.6	1.0	1.0	22	42
Steel	Epoxy	0.15-0.30	0.33	17.6	14.9	2.0	3.3	15	15
Concrete	Epoxy	0.15-0.30	0.33	2.1	1.4	2.0	3.3	70	65
Concrete	Oak Wood, Black	0.30-0.60	0.33	1.1	0.4	1.0	1.0	100	---
Steel	Aluminum	0.40-0.85	0.50	2.5	2.3	0.3	0.5	30	49
Steel	Concrete	0.30-0.60	0.50	8.4	10.6	0.9	2.3	20	25
Steel	Oak Wood, Black	0.30-0.65	0.50	9.0	4.6	1.0	1.0	20	33
Steel	Epoxy	0.15-0.30	0.50	17.6	14.9	2.0	3.3	13	11
Concrete	Epoxy	0.15-0.30	0.50	2.1	1.4	2.0	3.3	74	62
Concrete	Oak Wood, Black	0.30-0.60	0.50	1.1	0.4	1.0	1.0	88	---
Steel	Aluminum	0.40-0.85	0.67	2.5	2.3	0.3	0.5	29	45
Steel	Concrete	0.30-0.60	0. 67	8.4	10.6	0.9	2.3	21	25
Steel	Oak Wood, Black	0.30-0.65	0. 67	9.0	4.6	1.0	1.0	21	36
Steel	Epoxy	0.15-0.30	0. 67	17.6	14.9	2.0	3.3	14	13
Concrete	Epoxy	0.15-0.30	0. 67	2.1	1.4	2.0	3.3	76	63
Concrete	Oak Wood, Black	0.30-0.60	0. 67	1.1	0.4	1.0	1.0	87	---

6.10 Summary

The required parameters for designing the proposed stress wave attenuators are investigated in this section. These parameters include relative length of each layer, in-plane and out-of-plane dimensions, incident wave frequencies (wavelength), rigidity of the host structure, and impedance mismatch between different layers. The concurrent effects of these parameters are analyzed for a general two-dimensional stress wave attenuator, and comments are provided. It is observed that the efficiency of the stress wave attenuator is a complex function of all parameters, and varies significantly in different ranges. Furthermore, two quantitative examples are provided to illustrate a design process, and to highlight the collective interdependency of the design parameters with the stress wave attenuator efficiency. The analyses reflect that the impedance mismatch between different layers, R_{ZL}, incident wave frequencies (wavelength), R_{λ}, and rigidity of the host structure, R_{ZB}, are the most critical parameters for designing the stress wave attenuators.

SECTION 7
LAYERED COLLINEAR STRESS WAVE ATTENUATORS

7.1 Introduction

This section presents the procedure for designing layered collinear stress wave attenuators. These structures are one-dimensional layered systems with various material properties. The wave attenuation mechanism for these structures is mainly related to the impedance mismatch between the layers, which affects the reflected and transmitted waves as discussed in Section 3. The optimization procedure tries to arrange the layers in a configuration which can provide a high amount of attenuation. Therefore, material optimization is performed for the optimal design of these collinear systems as the geometry of the systems remains unaffected during the optimal design.

7.2 Optimal design parameters and characteristics of collinear stress wave attenuators

A schematic of a layered collinear stress wave attenuator and its corresponding design parameters are shown in Figure 7-1. It is assumed that the cross sectional area of these structures is small and one-dimensional wave propagation theory can be used for the analysis. Therefore, the in-plane (R_D) and out-of-plane (PS & PE) design parameters are not applicable for this type of stress wave attenuators.

The effect of the rigidity of the host structure (R_{ZB}) on the behavior of the stress wave attenuators was studied in Section 6. It was observed that the magnitude of the force at the end boundary of the stress wave attenuators increases by increasing the rigidity of the boundary, which is due to the larger impedance mismatch between the last layer and the host structure. Since we know this general trend, the optimal design of the layered collinear stress wave attenuators in this section is performed by considering a fixed value for R_{ZB}. It is assumed that the host structure is very rigid and R_{ZB} is infinity. However, the optimal design can be easily performed for any other value of R_{ZB}, if it is required. Another reason for considering a single value for R_{ZB} is to reduce the number of optimal designs, as each design process is quite time consuming.

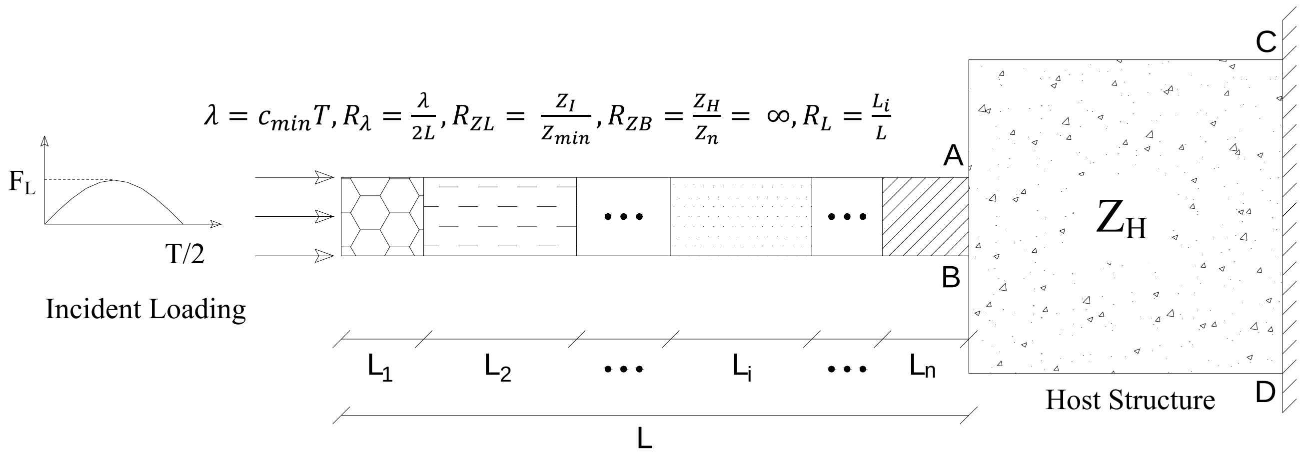

Figure 7-1 Schematic of a collinear stress wave attenuator and its design parameters

According to section 6, the impedance mismatch ratio (R_{ZL}) for a layer is the ratio between the impedance of the material of the layer to the minimum impedance of the materials available for the optimal design. In this section, four different types of materials are used for the optimal design of the collinear stress wave attenuators. These materials are introduced in the next section.

It is assumed that the relative length of each layer (R_L) is constant. This assumption is made to avoid the constraints in the GA optimization process. Therefore, R_L for each layer within the structure is $1/n$, where n is the total number of layers.

It was observed in Section 6 that the wavelength (frequency) of the incident pulse has a significant effect on the behavior of the stress wave attenuators. In fact, for each value of the wavelength (frequency) of the incident pulse a different structure can be obtained from the optimal design. As we know, the exact amount of the wavelength of the incident loadings is not a deterministic value in practical applications. Furthermore, it is not possible to perform the optimal design for a very large number of wavelength values because of the computational cost limitations. Therefore, in this section, the collinear stress wave attenuators will be optimized for 6 different wavelength ratios, i.e., $R_\lambda = 0.125, 0.25, 0.375, 0.50, 0.625,$ and 0.75.

All of the chosen values are smaller than unity because the efficiency of the stress wave attenuators decreases significantly when the incident pulse produces a very large wavelength. This is due to the fact that the number of reflection and transmission of the total incident pulse within the structure decreases by increasing the wavelength, and the stress wave attenuator cannot be effective in mitigating the amplitude of the waves. The minimum selected wavelength ratio is 0.125. This value is chosen based on the computational cost limitations. As we know, the size of the mesh in FE models decreases by reducing the wavelength associated with the loading (or increasing the frequency). Consequently, very fine meshed models should be used during the optimal design, which is very time consuming.

It should be noted that the wavelength ratios in this section are selected to provide appropriate examples for the optimal design procedure and highlighting its dependence on the wavelength (frequency) of the incident pulse. Therefore, the optimal design scheme is not limited to any specific value or range of the frequency content, and can be easily applied for designing the stress wave attenuators under different types of transient and dynamic loadings with a wide range of frequency content.

7.3 Material properties

Four different types of materials are selected for the optimal design of the layered collinear stress wave attenuators. These materials are Steel, Aluminum, HDPE, and Aluminum Foam, and their properties are listed in Table 7-1. The reason for selecting these materials is that they cover a wide range for the impedance parameter; consequently, the performance of the optimal design can be investigated well. Furthermore, these materials are real materials that are commonly used for various applications. It should be noted that the design procedure can be applied to any group of materials with different numbers and material properties and it is not restricted to the four materials that are presented in this section.

7.4 Optimization procedure

The general optimization procedure for designing the stress wave attenuators are explained in Section 5.5. In this section, the specific details for layered collinear stress wave attenuators are pointed out.

Table 7-1 Materials used for optimal design of the layered collinear stress wave attenuators

Material	index	Elastic modulus (GPa)	Density (kg/m^3)	Poisson's ratio	Velocity C (m/s)	Impedance (kg/m^2/s)
Steel	1	200.0	7850	0.30	5047	39.62
Aluminum	2	68.9	2700	0.33	5189	13.64
HDPE	3	1.2	950	0.42	1123	1.06
AL Foam	4	0.4	800	0.30	707	0.57

Consider the collinear layered stress wave attenuator in Figure 7-1 with total length of L, which is subjected to a half-sine transient pulse with the duration of $T/2$ and amplitude of F_L. It is assumed that the stress wave attenuator has n layers (with equal length) and the material properties of each layer can be selected from the group of four materials that are listed in Table 7-1.

As mentioned earlier, it is assumed that the stress wave attenuator is composed of the layers with equal length. The optimization procedure can be performed by assuming layers with variable length; however, as the total length of the structure is finite, constrained GA analysis should be utilized for the optimal design. Constrained optimization problems can be easily implemented in the GA procedure; however, because of the limitations on the type of the functions of the GA operators such as crossover and mutation, it is required to increase the size of the populations in order to avoid the premature convergence. Enlarging the population size increases the computation time significantly, especially for the problems in this research as the fitness function is calculated using Abaqus 6.12 FE software (Simulia (2012)). Consequently, the layered optimized structures in this research are designed by dividing the total length of the structure into equal parts.

During the optimization procedure, the material of each layer can be expressed with an integer number between 1 and 4, which means the optimization variables are integer-valued. The Global Optimization Toolbox of MATLAB (2012) can solve these types of problems by using special creation, crossover, and mutation functions. Further details can be found in the product help of the software.

The general procedure for finding the fitness function is explained in Section 5.5. It should be noted that the layered collinear stress wave attenuators are modeled using 2-node linear 2-D truss element from the Abaqus (Simulia 2012) element library (element T2D2).

7.5 Results and discussion

Consider the layered collinear stress wave attenuator in Figure 7-1 with $L = 8cm$. This structure is designed for 6 different wavelength ratios ranging from 0.125 to 0.75. The duration of the pulses which correspond to these wavelength ratios are presented in Table 7-2.

Based on the definition of the wavelength ratio in Figure 7-1, the duration of the sine pulse (T) can be found as:

$$T = \frac{2LR_{\lambda}}{C_{min}} \tag{7. 1}$$

where, C_{min} is the minimum longitudinal velocity of the available materials, which is Aluminum Foam in this section.

The structure is divided into 16 equal layers ($L_i = 5mm$), and an integer-valued GA optimization is performed for each wavelength ratio with 16 integer variables with lower bound of 1 and upper bound of 4. This means that the solution space is composed of $4^{16} = 4.29E9$ combinations, and, obviously, it is impossible to operate an exhaustive search for finding the best solution due to the extensive computational cost.

Table 7-2 Wavelength ratios and duration of the applied pulses

Wavelength ratio (R_λ)	C_{min} (m/sec)	Duration of the sine pulse (sec)	Duration of the half-sine pulse (sec)
0.125	707	2.83E-05	1.41E-05
0.250	707	5.66E-05	2.83E-05
0.375	707	8.49E-05	4.24E-05
0.500	707	1.13E-04	5.66E-05
0.625	707	1.41E-04	7.07E-05
0.750	707	1.70E-04	8.49E-05

The initial population of the GA is set to 100 for this problem, and the GA was run until the change in the fitness function value becomes less than the function tolerance of 1e-6. The GA procedure includes the elitism operator, and two of the best solutions in each generation are guaranteed to survive to the next generation, which increases the rate of convergence to the optimal point.

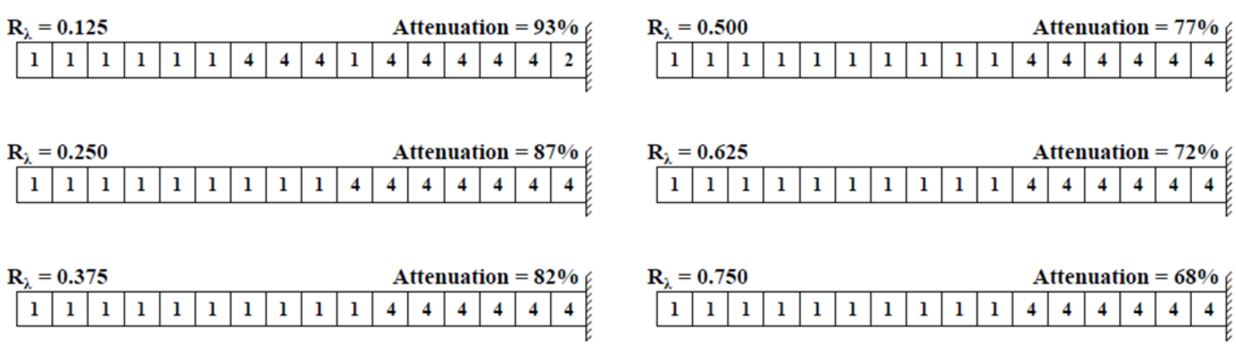

Figure 7-2 Optimal material string for the layered collinear stress wave attenuators

The final optimal design of the layered collinear stress wave attenuators for 6 different wavelength ratios are shown in Figure 7-2 and Figure 7-3. Figure 7-2 represents the material string of the optimized systems and the amount of the attenuation that can be achieved with each structure, while Figure 7-3 depicts the length and the material of each layer within each optimal design. The force history at the boundary of each optimized structure is presented in Figure 7-4.

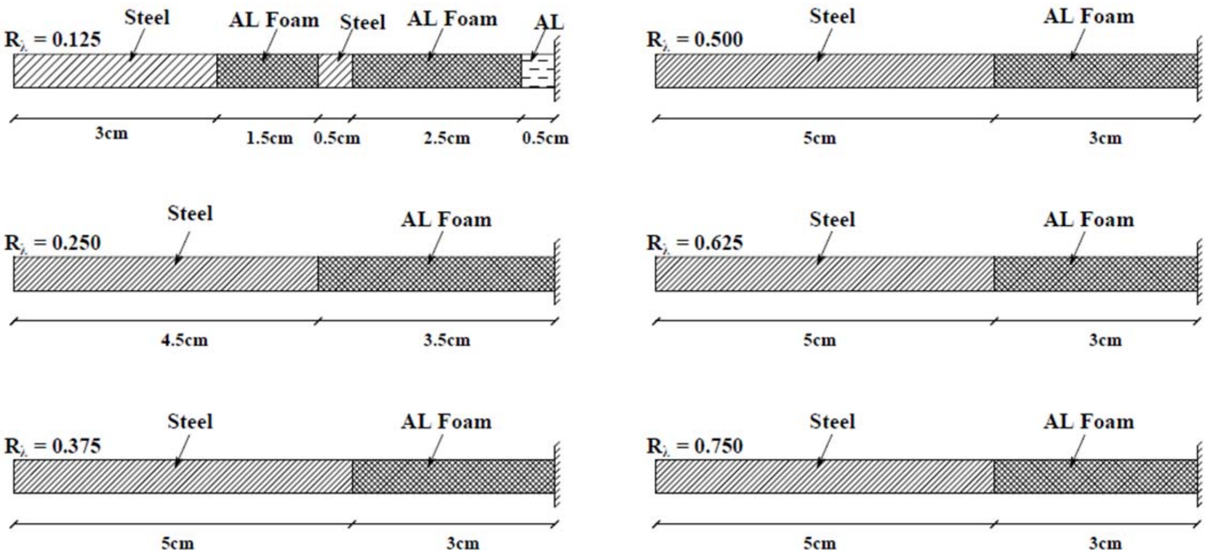

Figure 7-3 Optimal design of the collinear layered stress wave attenuators

According to Figure 7-2, Figure 7-3, and Figure 7-4, the following comments can be mentioned about the optimal design of each structure:

- For $R_\lambda = 0.125$, the optimal design is made of 5 layers with the length of 3, 1.5, 0.5, 2.5, and 0.5cm. The material of each layer from the left hand side is Steel, AL Foam, Steel, AL Foam, and AL. According to Figure 7-4 the amplitude of the force history at the boundary of this structure is attenuated as much as 93%.
- For $R_\lambda = 0.250$, the optimal design is made of 2 layers with the length of 4.5 and 3.5cm. The first layer is made of Steel which has the highest impedance, while the second layer is made of AL Foam which has the lowest impedance. According to Figure 7-4, the amount of attenuation at the boundary is 87%.
- For $R_\lambda = 0.375$, the optimal design is made of 2 layers with the length of 5 and 3cm. Similar to the previous case, layers 1 and 2 are made of Steel and AL Foam, respectively. The amount of attenuation at the boundary is 82%.

- For $R_\lambda = 0.500$, the length of the layers and their material properties are exactly the same as the structure which is optimized for $R_\lambda = 0.375$. The amount of attenuation at the boundary is 77%.
- For $R_\lambda = 0.625$, the length of the layers and their material properties are exactly the same as the structure which is optimized for $R_\lambda = 0.375$. The amount of attenuation at the boundary is 72%.
- For $R_\lambda = 0.750$, the length of the layers and their material properties are exactly the same as the structure which is optimized for $R_\lambda = 0.375$. The amount of attenuation at the boundary is 68%.

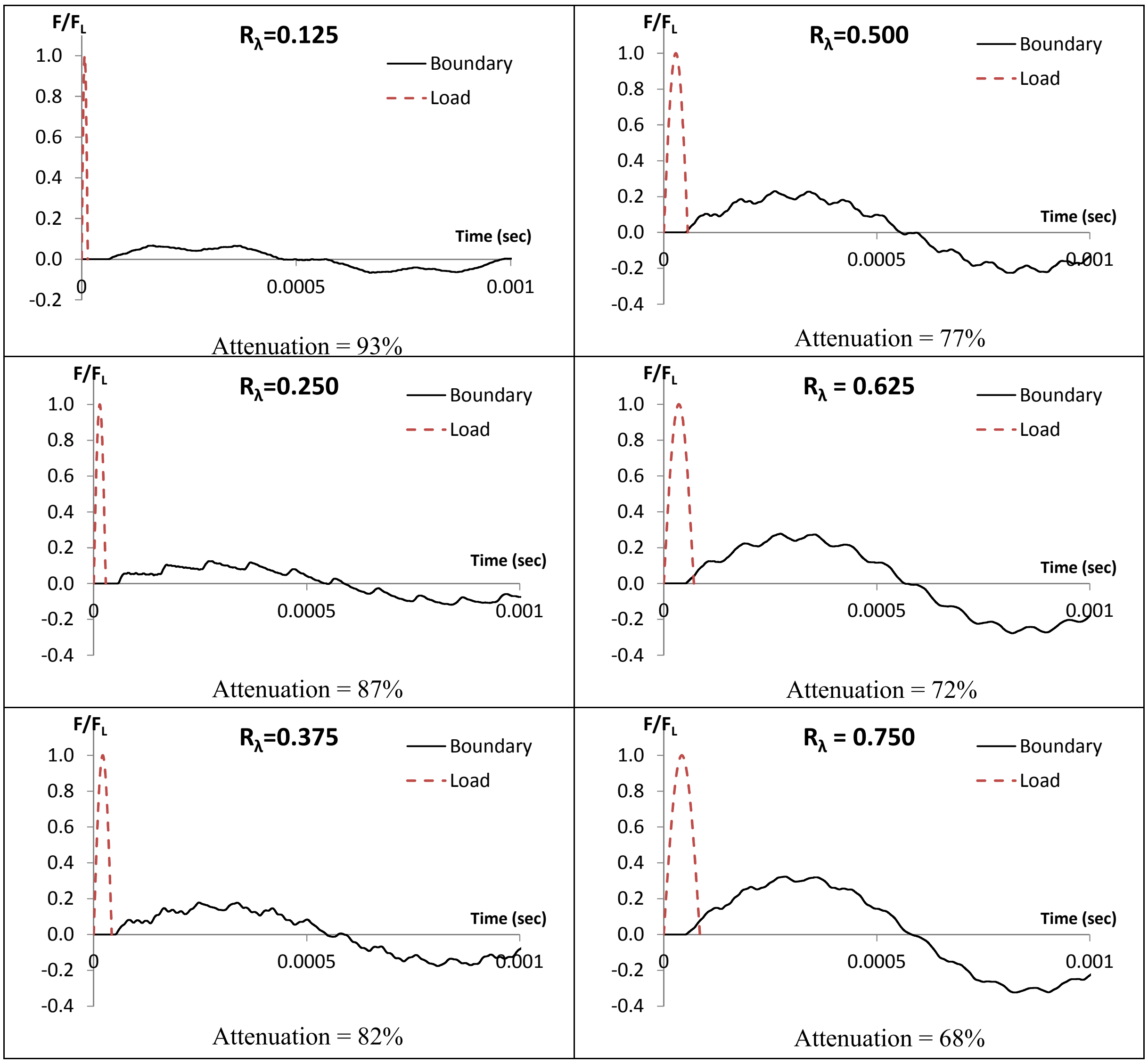

Figure 7-4 Force history at the boundary of the optimized structures

These results show that the optimized structures are mainly composed of the materials with the highest (Steel) and lowest (AL Foam) impedance values. In fact, all of the systems are composed of Steel and AL Foam except the structure that is designed for $R_\lambda = 0.125$, which has only a short layer of AL at its end. In addition, the results demonstrate that the layers should be arranged in a pattern in which the wave passes from a high impedance to a low impedance medium (except the structure which is optimized for $R_\lambda = 0.125$). These phenomena can be justified using Equation 3.47. According to this formula, the amount of the transmission of the stress waves at the intersection of two media decreases when a wave passes from a high to low impedance material. This reduction becomes more dramatic by increasing the impedance mismatch ratio.

Moreover, according to Figure 7-4, it can be observed that the amount of the attenuation at the boundary of the stress wave attenuators decreases significantly by increasing the wavelength ratio. Therefore, to achieve higher amount of attenuation, it is required to have long structures compared to the wavelength associated with the incident forces.

Optimized structures subjected to different wavelength ratios: To further explore the attenuation capacity of the optimal designs, each optimized structure is subjected to the loads with various wavelengths and the amount of attenuation at their boundary is presented in Table 7-3. Using this table, the amount of the force attenuation in each structure can be plotted versus the parameter R_λ, as it is shown in Figure 7-5. This figure shows that the attenuation capacity of the structures that are optimized for $R_\lambda = 0.25$ and $R_\lambda = 0.375, 0.5, 0.625,$ and 0.75 is much higher than the attenuation capacity of the structure which is optimized for $R_\lambda = 0.125$. The attenuation capacity for the structure that is optimized for $R_\lambda = 0.375, 0.5, 0.625,$ and 0.75 is slightly higher than the structure that is optimized for $R_\lambda = 0.25$. Therefore, for a collinear stress wave attenuator with the length of 8cm which is subjected to half-sine transient loadings with the wavelength ratios (R_λ) between 0.125 to 0.75, the best optimal design is a two-layered structure which has 5cm of steel and 3cm of AL Foam.

Table 7-3 Amount of attenuation of the optimized structures for different values of R_λ

Attenuation at R_λ (%)	Optimized for R_λ:					
	0.125	0.250	0.375	0.500	0.625	0.750
0.125	93	92	92	92	92	92
0.250	87	88	87	87	87	87
0.375	80	82	82	82	82	82
0.500	74	76	77	77	77	77
0.625	67	72	72	72	72	72
0.750	61	67	68	68	68	68

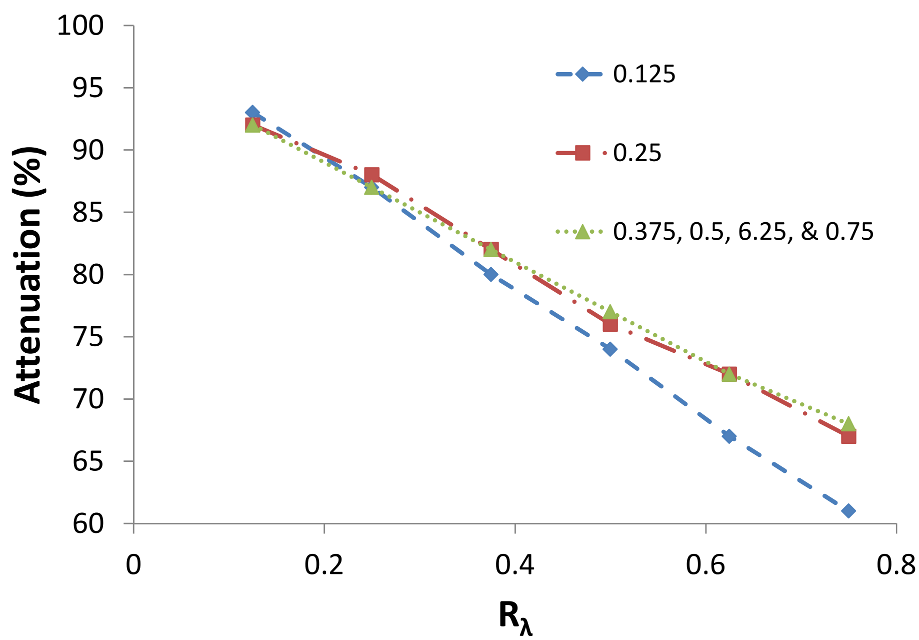

Figure 7-5 Attenuation vs. R_λ

7.6 Three dimensional structures with layered collinear stress wave attenuators

To provide a practical example, consider the three dimensional (3D) structure in Figure 7-6. In this structure, four layered collinear stress wave attenuators are sandwiched between two steel plates.

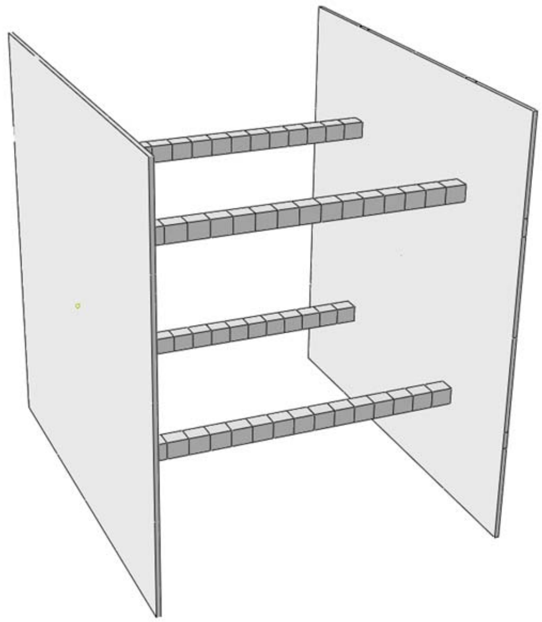

Figure 7-6 3D model with collinear stress wave attenuators

A transient half-sine force is applied to the plate on the left hand side, and the structure is fixed to a rigid boundary at the right hand side as shown in Figure 7-7. It is assumed that the layered stress wave attenuators have the best optimized structure as explained in the previous section; that is, they have two layers: 5cm of Steel and 3cm of AL Foam. The wavelength ratio (R_{λ}) and the amplitude of the applied transient loading are 0.375 and F_L, respectively.

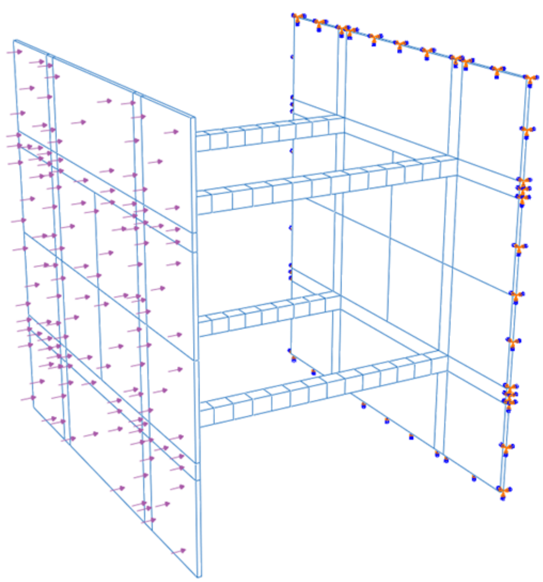

Figure 7-7 Boundary condition and loading of the 3D model

To investigate the attenuation capacity of the collinear layered stress wave attenuators, two 3D models are built in Abaqus, and the force history at the boundary of these models are compared. The first model is made of optimized collinear structures, while the second model is composed of the single-layered steel rods. The optimized and steel rods are shown in Figure 7-8.

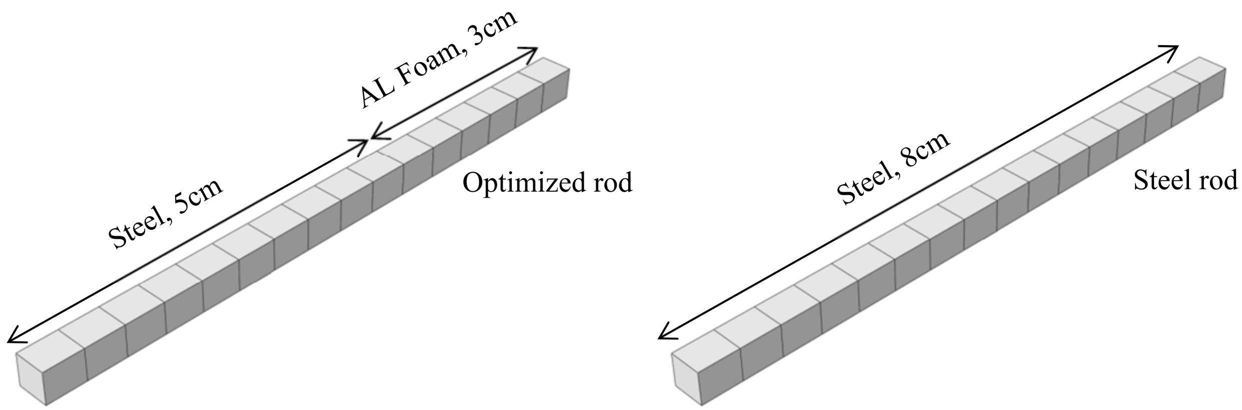

Figure 7-8 Two types of layered collinear structures used in the 3D model

The normalized force histories at the boundary of the two structures are presented in Figure 7-9. It is obvious that a significantly higher amount of attenuation can be achieved using the structure with optimized collinear stress wave attenuators.

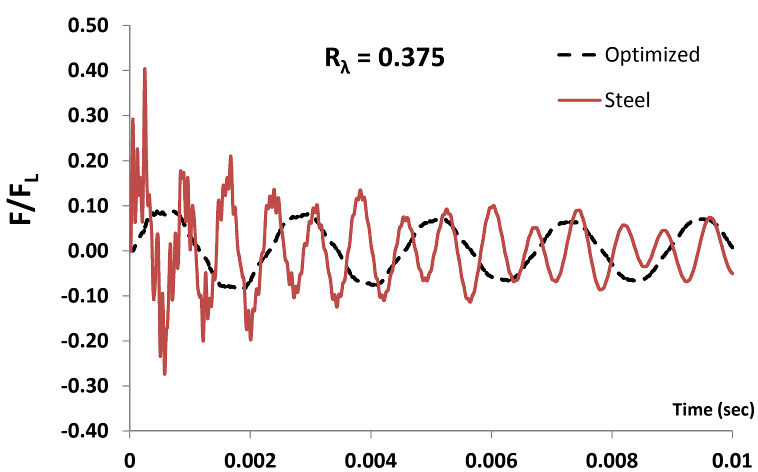

Figure 7-9 Force histories at the boundary of the 3D models with collinear stress wave attenuators

7.7 Summary

The optimal design of the layered collinear stress wave attenuators is explored in this section. It was observed that the optimized structures are mainly composed of the materials with the highest and lowest impedance values. Furthermore, it was observed that the structures are usually optimized in a pattern in which the waves should pass from a high to low impedance material. This is due to the fact that the magnitude of the transmitted waves is significantly affected when the waves pass through the intersection of two media with high impedance mismatch ratio.

It was also found that the attenuation capacity of the layered collinear stress wave attenuators increases significantly by decreasing the wavelength ratio (R_λ). This means that the impedance mismatch between the layers of the structure can highly influence the characteristics of the propagating waves when the applied force has a short wavelength, and the optimal design procedure can find more efficient attenuators.

At the end of the section, the optimized collinear stress wave attenuators were implemented in a three dimensional model to examine their attenuation capacity. It is observed that a significant amount of attenuation can be achieved in real 3D structures using the optimized layered collinear structures.

SECTION 8
NON-COLLINEAR STRESS WAVE ATTENUATORS

8.1 Introduction

The wave propagation characteristics of the layered collinear stress wave attenuators were studied in the previous section. It was observed that a reasonable amount of attenuation can be obtained by optimizing the material setup of each structure. In layered collinear systems, longitudinal wave reflection and transmission at the intersection of two layers is the only mechanism that can attenuate the amplitude of an applied pulse when it reaches the boundary. By changing the geometry of the collinear systems to non-collinear structures, flexure can occur during the wave propagation. As discussed in Section 4, flexural waves have a dispersive nature, and their characteristics change as they propagate within a system. This characteristic might provide a higher potential for the attenuation of the stress loadings, and can be implemented in our developed heuristic optimization tool to find more efficient stress wave attenuators.

In this section, the optimal design of non-collinear stress wave attenuators is studied extensively. These structures include multi-layered and single-layered non-collinear systems. The optimal design parameters and procedure for each type of the systems are presented, and their attenuation capacity is discussed in the following sections.

8.2 Non-collinear stress wave attenuators and effect of symmetry

In this research, the first attempt in changing the geometry of the stress wave attenuators was performed by inclining the middle section of a straight structure as shown in Figure 8-1. The total length of the structure is 8cm in the horizontal direction and its cross section is a rectangular section with the width of 2mm and height of 4mm. The angle of the inclined part with respect to the horizontal line is 45 degrees. It is assumed the structure is composed of two layers: 5cm of Steel and 3 cm of Aluminum foam. The properties of these materials are presented in Table 7.1.

To examine the behavior of this structure, a 3D model is built in Abaqus and a half-sine pulse is applied to the left hand side of the structure. This pulse generates the wavelength ratio (R_{λ}) of 0.375. The Abaqus 3D model is shown in Figure 8-2.

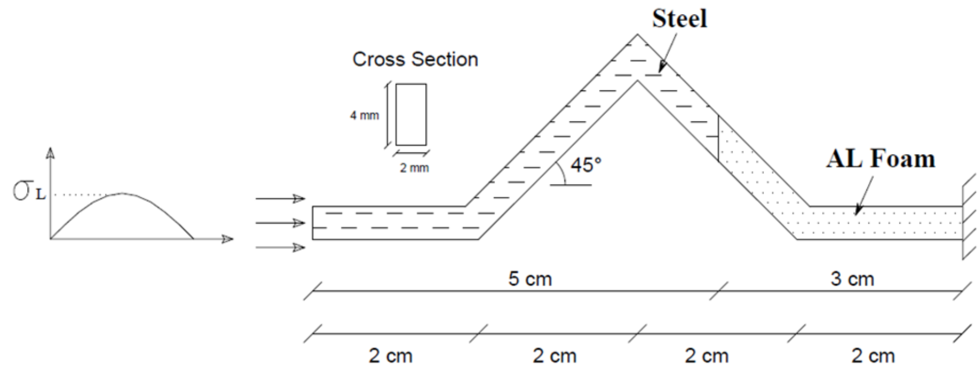

Figure 8-1 Non-symmetric inclined structure

In order to investigate the behavior at the boundary, five elements are selected at the surface of the fixed boundary and their stress histories are extracted from the Abaqus model. These elements are shown in Figure 8-3. The maximum normalized stresses at each element of the boundary are presented in Table 8-1. It should be noted that the normalized amount of the total force and moment at the boundary of the structure are $F_B/F_L = 9.63\%$ and $M_B/(F_L L) = 6.17\%$, respectively. F_B, F_L, M_B, and L represent the amplitude of the force at the clamped boundary, amplitude of the force at the loading surface, amplitude of the bending moment at the boundary, and the total horizontal length of the structure, respectively.

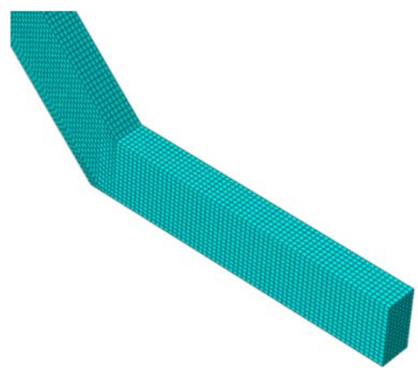

Figure 8-2 3D Abaqus model of the non-symmetric inclined structure

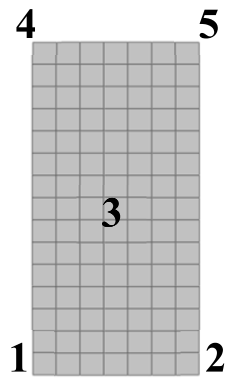

Figure 8-3 Element positions at the boundary

By looking closely at Table 8-1, it is obvious that the peak value of stress at the corner elements (Elements 1, 2, 4, and 5) is much higher than the stress at the mid-section (Element 3). This phenomenon can be justified by considering the effect of bending in the boundary surface. In fact, if the applied loading was a static load, there should have been no bending moment at the boundary of the structure since the load vector has no arm with respect to the center of the boundary surface. However, this is not true for the case of transient loading because when the load is passing through the inclined part of the structure, it makes a bending moment at the boundary. This is the reason for getting very large amount of stress at the elements far from the neutral axis.

Table 8-1 Normalized stress at the boundary of the non-symmetric structure

Element position	Normalized Stress (σ/σ_0)
1 (bottom left)	0.712
2 (bottom right)	0.712
3 (middle)	0.080
4 (top left)	0.600
5 (top right)	0.600

One of the best solutions for removing the effect of the bending moment at the boundary is making the structure symmetric about the centerline of the cross section. To investigate the effectiveness of this idea, the non-symmetric structure in Figure 8-1 is made symmetric by adding a lower inclined part as shown in Figure 8-4. This symmetric diamond-shape structure has the same layers and material properties as the non-symmetric structure, and it is subjected to a transient loading with the wavelength ratio (R_λ) of 0.375.

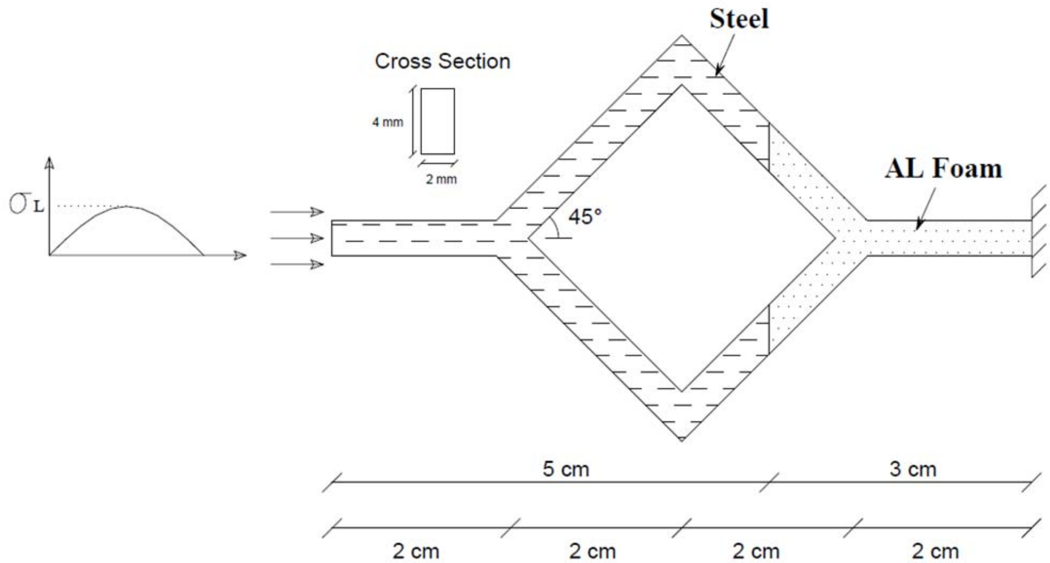

Figure 8-4 Symmetric diamond-shape structure

The 3D Abaqus model of the symmetric structure is shown in Figure 8-5. The maximum normalized stresses at each element of the boundary are presented in Table 8-2.

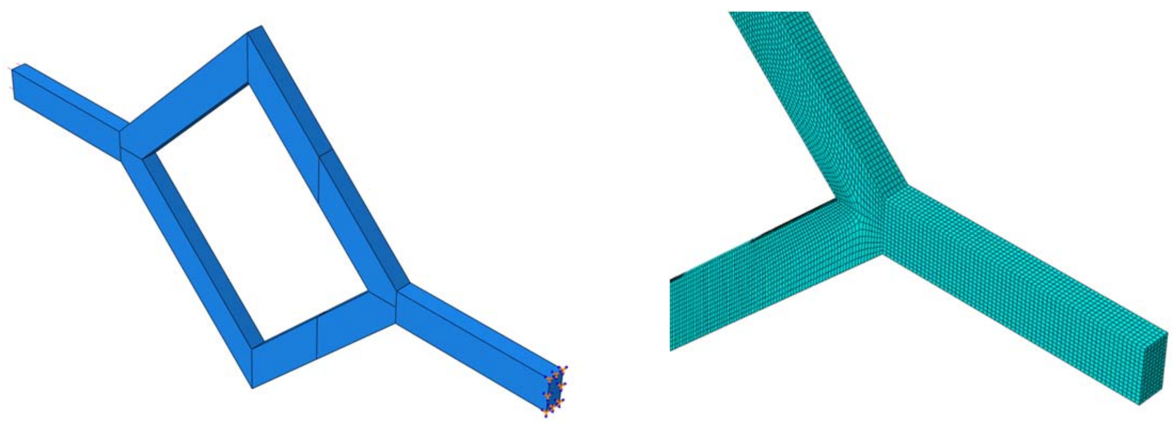

Figure 8-5 3D Abaqus model of the symmetric diamond-shape structure

By examining the results given in Table 8-2, it is obvious that there is no significant difference between the maximum stress amplitude of the corner and middle elements. This means that the distribution of the force over the surface of the boundary is even due to the symmetry, which means the effect of bending is removed successfully. This can be confirmed by checking the total force and moment at the clamped boundary of the structure. The results of the 3D Abaqus modeling reveals that the normalized amount of the total force and moment at the boundary of the structure are $F_B/F_L = 17.5\%$ and $M_B/(F_L L) = 0.22\%$, respectively. If we compare the amount of the normalized moment at the boundary of the symmetric diamond-shape structure with the non-symmetric inclined structure, we can observe that the moment at the boundary has significantly declined (compare 0.22% with 6.17%), which results in the reduction of the stress at the elements which are far from the neutral axis. It should be noted that the normalized amount of the force at the boundary of the diamond-shape structure is higher than the non-symmetric structure because all of the elements on the boundary of the symmetric structure would experience tension or compression simultaneously, and thus the force history will have higher amplitude. However, in the non-symmetric structure, the bending moment will cause the end boundary to experience both tension and compression at each time step, which results in lower total force.

Table 8-2 Normalized stress at the boundary of the symmetric diamond-shape structure

Element position	Normalized Stress (σ/σ_0)
1 (bottom left)	0.232
2 (bottom right)	0.232
3 (middle)	0.159
4 (top left)	0.232
5 (top right)	0.232

Considering the above facts about the symmetric and non-symmetric structures, it is desirable to utilize symmetric stress wave attenuators since these structures will produce even distribution of the stress at the boundary. Therefore, the total force at the cross section of the boundary, which is the target of the optimization, will give a better estimation of the amount of the all of the stresses at the cross section. Consequently, in the remainder of this section, the optimal design of the symmetric non-collinear structures will be sought extensively. The first type of these structures is the layered diamond-shape structure which has a constant geometry and the optimization algorithm tries to find the best material setup of the system for attenuation of an applied stress pulse. These structures are studied in section 8.3. The second type of the symmetric non-collinear stress wave attenuators are single-layered structures, and the optimization methodology tries to find their optimal geometry. These structures are studied in section 8.5.

8.3 Layered diamond-shape stress wave attenuators

In this section, the material optimization of a symmetric diamond-shape stress wave attenuator is introduced. A schematic of this structure and its corresponding design parameters are shown in Figure 8-6. It is assumed that the angle of the non-collinear part of the structure is 45 degrees and the cross sectional areas of the different parts are constant and small comparing to the length of the system. Therefore, the in-plane (R_D) and out-of-plane (PS & PE) design parameters are not applicable for this type of stress wave attenuators. It should be noted that the optimal design of this structure is provided to show the capability of the non-collinear layered systems in attenuating the stress waves, and it is not limited to this particular case. Therefore, the same procedure can be applied to any layered structure with multiple non-collinear parts and various angles.

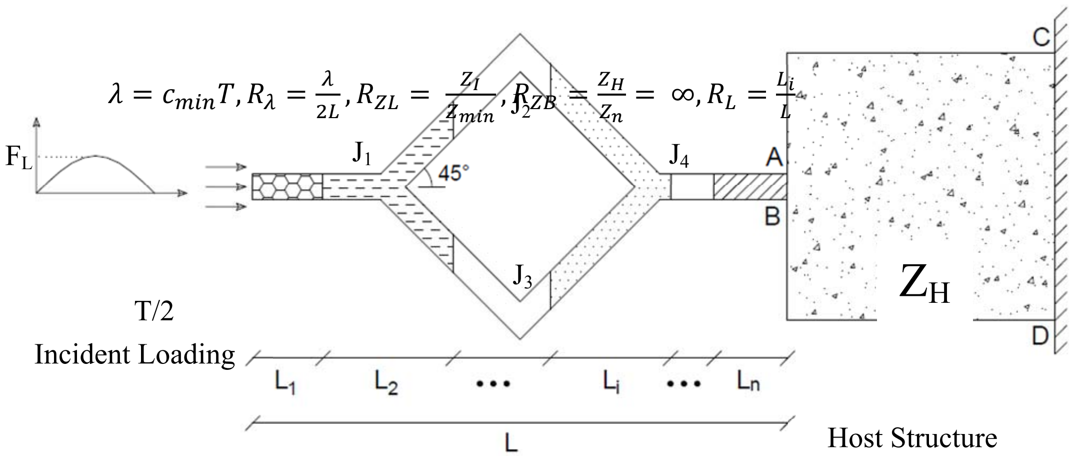

Figure 8-6 Schematic of a layered diamond-shape stress wave attenuator and its design parameters

Similar to the layered collinear systems in Section 7, the rigidity of the host structure (R_{ZB}) and the relative length of each layer (R_L) are infinity and $1/n$, respectively, where n is the total number of layers. Furthermore, the structures are optimized for 6 different wavelength ratios, i.e., $R_\lambda = 0.125, 0.25, 0.375, 0.50, 0.625,$ and 0.75. The materials that are used for the optimal design are also identical to the materials in Section 7, and their properties are presented in Table 7.1.

The optimization procedure is similar to the straight structures as described in section 7.4. To prevent constrained optimization, the structure is divided into equal layers, and an integer-valued GA optimization procedure is performed using MATLAB (2012). The integer variables can have a value in the range of 1 to 4 as there are four materials available for the optimal design. To keep the symmetry of the system, the material properties in the lower and upper branches of the diamond-shape part are exactly the same. The fitness function of the GA is calculated using Abaqus 6.12, and the structures are modeled using 2-node linear Timoshenko beam elements from the Abaqus (Simulia (2012)) element library (element B21).

8.3.1 Results and discussion

The optimal design of the diamond shape structure (Figure 8-6) with $L = 8cm$, which is subjected to 6 different wavelength ratios (R_λ) ranging from 0.125 to 0.75 is presented in this section. The duration of the half-sine pulses are calculated by considering the minimum longitudinal wave speed of the materials (Equation 7.1); therefore, all of the durations are the same as the values that are presented in Table 7.2. The reason for using the longitudinal wave speed for finding the durations is that the longitudinal waves are non-dispersive and their speed is not related to the frequency of loading.

The structure is divided into 16 equal layers in the horizontal direction and an integer-valued GA is performed for each wavelength ratio with 16 integer variables with lower and upper bounds of 1 and 4, respectively. Therefore, the solution space is composed of $4^{16} = 4.29E9$ combinations. Similar to the optimal design of the collinear systems, the population size and function tolerance are 100 and 1E-6, respectively, and the GA carries over the best two solutions in each generation to the next generation to provide the elitism in the optimization process.

The final optimal design of the layered non-collinear stress wave attenuators for 6 different wavelength ratios (R_λ) are shown in Table 8-3, Figure 8-7 and Figure 8-8. The force histories at the boundary of the optimized structures are depicted in Figure 8-9.

Table 8-3 Optimal material strings for the layered diamond-shape stress wave attenuators

Wavelength ratio (R_λ)	Optimal material string
0.125	1-1-1-1-1-1-4-4-4-1-4-4-1-4-4-3
0.250	1-1-1-1-1-4-4-4-4-1-4-4-3-4-2-1
0.375	1-1-1-1-1-1-4-4-4-4-1-4-4-4-1-1
0.500	1-1-1-1-1-1-4-4-4-4-1-4-4-4-2-2
0.625	1-1-1-1-1-1-4-4-4-4-1-4-4-4-1-1
0.750	1-1-1-1-1-4-4-4-4-1-4-4-3-3-1-1

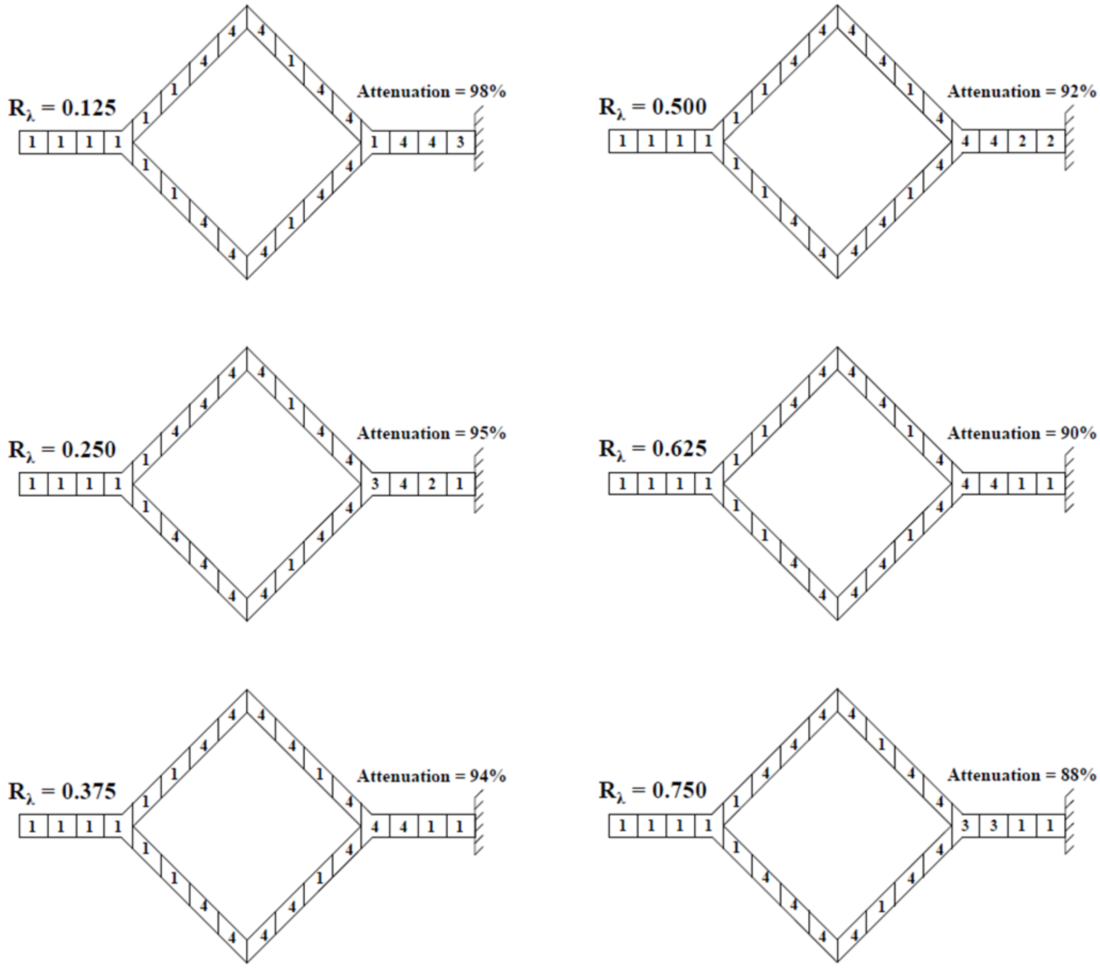

Figure 8-7 Optimal material strings for the layered diamond-shape stress wave attenuators

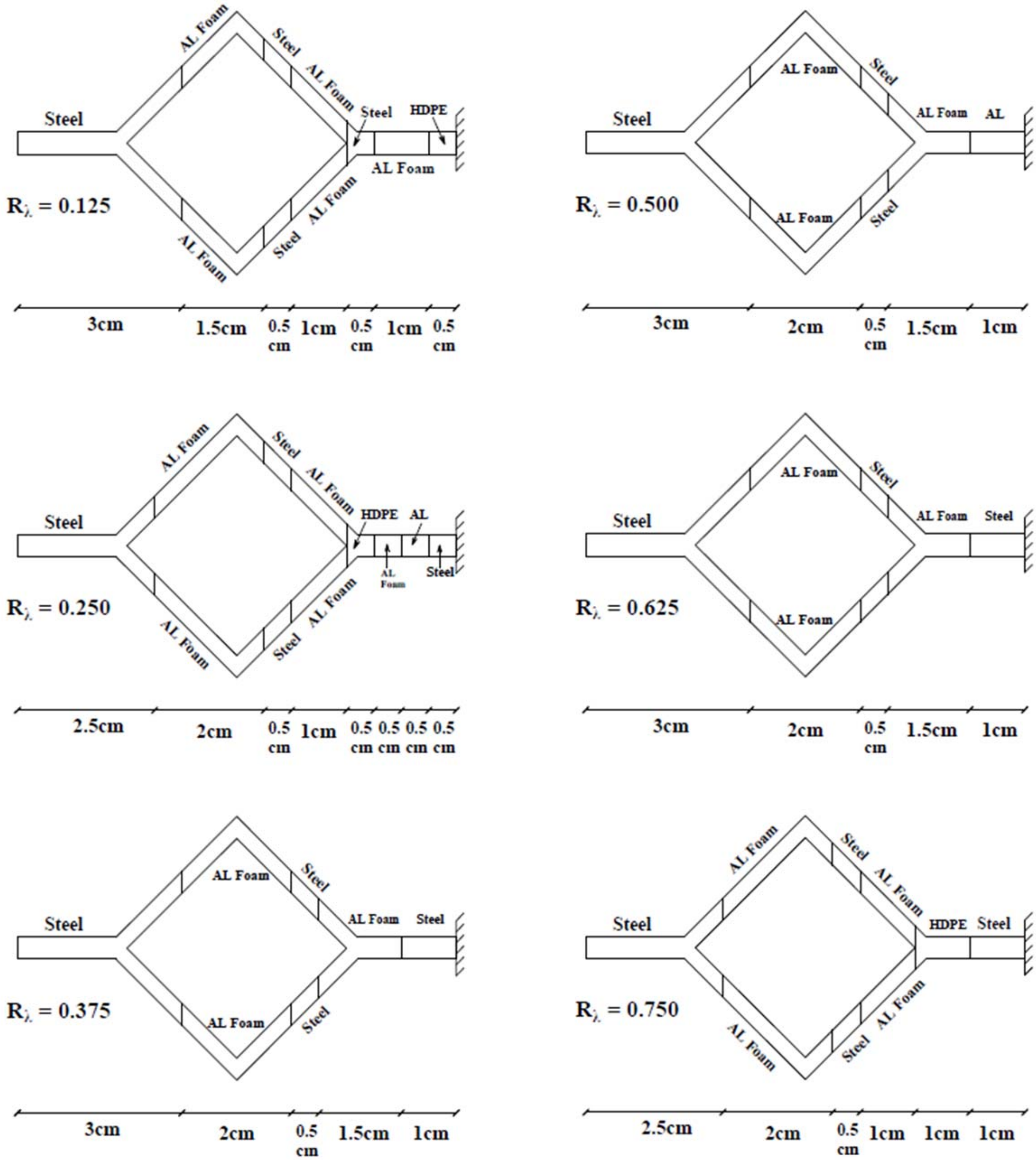

Figure 8-8 Optimal design of the layered diamond-shape stress wave attenuators

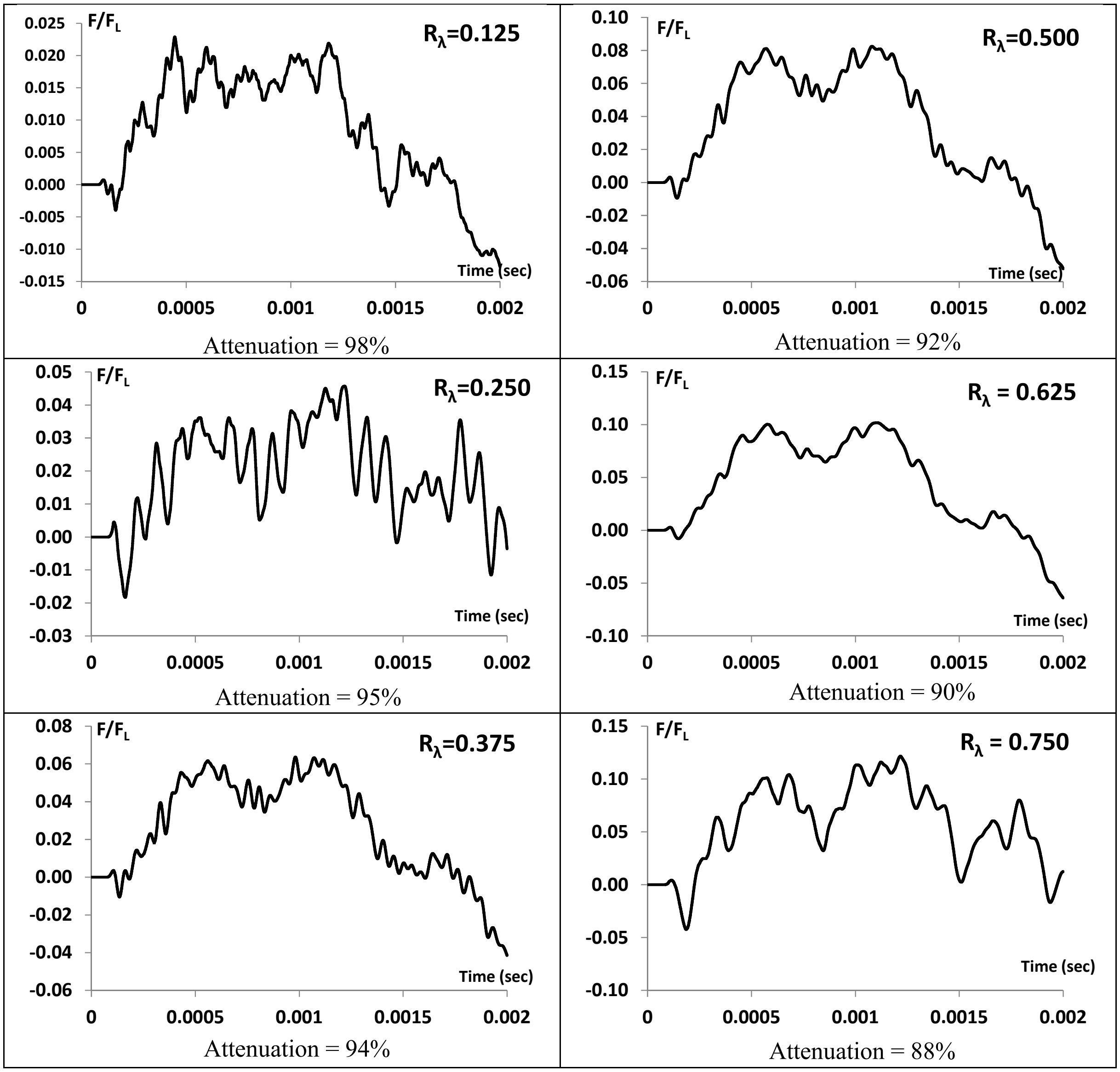

Figure 8-9 Force history at the boundary of the optimized diamond-shape structures

According to Figure 8-7 to Figure 8-9, the results of the optimization procedure for each wavelength ratio (R_λ) can be explained as follows:

- For $R_\lambda = 0.125$, the optimal design is made of 7 layers with the horizontal length of 3, 1.5, 0.5, 1, 0.5, 1, and 0.5cm. The material of each layer from the left hand side is Steel, AL Foam, Steel, AL Foam, Steel, AL Foam, and HDPE. The amount of attenuation that can be achieved with this structure is 98%.
- For $R_\lambda = 0.250$, the optimal design is made of 8 layers with the horizontal length of 2.5, 2, 0.5, 1, 0.5, 0.5, 0.5, and 0.5cm. The material of each layer from the left hand side is Steel, AL Foam, Steel,

AL Foam, HDPE, AL Foam, AL, and Steel. The amount of attenuation that can be achieved with this structure is 95%

- For $R_\lambda = 0.375$, the optimal design is made of 5 layers with the horizontal length of 3, 2, 0.5, 1.5, and 1cm. The material of each layer from the left hand side is Steel, AL Foam, Steel, AL Foam, and Steel. The amount of attenuation that can be achieved with this structure is 94%.
- For $R_\lambda = 0.500$, the optimal design is made of 5 layers with the horizontal length of 3, 2, 0.5, 1.5, and 1cm. The material of each layer from the left hand side is Steel, AL Foam, Steel, AL Foam, and AL. The amount of attenuation that can be achieved with this structure is 92%.
- For $R_\lambda = 0.625$, the length of the layers and their material properties are exactly the same as the optimal design for $R_\lambda = 0.375$. The amount of attenuation that can be achieved with this structure is 90%.
- For $R_\lambda = 0.750$, the optimal design is made of 6 layers with the horizontal length of 2.5, 2, 0.5, 1, 1, and 1cm. The material of each layer from the left hand side is Steel, AL Foam, Steel, AL Foam, HDPE, and Steel. The amount of attenuation that can be achieved with this structure is 88%.

These results show that the optimized structures are mainly composed of the materials with the highest (Steel) and lowest (AL Foam) impedance values, which is similar to the results that are obtained from the optimization of the collinear structures in Section 7. In addition, the first two layers of the structures are always composed of Steel (first layer) and AL Foam (second layer) and they have larger length compared to the other layers.

The joints of the diamond shape structure, J1, J2, J3, and J4, are shown in Figure 8-6. In all of the structures the first (J1) and the second (J2) joints are made of steel and AL Foam, respectively. The third joint (J3) is also made of AL Foam due to the symmetry. The material of the fourth joint (J4) is different for various wavelength ratios and is made of Steel for $R_\lambda = 0.125$, HDPE for $R_\lambda = 0.250$ and 0.750, and AL Foam for $R_\lambda = 0.375, 0.5, \& 0.625$.

Similar to the collinear structures, the amount of the attenuation at the boundary of the stress wave attenuators decreases by increasing the wavelength ratio (R_λ); however, the range of the attenuation is 88% (for $R_\lambda = 0.75$) to 98% (for $R_\lambda = 0.125$), which is significantly smaller than the similar range for the collinear structures (compare to 68 to 93). Therefore, it can be concluded that the optimized layered diamond-shape structures are more robust than the collinear structures in attenuating the stress waves with various amount of frequencies.

To further explore the attenuation capacity of the optimal designs, each optimized structure is subjected to the loadings with various wavelengths, and the amount of attenuation at their boundary is presented in

Table 8-4. Similar to the collinear structures in Section 7, the amount of the force attenuation in each structure is plotted versus the parameter R_λ, as it is shown in Figure 8-10. This figure shows that the attenuation capacity of the structures that are optimized for $R_\lambda = 0.125, 0.375., 0.5$, and 0.625 is higher than the attenuation capacity of the structures that are optimized for $R_\lambda = 0.25$ and 0.75. Therefore, for a diamond-shape stress wave attenuator with the horizontal length of 8cm under half-sine transient loadings with the wavelength ratios (R_λ) between 0.125 to 0.75, the best optimal design can be one of the structures that are optimized for $R_\lambda = 0.125, 0.375., 0.5$, and 0.625.

It should be noted that for $R_\lambda = 0.25$, the amount of attenuation that can be obtained from the structure which is optimized for $R_\lambda = 0.375, 0.5$, and 0.625 is higher than the attenuation which is achieved by the optimized structure for $R_\lambda = 0.25$. However, the values are very close to each other. This phenomenon happens because of the nature of the GA, as this method cannot always find the best possible solution; however, it provides acceptable results based on the type of the optimization problem.

Table 8-4 Attenuation at the optimized layered diamond-shape structures for different R_λ values

Attenuation at R_λ (%)	Optimized for R_λ:					
	0.125	0.250	0.375	0.500	0.625	0.750
0.125	98	98	98	98	98	97
0.250	96	95	96	96	96	94
0.375	94	93	94	94	94	93
0.500	92	91	92	92	92	91
0.625	90	89	90	90	90	89
0.750	88	87	88	88	88	88

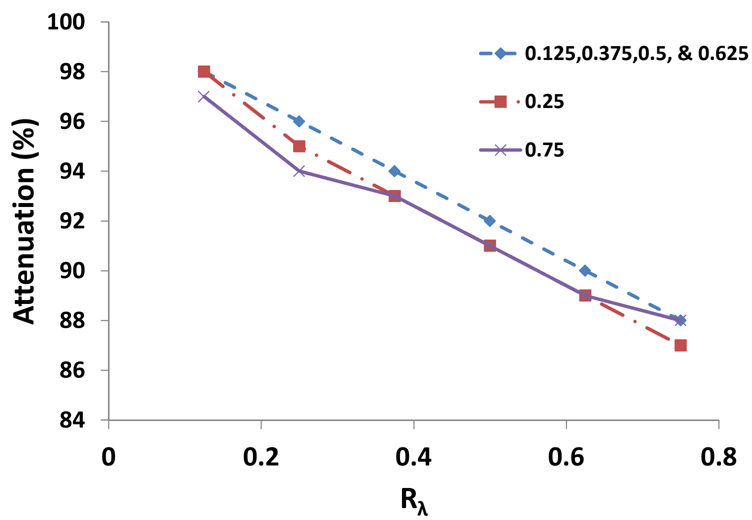

Figure 8-10 Attenuation vs. R_λ, Diamond-shape structure

8.4 Three dimensional structure with layered diamond-shape stress wave attenuators

Similar to Section 7, an example of using the layered diamond-shape structure in a 3D configuration is presented in this section. In this structure, four layered diamond-shape stress wave attenuators are sandwiched between two steel plates as shown in Figure 8-11. It is assumed that each layered stress wave attenuator supports a square area with the dimensions of 5cm by 5cm. Therefore, the front and back plates have the dimension of 10cm by 10cm. Other dimensions are shown in Figure 8-11.

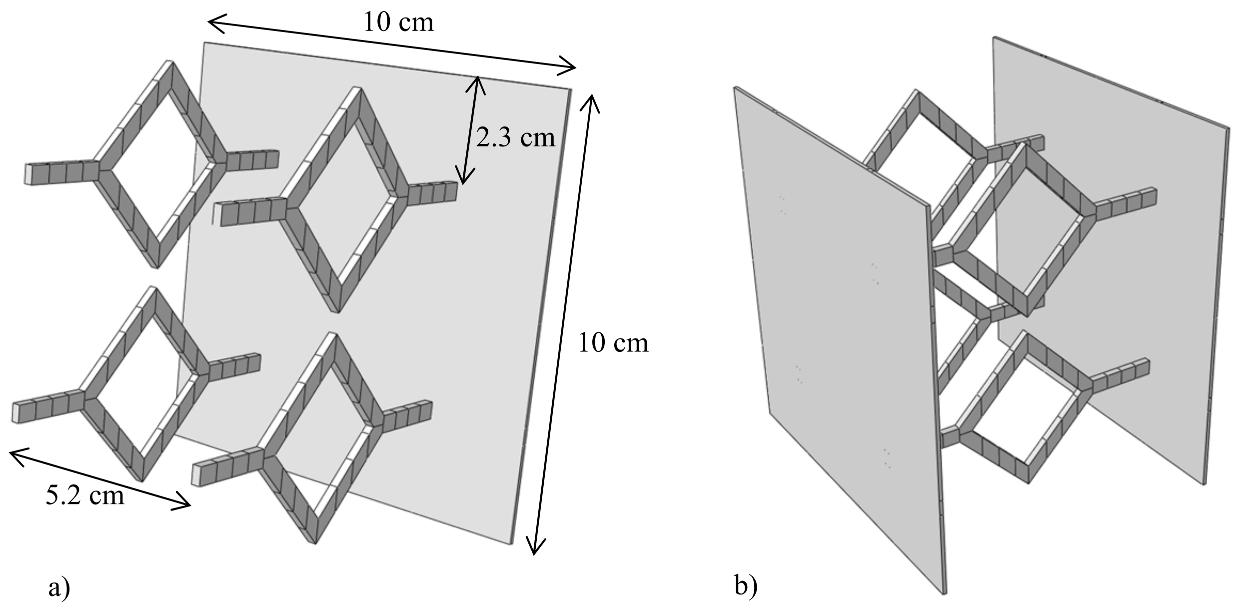

Figure 8-11 3D model with layered diamond-shape stress wave attenuators, a) dimensions, b) whole model

As mentioned in the previous section, the diamond-shape structures that are optimized for $R_{\lambda} = 0.125, 0.375., 0.5,$ and 0.625 have high attenuation capacity comparing to the other structures. Therefore, to show the efficiency of this structure, the optimal design for $R_{\lambda} = 0.125$ is used in the 3D model. The material setup for this structure is presented in Figure 8-7 and Figure 8-8.

The boundary conditions of the 3D structure are shown in Figure 8-12. A transient half-sine load with the wavelength ratio of 0.125 and amplitude of F_L is applied to the front plate, and the back plate is constrained for all of the displacements and rotations.

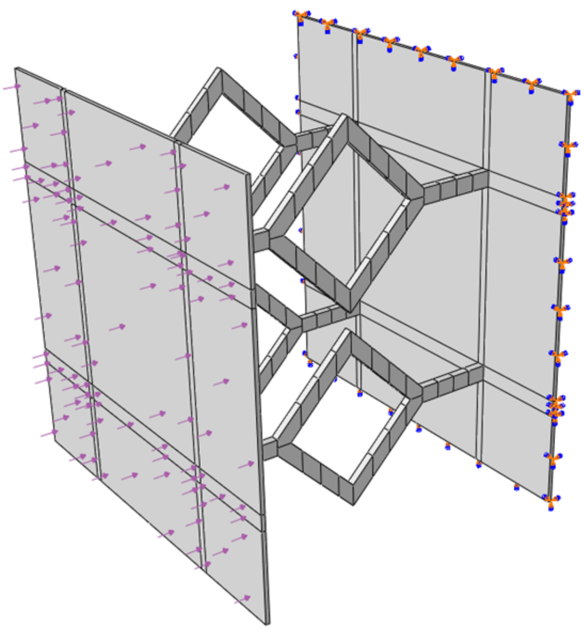

Figure 8-12 Boundary condition and loading of the 3D model with diamond-shape stress wave attenuators

To investigate the attenuation capacity of the layered diamond-shape stress wave attenuators, two 3D models are built in Abaqus and the force history at the boundary of these models are compared to each other. The material properties of the diamond-shape structures of the first model are the same as the structure that is optimized for $R_{\lambda} = 0.125$, while in the second model, the diamond shape structures are only made of steel.

The normalized force histories at the boundary of the two structures are presented in Figure 8-13. It is obvious that a significantly higher amount of attenuation can be achieved using the structure with optimized diamond-shape stress wave attenuators.

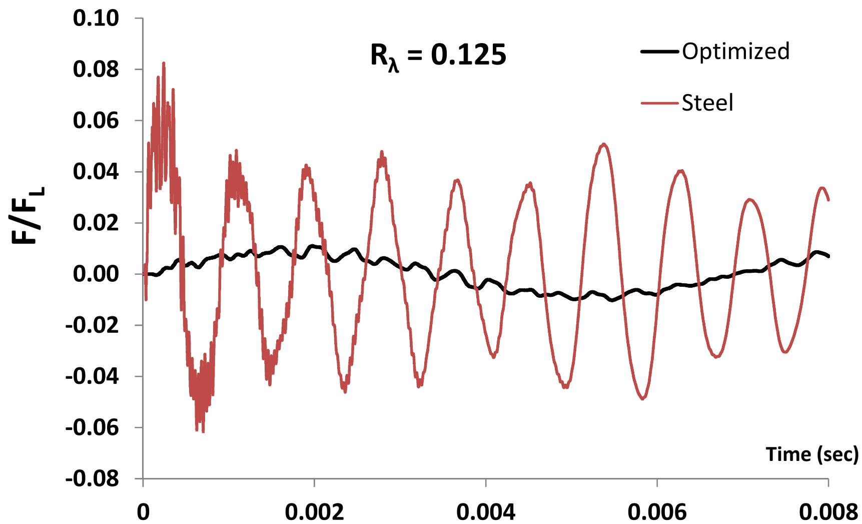

Figure 8-13 Force histories at the boundary of the 3D models with diamond-shape stress wave attenuators

8.5 Non-collinear single-layered stress wave attenuators

Up to the present moment, all of the studied stress wave attenuators had a constant geometry, and their attenuation capacity was mainly due to the impedance mismatch between the multiple layers within the structure. As mentioned in Section 4, the geometric discontinuities such as angled joints in beams can affect the wave propagation characteristics of a system by generating new reflected and transmitted waves. In this section, it will be shown how a geometric discontinuity such as angled joints can be utilized in optimal design of the structures that are made of Timoshenko beam members. These structures are only made of a single material and geometry optimization is performed to find the most efficient mitigating configuration. In the remainder of this research, these structures are called "non-collinear stress wave attenuators".

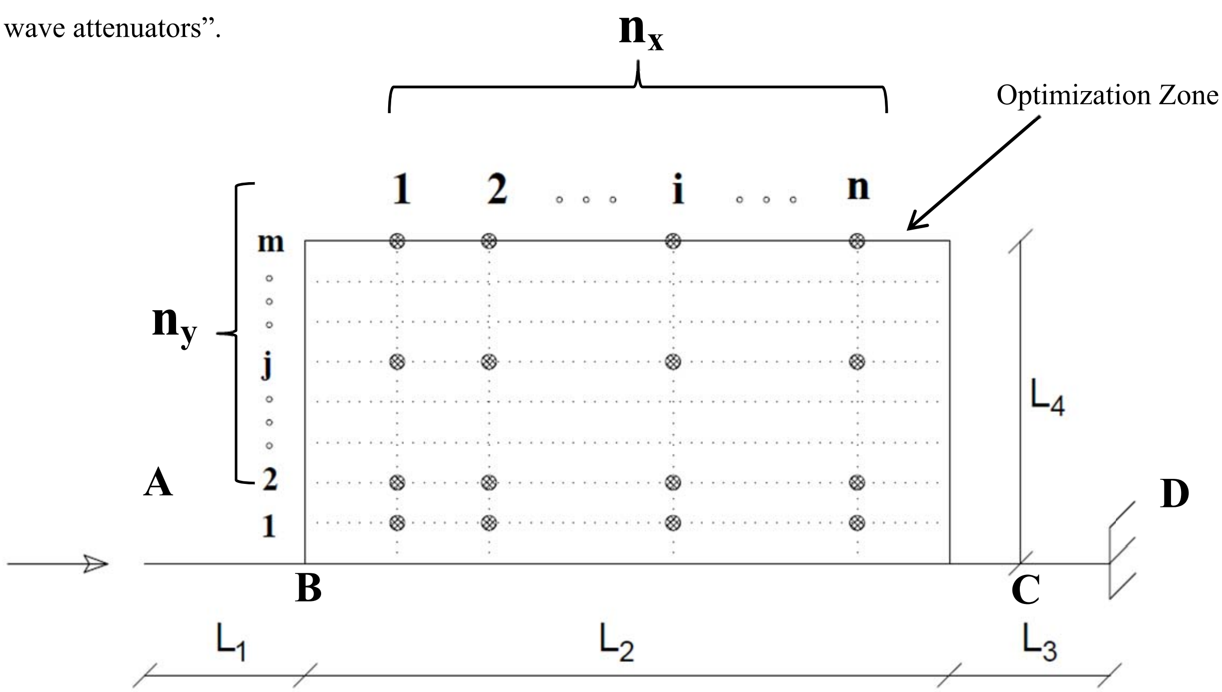

Figure 8-14 Concept of geometry optimization for non-collinear stress wave attenuators

To introduce the geometry optimization procedure for designing non-collinear stress wave attenuators, consider the structure that is shown in Figure 8-14. This structure is composed of three different parts with the lengths of L_1, L_2, and L_3 in the horizontal direction. It is assumed that the load is applied to point A and the structure is clamped at point D. The first and the third part of the structure (L_1 and L_3) are collinear, while the second part consists of non-collinear members. The second part has the horizontal and vertical length of L_2 and L_4, respectively, and it is called the "optimization zone". To perform the optimal design procedure, the optimization zone can be divided into $n_x = n$ and $n_y = m$ segments in the horizontal and vertical directions to generate an $n \times m$ grid, and the GA will try to select the grid points to find the best attenuating pattern. For example, if L_2 and L_4 are divided into n and m segments, the solution space will contain m^n combinations, and a GA optimization can be performed with n integer variables with the lower and upper bounds of 1 and m, respectively. To clarify more, consider the example in Figure 8-15 which is divided into 6 and 8 segments in the horizontal and vertical directions, respectively. Points B and C are fixed, and the GA will choose the best path by connecting the points in the 6×8 grid. For instance, the path that is shown in Figure 8-15, is made by connecting 6 points along the horizontal direction which have the vertical positions (n_y) of 2, 5, 3, 2, 4, and 8. Due to the reasons that are declared in section 8.2, all of the non-collinear structures in this research have a symmetric configuration. Therefore, the path in the optimization zone is mirrored with respect to line BC to keep the symmetry.

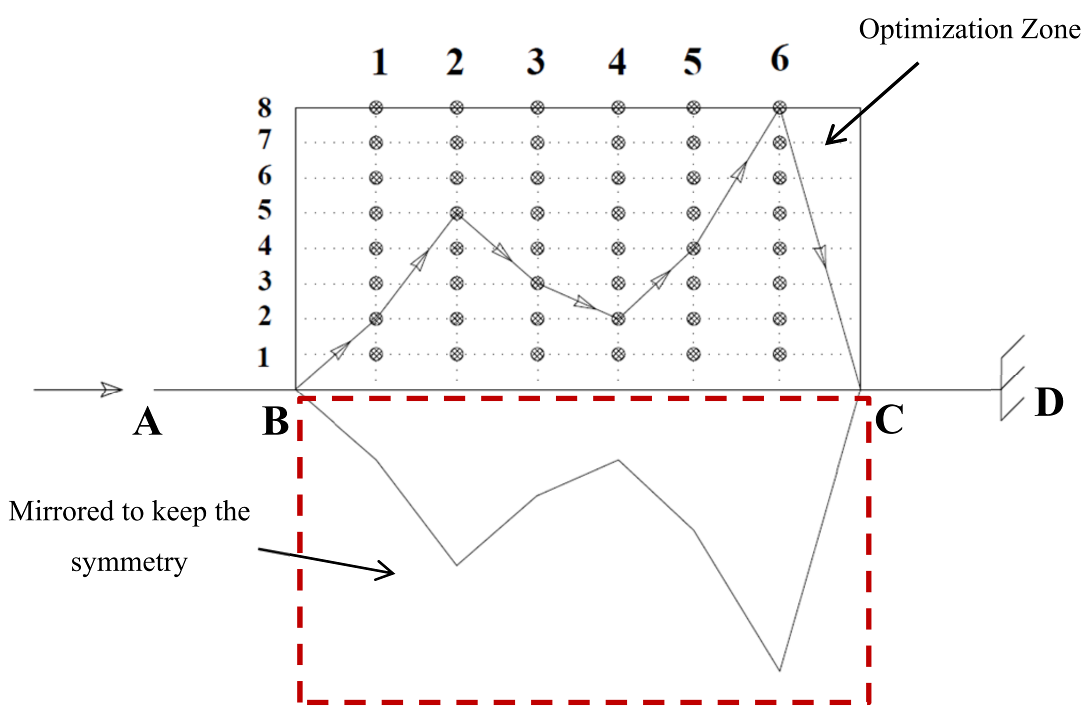

Figure 8-15 Example for the geometry optimization of non-collinear stress wave attenuators

In the following sections, the optimal design of the non-collinear stress wave attenuators will be pursued for different grid numbers. For all of the structures, it is assumed that sections AB and CD have equal length of $2cm$ and the optimization zone has the dimension of $L_2 \times 0.5L_2$, with $L_2 = 18cm$. Therefore, the total length of the structure in the horizontal direction is $22cm$. All of the sections of the structure are made of a single material which is Aluminum with the properties that are mentioned in Table 7.1. The structure has a constant cross section with the width and height of 2mm and 4mm, respectively. The number of the vertical points in the optimization zone (n_y) is kept to be 8 in all of the structures, and optimization is performed for different values of n_x which is changing from 1 to 8. Since the solution space is not very large for the structures with $n_x = 1$ to 4, exhaustive search has been performed to find the most attenuating configurations. However, for higher values of n_x, GA optimization methodology is utilized for this purpose.

Each structure is subjected to 6 different wavelength ratios (R_λ) ranging from 0.125 to 0.75. The duration of the half-sine pulses are calculated by substituting the longitudinal wave speed of Aluminum in Equation 7.1, and their values are presented in Table 8-5. Similar to the diamond-shape structures, longitudinal wave speed is used for finding the duration of the loads because of their non-dispersive nature.

Table 8-5 Wavelength ratios and duration of the applied pulses on the non-collinear structures

Wavelength ratio (R_λ)	C_{min} (m/sec)	Duration of the sine pulse (sec)	Duration of the half-sine pulse (sec)
0.125	5052	1.09E-05	5.44E-06
0.250	5052	2.18E-05	1.09E-05
0.375	5052	3.27E-05	1.63E-05
0.500	5052	4.36E-05	2.18E-05
0.625	5052	5.44E-05	2.72E-05
0.750	5052	6.53E-05	3.27E-05

In the following sections, the optimized configurations for the structures with different values of n_x will be presented in detail.

8.5.1 Non-collinear stress wave attenuator with $n_x = 1$

The optimization zone for the stress wave attenuator with $n_x = 1$ is shown in Figure 8-16. As mentioned above, the number of vertical points is constant and equal to 8 for all of the non-collinear structures in this section. Therefore, for each value of wavelength ratio (R_λ), there are only 8 combinations available for the structure with $n_x = 1$, and the best solution can be easily found by an exhaustive search.

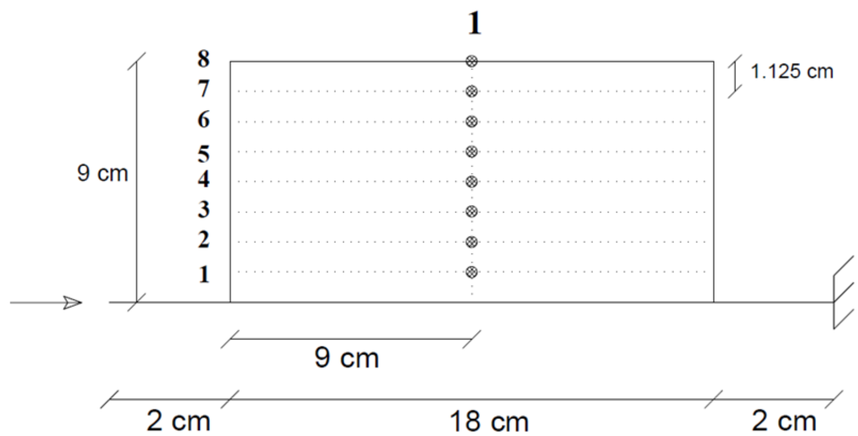

Figure 8-16 Optimization zone for the non-collinear structure with $n_y = 8$ and $n_x = 1$

The vertical position string for the structure with $n_x = 1$ contains only one number. The optimized vertical string is shown in Table 8-6, and the optimized structures and their attenuation capacities are depicted in Figure 8-17. In addition, the force histories at the boundary of the optimized structures are presented in Figure 8-18.

Table 8-6 Optimized vertical position string for the non-collinear structure with $n_x = 1$

R_λ	0.125	0.250	0.375	0.500	0.625	0.750
n_y	5	5	6	8	5	5

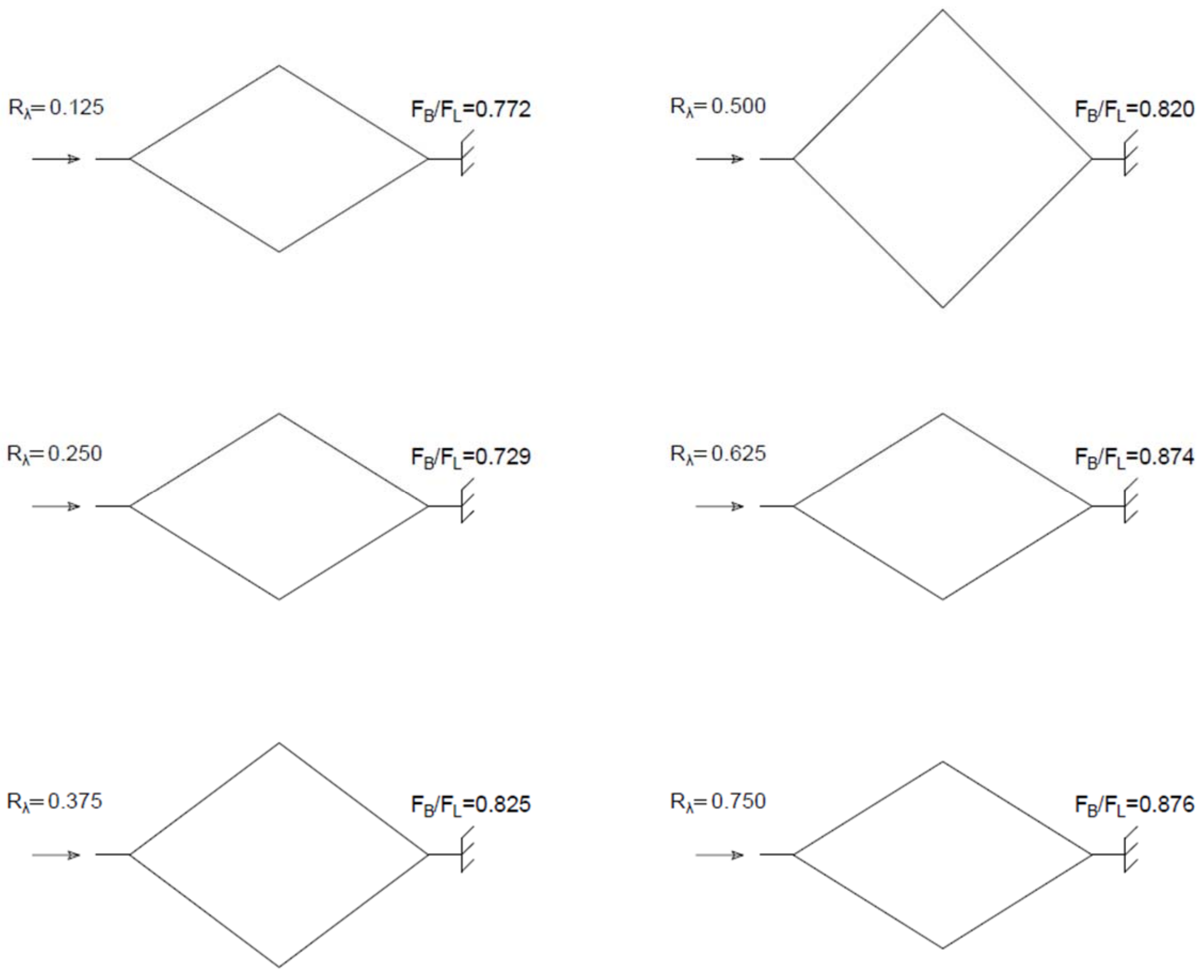

Figure 8-17 Optimal design of the non-collinear stress wave attenuators, $n_x = 1$

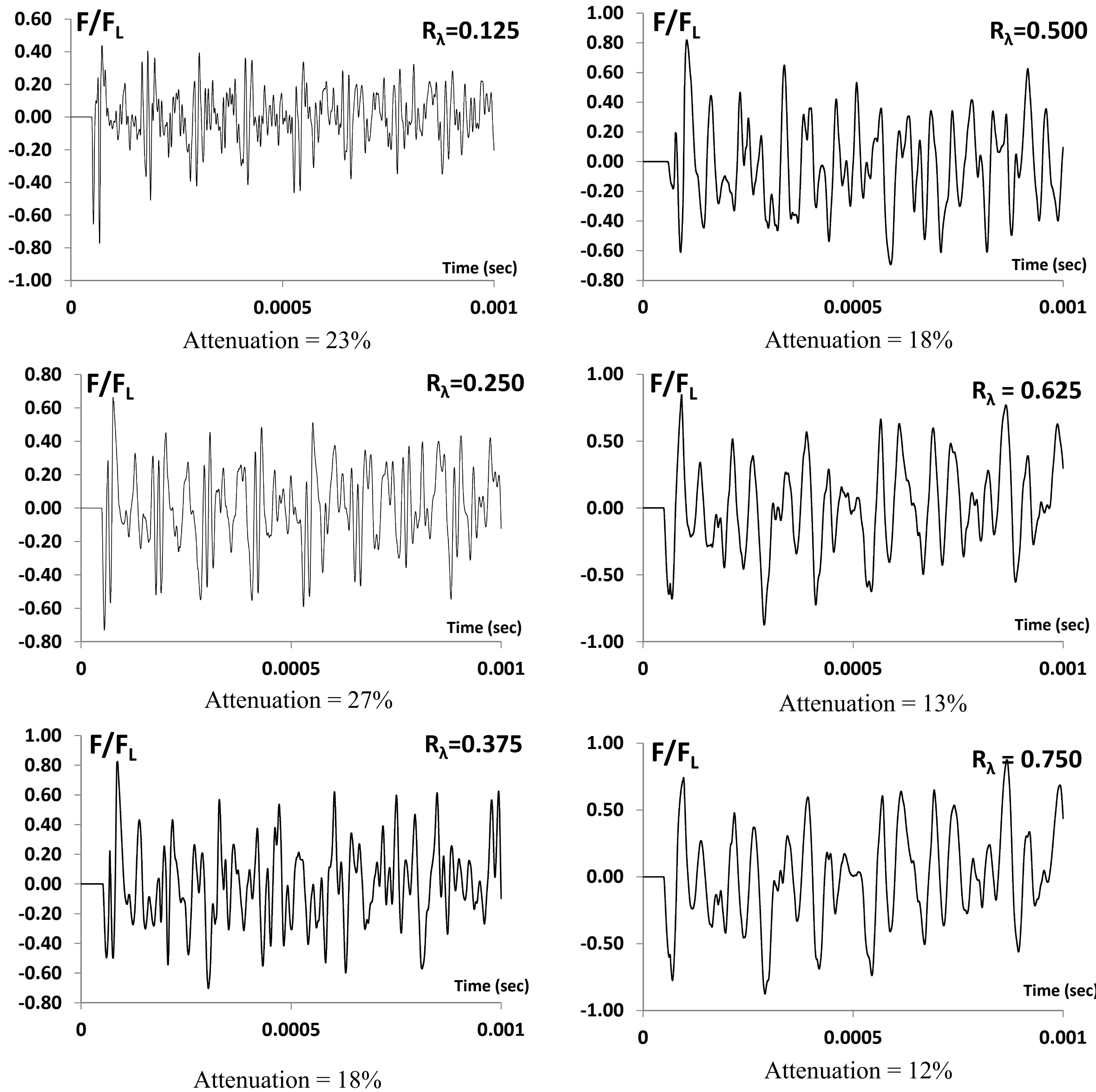

Figure 8-18 Force history at the boundary of the optimized non-collinear structures with $n_x = 1$

According to Figure 8-17 and Figure 8-18, the results of the exhaustive search for the structure with $n_x = 1$ can be explained as follows:

- For $R_\lambda = 0.125, 0.250, 0.625,$ and 0.750, the vertical position string (n_y) for the optimized structure is 5, and the amount of attenuation at the boundary of each structure is 23, 27, 13, and 12%.

- For $R_\lambda = 0.375$, the vertical position string (n_y) for the optimized structure is 6, and the amount of attenuation at the boundary is 18%.
- For $R_\lambda = 0.500$, the vertical position string (n_y) for the optimized structure is 8, and the amount of attenuation at the boundary is 18%.

To further explore the attenuation capacity of the optimal designs, each optimized structure is subjected to the loads with various wavelength ratios and the amount of attenuation at their boundary is presented in Table 8-7. Using this table, the force attenuation versus the wavelength ratio is plotted in Figure 8-19. This figure shows that the optimized structures for $R_\lambda = 0.125, 0.25, 0.625$, and 0.750 have, generally, higher attenuation capacity and thus for a non-collinear stress wave attenuator with $n_x = 1$ which is subjected to half-sine transient loading with the wavelength ratios (R_λ) between 0.125 to 0.75, the vertical position string for the best optimal design is 5. In addition, according to Table 8-7 and Figure 8-19, the attenuation range for the non-collinear structure with $n_x = 1$ is 37% with the lowest and highest values of -10 and 27%, respectively. The minimum amount of attenuation (-10%) happens in the structure which is optimized for $R_\lambda = 0.5$ and is subjected to the load with wavelength ratio $R_\lambda = 0.25$, while the maximum amount of attenuation (27%) happens in the structure which is optimized for $R_\lambda = 0.125, 0.25, 0.625$, and 0.750 and is subjected to the loads with the same wavelength ratio. It should be noted that the negative attenuation means that the maximum amount of the force history at the boundary is larger than the amplitude of the applied force and the structure experiences amplification at its boundary.

Table 8-7 Attenuation at the optimized non-collinear structures for different R_λ values, $n_x = 1$

Attenuation at R_λ (%)	Optimized for R_λ:					
	0.125	0.250	0.375	0.500	0.625	0.750
0.125	23	23	0	-6	23	23
0.250	27	27	25	-10	27	27
0.375	14	14	18	17	14	14
0.500	10	10	3	18	10	10
0.625	13	13	0	4	13	13
0.750	12	12	6	-3	12	12
Range (%)	10-27	12-27	0-25	-10-18	10-27	10-27

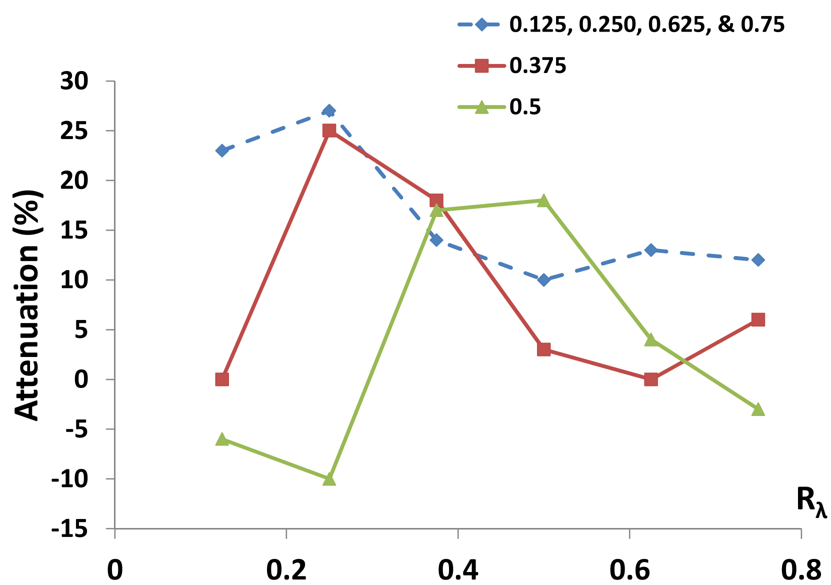

Figure 8-19 Attenuation vs. R_λ, non-collinear structure with $n_x = 1$

8.5.2 Non-collinear stress wave attenuator with $n_x = 2$

The optimization zone for the non-collinear stress wave attenuator with $n_x = 2$ is shown in Figure 8-20. The solution space for this problem is composed of $8^2 = 64$ combinations and an exhaustive search can be easily performed to find the best solution for each value of the wavelength ratio. The optimized vertical position string for this structure is composed of two numbers and is presented in Table 8-8. Schematics of the optimal designs (with their attenuation capacity) and their corresponding force histories at the boundary are depicted in Figure 8-21 and Figure 8-22, respectively.

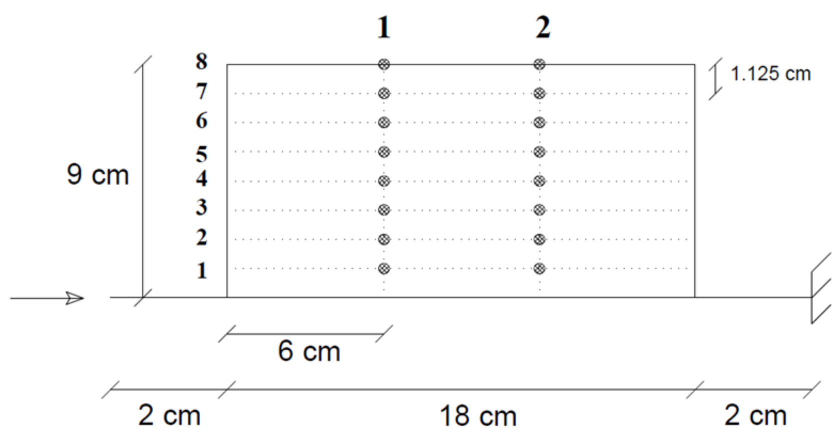

Figure 8-20 Optimization zone for the non-collinear structure with $n_y = 8$ and $n_x = 2$

According to Figure 8-21and Figure 8-22, the results of the exhaustive search for the structure with $n_x = 2$ can be explained as follows:

- For $R_\lambda = 0.125$ the vertical position string (n_y) for the optimized structure is 3-5, and the amount of attenuation at the boundary is 39%.
- For $R_\lambda = 0.25$ the vertical position string (n_y) for the optimized structure is 8-4, and the amount of attenuation at the boundary is 33%.
- For $R_\lambda = 0.375$ the vertical position string (n_y) for the optimized structure is 8-5, and the amount of attenuation at the boundary is 42%.

Table 8-8 Optimized vertical position string for the non-collinear structure with $n_x = 2$

R_λ	0.125	0.250	0.375	0.500	0.625	0.750
n_y	3-5	8-4	8-5	3-7	4-7	3-7

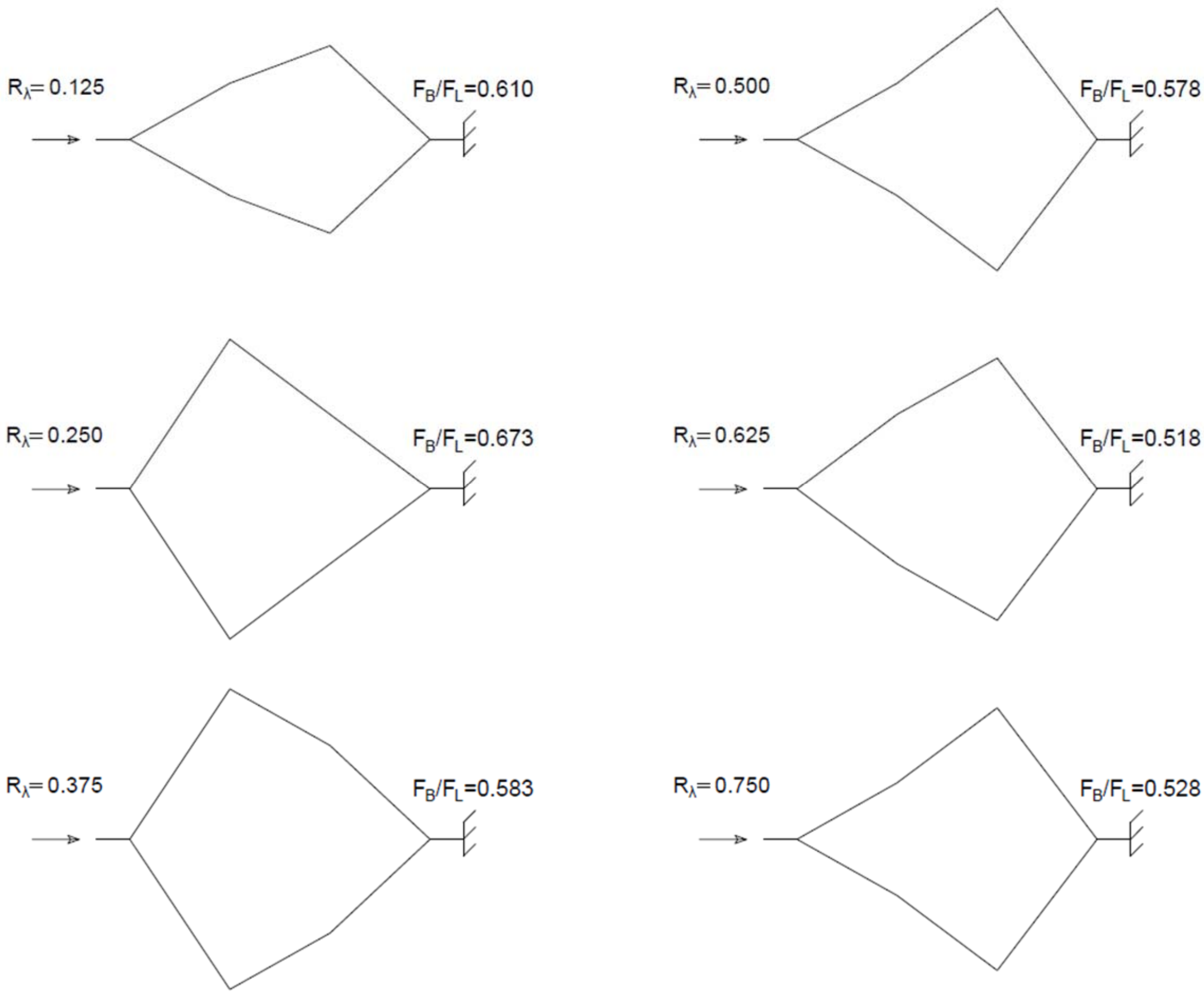

Figure 8-21 Optimal design of the non-collinear stress wave attenuators, $n_x = 2$

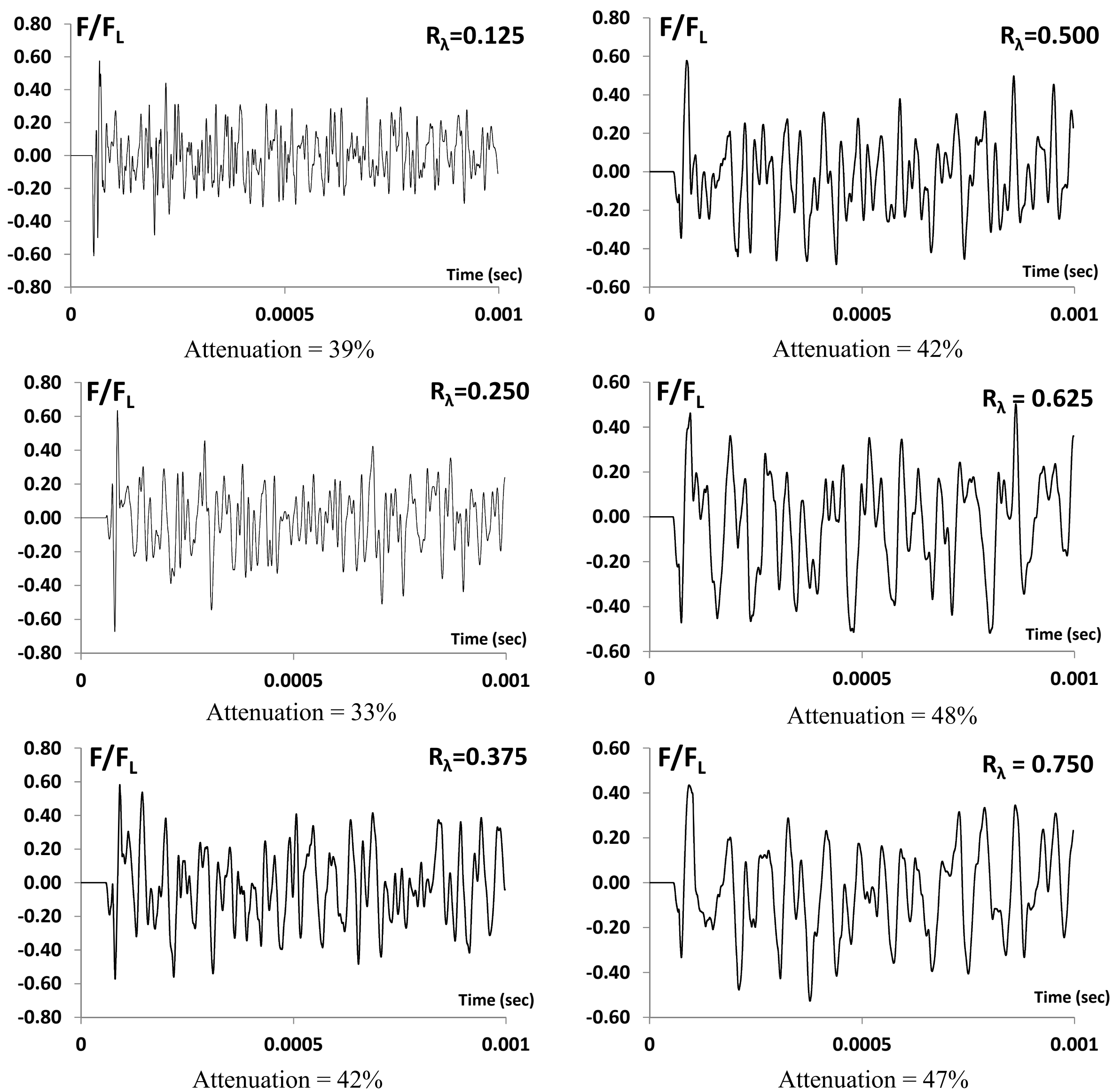

Figure 8-22 Force history at the boundary of the optimized non-collinear structures with $n_x = 2$

- For $R_\lambda = 0.5$ and 0.75 the vertical position strings (n_y) for the optimized structures is 3-7, and the amount of attenuation at the boundary of each structure is 42 and 47%, respectively.
- For $R_\lambda = 0.625$ the vertical position string (n_y) for the optimized structure is 4-7, and the amount of attenuation at the boundary is 48%.

The amount of attenuation for each optimized structure at different values of wavelength ratios are presented in Table 8-9 and the attenuation-R_λ curve is plotted in Figure 8-23. According to this figure, it is difficult to say which structure has the highest attenuation capacity for the total range of R_λ values. However, the range of attenuation for each optimized structure can be found using Table 8-9, and the best structure can be selected using these information. The attenuation range for the structures that are optimized for $R_\lambda = 0.125, 0.25, 0.375, 0.5, 0.625$, and 0.750 are "14-39", "20-38", "25-42", "5-47", "13-48", and "5-47", respectively. These results show that the minimum value of attenuation for the structure that is optimized for $R_\lambda = 0.375$ is 25% which is higher than the other structures; therefore, it can be recommended to use this structure (with vertical position string 8-5) for attenuating the applied stress waves with the wavelength ratio of 0.125 to 0.75.

The global attenuation range for the structure with $n_x = 2$ is 5-48%, and the structures are sensitive to the wavelength ratio. The minimum attenuation value (5%) occurs for the structure which is optimized for $R_\lambda = 0.5$ and is subjected to the load with $R_\lambda = 0.25$, while the maximum attenuation value (48%) relates to the structure that is optimized for $R_\lambda = 0.625$ and is subjected to the load with the same value of R_λ. It should be noted that the amount of attenuation is increasing (except for $R_\lambda = 0.25$) by increasing the value of wavelength ratio (R_λ), which is in contrast to the trends that have been observed for the layered stress wave attenuators.

Table 8-9 Attenuation at the optimized non-collinear structures for different R_λ values, $n_x = 2$

Attenuation at R_λ (%)	Optimized for R_λ:					
	0.125	0.250	0.375	0.500	0.625	0.750
0.125	39	20	25	28	27	28
0.250	19	33	27	5	13	5
0.375	35	38	42	21	23	21
0.500	24	37	34	42	41	42
0.625	25	33	31	47	48	47
0.750	14	33	35	47	35	47
Range (%)	14-39	20-38	25-42	5-47	13-48	5-47

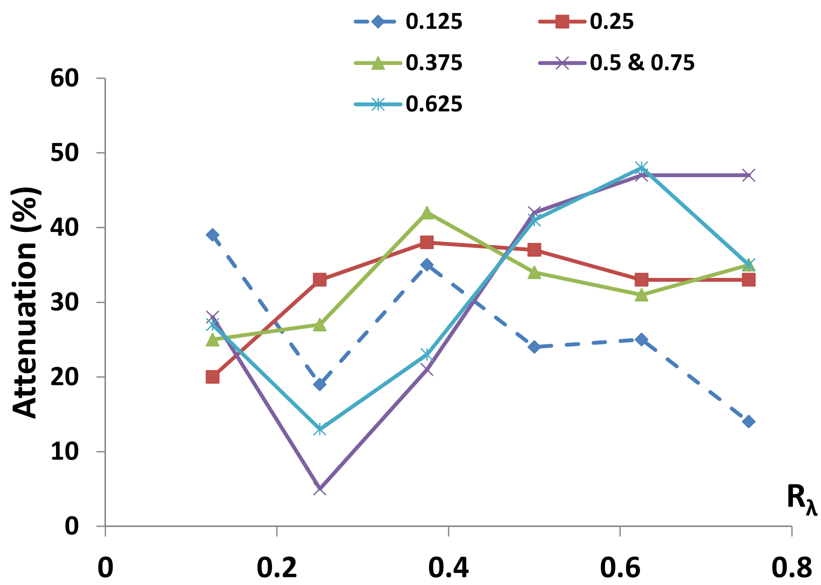

Figure 8-23 Attenuation vs. R_λ, non-collinear structure with $n_x = 2$

8.5.3 Non-collinear stress wave attenuator with $n_x = 3$

The optimization zone for the non-collinear stress wave attenuator with $n_x = 3$ is shown in Figure 8-24. The solution space for this problem is composed of $8^3 = 512$ combinations, and an exhaustive search is performed to find the best solution for each value of the wavelength ratio. The optimized vertical position string for this structure is composed of three numbers and it is presented in Table 8-10. Schematics of the optimal designs (with their attenuation capacity) and their corresponding force histories at the boundary are depicted in Figure 8-25 and Figure 8-26, respectively.

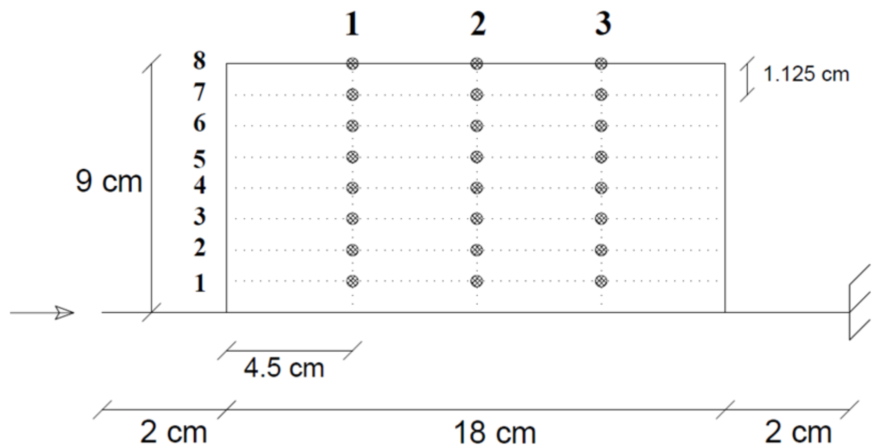

Figure 8-24 Optimization zone for the non-collinear structure with $n_y = 8$ and $n_x = 3$

According to Figure 8-25 and Figure 8-26, the results of the exhaustive search for the structure with $n_x = 3$ can be explained as follows:

- For $R_\lambda = 0.125$, the vertical position string (n_y) for the optimized structure is 7-1-7, and the amount of attenuation at the boundary is 68%.
- For $R_\lambda = 0.25$, the vertical position string (n_y) for the optimized structure is 8-1-8, and the amount of attenuation at the boundary is 61%.
- For $R_\lambda = 0.375$, the vertical position string (n_y) for the optimized structure is 8-2-8, and the amount of attenuation at the boundary is 60%.
- For $R_\lambda = 0.5$, the vertical position string (n_y) for the optimized structure is 3-8-2, and the amount of attenuation at the boundary is 61%.
- For $R_\lambda = 0.625$ and 0.75, the vertical position string (n_y) for the optimized structure is 8-3-5, and the amount of attenuation at the boundary of each structure is 62 and 65%, respectively.

Table 8-10 Optimized vertical position string for the non-collinear structure with $n_x = 3$

R_λ	0.125	0.250	0.375	0.500	0.625	0.750
n_y	7-1-7	8-1-8	8-2-8	3-8-2	8-3-5	8-3-5

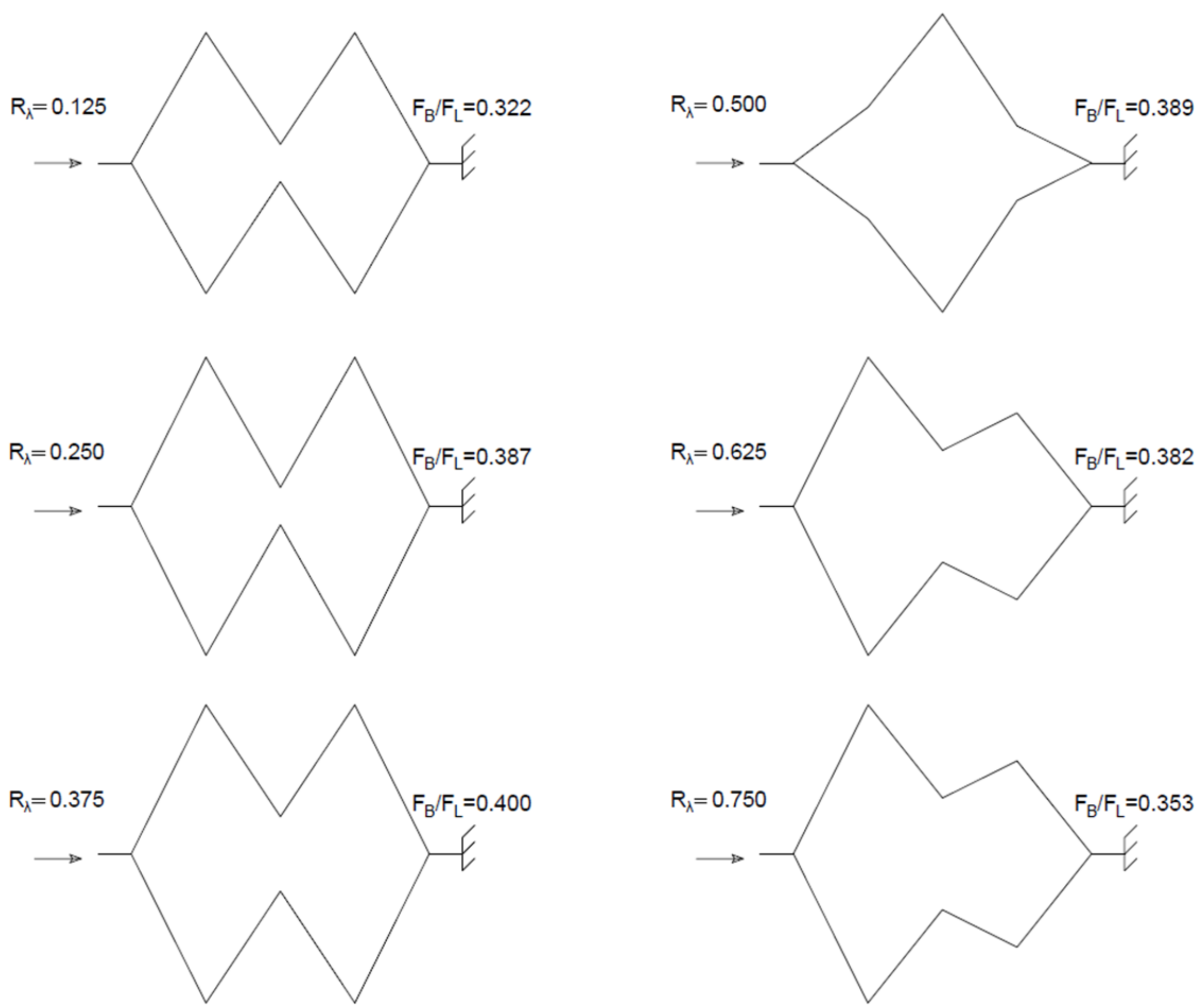

Figure 8-25 Optimal design of the non-collinear stress wave attenuators, $n_x = 3$

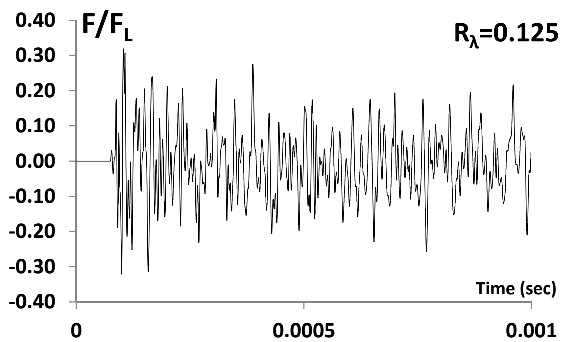

Attenuation = 68%

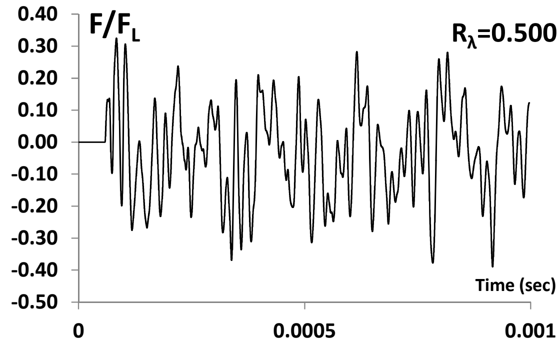

Attenuation = 61%

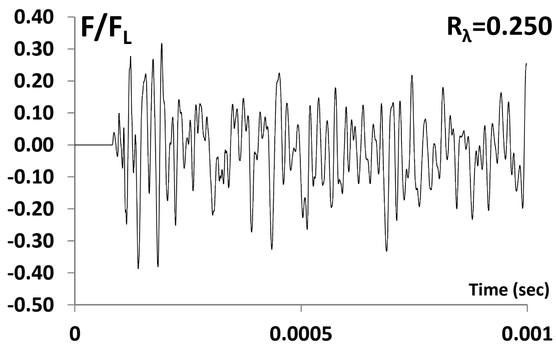

Attenuation = 61%

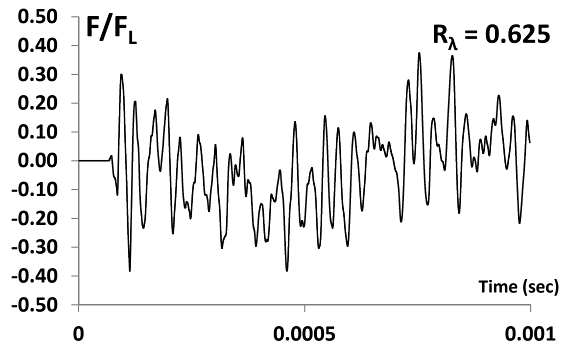

Attenuation = 62%

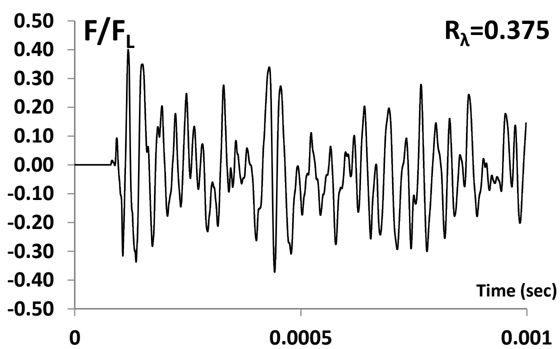

Attenuation = 60%

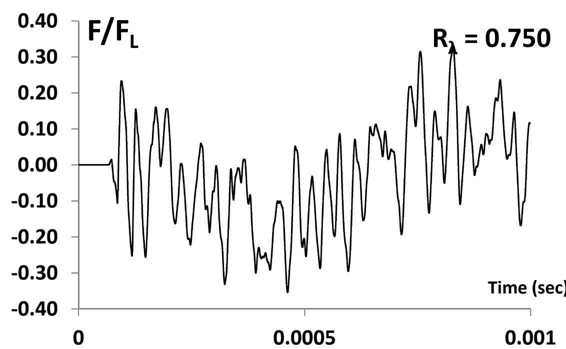

Attenuation = 65%

Figure 8-26 Force history at the boundary of the optimized non-collinear structures with $n_x = 3$

The amount of attenuation for each optimized structure at different values of wavelength ratios are presented in Table 8-11, and the attenuation-R_λ curve is plotted in Figure 8-27. The attenuation ranges in Table 8-11 show that the minimum value of attenuation for the structure that is optimized for $R_\lambda = 0.25$ is 56% which is higher than the other structures; therefore, it can be recommended to use the structure with the vertical position string of "8-1-8" for attenuating the loads with the wavelength ratios of 0.125 to 0.75.

The global attenuation range for the structure with $n_x = 3$ is from 20 to 68%. The minimum attenuation value (20%) occurs for the structure which is optimized for $R_\lambda = 0.5$ and is subjected to the load with $R_\lambda = 0.25$, while the maximum attenuation value (68%) relates to the structure that is optimized for $R_\lambda = 0.125$ and is subjected to the load with the same value of R_λ. It should be noted that the amount of attenuation decreases by increasing the value of wavelength ratio (R_λ) from 0.125 to 0.375, while it increases by increasing the value of wavelength ratio (R_λ) from 0.5 to 0.75.

Table 8-11 Attenuation at the optimized non-collinear structures for different R_λ values, $n_x = 3$

Attenuation at R_λ (%)	Optimized for R_λ:					
	0.125	0.250	0.375	0.500	0.625	0.750
0.125	68	64	53	24	29	29
0.250	54	61	48	20	41	41
0.375	59	59	60	50	51	51
0.500	50	59	57	61	54	54
0.625	52	56	56	61	62	62
0.750	51	58	56	63	65	65
Range (%)	50-68	56-64	48-60	20-63	29-65	29-65

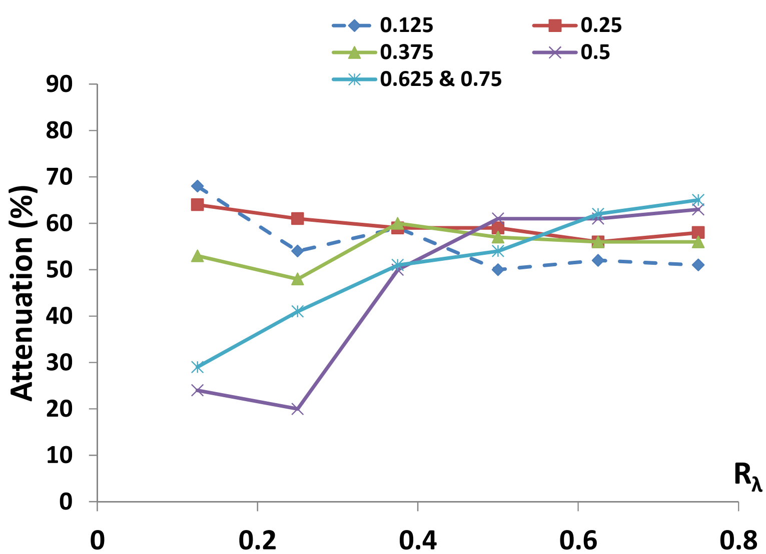

Figure 8-27 Attenuation vs. R_λ, non-collinear structure with $n_x = 3$

8.5.4 Non-collinear stress wave attenuator with $n_x = 4$

The optimization zone for the non-collinear stress wave attenuator with $n_x = 4$ is shown in Figure 8-28. The solution space for this problem is composed of $8^4 = 4096$ combinations and an exhaustive search is performed to find the best solution for each value of the wavelength ratio. The optimized vertical position string for this structure is composed of four numbers and it is presented in Table 8-12. Schematics of the optimal designs and their corresponding force histories at the boundary are depicted in Figure 8-29 and Figure 8-30, respectively.

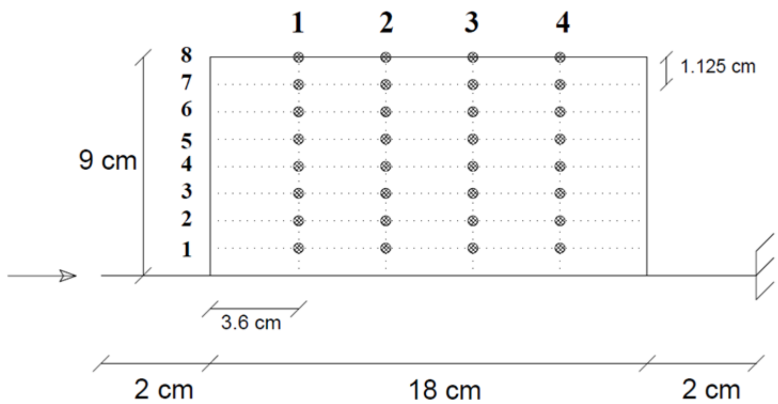

Figure 8-28 Optimization zone for the non-collinear structure with $n_y = 8$ and $n_x = 4$

According to Figure 8-29 and Figure 8-30, the results of the exhaustive search for the structure with $n_x = 4$ can be explained as follows:

- For $R_\lambda = 0.125$ and 0.25, the vertical position string (n_y) for the optimized structure is 8-5-2-8, and the amount of attenuation at the boundary of each structure is 82 and 75%, respectively.
- For $R_\lambda = 0.375$ and 0.5, the vertical position string (n_y) for the optimized structure is 7-2-8-1, and the amount of attenuation at the boundary of each structure is 73 and 70%, respectively.
- For $R_\lambda = 0.625$ and 0.75 the vertical position string (n_y) for the optimized structure is 7-1-8-5, and the amount of attenuation at the boundary of each structure is 73 and 76%, respectively.

Table 8-12 Optimized vertical position string for the non-collinear structure with $n_x = 4$

R_λ	0.125	0.250	0.375	0.500	0.625	0.750
n_y	8-5-2-8	8-5-2-8	7-2-8-1	7-2-8-1	7-1-8-5	7-1-8-5

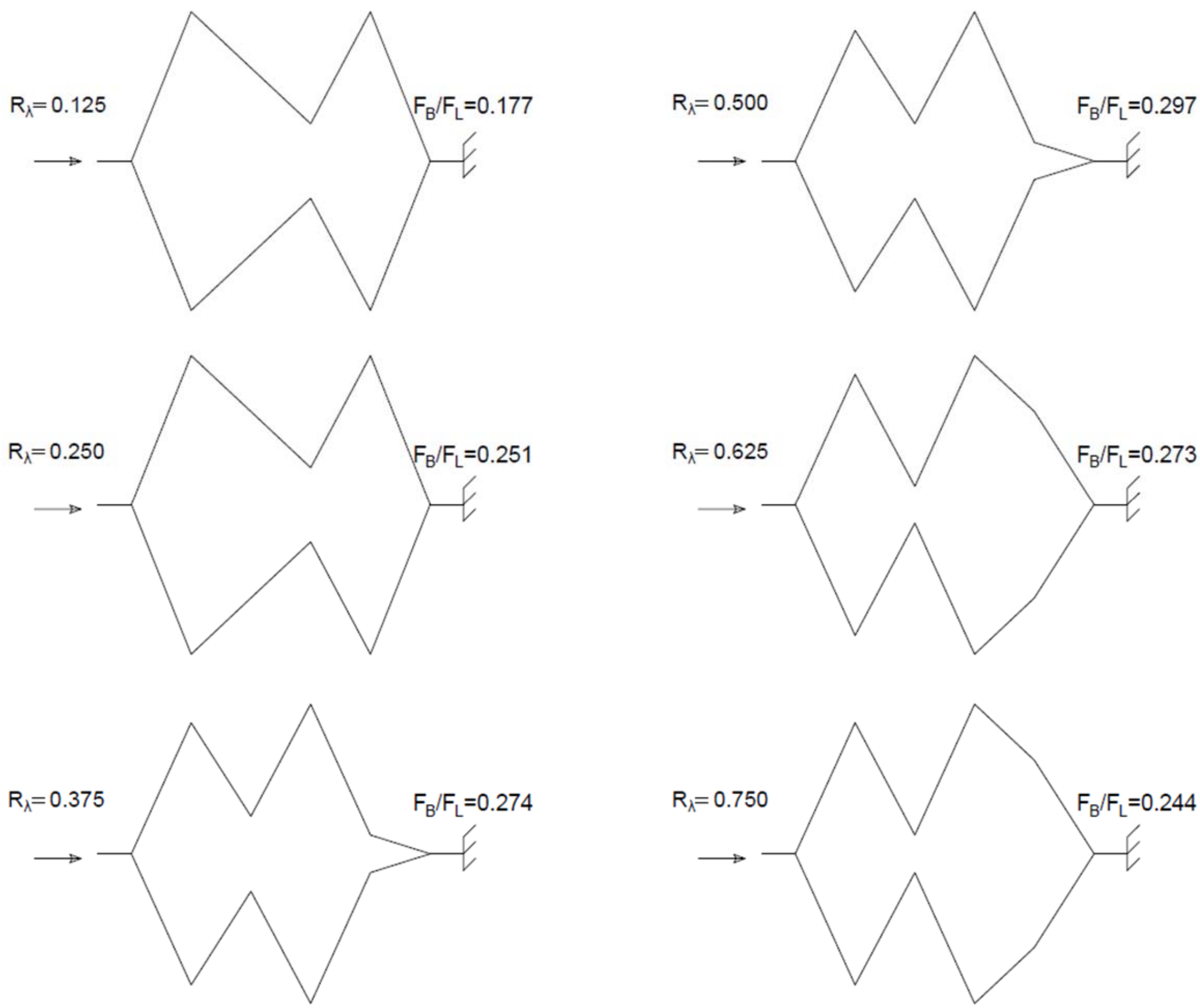

Figure 8-29 Optimal design of the non-collinear stress wave attenuators, $n_x = 4$

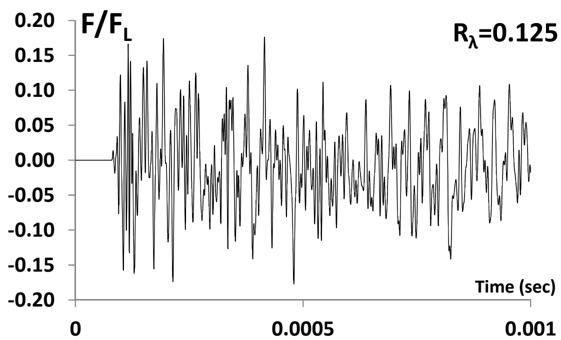

Attenuation = 82%

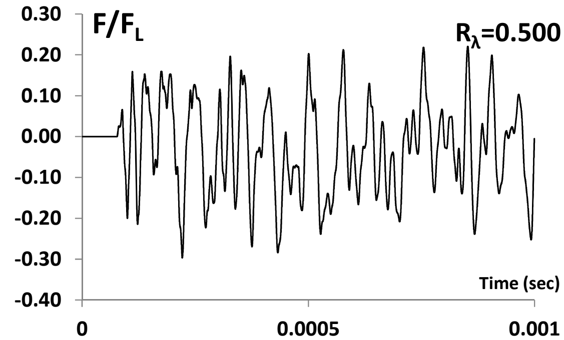

Attenuation = 70%

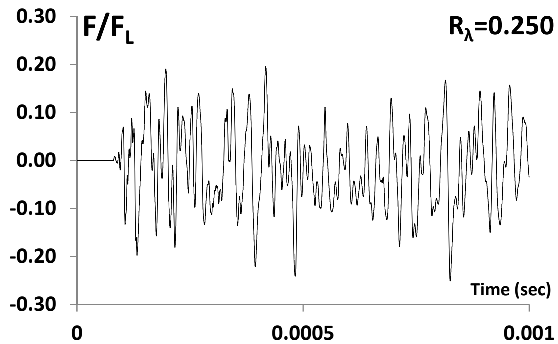

Attenuation = 75%

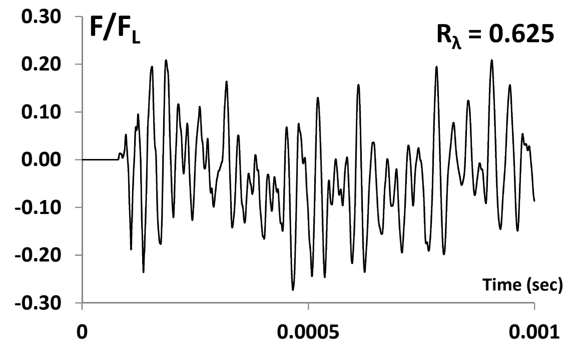

Attenuation = 73%

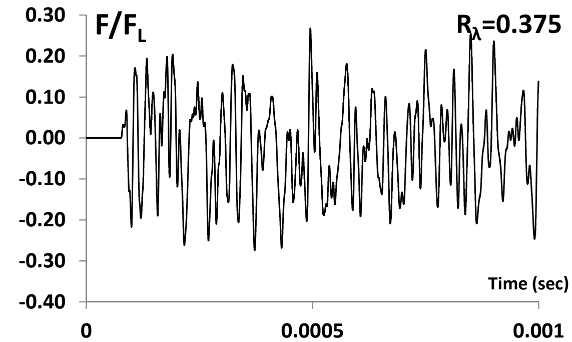

Attenuation = 73%

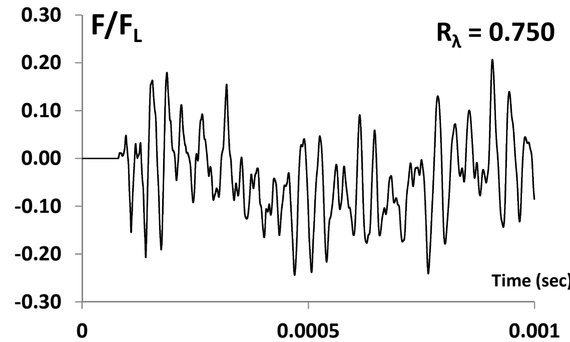

Attenuation = 76%

Figure 8-30 Force history at the boundary of the optimized non-collinear structures with $n_x = 4$

The amount of attenuation for each optimized structure at different values of wavelength ratios are presented in Table 8-13 and the attenuation-R_λ curve is plotted in Figure 8-31. The attenuation ranges in Table 8-13 show that the minimum value of attenuation for the structure that is optimized for $R_\lambda = 0.375$ and 0.5 is 65% which is higher than the other structures; therefore, it can be recommended to use the structure with the vertical position string of "7-2-8-1" for attenuating the loads with the wavelength ratios of 0.125 to 0.75.

The global attenuation range for the structure with $n_x = 4$ is from 52 to 82%. The minimum attenuation value (52%) occurs for the structure which is optimized for $R_\lambda = 0.625$ and is subjected to the load with $R_\lambda = 0.125$, while the maximum attenuation value (82%) relates to the structure that is optimized for $R_\lambda = 0.125$ and is subjected to the load with the same value of R_λ. Similar to the structure with $n_x = 3$, the amount of attenuation decreases by increasing the value of wavelength ratio (R_λ) from 0.125 to 0.375, while it increases by increasing the value of R_λ from 0.5 to 0.75.

Table 8-13 Attenuation at the optimized non-collinear structures for different R_λ values, $n_x = 4$

Attenuation at R_λ (%)	Optimized for R_λ:					
	0.125	0.250	0.375	0.500	0.625	0.750
0.125	82	82	65	65	52	52
0.250	75	75	69	69	60	60
0.375	70	70	73	73	65	65
0.500	66	66	70	70	69	69
0.625	64	64	70	70	73	73
0.750	61	61	68	68	76	76
Range(%)	61-82	61-82	65-73	65-73	52-76	52-76

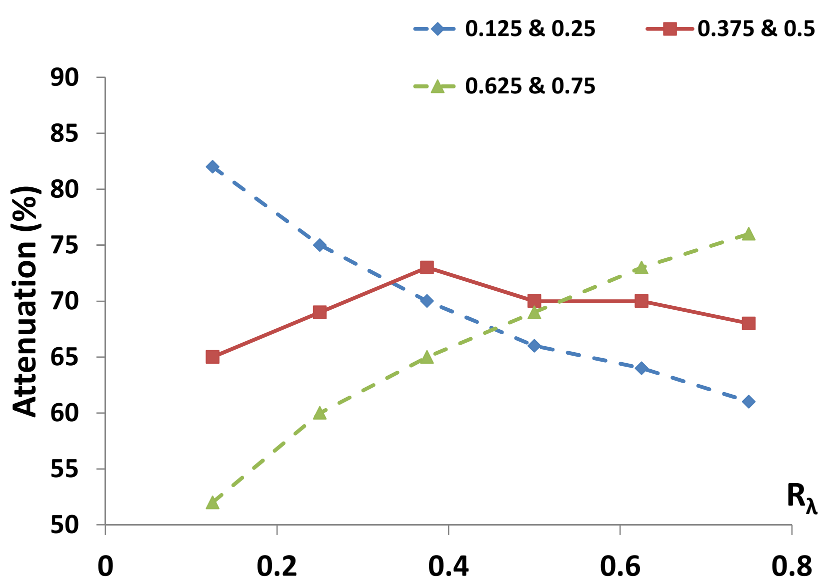

Figure 8-31 Attenuation vs. R_λ, non-collinear structure with $n_x = 4$

8.5.5 Non-collinear stress wave attenuator with $n_x = 5$

The optimization zone for the non-collinear stress wave attenuator with $n_x = 5$ is shown in Figure 8-32. The solution space for this problem is composed of $8^5 = 32768$ combinations and it is very time consuming to perform an exhaustive search for finding the best solution. Therefore, the developed GA-FE optimization methodology is utilized for finding the optimal design of the structures. An integer-valued GA is performed for each wavelength ratio with 5 integer variables with lower and upper bounds of 1 and 8, respectively. The details of the GA are similar to the optimization of the collinear structures. The population size and function tolerance are 100 and 1E-6, respectively.

The optimized vertical position string for this structure is composed of five numbers and it is presented in Table 8-14. Schematic of the optimal designs (with their attenuation capacity) and their corresponding force histories at the boundary are depicted in Figure 8-33 and Figure 8-34, respectively.

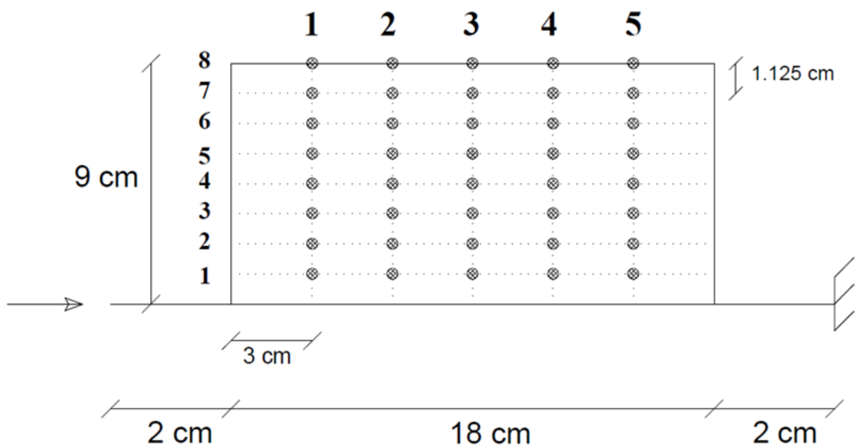

Figure 8-32 Optimization zone for the non-collinear structure with $n_y = 8$ and $n_x = 5$

Considering the results presented in Figure 8-33 and Figure 8-34, the outcome of the GA optimization for the structure with $n_x = 5$ can be explained as follows:

- For $R_\lambda = 0.125$, the vertical position string (n_y) for the optimized structure is 8-1-6-1-6, and the amount of attenuation at the boundary is 81%.
- For $R_\lambda = 0.25$, the vertical position string (n_y) for the optimized structure is 8-1-7-1-8, and the amount of attenuation at the boundary is 82%.
- For $R_\lambda = 0.375$, the vertical position string (n_y) for the optimized structure is 8-3-8-4-5, and the amount of attenuation at the boundary is 78%.

- For $R_\lambda = 0.5, 0.625$ and 0.75, the vertical position string (n_y) for the optimized structure is 8-2-5-3-8, and the amount of attenuation at the boundary of each structure is 83, 82, and 82%, respectively.

Table 8-14 Optimized vertical position string for the non-collinear structure with $n_x = 5$

R_λ	0.125	0.250	0.375	0.500	0.625	0.750
n_y	8-1-6-1-6	8-1-7-1-8	8-3-8-4-5	8-2-5-3-8	8-2-5-3-8	8-2-5-3-8

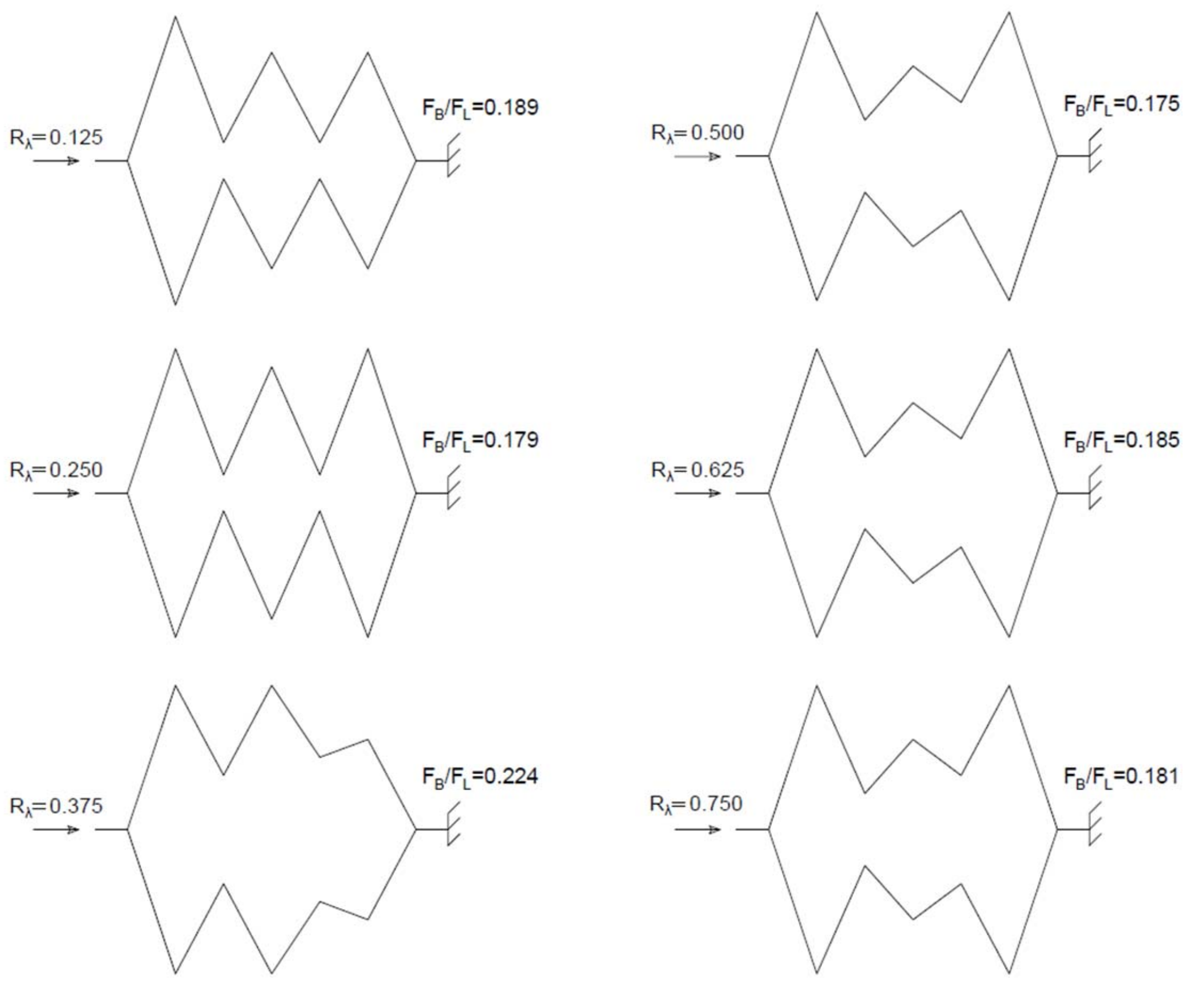

Figure 8-33 Optimal design of the non-collinear stress wave attenuators, $n_x = 5$

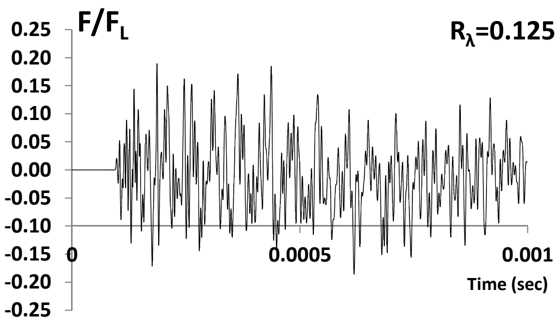

Attenuation = 81%

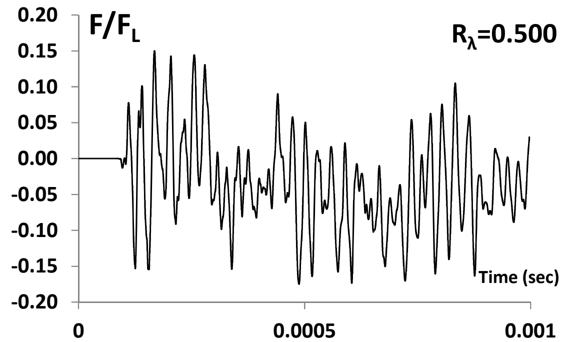

Attenuation = 83%

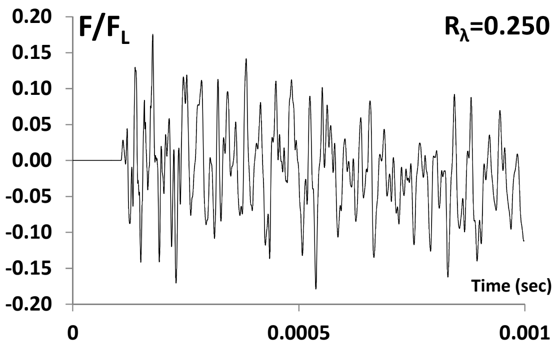

Attenuation = 82%

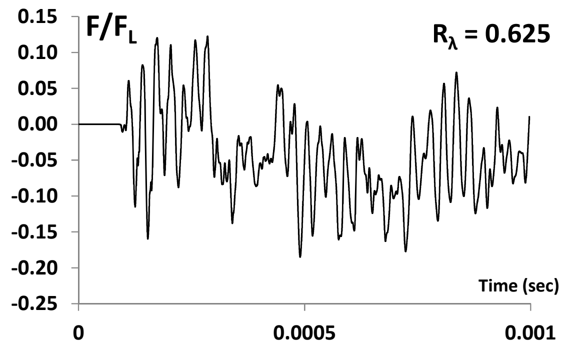

Attenuation = 82%

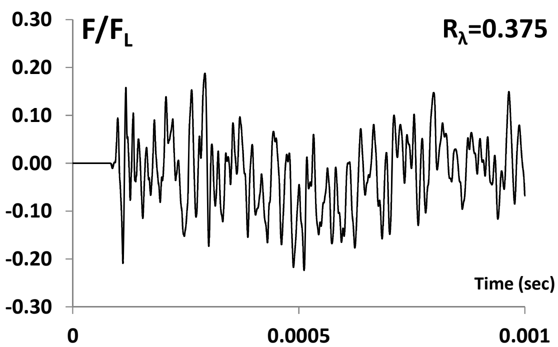

Attenuation = 78%

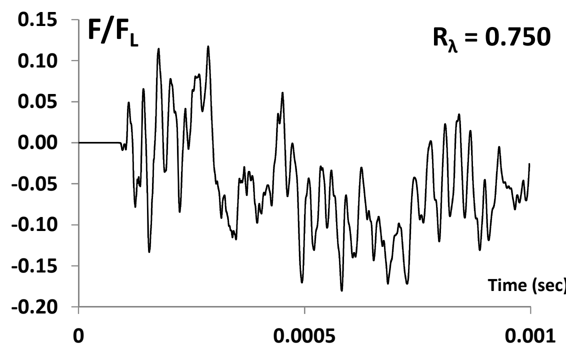

Attenuation = 82%

Figure 8-34 Force history at the boundary of the optimized non-collinear structures with $n_x = 5$

The amount of attenuation, for each optimized structure at different values of wavelength ratios, is presented in Table 8-15 and the attenuation-R_λ curve is plotted in Figure 8-35. The attenuation ranges in Table 8-15 show that the minimum value of attenuation for the structure that is optimized for $R_\lambda = 0.5, 0.625,$ and 0.75 is 78% which is higher than the other structures; therefore, it can be recommended to use the structure with the vertical position string of "8-2-5-3-8" for attenuating the transient loadings with the wavelength ratios of 0.125 to 0.75.

The global attenuation range for the structure with $n_x = 5$ is 56-83%. The minimum attenuation value (56%) occurs at the structure which is optimized for $R_\lambda = 0.125$ and is subjected to the load with $R_\lambda = 0.75$, while the maximum attenuation value (83%) happens at the structure that is optimized for $R_\lambda = 0.5, 0.625$, and 0.75 and is subjected to the loading with the same value of R_λ.

To check the efficiency of the developed GA procedure, the amount of attenuation in a structure which has the vertical position string of "8-1-8-1-8" is found for various values of R_λ and presented in Table 8-15. This structure has the maximum length of the optimization zone, and one might predict that it can have the highest attenuation capacity. However, the results show that, for all of the wavelength ratios, this structure has lower amount of attenuation in comparison to the optimized structures, which proves the efficiency of the GA optimization procedure.

Table 8-15 Attenuation at the optimized non-collinear structures for different R_λ values, $n_x = 5$

Attenuation at R_λ (%)	Optimized for R_λ:						Arrangement 8-1-8-1-8
	0.125	0.250	0.375	0.500	0.625	0.750	
0.125	81	77	66	80	80	80	79
0.250	74	82	72	77	77	77	74
0.375	70	82	78	78	78	78	70
0.500	63	78	77	83	83	83	72
0.625	60	74	75	82	82	82	76
0.750	56	72	73	82	82	82	76
Range (%)	56-81	72-82	66-78	78-83	78-83	78-83	70-79

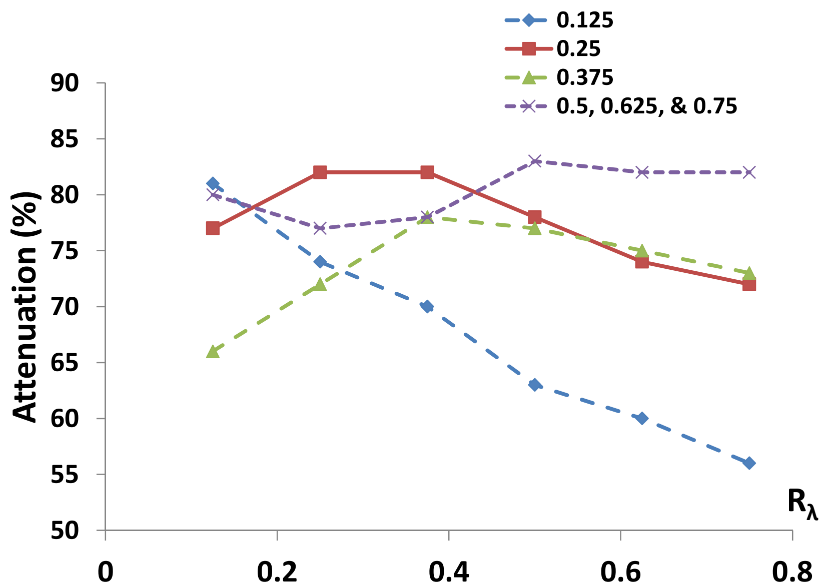

Figure 8-35 Attenuation vs. R_λ, non-collinear structure with $n_x = 5$

8.5.6 Non-collinear stress wave attenuator with $n_x = 6$

The optimization zone for the non-collinear stress wave attenuator with $n_x = 6$ is shown in Figure 8-36. The solution space for this problem is composed of $8^6 = 262{,}144$ combinations and the GA optimization methodology is utilized for the optimal design of the structures. An integer-valued GA is performed for each wavelength ratio with 6 integer variables with lower and upper bounds of 1 and 8, respectively. The population size and function tolerance of GA are 100 and 1E-6, respectively.

The optimized vertical position string for this structure is composed of 6 numbers and is presented in Table 8-16. Schematic of the optimal designs (with their attenuation capacity) and their corresponding force histories at the boundary are depicted in Figure 8-37 and Figure 8-38, respectively.

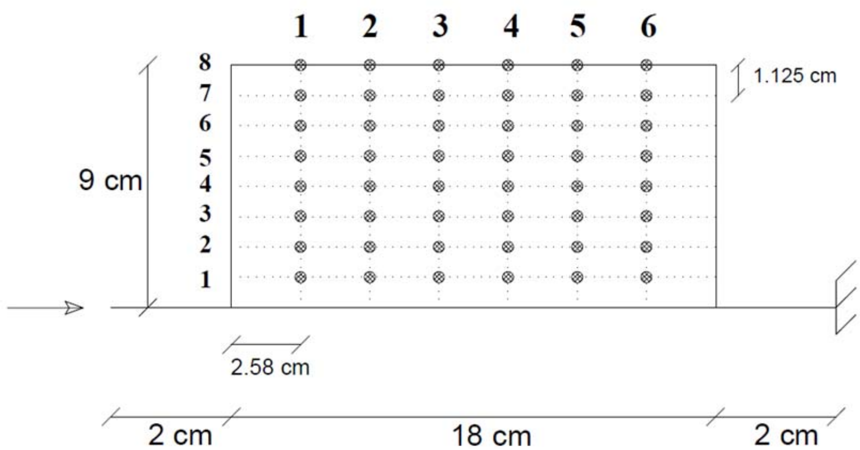

Figure 8-36 Optimization zone for the non-collinear structure with $n_y = 8$ and $n_x = 6$

According to Figure 8-37 and Figure 8-38, the results of the GA optimization for the structure with $n_x = 6$ can be explained as follows:

- For $R_\lambda = 0.125$, the vertical position string (n_y) for the optimized structure is 8-1-5-7-1-8, and the amount of attenuation at the boundary is 86%.
- For $R_\lambda = 0.25$, the vertical position string (n_y) for the optimized structure is 8-1-7-6-1-8, and the amount of attenuation at the boundary is 85%.
- For $R_\lambda = 0.375$, the vertical position string (n_y) for the optimized structure is 8-1-4-3-2-8, and the amount of attenuation at the boundary is 85%.
- For $R_\lambda = 0.5$, the vertical position string (n_y) for the optimized structure is 8-2-4-3-2-8, and the amount of attenuation at the boundary is 85%.

- For $R_\lambda = 0.625$, the vertical position string (n_y) for the optimized structure is 8-1-4-3-1-8, and the amount of attenuation at the boundary is 84%.
- For $R_\lambda = 0.75$, the vertical position string (n_y) for the optimized structure is 7-3-8-1-7-8, and the amount of attenuation at the boundary is 84%.

Table 8-16 Optimized vertical position string for the non-collinear structure with $n_x = 6$

R_λ	0.125	0.250	0.375	0.500	0.625	0.750
n_y	8-1-5-7-1-8	8-1-7-6-1-8	8-1-4-3-2-8	8-2-4-3-2-8	8-1-4-3-1-8	7-3-8-1-7-8

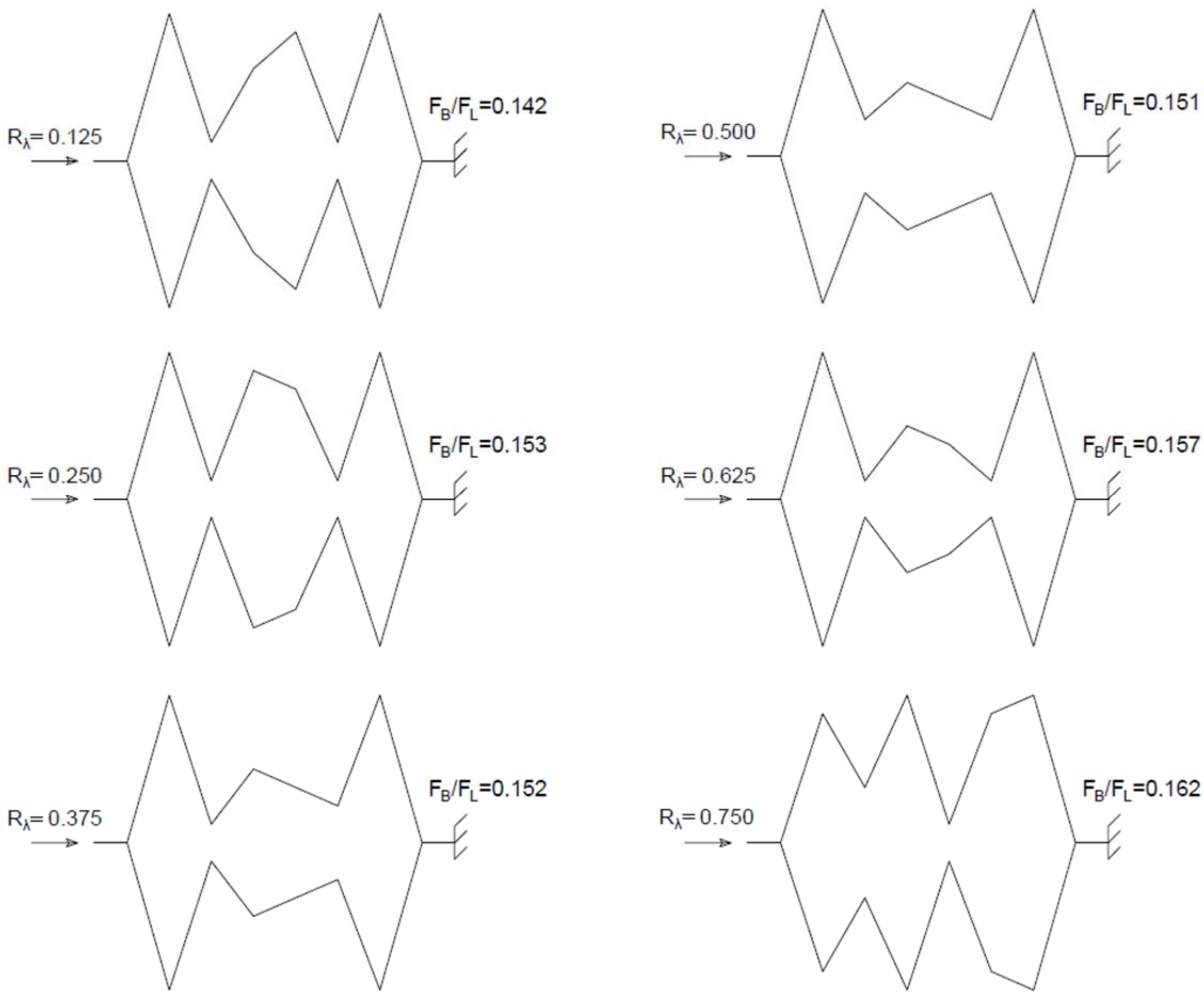

Figure 8-37 Optimal design of the non-collinear stress wave attenuators, $n_x = 6$

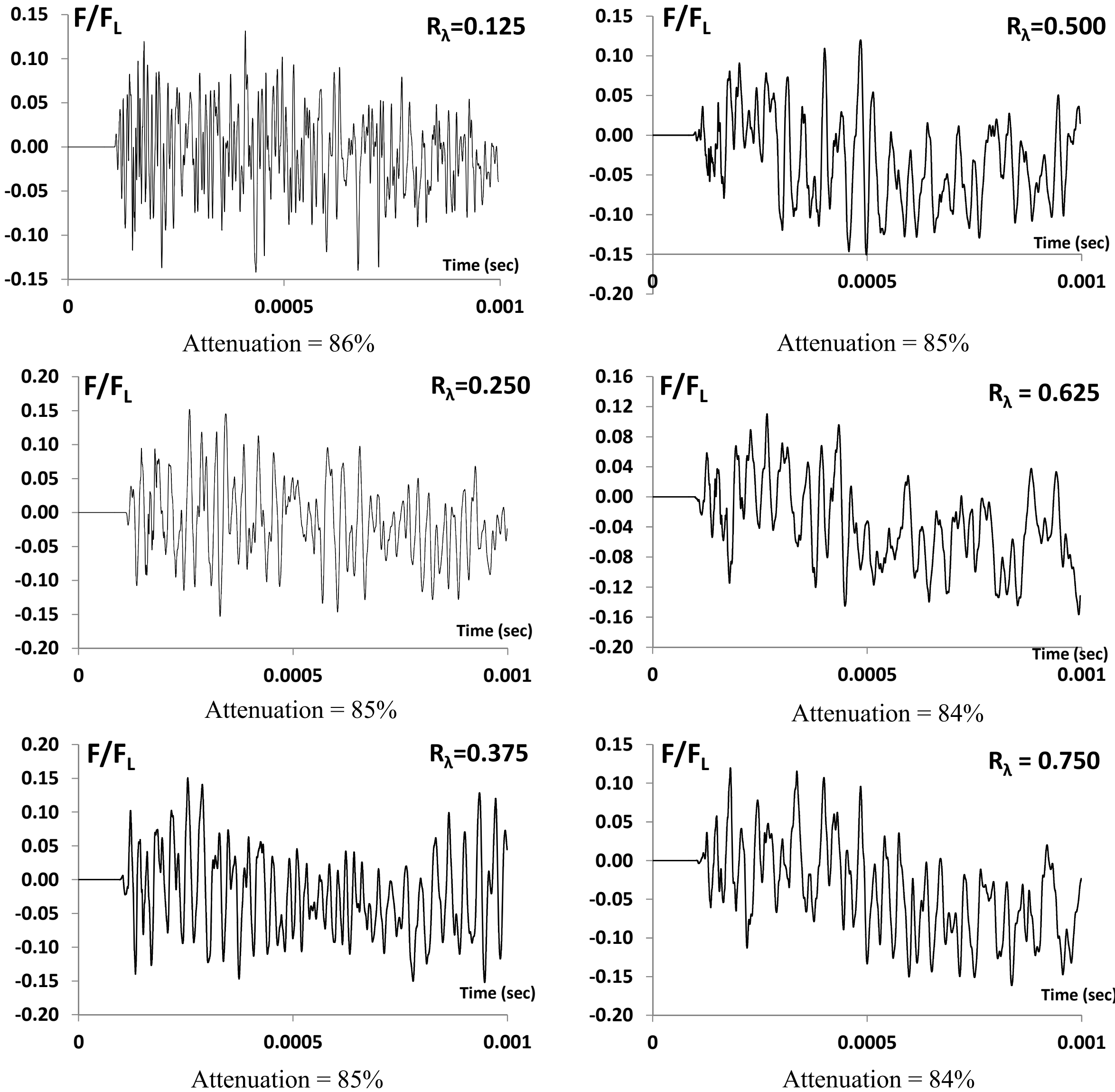

Figure 8-38 Force history at the boundary of the optimized non-collinear structures with $n_x = 6$

The amounts of attenuation for each optimized structure at different values of wavelength ratios are presented in Table 8-17, and the attenuation-R_λ curve is plotted in Figure 8-39. The attenuation ranges in Table 8-17 show that the minimum value of attenuation for the structure that is optimized for $R_\lambda = 0.5$ is 82%, which is higher than the other structures; therefore, it can be recommended to use the structure with the vertical position string of “8-2-4-3-2-8” for attenuating the loads with the wavelength ratios of 0.125 to 0.75.

The global attenuation range for the structure with $n_x = 6$ is from 74 to 86%. The minimum attenuation value (74%) occurs at the structure which is optimized for $R_\lambda = 0.125$ and is subjected to the load with $R_\lambda = 0.75$, while the maximum attenuation value (86%) happens at the structure that is optimized for $R_\lambda = 0.375$ and is subjected to the load with the same value of R_λ.

The attenuation values for the structure with the vertical position string of "8-1-8-1-8-1" are presented in Table 8-17, and it is obvious that this structure has a significantly lower attenuation capacity in comparison to the optimized configurations.

Table 8-17 Attenuation at the optimized non-collinear structures for different R_λ values, $n_x = 6$

Attenuation at R_λ (%)	Optimized for R_λ:						Arrangement 8-1-8-1-8-1
	0.125	0.250	0.375	0.500	0.625	0.750	
0.125	86	84	84	83	82	73	77
0.250	76	85	86	83	81	74	72
0.375	76	82	85	82	82	78	70
0.500	76	83	83	85	83	80	71
0.625	75	82	81	83	84	82	69
0.750	74	79	79	82	83	84	67
Range (%)	74-86	79-85	79-86	82-85	81-84	73-84	67-77

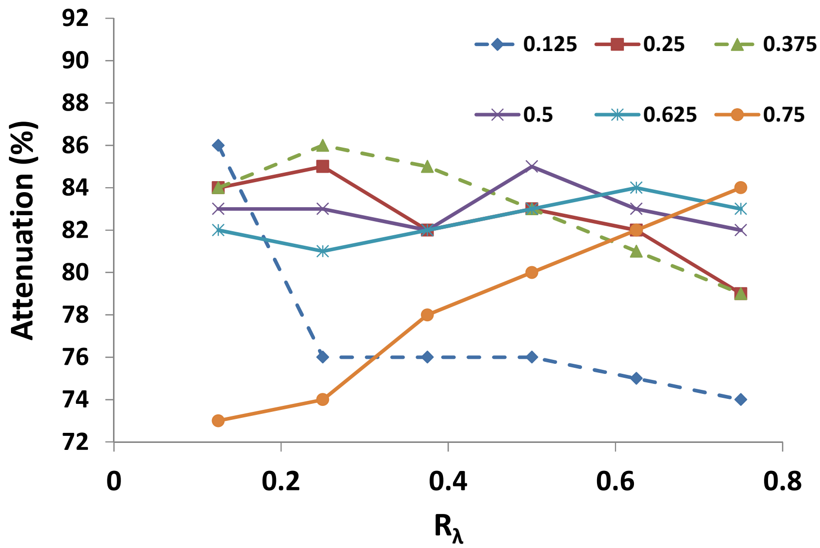

Figure 8-39 Attenuation vs. R_λ, non-collinear structure with $n_x = 6$

8.5.7 Non-collinear stress wave attenuator with $n_x = 7$

The optimization zone for the non-collinear stress wave attenuator with $n_x = 7$ is shown in Figure 8-40. The solution space for this problem is composed of $8^7 = 2{,}097{,}152$ combinations, and the GA optimization procedure is utilized for the optimal design. An integer-valued GA is performed for each wavelength ratio with 7 integer variables with lower and upper bounds of 1 and 8, respectively. The population size and function tolerance of GA are 100 and 1E-6, respectively.

The optimized vertical position string for this structure is composed of 7 numbers and it is presented in Table 8-18. Schematic of the optimal designs (with their attenuation capacity) and their corresponding force histories at the boundary are depicted in Figure 8-41 and Figure 8-42.

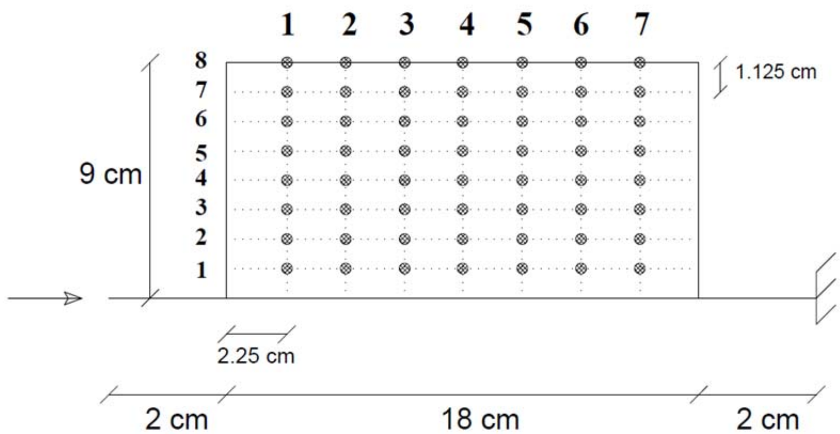

Figure 8-40 Optimization zone for the non-collinear structure with $n_y = 8$ and $n_x = 7$

The results of the GA optimization for the structure with $n_x = 7$ can be explained as follows (see Figure 8-41 and Figure 8-42):

- For $R_\lambda = 0.125$, the vertical position string (n_y) for the optimized structure is 8-1-5-1-7-1-8, and the amount of attenuation at the boundary is 89%.
- For $R_\lambda = 0.25$, the vertical position string (n_y) for the optimized structure is 8-1-3-1-7-1-8, and the amount of attenuation at the boundary is 90%.
- For $R_\lambda = 0.375$, the vertical position string (n_y) for the optimized structure is 8-1-4-5-7-1-8, and the amount of attenuation at the boundary is 89%.
- For $R_\lambda = 0.5$, the vertical position string (n_y) for the optimized structure is 8-1-4-5-7-1-8, and the amount of attenuation at the boundary is 89%.

- For $R_\lambda = 0.625$, the vertical position string (n_y) for the optimized structure is 4-1-8-6-8-1-8, and the amount of attenuation at the boundary is 89%.
- For $R_\lambda = 0.75$, the vertical position string (n_y) for the optimized structure is 8-3-8-1-3-1-8, and the amount of attenuation at the boundary is 88%.

Table 8-18 Optimized vertical position string for the non-collinear structure with $n_x = 7$

R_λ	0.125	0.250	0.375	0.500	0.625	0.750
n_y	8-1-5-1-7-1-8	8-1-3-1-7-1-8	8-1-4-5-7-1-8	8-1-4-5-7-1-8	4-1-8-6-8-1-8	8-3-8-1-3-1-8

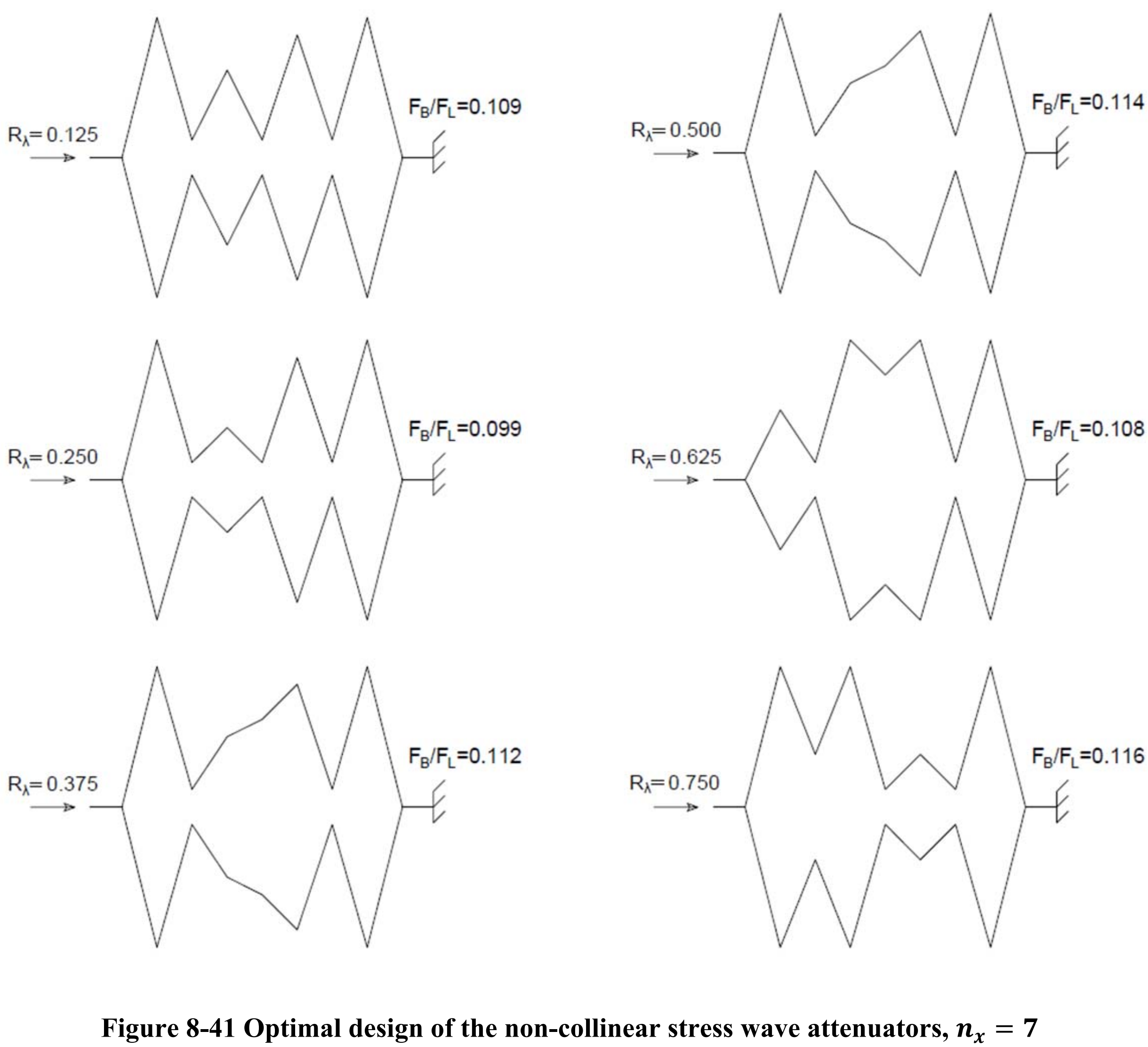

Figure 8-41 Optimal design of the non-collinear stress wave attenuators, $n_x = 7$

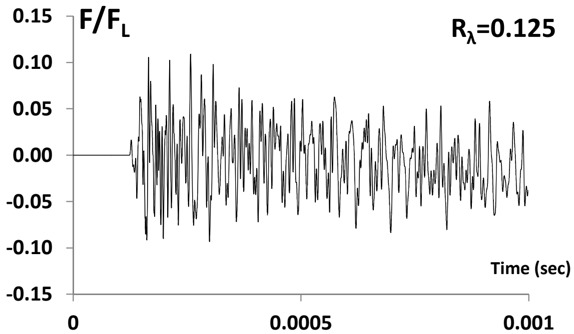

Attenuation = 89%

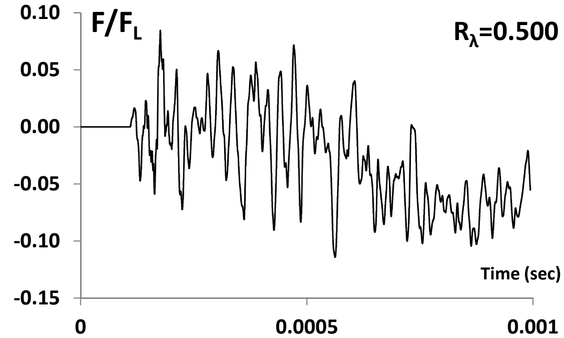

Attenuation = 89%

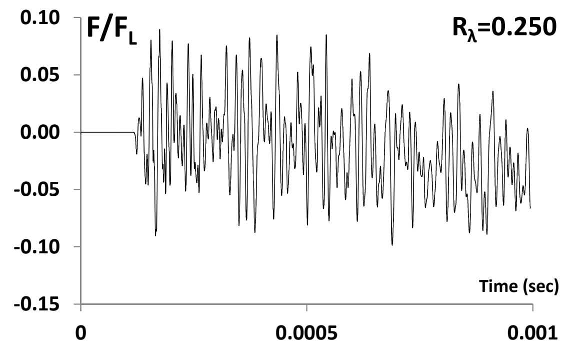

Attenuation = 90%

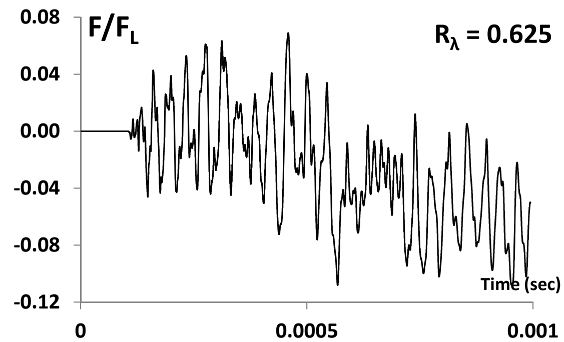

Attenuation = 89%

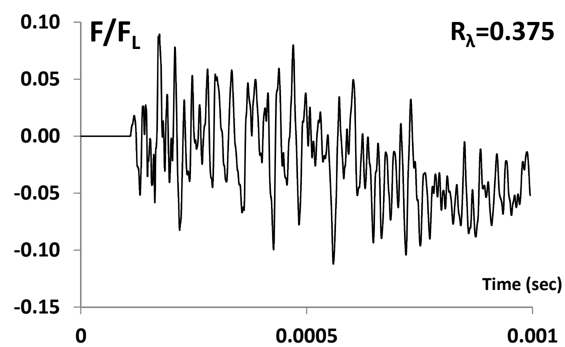

Attenuation = 89%

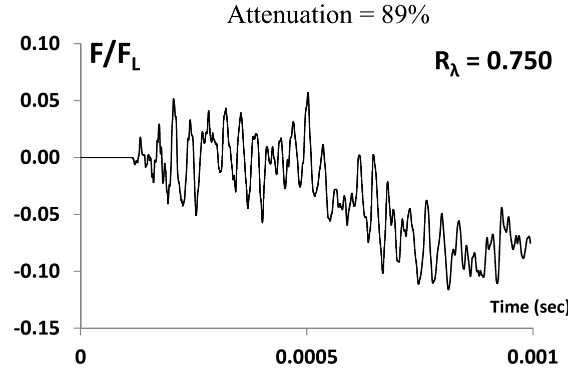

Attenuation = 88%

Figure 8-42 Force history at the boundary of the optimized non-collinear structures with $n_x = 7$

The amounts of attenuation for each optimized structure at different values of wavelength ratios are presented in Table 8-19 and the attenuation-R_λ curve is plotted in Figure 8-43. The attenuation ranges in Table 8-19 show that the minimum value of attenuation for the structure that is optimized for $R_\lambda = 0.25, 0.375$, and 0.5 is 85% which is higher than the other structures; therefore, it can be recommended to use the structure with the vertical position strings of “8-1-3-1-7-1-8” and “8-1-4-5-7-1-8” for attenuating the loads with the wavelength ratios of 0.125 to 0.75.

The global attenuation range for the structure with $n_x = 7$ is 80-90%. The minimum attenuation value (80%) occurs at the structure which is optimized for $R_\lambda = 0.75$ and is subjected to the load with $R_\lambda = 0.125$, while the maximum attenuation value (90%) relates to the structure that is optimized for $R_\lambda = 0.25$ and is subjected to the load with the same value of R_λ.

The attenuation values for the structure with the vertical position string of “8-1-8-1-8-1-8” are presented in Table 8-19. The results show that the optimized structures have much higher attenuation capacity.

Table 8-19 Attenuation at the optimized non-collinear structures for different R_λ values, $n_x = 7$

Attenuation at R_λ (%)	Optimized for R_λ:						Arrangement 8-1-8-1-8-1-8
	0.125	0.250	0.375	0.500	0.625	0.750	
0.125	89	86	88	88	85	80	82
0.250	87	90	88	88	83	85	73
0.375	83	89	89	89	87	85	69
0.500	84	86	89	89	90	86	73
0.625	84	86	87	87	89	87	80
0.750	84	85	85	85	88	88	80
Range (%)	83-89	85-90	85-89	85-89	83-90	80-88	69-82

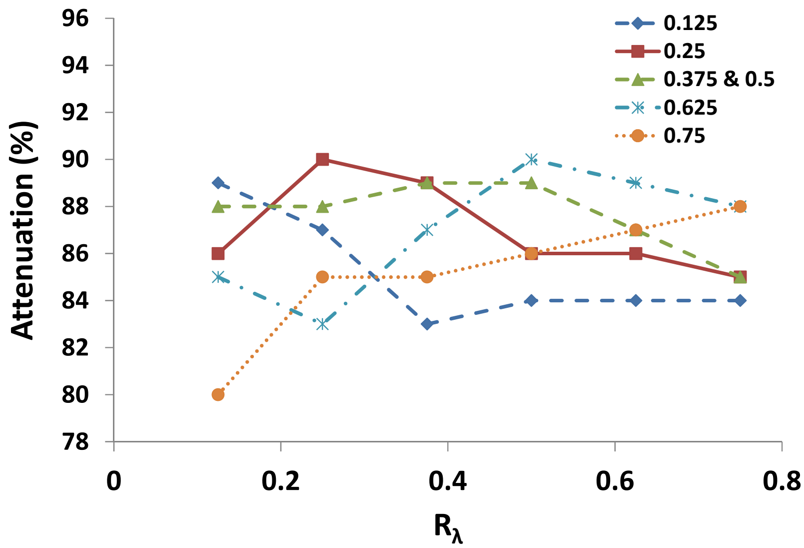

Figure 8-43 Attenuation vs. R_λ, non-collinear structure with $n_x = 7$

8.5.8 Non-collinear stress wave attenuator with $n_x = 8$

The optimization zone for the non-collinear stress wave attenuator with $n_x = 8$ is shown in Figure 8-44. The solution space for this problem is composed of $8^8 = 16{,}777{,}216$ combinations and the GA optimization methodology is utilized for the optimal design. An integer-valued GA is performed for each wavelength ratio with 8 integer variables with lower and upper bounds of 1 and 8, respectively. The population size and function tolerance of GA are 100 and 1E-6, respectively.

The optimized vertical position string for this structure is composed of 8 numbers, and it is presented in Table 8-20. Schematic of the optimal designs (with their attenuation capacity) and their corresponding force histories at the boundary are depicted in Figure 8-45 and Figure 8-46.

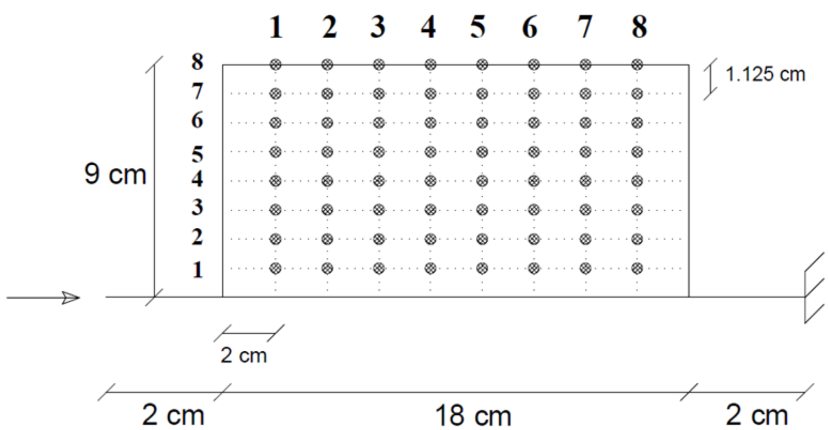

Figure 8-44 Optimization zone for the non-collinear structure with $n_y = 8$ and $n_x = 8$

According to Figure 8-45 and Figure 8-46, the results of the GA optimization for the structure with $n_x = 8$ can be explained as follows:

- For $R_\lambda = 0.125$, the vertical position string (n_y) for the optimized structure is 8-1-7-5-8-6-1-8, and the amount of attenuation at the boundary is 91%.
- For $R_\lambda = 0.25$, the vertical position string (n_y) for the optimized structure is 8-1-8-1-8-1-3-8, and the amount of attenuation at the boundary is 91%.
- For $R_\lambda = 0.375$, the vertical position string (n_y) for the optimized structure is 8-1-7-5-8-3-1-5, and the amount of attenuation at the boundary is 89%.
- For $R_\lambda = 0.5$, the vertical position string (n_y) for the optimized structure is 8-1-1-8-1-7-1-8, and the amount of attenuation at the boundary is 90%.
- For $R_\lambda = 0.625$, the vertical position string (n_y) for the optimized structure is 8-1-4-8-1-5-1-8, and the amount of attenuation at the boundary is 90%.

- For $R_\lambda = 0.75$ the vertical position string (n_y) for the optimized structure is 8-1-8-8-1-5-1-8, and the amount of attenuation at the boundary is 90%.

Table 8-20 Optimized vertical position string for the non-collinear structure with $n_x = 8$

R_λ	0.125	0.250	0.375	0.500	0.625	0.750
n_y	8-1-7-5-8-6-1-8	8-1-8-1-8-1-3-8	8-1-7-5-8-3-1-5	8-1-1-8-1-7-1-8	8-1-4-8-1-5-1-8	8-1-8-8-1-5-1-8

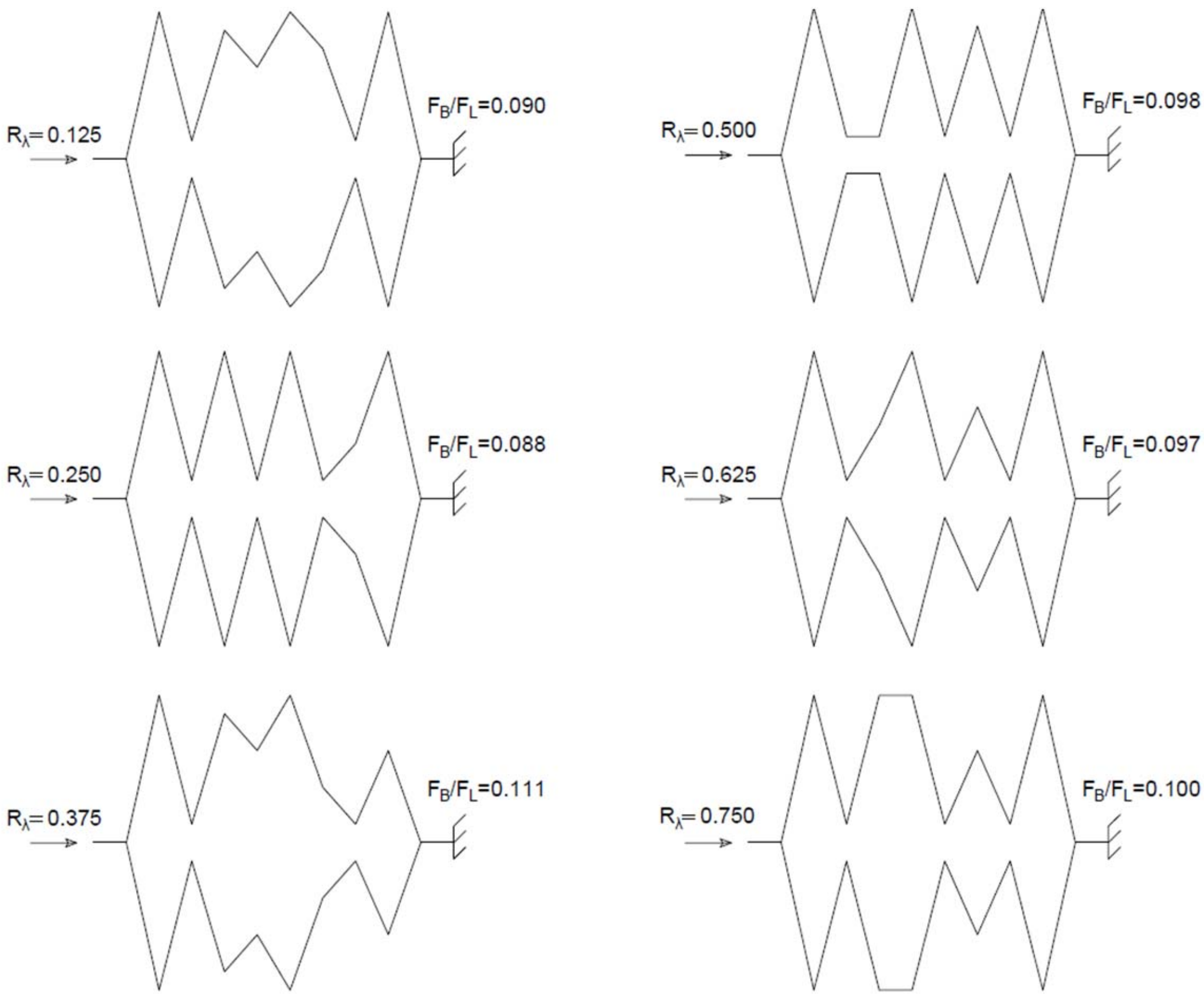

Figure 8-45 Optimal design of the non-collinear stress wave attenuators, $n_x = 8$

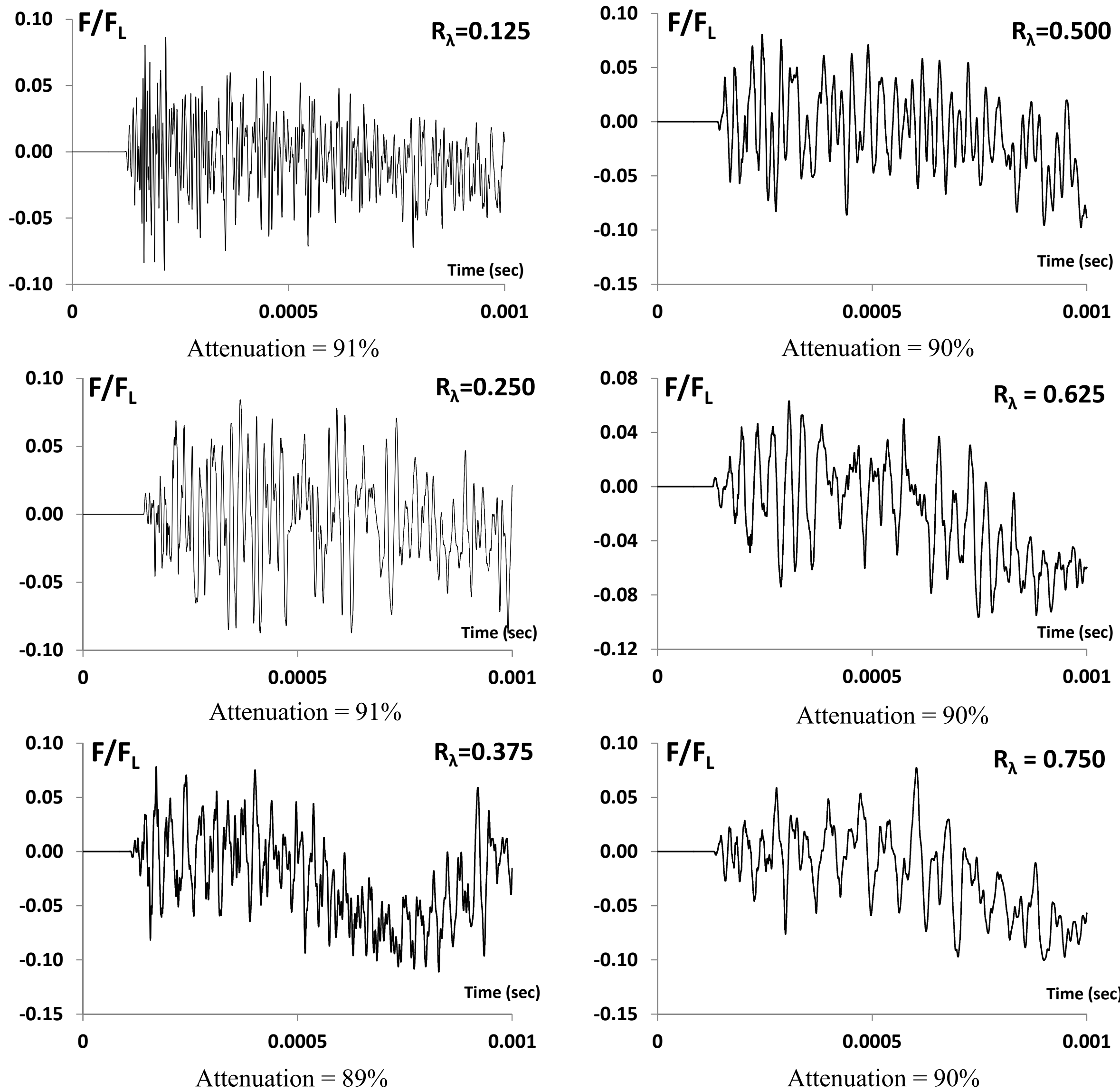

Figure 8-46 Force history at the boundary of the optimized non-collinear structures with $n_x = 8$

The amounts of attenuation for each optimized structure at different values of wavelength ratios are presented in Table 8-21 and the attenuation-R_λ curve is plotted in Figure 8-47. The attenuation ranges in Table 8-21 show that the minimum value of attenuation for the structure that is optimized for $R_\lambda = 0.25$ is 89% which is higher than the other structures; therefore, it can be recommended to use the structure with the vertical position string of “8-1-8-1-8-1-3-8” for attenuating the loads with the wavelength ratios of 0.125 to 0.75.

The global attenuation range for the structure with $n_x = 8$ is 82-91%. The minimum attenuation value (82%) occurs for the structure which is optimized for $R_\lambda = 0.375$ and is subjected to the load with $R_\lambda = 0.75$, while the maximum attenuation value (91%) relates to the structure that is optimized for $R_\lambda = 0.25$ and is subjected to the load with the same value of R_λ.

The attenuation values for the structure with the vertical position string of "8-1-8-1-8-1-8-1" are presented in Table 8-21. The results show that the optimized structures have much higher attenuation capacity.

Table 8-21 Attenuation at the optimized non-collinear structures for different R_λ values, $n_x = 8$

Attenuation at R_λ (%)	Optimized for R_λ:						Arrangement 8-1-8-1-8-1-8-1
	0.125	0.250	0.375	0.500	0.625	0.750	
0.125	91	90	86	85	90	84	78
0.250	90	91	90	89	89	83	76
0.375	88	89	89	90	87	87	73
0.500	87	90	87	90	89	88	78
0.625	86	90	85	89	90	89	80
0.750	84	89	82	86	89	90	81
Range (%)	84-91	89-91	82-90	85-90	87-90	83-90	73-81

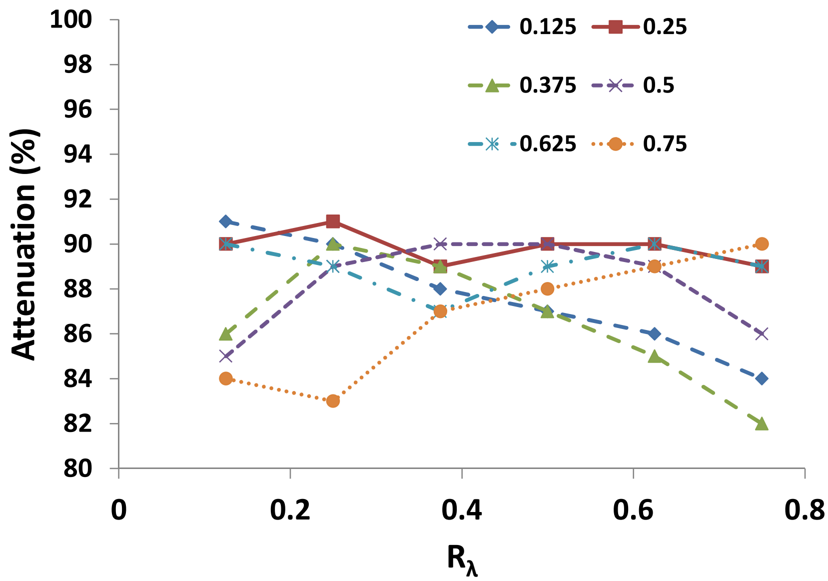

Figure 8-47 Attenuation vs. R_λ, non-collinear structure with $n_x = 8$

8.5.9 Effect of n_x on the attenuation capacity

The attenuation range for the non-collinear stress wave attenuators with various values of n_x are presented in Table 8-22. The numbers show that the attenuation capacity increases significantly by increasing n_x, and more robust solutions can be obtained for higher values of n_x.

Table 8-22 Attenuation range for various n_x values

n_x	1	2	3	4	5	6	7	8
Attenuation range (%)	-10 to 27	5 to 48	20 to 68	52 to 82	56 to 83	74 to 86	80 to 90	82 to 91

8.6 Summary

The optimal design of the non-collinear stress wave attenuators is explored in this section. Two types of non-collinear structures were thoroughly studied—namely, multi-layered diamond shape structure with constant geometry and single layered structure with varying non-collinear segments. It was observed that the multi-layered structures have very high attenuation capacity in comparison to the collinear structures because of the existence of the flexural waves. A very good amount of attenuation is also achieved with single-layered structures, especially for higher values of the vertical positions, n_x. The major amount of attenuation in non-collinear structures happens due to the existence of angled joints. The angled joints generate new reflected and transmitted waves within the structure, and the developed optimization methodology tries to arrange them in a configuration that can provide high amount of attenuation.

The results of this section show that the developed GA-FE tool is very efficient for designing the non-collinear stress wave attenuators, and robust structures can be obtained for a wide range of frequencies.

SECTION 9
STRESS WAVE ATTENUATION IN POROUS PLATES

9.1 Introduction

The optimal design of the non-collinear stress wave attenuators was studied in the previous section, and it was found that the geometry optimization can be very effective in mitigating the stress waves within the structures that are made of a single material.

In this section, this concept will be examined for two-dimensional (2D) structures (plates) with circular holes. These holes are the geometric discontinuities which affect the wave propagation characteristics of the plates and they can attenuate the stress waves if they are arranged in appropriate patterns. To do so, the developed heuristic optimization methodology will try to spread the circular holes with various diameters within the area of a plate (optimization zone) to find the most mitigating configuration. In the following, a detailed procedure for the geometric optimization of the structures with circular holes will be explained and the optimization results will be presented for the plates with various dimensions.

9.2 Geometry optimization of porous plates for stress wave attenuation

In this section, it will be shown how the dimensions and positions of the circular holes can be optimized for stress wave mitigation in plates. These plates are made of a single material (Aluminum in this research), and are called "2D porous stress wave attenuators".

To introduce the geometry optimization procedure for designing 2D porous stress wave attenuators consider the structure that is shown in Figure 9-1. This structure is an Aluminum plate with the length and height of L_x and L_y, respectively. A transient load is applied to the left hand side of the plate and the structure is clamped at the right hand side. To perform the optimal design procedure, the whole area of the plate is considered as the "optimization zone", and it is divided into $n_x = n$ (along x-axis) and $n_y = m$ (along y-axis) parts to generate a grid with an $n \times m$ rectangular segments. It is assumed that there are r different diameter coefficients (α_i) available for the circular holes, which can be used for finding the diameters using:

$$D_i = \alpha_i h \tag{9. 1}$$

where, h is the minimum dimension of the rectangular segments. For each segment along the x-axis (n_x), the developed GA optimization methodology will try to select one rectangular segment in the vertical direction (n_y) and a diameter coefficient (α_i). Therefore, two optimization strings will be generated: "position string" and "diameter string". The position string consists of n integer numbers with the lower and upper bounds of 1 and m, respectively. Similarly, the diameter string is formed of n integer numbers with the lower and upper bounds of 1 and r. After defining the optimization strings, the developed GA-FE tool will insert the holes with the selected diameters into the selected segments to generate the geometry of the 2D porous stress wave attenuator. Figure 9-2 provides an example for a plate with the width of L_x and height of $\left(\frac{3}{8}\right) L_x$ which is divided into 8 and 3 square segments along the horizontal and vertical directions, respectively. There are four diameter coefficients available for this structure ($r = 4$) and the figure depicts the 2D porous stress wave attenuator with the position string of "1-3-3-1-2-2-1-3" and diameter string of "1-4-4-2-3-1-1-4".

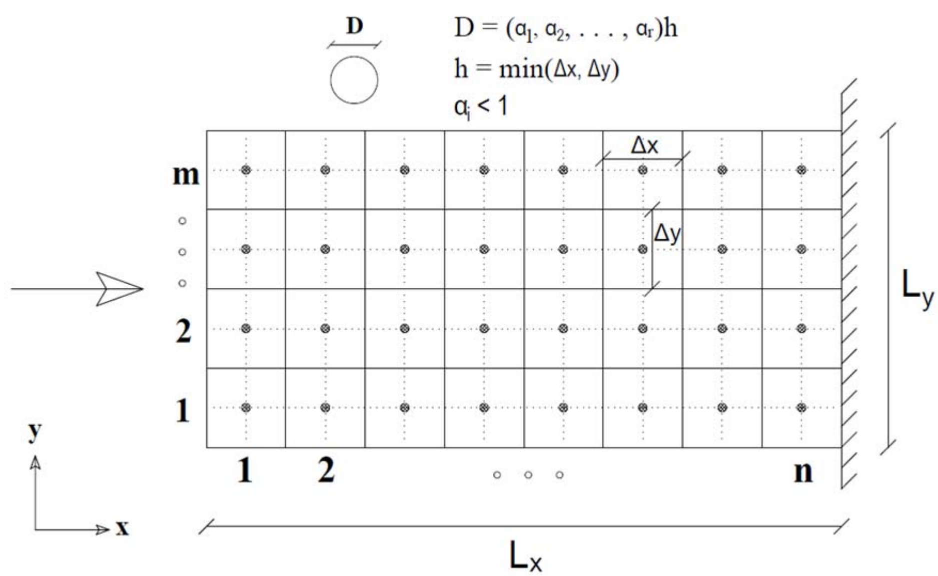

Figure 9-1 Concept of geometry optimization for 2D porous stress wave attenuators

It should be noted that for a plate with $n \times m$ grid and r diameter coefficients, the solution space contains $(m \times r)^n$ combinations and a GA optimization can be performed with $2n$ integer variables with the bounds of $[1, m]$ for the variables 1 to n and $[1, r]$ for the variables $n + 1$ to $2n$. For the example shown in Figure 9-2, the GA optimization should be performed with 16 integer variables. The lower and upper bounds of the first 8 variables are 1 and 3, while for the variables 9 to 16 these bounds are 1 and 4, respectively.

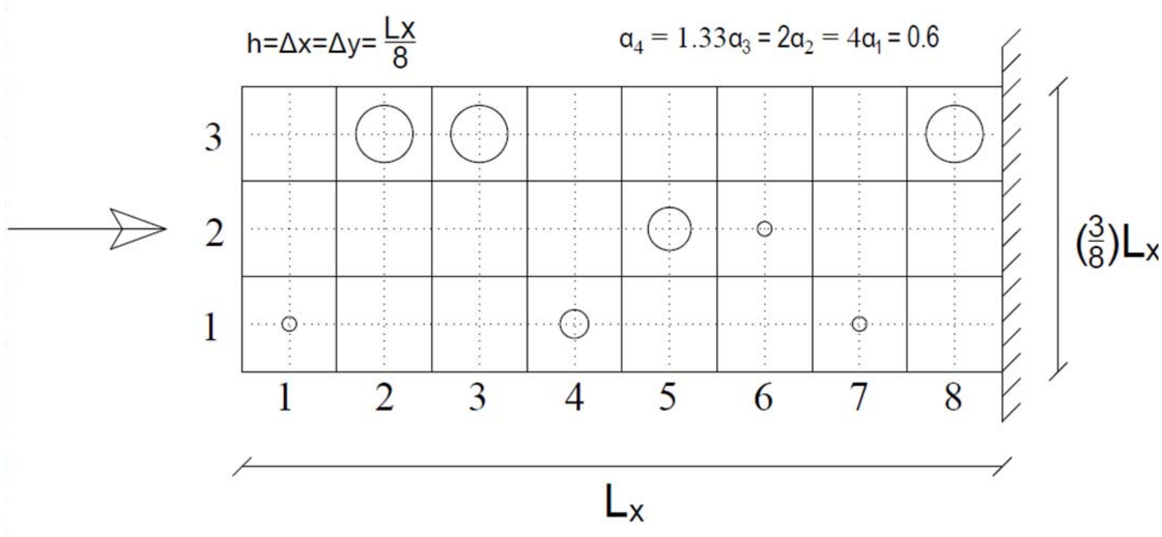

Figure 9-2 Example for geometry optimization of 2D porous stress wave attenuators

In the following sections, the optimal design of the 2D porous stress wave attenuators will be pursued for different grid and diameter numbers. It is assumed that all of the plates are made of Aluminum (with the properties as shown in Table 7.1) with the width (L_x) of 30.48cm (12in), and there are four different values available for the height (L_y) of the plates which are: $L_x/8$, $L_x/4$, $3L_x/8$, and $L_x/2$. In addition, it is assumed that four different diameter coefficients (α_i) are available for the circular holes with the values of 0.15, 0.30, 0.45, and 0.6. The thicknesses of the plates are chosen to be $L_x/190.5 = 0.16cm$, which is small enough to perform plane stress analysis.

For all of the structures, the number of horizontal segments in the optimization zone (n_x) and the number of diameter coefficients are kept to be eight and four, respectively, and optimization is performed for different values of n_y which are changing from 1 to 4. Unlike the non-collinear structures, no exhaustive search is performed for 2D porous stress wave attenuators because the solution spaces are quite large as the optimal design of these structures requires one extra optimization variable in addition to the grid variables, which is the diameter coefficient.

Each structure is subjected to 6 different wavelength ratios (R_λ) ranging from 0.125 to 0.75 with the steps of 0.125. The duration of the half-sine pulses (corresponding to these wavelength ratios) are presented in Table 9-1. These values are calculated by substituting the shear wave speed of Aluminum in Equation 7.1. The shear wave speed in Aluminum is:

$$V_s = \sqrt{\frac{E}{2\rho(1+\vartheta)}} = \sqrt{\frac{68.9E9}{2\times2700\times(1+0.33)}} = 3097.3\,\frac{m}{s}$$

In the following sections the design parameters for 2D porous stress wave attenuators will be introduced, and the optimized configurations for the structures with different values of n_y will be presented in detail.

Table 9-1 Wavelength ratios and duration of the applied pulses on the 2D porous stress wave attenuators

Wavelength ratio (R_λ)	C_s (m/sec)	Duration of the sine pulse (sec)	Duration of the half-sine pulse (sec)
0.125	3097	2.46E-05	1.23E-05
0.250	3097	4.92E-05	2.46E-05
0.375	3097	7.38E-05	3.69E-05
0.500	3097	9.84E-05	4.92E-05
0.625	3097	1.23E-04	6.15E-05
0.750	3097	1.48E-04	7.38E-05

9.3 Design parameters for 2D porous stress wave attenuators

A schematic of a 2D porous stress wave attenuator and its corresponding design parameters are shown in Figure 9-3. The in-plane dimension parameter (R_D) of this structure is h/L. Since the thickness of the plate (out-of-plane dimension) is small comparing to the other dimensions of the plate, plane stress (PS) analysis is performed. Similar to the other stress wave attenuators, the rigidity of the host structure R_{ZB} is assumed to be infinity. As shown in Figure 9-3, this type of stress wave attenuator is not a layered structure; however, the impedance mismatch ratio (R_{ZI}) can be considered as the ratio of the impedance of the circular holes (Z_I) over the impedance of the plate (Z_P), which is zero. As mentioned above, the structures are optimized for 6 different wavelength ratios (R_λ) with the values of 0.125, 0.25, 0.375, 0.5, 0.625, and 0.75.

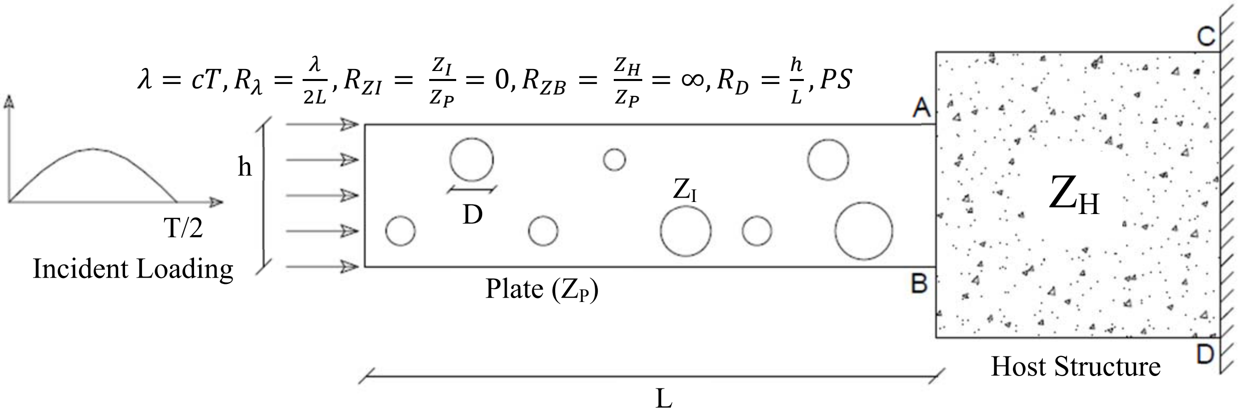

Figure 9-3 Schematic of a 2D porous stress wave attenuator and its design parameters

The general optimization procedure is similar to the non-collinear stress wave attenuators, and integer-valued GA optimization is performed using MATLAB. The fitness function of the GA is calculated by employing the Python Abaqus scripts, and the structures are modeled with 4-node bilinear plane stress quadrilateral elements from the Abaqus element library (element CPS4R).

Thus far, the amount of attenuation that can be achieved by stress wave attenuators was calculated by comparing the maximum amplitude of the force at the boundary with the amplitude of the applied transient load. However, this is not appropriate for 2D porous stress wave attenuators as the amount of the mitigation of the applied load is not significant for the loads with large wavelength ratios. Therefore, to provide a better description of the attenuation capacity of the porous structures, the amount of attenuation is calculated by comparing the maximum force amplitude at the boundary of the optimized structure with the maximum force amplitude at the boundary of a solid plate (with the same dimensions) with no holes:

$$Attenuation\ (\%) = \left(1 - \frac{F_{BO}}{F_{BS}}\right) \times 100 \tag{9. 2}$$

where, F_{BO} and F_{BS} are the maximum amplitude at the boundary of the optimized and solid plates, respectively.

9.4 2D porous stress wave attenuators with $n_y = 1$

The optimization zone for the 2D porous stress wave attenuator with $n_y = 1$ is shown in Figure 9-4. The solution space for this problem is composed of $(1 \times 4)^8 = 65{,}536$ combinations and GA optimization procedure is utilized for the optimal design. In fact, since there is only one segment available in the vertical direction (for each x value), the position string is "1-1-1-1-1-1-1-1" and the diameter string should only be optimized. To do so, an integer-valued GA is performed for each wavelength ratio with 8 integer variables with lower and upper bounds of 1 and 4, respectively. The population size and function tolerance of GA are 100 and 1E-6, respectively.

The optimized diameter string for this structure is composed of eight numbers and it is presented in Table 9-2. Schematics of the optimal designs (with their attenuation capacity) and their corresponding force histories at the boundary are depicted in Figure 9-5 and Figure 9-6, respectively. To provide a better comparison, the force histories at the boundary of a solid plate with similar dimensions are also depicted in Figure 9-6 for each value of R_λ.

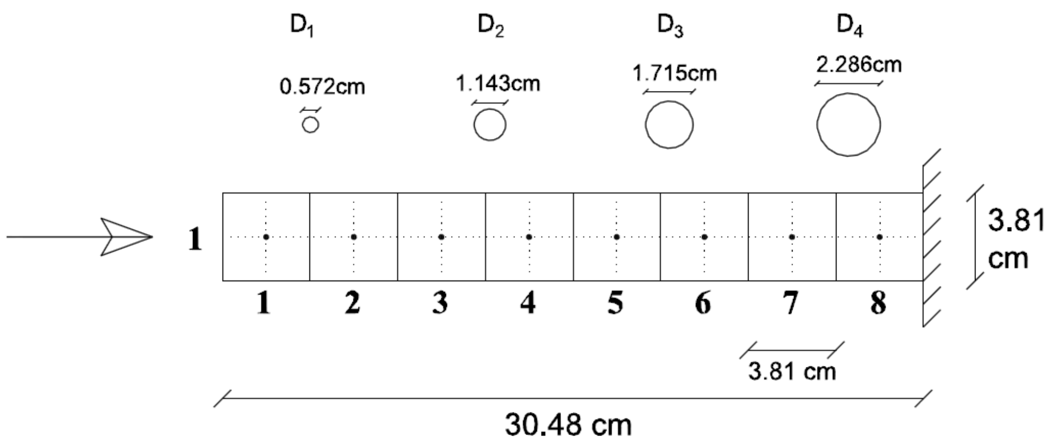

Figure 9-4 Optimization zone for the 2D porous structure with $n_x = 8$, $n_r = 4$, and $n_y = 1$

Table 9-2 Optimized diameter string for the 2D porous structure with $n_y = 1$

R_λ	n_r
0.125	1-1-4-4-2-2-4-4
0.25	1-1-4-4-1-1-4-4
0.375	1-1-4-4-1-1-4-4
0.5	1-1-1-4-1-1-4-4
0.625	1-1-1-4-1-1-4-4
0.75	1-1-1-4-4-4-4-4

The ratio of the amplitude of the boundary force over the amplitude of the applied transient load F_B/F_L is presented in Table 9-3 for different wavelength ratios. Using this table, the amount of attenuation for each optimized structure under the transient loadings with different wavelength ratios are presented in Table 9-4.

Examining Figure 9-5 and Figure 9-6 along with Table 9-4 shows that the results of the GA optimization for the porous structure with $n_y = 1$ can be explained as follows:

- For $R_\lambda = 0.125$, the diameter string (n_r) of the optimized structure is 1-1-4-4-2-2-4-4, and the ratio of the amplitude of the force at the boundary to the amplitude of loading (F_B/F_L) is 0.481. For a solid plate with no holes, the amount of F_B/F_L is 1.409; therefore, the amount of attenuation that can be obtained with this optimized structure is $1 - 0.481/1.409 = 66\%$.
- For $R_\lambda = 0.250$, the diameter string (n_r) of the optimized structure is 1-1-4-4-1-1-4-4, and the amplitude ratio (F_B/F_L) is 0.825. For a similar solid plate F_B/F_L is 2.042, and thus the amount of attenuation is 60%.
- For $R_\lambda = 0.375$, the diameter string is similar to the structure that is optimized for $R_\lambda = 0.250$, which is 1-1-4-4-1-1-4-4. The amplitude ratios of the optimized and solid structures are 1.138 and 2.053, respectively, and the amount of attenuation is 45%.
- For $R_\lambda = 0.5$, the diameter string (n_r) for the optimized structure is 1-1-1-4-1-1-4-4. The values of F_B/F_L for the optimized and solid structures are 1.428 and 2.093, respectively. The amount of attenuation is 32%.
- For $R_\lambda = 0.625$, the diameter string is similar to the structure that is optimized for $R_\lambda = 0.50$, which is 1-1-1-4-1-1-4-4. F_B/F_L values for the optimized and solid plates are 1.524 and 2.022, respectively, which gives an attenuation value of 25%.

- For $R_\lambda = 0.75$, the diameter string (n_r) for the optimized structure is 1-1-1-4-4-4-4-4, and F_B/F_L for the optimized and solid plates are 1.539 and 2.023, respectively. The amount of attenuation for this structure is 24%.

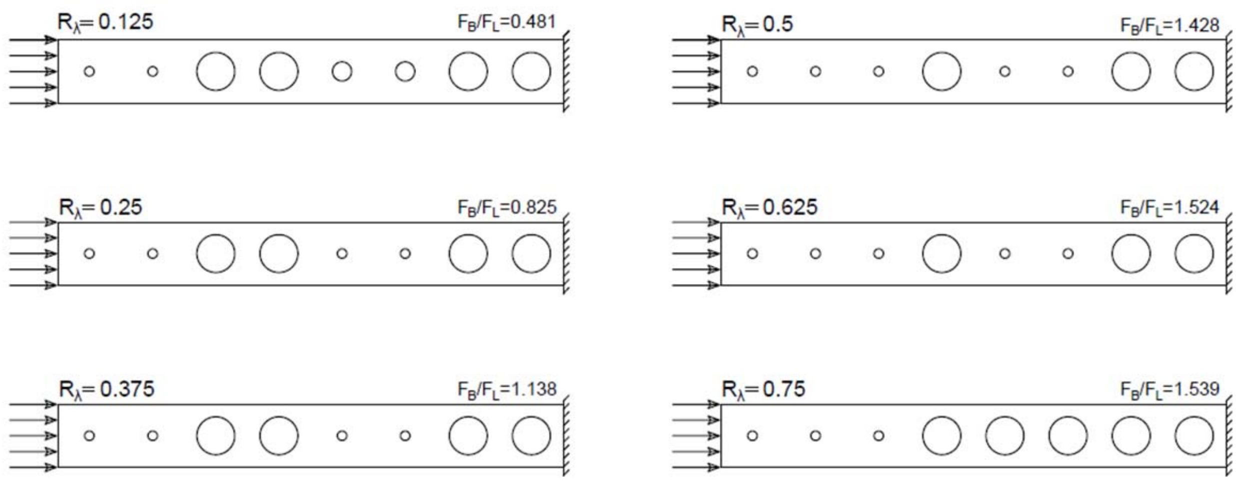

Figure 9-5 Optimal design of the 2D porous stress wave attenuators, $n_y = 1$

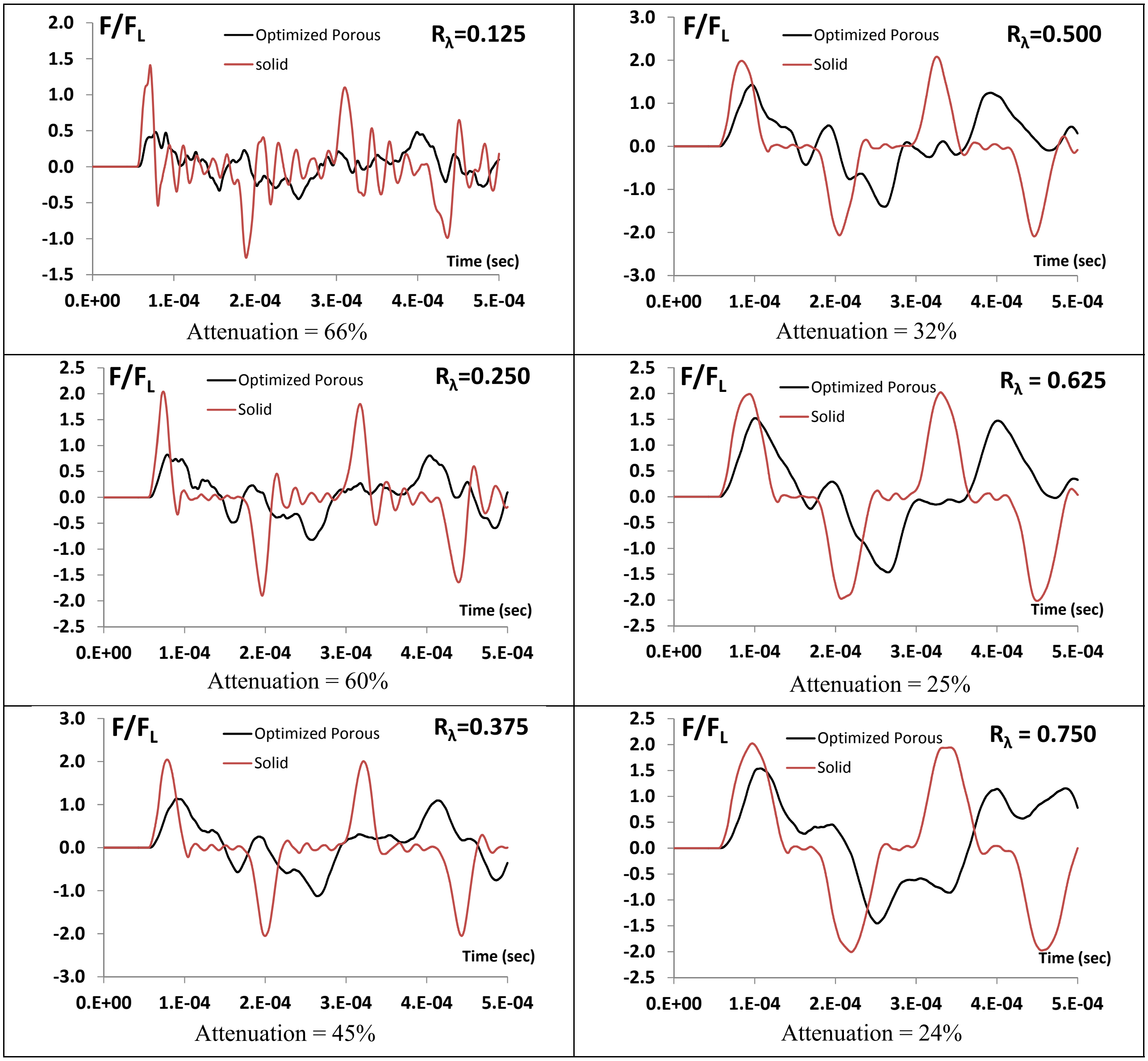

Figure 9-6 Force history at the boundary of the optimized 2D porous structures with $n_y = 1$

The optimization results for the plate with $n_y = 1$ shows that in all of the structures, the first and the last holes have the smallest and largest diameters, respectively. Generally, it can be observed that the holes are repeated in a pattern in which the large holes are preceded by small holes. Moreover, in all of the structures, except the structure that is optimized for $R_\lambda = 0.125$, the holes have the smallest and largest available diameters. These observations are similar to the results that are obtained for the material optimization of the layered structures. In layered structures, it was observed that the optimized structures are generally composed of the materials with lowest and highest impedances, and the materials are usually arranged in a pattern that the wave passes from a high to low impedance medium. For the porous structures, the part of the structure that has a hole with a small diameter is similar to a high impedance material as it behaves more stiffly. For the parts with larger holes, the stiffness is lower and thus the zones with large holes behave similar to the low impedance materials.

Table 9-3 F_B/F_L of the optimized structures for different values of R_λ, 2D porous structure ($n_y = 1$)

F_B/F_L at R_λ	Optimized for R_λ:						Solid plate
	0.125	0.250	0.375	0.500	0.625	0.750	
0.125	0.481	0.513	0.513	0.703	0.703	0.587	1.409
0.250	0.876	0.825	0.825	1.085	1.085	0.872	2.042
0.375	1.188	1.138	1.138	1.324	1.324	1.269	2.053
0.500	1.442	1.43	1.43	1.428	1.428	1.484	2.093
0.625	1.60	1.583	1.583	1.524	1.524	1.559	2.022
0.750	1.70	1.692	1.692	1.642	1.642	1.539	2.023

Table 9-4 Attenuation at the optimized 2D porous structures for different R_λ values, ($n_y = 1$)

Attenuation at R_λ (%)	Optimized for R_λ:					
	0.125	0.250	0.375	0.500	0.625	0.750
0.125	66	64	64	50	50	58
0.250	57	60	60	47	47	57
0.375	42	45	45	36	36	38
0.500	31	32	32	32	32	29
0.625	21	22	22	25	25	23
0.750	16	16	16	19	19	24
Range (%)	16-66	16-64	16-64	19-50	19-50	23-58

Using the attenuation values in Table 9-4, the attenuation-R_λ curve for the porous structure with $n_y = 1$ is plotted in Figure 9-7. The attenuation ranges in Table 9-4 show that the minimum value of attenuation for the structure that is optimized for $R_\lambda = 0.75$ is 23% which is higher than the other structures; therefore, it can be recommended to use the structure with the diameter string of "1-1-1-4-4-4-4-4" for attenuating the loads with the wavelength ratios of 0.125 to 0.75.

The global attenuation range for the structure with $n_y = 1$ is 16 to 66%. The minimum attenuation value (16%) occurs for the structures which are optimized for $R_\lambda = 0.125, 0.25, 0.375$ and are subjected to the load with $R_\lambda = 0.75$, while the maximum attenuation value (66%) relates to the structure that is optimized for $R_\lambda = 0.125$ and is subjected to the transient loading with the same value of R_λ.

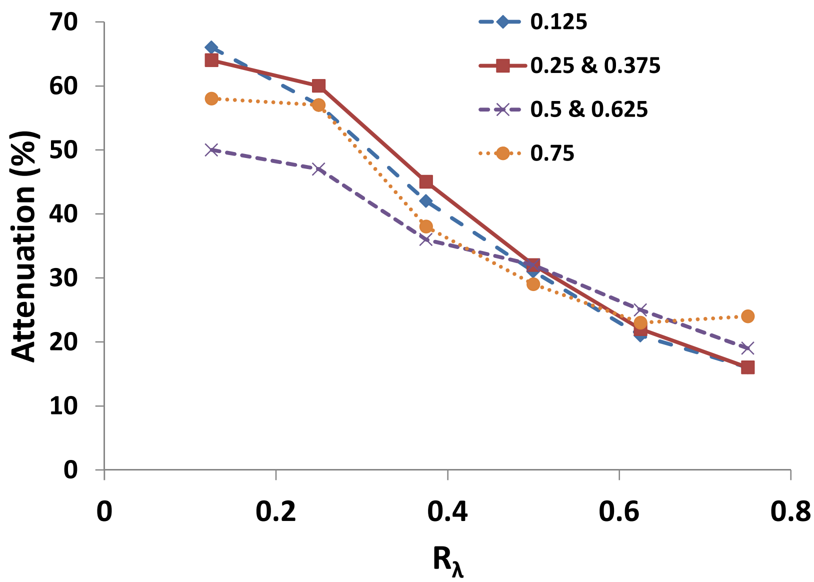

Figure 9-7 Attenuation vs. R_λ, 2D Porous structure with $n_y = 1$

9.5 2D porous stress wave attenuators with $n_y = 2$

The optimization zone for the 2D porous stress wave attenuator with $n_y = 2$ is shown in Figure 9-8. The solution space for this problem is composed of $(2 \times 4)^8 = 16{,}777{,}216$ combinations and GA optimization procedure is utilized for the optimal design. Unlike the structure with $n_y = 1$, both the position and diameter strings should be optimized for the structure with $n_y = 2$. To do so, an integer-valued GA is performed for each wavelength ratio with 16 integer variables. The first 8 variables are related to the position of the holes, and since there are only two vertical positions available at each n_x, the lower and upper bounds are 1 and 2, respectively. Variables 9 to 16 are related to the diameter of the holes and their lower and upper bounds are 1 and 4. Similar to the previous case, the population size and function tolerance of GA are 100 and 1E-6, respectively.

The optimized position and diameter strings for this structure are presented in Table 9-5. Schematic of the optimal designs and their corresponding force histories at the boundary are depicted in Figure 9-9 and Figure 9-10. To provide a better understanding of the behavior, the force histories at the boundary of a solid plate with similar dimensions are also depicted in Figure 9-10 for each value of R_λ. The values of F_B/F_L and amount of attenuation at each porous plate are presented in Table 9-6 and Table 9-7.

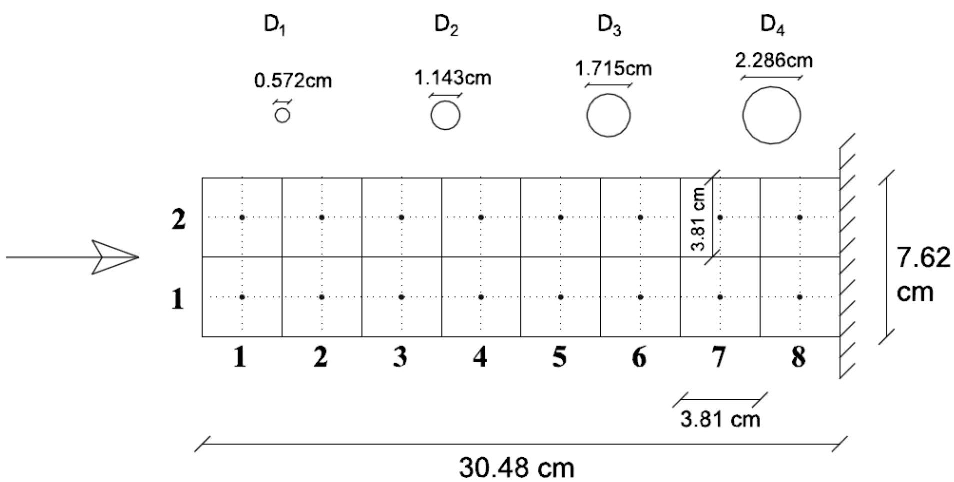

Figure 9-8 Optimization zone for the porous structure with $n_x = 8$, $n_r = 4$, and $n_y = 2$

Table 9-5 Optimized position and diameter string for the 2D porous structure with $n_y = 2$

R_λ	n_y	n_r
0.125	1-1-2-1-2-2-2-1	1-4-4-4-4-4-4-4
0.25	1-1-2-1-2-1-2-1	1-1-4-4-4-3-4-4
0.375	1-1-1-2-2-1-1-2	1-1-4-4-4-4-4-4
0.5	1-1-1-1-2-2-2-1	1-1-4-4-4-4-4-4
0.625	1-2-2-1-1-2-2-1	1-1-1-4-4-4-4-4
0.75	2-2-2-2-2-1-2-1	1-1-1-4-1-4-4-4

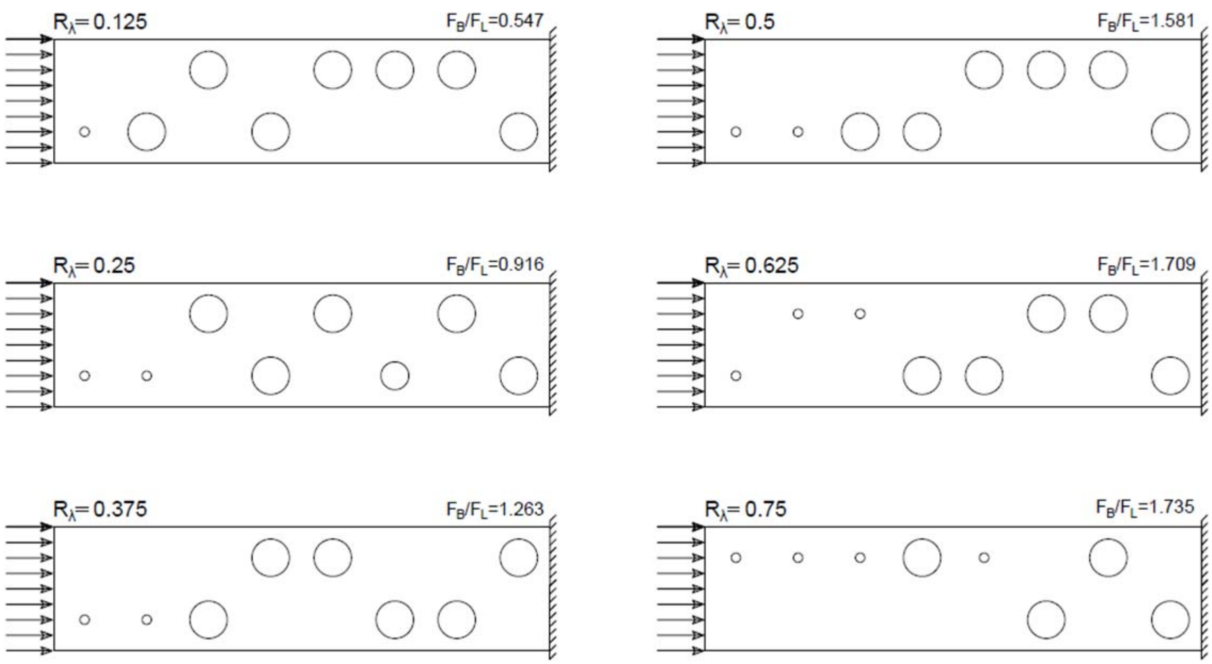

Figure 9-9 Optimal design of the 2D porous stress wave attenuators, $n_y = 2$

According to Figure 9-9 and Figure 9-10, Table 9-6 and Table 9-7, the results of the GA optimization for the porous structure with $n_y = 2$ can be explained as follows:

- For $R_\lambda = 0.125$, the position (n_y) and diameter (n_r) strings for the optimized structure are 1-1-2-1-2-2-2-1 and 1-4-4-4-4-4-4-4, respectively. The ratio of the amplitude of the force at the boundary to the amplitude of the loading (F_B/F_L) is 0.547. For a solid plate with no holes, the amount of F_B/F_L is 1.232; therefore, the amount of attenuation that can be obtained with the optimized structure is $1 - 0.547/1.232 = 56\%$.

- For $R_\lambda = 0.250$, the position (n_y) and diameter (n_r) strings for the optimized structure are 1-1-2-1-2-1-2-1 and 1-1-4-4-4-3-4-4, respectively. The amplitude ratio (F_B/F_L) for the optimized and solid structures and the amount of attenuation are 0.916, 1.516, and 40%, respectively.
- For $R_\lambda = 0.375$, the position (n_y) and diameter (n_r) strings for the optimized structure are 1-1-1-2-2-1-1-2 and 1-1-4-4-4-4-4-4, respectively. The amplitude ratio (F_B/F_L) for the optimized and solid structures and the amount of attenuation are 1.263, 1.930, and 35%, respectively.
- For $R_\lambda = 0.5$, the position (n_y) and diameter (n_r) strings for the optimized structure are 1-1-1-1-2-2-2-1 and 1-1-4-4-4-4-4-4, respectively. The amplitude ratio (F_B/F_L) for the optimized and solid structures and the amount of attenuation are 1.581, 2.109, and 25%, respectively.
- For $R_\lambda = 0.625$, the position (n_y) and diameter (n_r) strings for the optimized structure are 1-2-2-1-1-2-2-1 and 1-1-1-4-4-4-4-4, respectively. The amplitude ratio (F_B/F_L) for the optimized and solid structures and the amount of attenuation are 1.709, 2.083, and 18%, respectively.
- For $R_\lambda = 0.75$, the position (n_y) and diameter (n_r) strings for the optimized structure are 2-2-2-2-2-1-2-1 and 1-1-1-4-1-4-4-4, respectively. The amplitude ratio (F_B/F_L) for the optimized and solid structures and the amount of attenuation are 1.735, 2.108, and 18%, respectively.

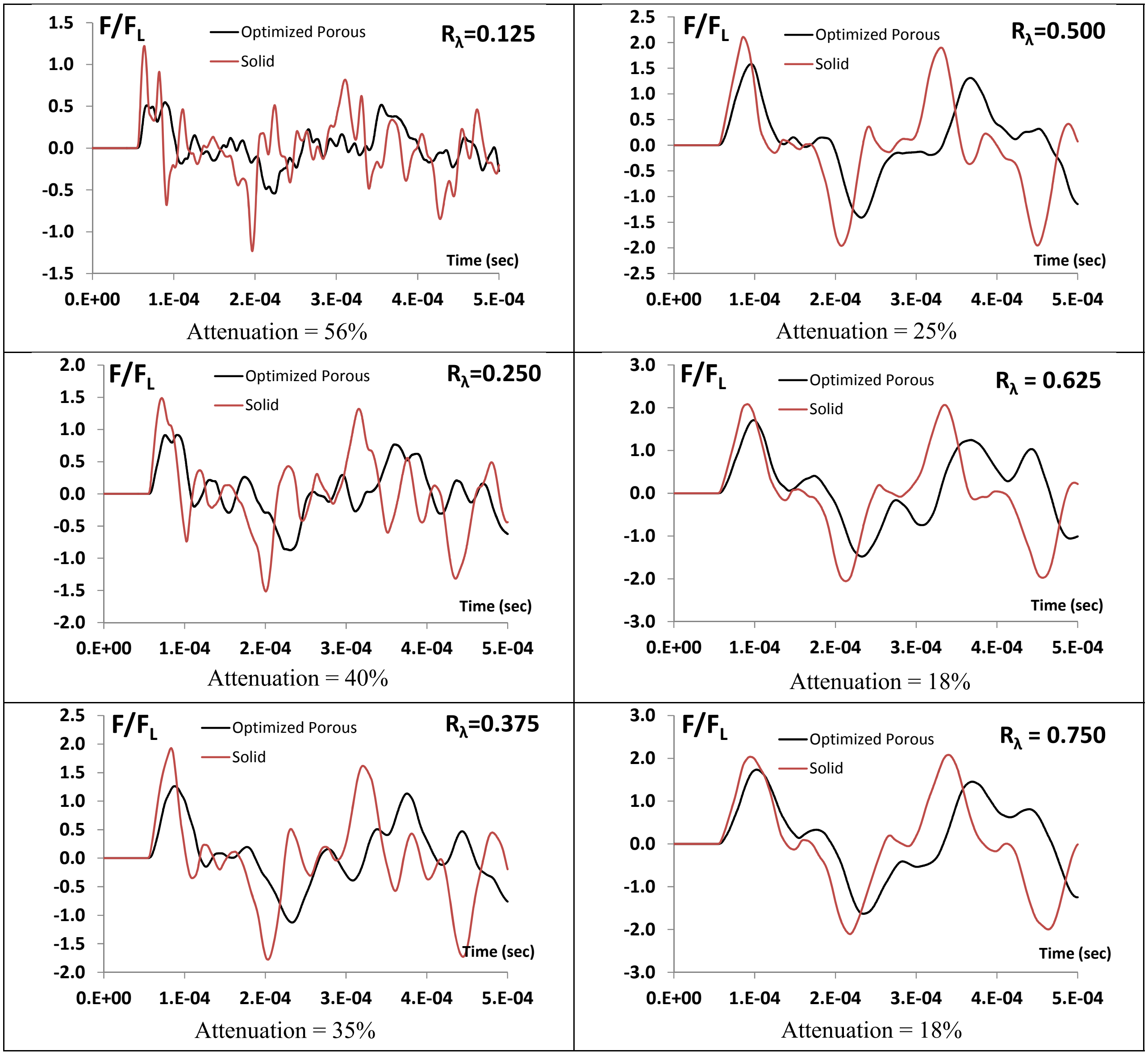

Figure 9-10 Force history at the boundary of the optimized 2D porous structures with $n_y = 2$

Similar to the structure with $n_y = 1$, it can be observed that the first and last holes of the optimized structures with $n_y = 2$ have the smallest and largest diameters. In addition, all of the optimized structures (except the structure which is optimized for $R_\lambda = 0.25$) contain the holes with the smallest and largest diameters.

Table 9-6 F_B/F_L of the optimized structures for different values of R_λ, 2D porous structure ($n_y = 2$)

F_B/F_L at R_λ	Optimized for R_λ:						Solid plate
	0.125	0.250	0.375	0.500	0.625	0.750	
0.125	0.547	0.606	0.589	0.643	0.666	0.668	1.232
0.250	0.994	0.916	0.984	1.047	1.059	1.021	1.516
0.375	1.366	1.345	1.263	1.294	1.325	1.397	1.930
0.500	1.718	1.656	1.579	1.581	1.585	1.630	2.109
0.625	1.890	1.779	1.742	1.739	1.709	1.718	2.083
0.750	1.953	1.828	1.804	1.781	1.735	1.735	2.108

Table 9-7 Attenuation at the optimized 2D porous structures for different R_λ values, ($n_y = 2$)

Attenuation at R_λ (%)	Optimized for R_λ:					
	0.125	0.250	0.375	0.500	0.625	0.750
0.125	56	51	52	48	46	46
0.250	34	40	35	31	30	33
0.375	29	30	35	33	31	28
0.500	19	21	25	25	25	23
0.625	9	15	16	17	18	18
0.750	7	13	14	16	18	18
Range (%)	7-56	13-51	14-52	16-48	18-46	18-46

The attenuation-R_λ curve for the porous structure with $n_y = 2$ is plotted in Figure 9-11. This figure and the attenuation ranges in Table 9-7 show that the minimum value of attenuation for the structure that is optimized for $R_\lambda = 0.625$ and 0.75 is 18% which is higher than the other structures; therefore, for the structure with $n_y = 2$, it can be recommended to use the optimized structures for $R_\lambda = 0.625$ and 0.75 for attenuating the loads with the wavelength ratios of 0.125 to 0.75.

The global attenuation range for the structure with $n_y = 2$ is 7-56%. The minimum attenuation value (7%) occurs at the structure which is optimized for $R_\lambda = 0.125$ and is subjected to the loading with $R_\lambda = 0.75$, while the maximum attenuation value (56%) happens for the structure that is optimized for $R_\lambda = 0.125$ and is subjected to the loading with the same value of R_λ.

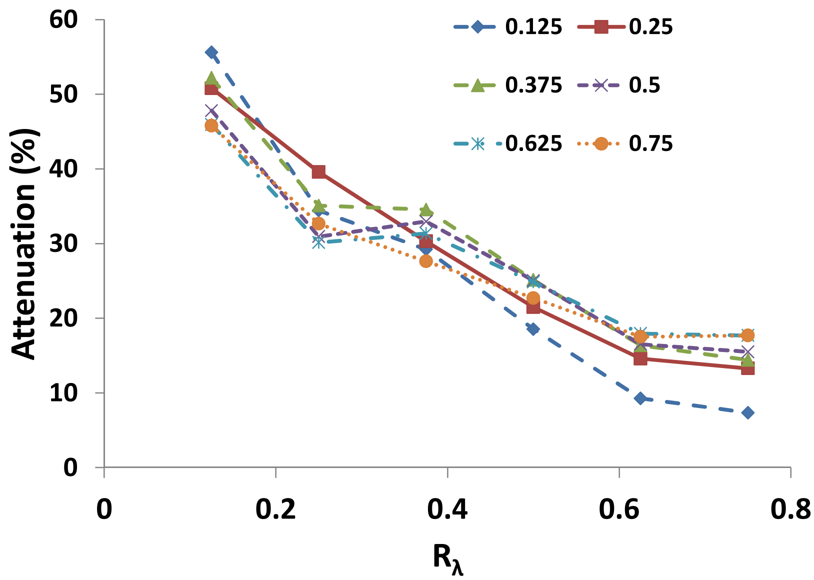

Figure 9-11 Attenuation vs. R_λ, 2D Porous structure with $n_y = 2$

9.6 2D porous stress wave attenuators with $\mathbf{n_y = 3}$

The optimization zone for the 2D porous stress wave attenuator with $n_y = 3$ is shown in Figure 9-12. The solution space for this problem is composed of $(3 \times 4)^8 = 429{,}981{,}696$ combinations and the GA optimization procedure is utilized for the optimal design. Similar to the structure with $n_y = 2$, an integer-valued GA is performed for each wavelength ratio with 16 integer variables. The first eight variables, which represent the position of the holes, have the lower and upper bound values of 1 and 3, respectively. Variables 9 to 16 are related to the diameter of the holes and their lower and upper bounds are 1 and 4. Similar to the previous case, the population size and function tolerance of GA are 100 and 1E-6, respectively.

The optimized position and diameter strings for this structure are presented in Table 9-8. Schematics of the optimal designs (with their attenuation capacity) and their corresponding force histories at the boundary are depicted in Figure 9-13 and Figure 9-14, respectively. To provide a better comparison, the force histories at the boundary of a solid plate with similar dimensions are also depicted in Figure 9-14 for each value of R_λ. The values of F_B/F_L and amount of attenuation for each porous plate are presented in Table 9-9 and Table 9-10.

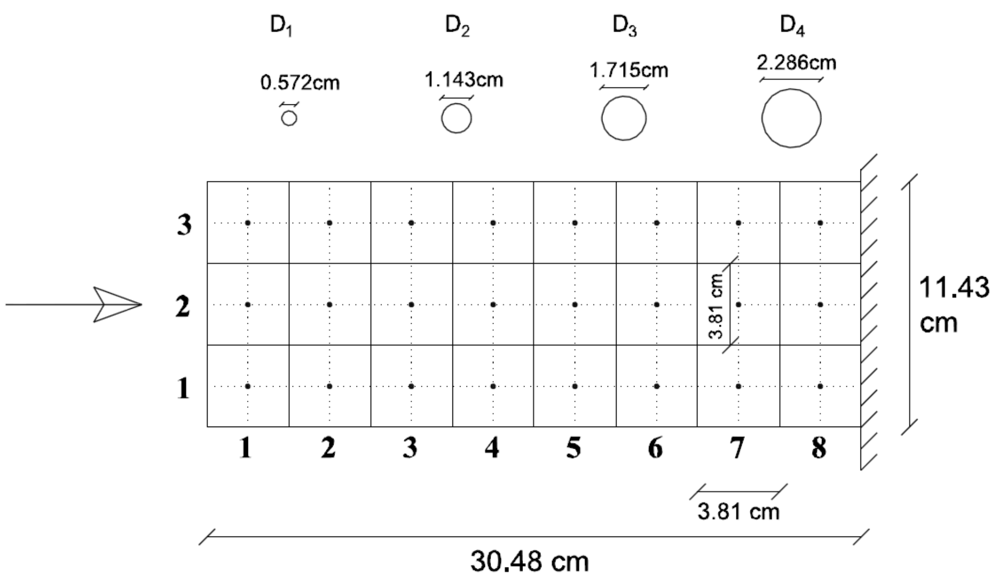

Figure 9-12 Optimization zone for the porous structure with $n_x = 8$, $n_r = 4$, and $n_y = 3$

Table 9-8 Optimized position and diameter string for the 2D porous structure with $n_y = 3$

R_λ	n_y	n_r
0.125	3-2-3-1-3-1-2-3	4-4-4-4-4-4-4-4
0.25	2-1-3-3-1-3-1-3	1-4-1-4-4-4-4-4
0.375	2-1-1-2-1-3-2-1	1-1-4-4-4-4-4-4
0.5	3-2-3-2-1-2-3-1	1-1-1-4-4-4-4-4
0.625	1-2-2-3-2-1-2-3	1-1-4-4-4-4-4-4
0.75	1-1-2-2-2-1-2-3	1-1-1-4-4-4-4-4

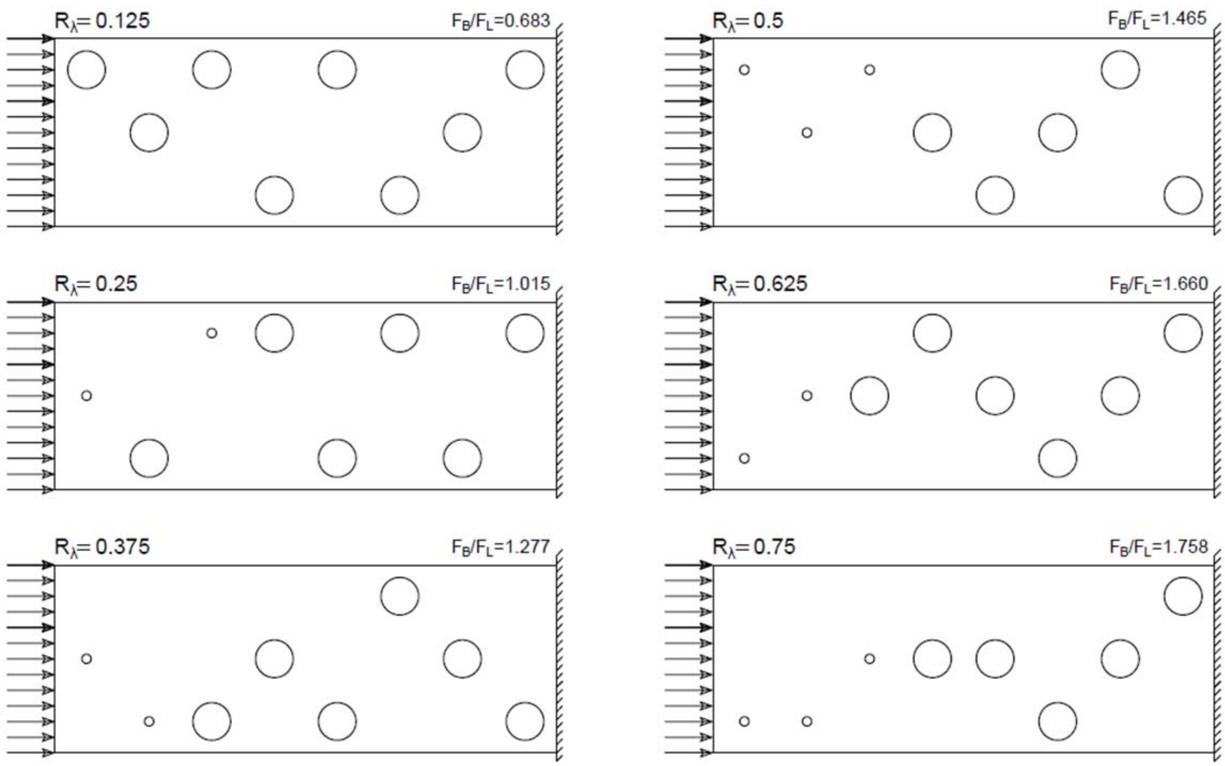

Figure 9-13 Optimal design of the 2D porous stress wave attenuators, $n_y = 3$

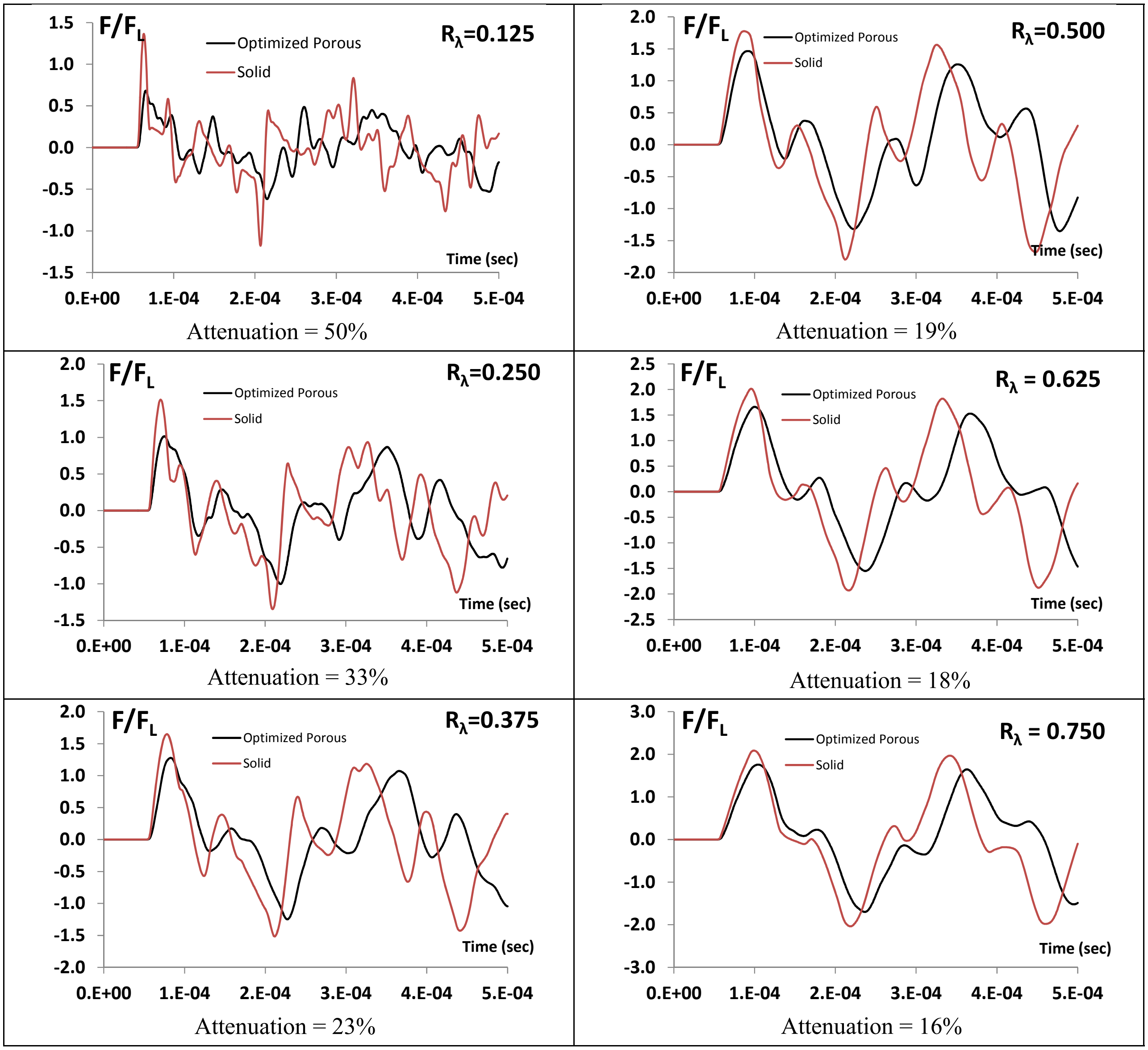

Figure 9-14 Force history at the boundary of the optimized 2D porous structures with $n_y = 3$

According to Figure 9-13, Figure 9-14, Table 9-9 and Table 9-10, the results of the GA optimization for the porous structure with $n_y = 3$ can be explained as follows:

- For $R_\lambda = 0.125$, the position (n_y) and diameter (n_r) strings for the optimized structure are 3-2-3-1-3-1-2-3 and 4-4-4-4-4-4-4-4, respectively. The ratio of the amplitude of the force at the boundary to the amplitude of the loading (F_B/F_L) is 0.683. For a solid plate with no holes, the amount of F_B/F_L is 1.364; therefore, the amount of attenuation that can be obtained with the optimized structure is $1 - 0.683/1.364 = 50\%$.

- For $R_\lambda = 0.250$, the position (n_y) and diameter (n_r) strings for the optimized structure are 2-1-3-3-1-3-1-3 and 1-4-1-4-4-4-4-4, respectively. The amplitude ratio (F_B/F_L) for the optimized and solid structures and the amount of attenuation are 1.015, 1.514, and 33%, respectively.
- For $R_\lambda = 0.375$, the position (n_y) and diameter (n_r) strings for the optimized structure are 2-1-1-2-1-3-2-1 and 1-1-4-4-4-4-4-4, respectively. The amplitude ratio (F_B/F_L) for the optimized and solid structures and the amount of attenuation are 1.277, 1.649, and 23%, respectively.
- For $R_\lambda = 0.5$, the position (n_y) and diameter (n_r) strings for the optimized structure are 3-2-3-2-1-2-3-1 and 1-1-1-4-4-4-4-4, respectively. The amplitude ratio (F_B/F_L) for the optimized and solid structures and the amount of attenuation are 1.465, 1.798, and 19%, respectively.
- For $R_\lambda = 0.625$, the position (n_y) and diameter (n_r) strings for the optimized structure are 1-2-2-3-2-1-2-3 and 1-1-4-4-4-4-4-4, respectively. The amplitude ratio (F_B/F_L) for the optimized and solid structures and the amount of attenuation are 1.660, 2.015, and 18%, respectively.
- For $R_\lambda = 0.75$, the position (n_y) and diameter (n_r) strings for the optimized structure are 1-1-2-2-2-1-2-3 and 1-1-1-4-4-4-4-4, respectively. The amplitude ratio (F_B/F_L) for the optimized and solid structures and the amount of attenuation are 1.758, 2.087, and 16%, respectively.

The results show that similar to the structures with $n_y = 1$ and $n_y = 2$, the optimized structures are mainly composed of the holes with the smallest and largest diameters except for the structure that is optimized for $R_\lambda = 0.125$, which only contains the holes with large diameters. It can also be observed that the first hole has a smallest diameter, while the last hole has the largest possible dimension.

Table 9-9 F_B/F_L of the optimized structures for different values of R_λ, 2D porous structure ($n_y = 3$)

F_B/F_L at R_λ	Optimized for R_λ:						Solid plate
	0.125	0.250	0.375	0.500	0.625	0.750	
0.125	0.683	0.782	0.790	0.880	0.813	0.923	1.364
0.250	1.112	1.015	1.128	1.197	1.185	1.293	1.514
0.375	1.418	1.423	1.277	1.323	1.293	1.359	1.649
0.500	1.677	1.686	1.506	1.465	1.460	1.500	1.798
0.625	1.898	1.892	1.714	1.706	1.660	1.667	2.015
0.750	2.000	1.969	1.826	1.844	1.798	1.758	2.087

Table 9-10 Attenuation at the optimized 2D porous structures for different R_λ values, ($n_y = 3$)

Attenuation at R_λ (%)	Optimized for R_λ:					
	0.125	0.250	0.375	0.500	0.625	0.750
0.125	50	43	42	35	40	32
0.250	27	33	25	21	22	15
0.375	14	14	23	20	22	18
0.500	7	6	16	19	19	17
0.625	6	6	15	15	18	17
0.750	4	6	13	12	14	16
Range (%)	4-50	6-43	13-42	12-35	14-40	16-32

The attenuation-R_λ curve for the porous structure with $n_y = 3$ is plotted in Figure 9-15. This figure and the attenuation ranges in Table 9-10 show that the minimum value of attenuation for the structure that is optimized for $R_\lambda = 0.75$ is 16% which is higher than the other structures; therefore, for the structure with $n_y = 3$, it can be recommended to use the structure with the position string of 1-1-2-2-2-1-2-3 and diameter string of 1-1-1-4-4-4-4-4 for attenuating the loadings with the wavelength ratios of 0.125 to 0.75.

The global attenuation range for the structure with $n_y = 3$ is 4 to 50%. The minimum attenuation value (4%) occurs for the structure which is optimized for $R_\lambda = 0.125$ and is subjected to the transient loading with $R_\lambda = 0.75$, while the maximum attenuation value (50%) happens at the structure that is optimized for $R_\lambda = 0.125$ and is subjected to the loading with the same value of R_λ.

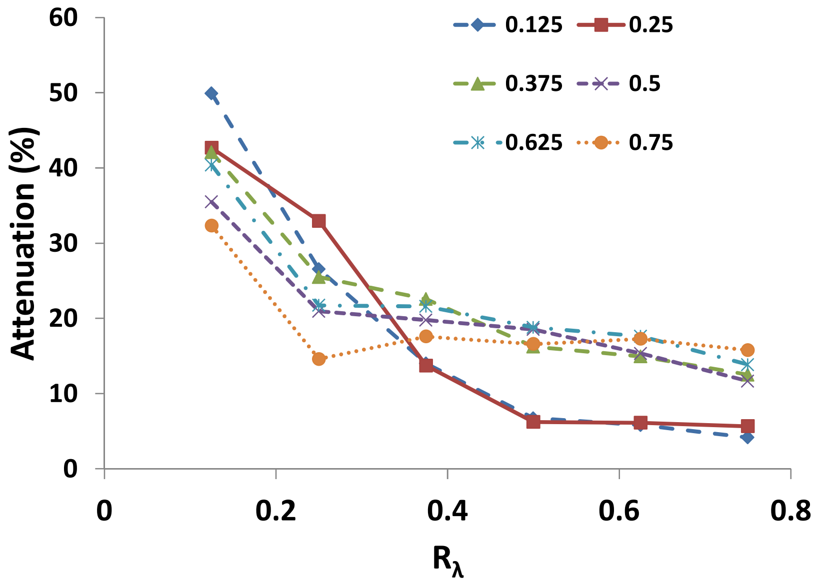

Figure 9-15 Attenuation vs. R_λ, 2D Porous structure with $n_y = 3$

9.7 2D porous stress wave attenuators with $n_y = 4$

The optimization zone for the 2D porous stress wave attenuator with $n_y = 4$ is shown in Figure 9-16. The solution space for this problem is composed of $(4 \times 4)^8 = 4{,}294{,}967{,}296$ combinations and GA optimization procedure is utilized for the optimal design. An integer-valued GA is performed for each wavelength ratio with 16 integer variables. The first eight variables which represent the position of the holes have the lower and upper bound values of 1 and 4, respectively. Variables 9 to 16 are related to the diameter of the holes and their lower and upper bounds are 1 and 4. Similar to the previous cases, the population size and function tolerance of GA are 100 and 1E-6, respectively.

The optimized position and diameter strings for this structure are presented in Table 9-11. Schematics of the optimal designs (with their attenuation capacity) and their corresponding force histories at the boundary are depicted in Figure 9-17 and Figure 9-18, respectively. To provide a better comparison, the force histories at the boundary of a solid plate with similar dimensions are also depicted in Figure 9-18 for each value of R_λ. The values of F_B/F_L and amount of attenuation at each porous plate are presented in Table 9-12 and Table 9-13.

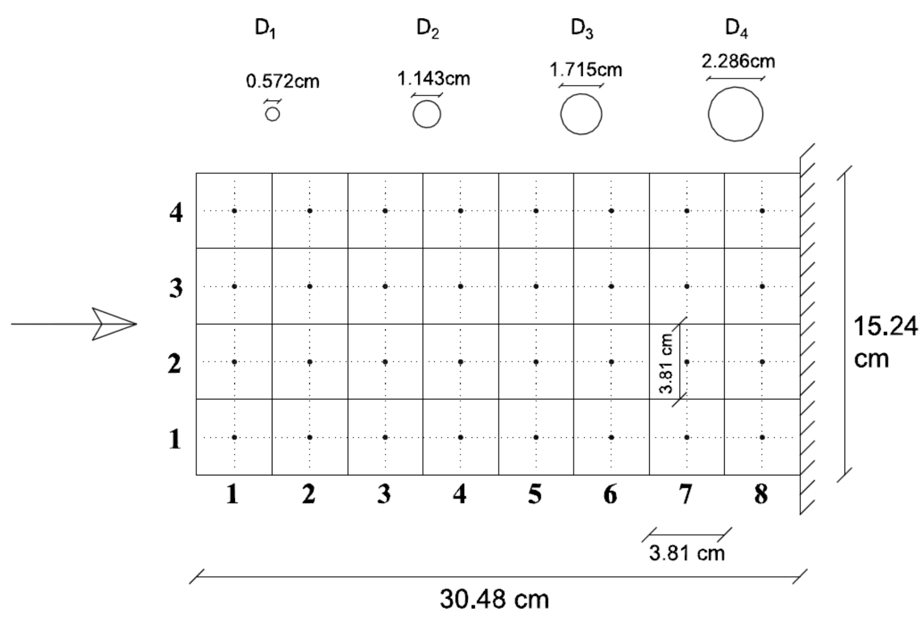

Figure 9-16 Optimization zone for the porous structure with $n_x = 8$, $n_r = 4$, and $n_y = 4$

Table 9-11 Optimized position and diameter string for the 2D porous structure with $n_y = 4$

R_λ	n_y	n_r
0.125	1-2-1-2-4-1-2-4	4-4-4-4-4-4-4-4
0.25	4-1-4-1-4-1-4-1	1-4-4-4-4-4-4-4
0.375	2-1-1-4-2-1-4-1	1-1-4-4-4-4-4-4
0.5	2-2-1-2-3-2-3-1	1-1-4-4-4-4-4-4
0.625	4-2-2-3-2-3-2-1	1-1-4-4-4-4-4-4
0.75	2-3-2-3-2-1-3-4	1-1-4-4-4-4-4-4

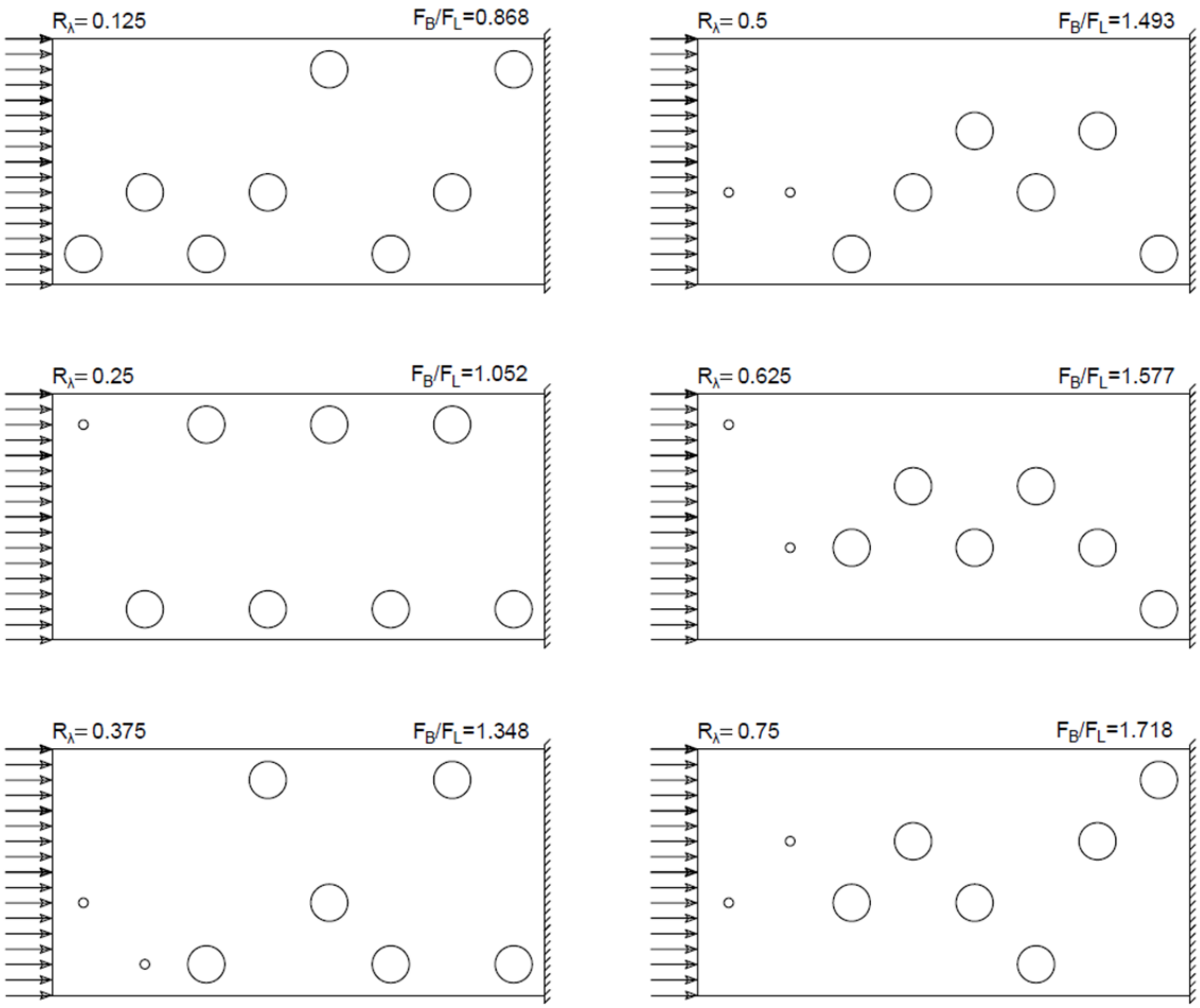

Figure 9-17 Optimal design of the 2D porous stress wave attenuators, $n_y = 4$

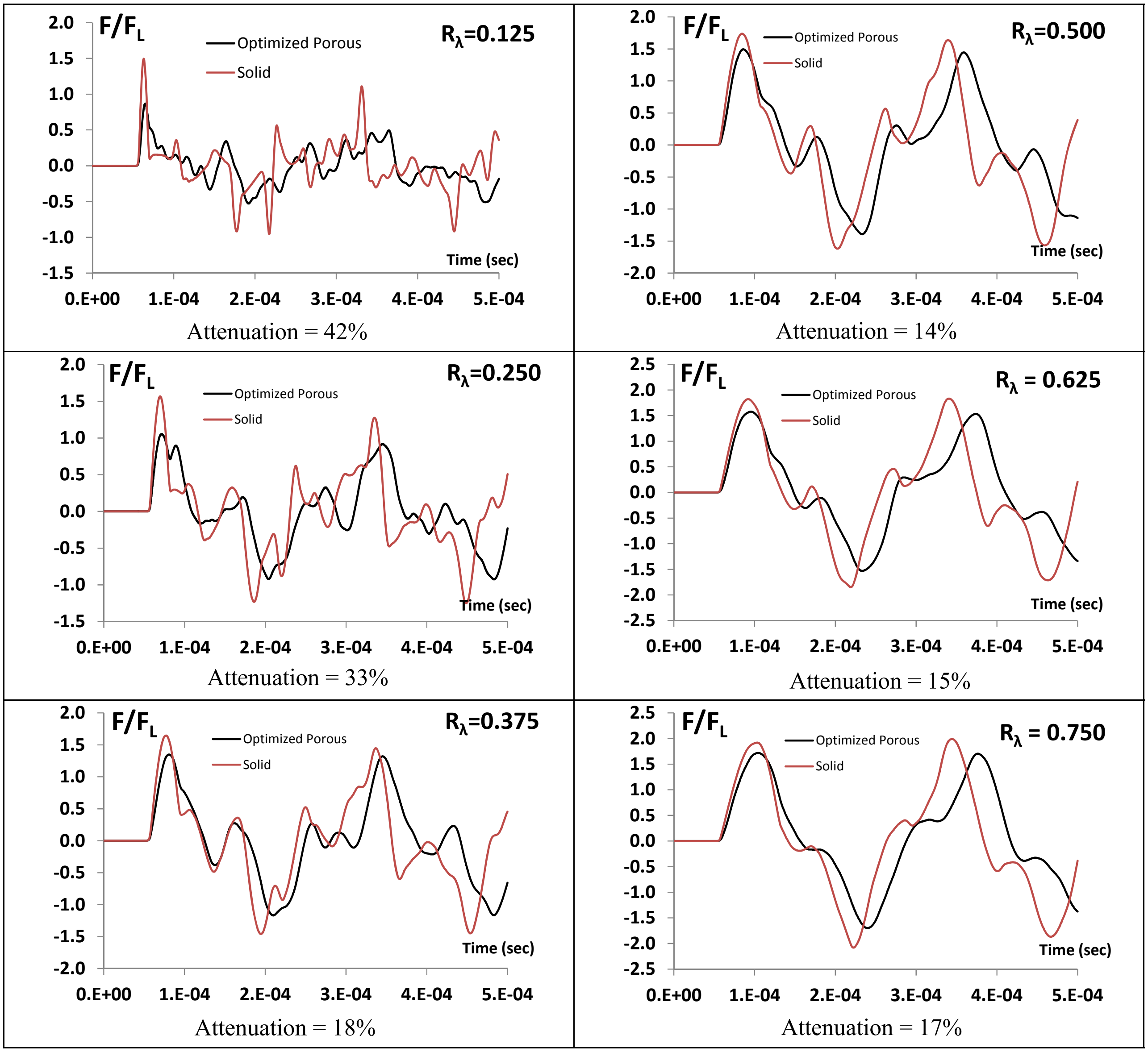

Figure 9-18 Force history at the boundary of the optimized 2D porous structures with $n_y = 4$

According to Figure 9-17, Figure 9-18, Table 9-12 and Table 9-13, the results of the GA optimization for the porous structure with $n_y = 4$ can be explained as follows:

- For $R_\lambda = 0.125$, the position (n_y) and diameter (n_r) strings for the optimized structure are 1-2-1-2-4-1-2-4and 4-4-4-4-4-4-4-4, respectively. The ratio of the amplitude of the force at the boundary to the amplitude of the loading (F_B/F_L) is 0.868. For a solid plate with no holes, the amount of F_B/F_L is 1.494; therefore, the amount of attenuation that can be obtained with the optimized structure is $1 - 0.868/1.494 = 42\%$.

- For $R_\lambda = 0.250$, the position (n_y) and diameter (n_r) strings for the optimized structure are 4-1-4-1-4-1-4-1 and 1-4-4-4-4-4-4-4, respectively. The amplitude ratio (F_B/F_L) for the optimized and solid structures and the amount of attenuation are 1.052, 1.567, and 33%, respectively.
- For $R_\lambda = 0.375$, the position (n_y) and diameter (n_r) strings for the optimized structure are 2-1-1-4-2-1-4-1 and 1-1-4-4-4-4-4-4, respectively. The amplitude ratio (F_B/F_L) for the optimized and solid structures and the amount of attenuation are 1.348, 1.647, and 18%, respectively.
- For $R_\lambda = 0.5$ the position (n_y) and diameter (n_r) strings for the optimized structure are 2-2-1-2-3-2-3-1 and 1-1-4-4-4-4-4-4, respectively. The amplitude ratio (F_B/F_L) for the optimized and solid structures and the amount of attenuation are 1.493, 1.737, and 14%, respectively.
- For $R_\lambda = 0.625$ the position (n_y) and diameter (n_r) strings for the optimized structure are 4-2-2-3-2-3-2-1 and 1-1-4-4-4-4-4-4, respectively. The amplitude ratio (F_B/F_L) for the optimized and solid structures and the amount of attenuation are 1.577, 1.849, and 15%, respectively.
- For $R_\lambda = 0.75$ the position (n_y) and diameter (n_r) strings for the optimized structure are 2-3-2-3-2-1-3-4 and 1-1-4-4-4-4-4-4, respectively. The amplitude ratio (F_B/F_L) for the optimized and solid structures and the amount of attenuation are 1.718, 2.080, and 17%, respectively.

Table 9-12 F_B/F_L of the optimized structures for different values of R_λ, 2D porous structure ($n_y = 4$)

F_B/F_L at R_λ	Optimized for R_λ:						Solid plate
	0.125	0.250	0.375	0.500	0.625	0.750	
0.125	0.868	0.904	0.972	1.023	1.045	1.010	1.494
0.250	1.249	1.052	1.163	1.358	1.440	1.365	1.567
0.375	1.472	1.405	1.348	1.425	1.488	1.432	1.647
0.500	1.648	1.725	1.578	1.493	1.522	1.536	1.737
0.625	1.767	1.880	1.762	1.636	1.577	1.639	1.849
0.750	1.912	1.979	1.927	1.851	1.770	1.718	2.080

Table 9-13 Attenuation at the optimized 2D porous structures for different R_λ values, ($n_y = 4$)

Attenuation at R_λ (%)	Optimized for R_λ:					
	0.125	0.250	0.375	0.500	0.625	0.750
0.125	42	39	35	32	30	32
0.250	20	33	26	13	8	13
0.375	11	15	18	13	10	13
0.500	5	1	9	14	12	12
0.625	4	-2	5	12	15	11
0.750	8	5	7	11	15	17
Range (%)	4-42	-2-39	5-35	11-32	8-30	11-32

The attenuation-R_λ curve for the porous structure with $n_y = 4$ is plotted in Figure 9-19. This figure and the attenuation ranges in Table 9-13 show that the minimum value of attenuation for the structure that is optimized for $R_\lambda = 0.5$ and 0.75 is 11% which is higher than the other structures; therefore, for the structure with $n_y = 4$, it can be recommended to use the optimized structures for $R_\lambda = 0.5$ and 0.75 for attenuating the loads with the wavelength ratios of 0.125 to 0.75.

The global attenuation range for the structure with $n_y = 4$ is -2 to 42%. The minimum attenuation value (-2%) occurs for the structures which is optimized for $R_\lambda = 0.25$ and is subjected to the load with $R_\lambda = 0.625$, while the maximum attenuation value (42%) relates to the structure that is optimized for $R_\lambda = 0.125$ and is subjected to the load with the same value of R_λ.

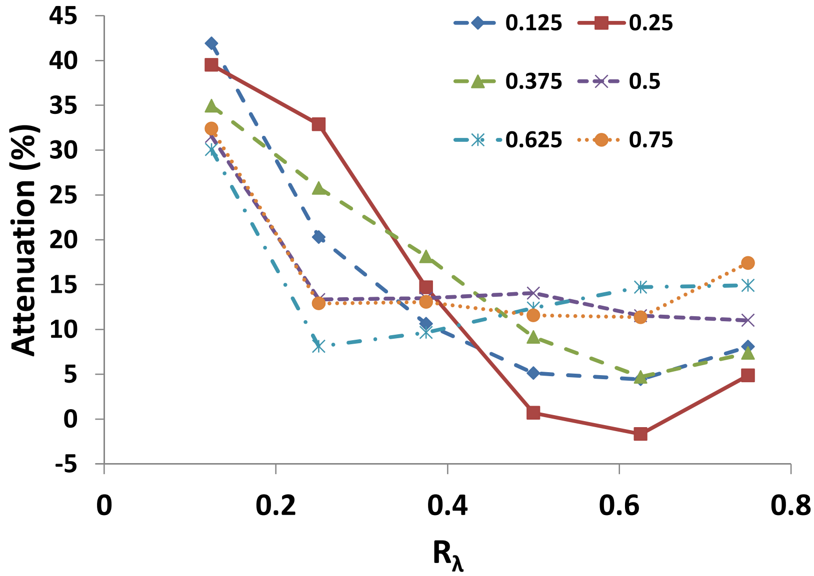

Figure 9-19 Attenuation vs. R_λ, 2D Porous structure with $n_y = 4$

9.8 Effect of n_y on the attenuation capacity

The global attenuation range for the 2D porous stress wave attenuators with different values of n_y are presented in Table 9-14. The numbers show that the attenuation capacity decreases by increasing n_y, which reveals that the porous plates with small values of width/height ratios are more effective stress wave attenuators. In fact, this behavior was predictable because all of the plates have a constant number (eight) of circular holes; therefore, the ratio of the volume (area) of the holes to the volume of the plates decreases by increasing the dimensions of the plates. Consequently, the amount of attenuation dwindles in larger plates as the discontinuities occupy a smaller portion of the structure and they cannot affect the waves significantly.

Table 9-14 Global attenuation range for different n_y values, 2D porous stress wave attenuators

n_y	1	2	3	4
Attenuation range (%)	16 to 66	7 to 56	4 to 50	-2 to 42

9.9 2D porous stress wave attenuators with $\mathbf{n_y = 4, n_r = 1}$

To explore the efficiency of the porous plates further, the optimal design of a plate with $n_y = 4$ is investigated when there is only one dimension available for the diameter of the holes, i.e. $n_r = 1$. The optimization zone for this structure is shown in Figure 9-20.The global search space for this problem has $(4 \times 1)^8 = 65{,}536$ combinations and an integer-valued GA optimization (with 8 variables with the values between 1 and 4) is performed with the population size and tolerance function of 100 and 1E-6, respectively. The position string, schematic of the optimal designs, and the stress history at the boundaries are presented in Table 9-15, Figure 9-21, and Figure 9-22.

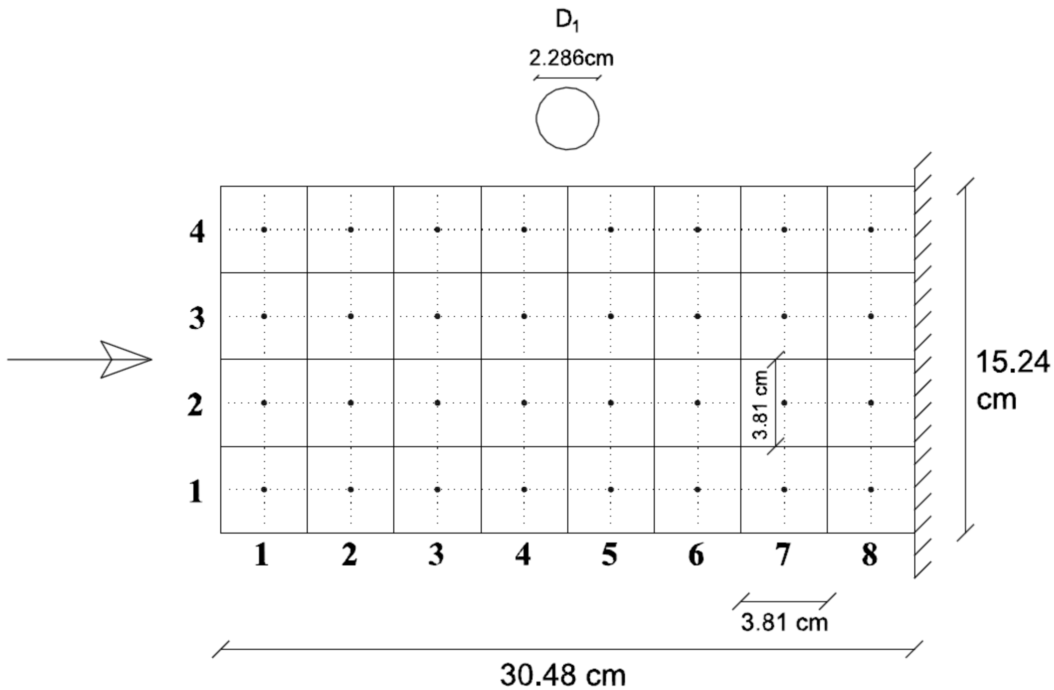

Figure 9-20 Optimization zone for the porous structure with $n_x = 8, n_r = 1$, and $n_y = 4$

Table 9-15 Optimized position and diameter string for the 2D porous structure with $n_y = 4$ and $n_r = 1$

R_λ	n_y
0.125	4-3-4-1-4-3-4-1
0.25	1-4-1-4-1-4-1-4
0.375	3-4-1-4-1-4-3-4
0.5	3-4-3-2-4-3-2-4
0.625	3-2-3-2-3-2-3-4
0.75	1-2-3-2-3-4-2-1

The results of the optimization show that the position of the holes are significantly dependent on the value of wavelength ratio (R_λ). For example, in the optimal design for $R_\lambda = 0.25$, all of the holes are located at the bottom and top of the plate (the position string is 1-4-1-4-1-4-1-4) while for $R_\lambda = 0.625$ all of the holes (except the last hole) are located in positions 2 and 3, which are in the middle of the plate. For $R_\lambda = 0.125$, we can observe that there is no hole in the second position. Moreover, the position string of 4-3-4-1 is repeated twice for this structure. There is no special repeating pattern for $R_\lambda = 0.375, 0.5$, and 0.75, and there is no hole in positions 2 and 1 for the optimal design of the structures with $R_\lambda = 0.375$, and 0.5, respectively. By comparing the attenuation values of the structure with $n_y = 4$ and $n_r = 1$ with the structure with $n_y = 4$ and $n_r = 4$, it can be observed that the structure with $n_y = 4$ and $n_r = 4$ has slightly higher attenuation capacity (about 2-3% except for $R_\lambda = 0.125$ which has lower attenuation capacity). Therefore, it can be concluded that it is better to have a combination of small and large holes for optimizing the porous plates. Another important issue which should be noted is that the size of the solution space for these two structures is completely different (compare 65,536 with 4,294,967,296). This means the likelihood of a better existing solution for the structure with $n_y = 4$ and $n_r = 4$ is much higher than the structure with $n_y = 4$ and $n_r = 1$ due to having a very large solution space. Therefore, it can be concluded that the structures with different diameter dimensions have higher attenuation potentials.

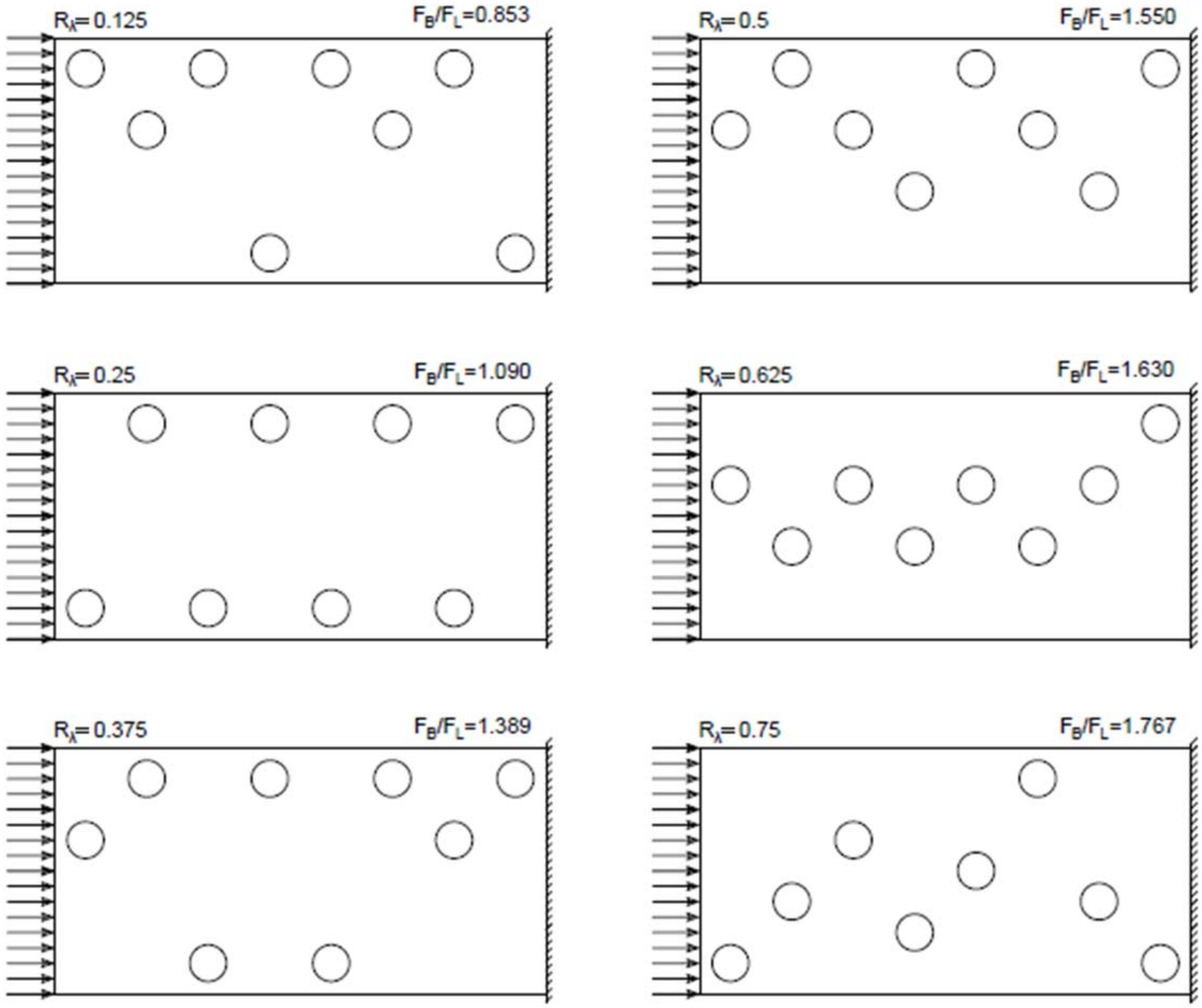

Figure 9-21 Optimal design of the 2D porous stress wave attenuators, $n_y = 4$, $n_r = 1$

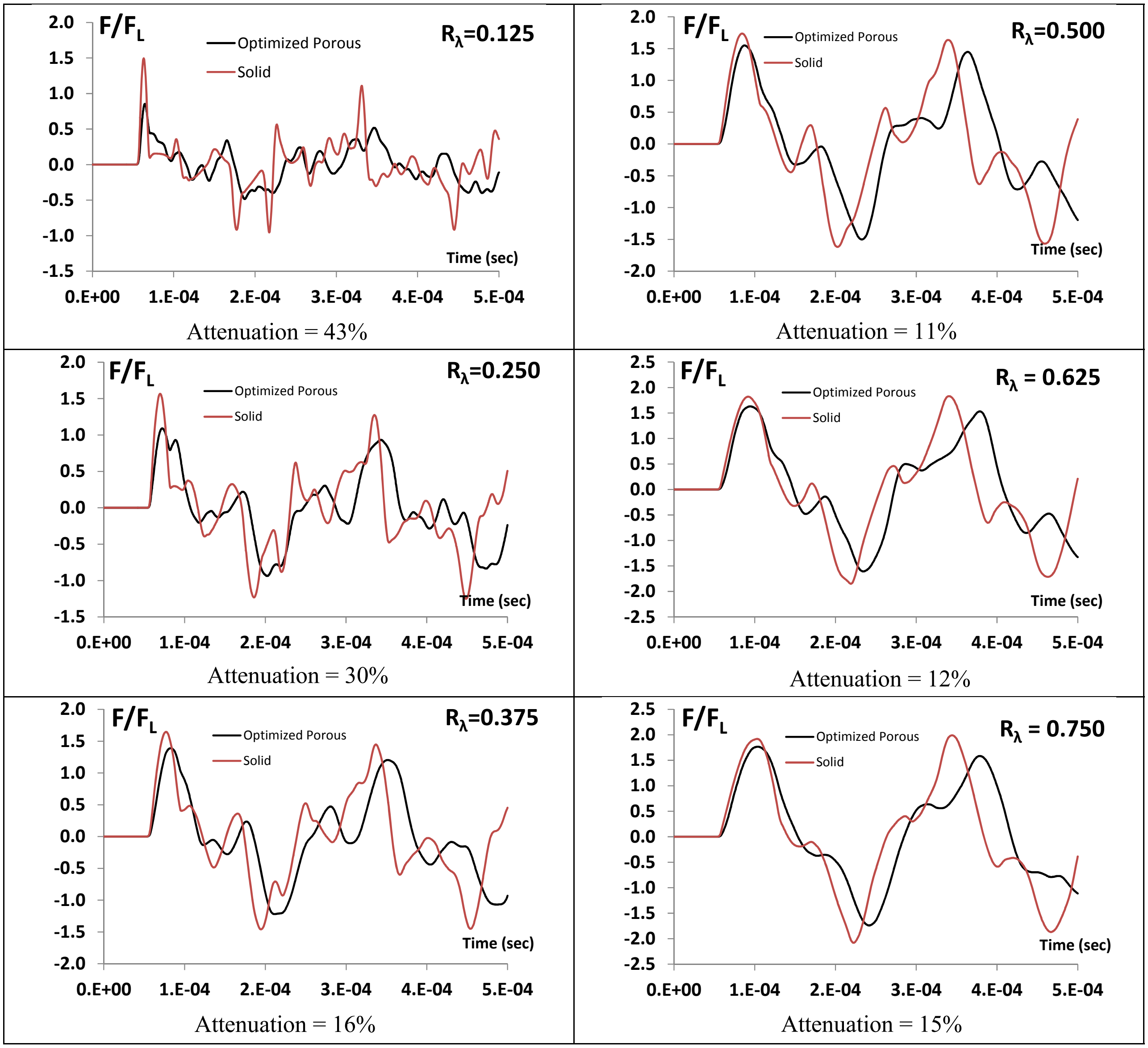

Figure 9-22 Force history at the boundary of the optimized 2D porous structures with $n_y = 4$, $n_r = 1$

Table 9-16 F_B/F_L of the optimized structures for different values of R_λ, 2D porous structure ($n_y = 4, n_r = 1$)

F_B/F_L at R_λ	Optimized for R_λ:						Solid plate
	0.125	0.250	0.375	0.500	0.625	0.750	
0.125	0.853	0.875	0.910	0.945	0.994	0.933	1.494
0.250	1.181	1.090	1.188	1.366	1.510	1.398	1.567
0.375	1.456	1.482	1.388	1.461	1.590	1.539	1.647
0.500	1.671	1.792	1.701	1.550	1.615	1.631	1.737
0.625	1.814	1.927	1.880	1.738	1.631	1.701	1.849
0.750	2.019	2.020	1.974	1.891	1.851	1.767	2.080

Table 9-17 Amount of attenuation of the optimized structures for different values of R_λ, 2D porous structure ($n_y = 4, n_r = 1$)

Attenuation at R_λ (%)	Optimized for R_λ:					
	0.125	0.250	0.375	0.500	0.625	0.750
0.125	43	41	39	37	33	38
0.250	25	30	24	13	4	11
0.375	12	10	16	11	3	7
0.500	4	-3	2	11	7	6
0.625	2	-4	-2	6	12	8
0.750	3	3	5	9	11	15
Range (%)	2-43	-4-41	-2-39	6-37	3-33	6-38

The attenuation-R_λ curve for the porous structure with $n_y = 4$ and $n_r = 1$ is plotted in Figure 9-23. This figure and the attenuation ranges in Figure 9-16 show that the minimum value of attenuation for the structure that is optimized for $R_\lambda = 0.5$ and 0.75 is 6%, which is higher than the other structures; therefore, for the structure with $n_y = 4$ and $n_r = 1$, it can be recommended to use the optimized structures for $R_\lambda = 0.5$ and 0.75 for attenuating the loads with the wavelength ratios of 0.125 to 0.75.

The global attenuation range for the structure with $n_y = 4$ and $n_r = 1$ is -4 to 43%. The minimum attenuation value (-4%) occurs for the structures which is optimized for $R_\lambda = 0.25$ and is subjected to the load with $R_\lambda = 0.625$, while the maximum attenuation value (43%) relates to the structure that is optimized for $R_\lambda = 0.125$ and is subjected to the load with the same value of R_λ.

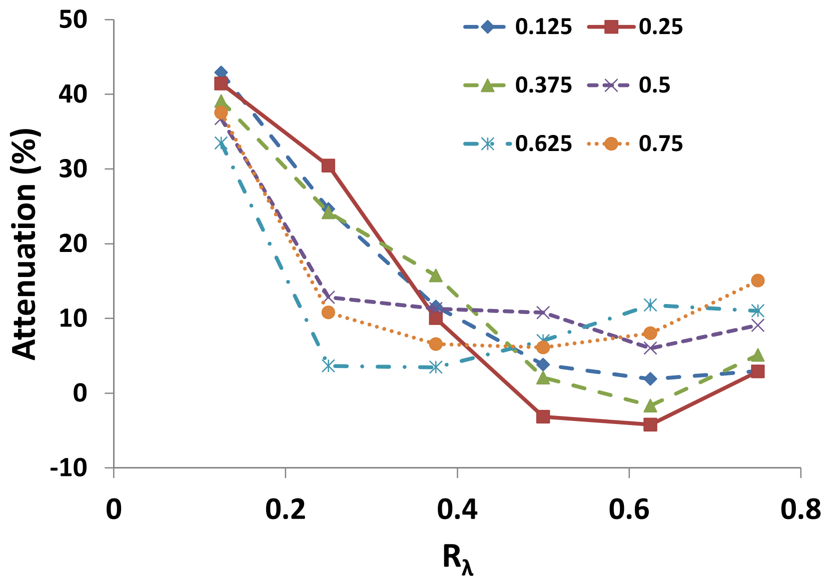

Figure 9-23 Attenuation vs. R_λ, 2D Porous structure with $n_y = 4$

9.10 Verifying the coupled GA-FE optimization methodology using exhaustive search

To evaluate the performance of the developed coupled GA-FE optimization methodology, an exhaustive search is performed for the porous structure with $n_y = 4$ and $n_r = 1$. The solution space for this structure is small (it has 65,536 combinations) compared to the other structures and it is feasible to perform an exhaustive search. The results of the exhaustive search are presented in Table 9-18 and Figure 9-24. By comparing these results with the GA optimization results in Table 9-15 and Figure 9-21, it is obvious that the developed GA-FE tool generates very close results to the exhaustive search.

For $R_\lambda = 0.125$, the position strings for GA and exhaustive search results are "4-3-4-1-4-3-4-1" and "1-2-1-4-1-2-1-4", respectively, which are exactly the same if we consider the symmetry of the patterns (replace 4 with 1 and 3 with 2 and vice versa). The same thing is true for $R_\lambda = 0.25, 0.375$ and the results are exactly the same. For $R_\lambda = 0.5$, the optimized position string from GA is 3-4-3-2-4-3-2-4, which has a symmetric string of 2-1-2-3-1-2-3-1. The position string from the exhaustive search for $R_\lambda = 0.5$ is 2-1-3-2-1-2-3-1, which means that the position of third and fourth holes are different than the GA result. However, the amounts of F_B/F_L in both of these structures are very close to each other, and the GA optimized structure has a very close behavior to the best solution. For $R_\lambda = 0.625$, the exhaustive search and GA results are exactly the same. For $R_\lambda = 0.75$ the results of the GA and exhaustive search are quite different; however, the value of F_B/F_L are very close to each other (compare 1.767 with 1.760). This means that the GA has converged to a satisfactory solution although it is not the best, which is not unexpected due to the nature of the heuristic algorithms.

Although the performance of the developed GA-FE methodology is verified for a problem that has a small solution space (because it is not feasible to do exhaustive search for larger problems); however, as the optimization results exactly generate the best available solution (except for $R_\lambda = 0.5$ and 0.75), it can be concluded that this coupled GA-FE optimization methodology is appropriate for optimal design of the stress wave attenuators.

Table 9-18 Position and diameter string for the 2D porous structure with $n_y = 4$ and $n_r = 1$ from the exhaustive search

R_λ	n_y
0.125	1-2-1-4-1-2-1-4
0.25	4-1-4-1-4-1-4-1
0.375	2-1-4-1-4-1-2-1
0.5	2-1-3-2-1-2-3-1
0.625	3-2-3-2-3-2-3-4
0.75	4-2-2-3-3-3-2-1

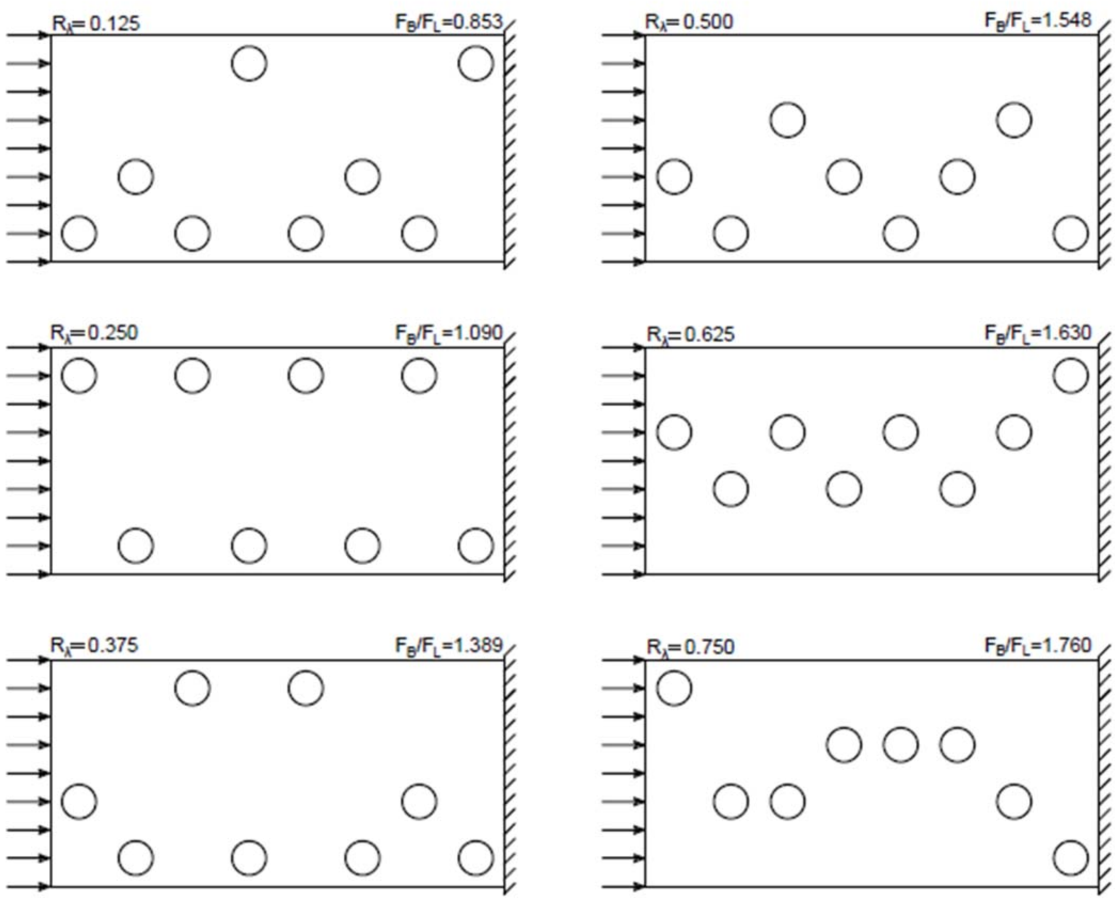

Figure 9-24 Exhaustive search results for 2D porous stress wave attenuators with $n_y = 4$ and $n_r = 1$

9.11 Summary

The optimal design of the 2D porous stress wave attenuators was studied in this section. The optimization was performed for the structures with different numbers of holes in the vertical direction (n_y) and different numbers of dimensions for the diameter of the holes (n_r). It was observed that the optimized stress wave attenuators are usually composed of the holes with the smallest and largest diameters, and the holes are usually arranged in a pattern in which the small holes are located close to the loading surface while the large holes are neighboring the fixed boundary. In addition, in the majority of the optimal designs, the first and the last holes have the minimum and maximum diameters. These observations are similar to the results that are found for the layered stress wave attenuators if we presume that the zones with small and large holes are similar to the high and low impedance materials, respectively.

At the end of the section, an exhaustive search was performed to verify the performance of the developed GA-FE optimization methodology. The comparison of the GA results with the exhaustive search revealed that this optimization methodology works very well for these types of problems, and the results are very close to the best solutions.

SECTION 10
INTERFACE PROFILE OPTIMIZATION FOR STRESS WAVE ATTENUATION IN BI-LAYERED PLATES

10.1 Introduction

Most of the research on wave propagation in layered structures has focused on the effect of impedance mismatch between the layers and the way that the change in the material properties occur, i.e., graded or abrupt. This means that the major parameter, which is explored in the literature, is the material effect. For this reason, many of these studies are based on one-dimensional wave propagation, even in two-dimensional structures, such as plates. In fact, in many practical applications, the structures have more than one dimension and their wave propagation behavior depends on their geometric specifications in addition to their material properties. For layered systems, the geometric properties can be attributed to the global shape of the structure and the interface profile between the layers. By changing the geometry of the interface profile between the layers, the wave propagation characteristics and the attenuation capacity of the layered structures can be altered.

This section investigates the effect of the interface profile between two media in layered structures and illustrates the development of a methodology for optimizing the shape of this profile for the objective of stress wave attenuation in finite bi-layered plates.

10.2 Theory and background

Discontinuity in material and geometric properties leads to wave scattering in elastic media. The general case of wave scattering happens for an incident wave at an oblique angle associated with the interface of two different materials, as shown in Figure 10-1. The two materials can be solid, fluid, vacuum, or any other combination. The continuity in displacement and stress at an interface results in wave scattering through reflection and transmission in two media at different angles. Solids can sustain both dilatational and shear waves, and each one of these waves generates dilatational plus shear waves at an interface. Thus, for dilatational and shear wave incident on an interface at an oblique angle, eight new waves will be generated, as shown in Figure 10-1. However, in fluids and vacuum, fewer waves will be generated because shear waves do not travel in non-viscous fluids, and longitudinal and shear waves do not propagate in vacuum.

Figure 10-1 shows the scattering of stress waves at the interface of two solid materials. In this figure, I_D and I_S represent displacement amplitudes of incident dilatational and shear waves and R_{D-S}, R_{D-D}, T_{D-S} and T_{D-D} correspond to the displacement amplitude of reflected shear, reflected dilatational, transmitted shear, and transmitted dilatational waves for a dilatation incident wave (I_D), respectively. Similar notations are used for a shear incident wave (I_S) by converting the first index from D to S, i.e., R_{S-S}, R_{S-D}, T_{S-S} and T_{S-D}.

The direction of reflected and transmitted waves is governed by Snell's law (Auld (1973)), which can be expressed for incident dilatational and shear waves using Eq. (10.1) and (10.2) as follows:

$$\frac{sin(\theta_{D-I})}{c_{D1}} = \frac{sin(\theta_{D-SR})}{c_{S1}} = \frac{sin(\theta_{D-DR})}{c_{D1}} = \frac{sin(\theta_{D-ST})}{c_{S2}} = \frac{sin(\theta_{D-DT})}{c_{D2}} \tag{10.1}$$

$$\frac{sin(\theta_{S-I})}{c_{S1}} = \frac{sin(\theta_{S-SR})}{c_{S1}} = \frac{sin(\theta_{S-DR})}{c_{D1}} = \frac{sin(\theta_{S-ST})}{c_{S2}} = \frac{sin(\theta_{S-DT})}{c_{D2}} \tag{10.2}$$

where, $D-I$ and $\mathrm{S}-I$ represent the dilatational and shear incident waves. Here, $D-SR$, $D-DR$, $D-ST$, and $D-DT$ represent shear reflected, dilatational reflected, shear transmitted, and dilatational transmitted waves that are generated from a dilatational incident wave, respectively (see Figure 10-1a). Similarly, $S-SR$, $S-DR$, $S-ST$, and $S-DT$ represent shear reflected, dilatational reflected, shear transmitted, and dilatational transmitted waves that are generated from a shear incident wave, respectively (see Figure 10-1b). Furthermore, c_{D1}, c_{D2}, c_{S1}, and c_{S2} are the dilatational wave velocity in material 1, dilatational wave velocity in material 2, shear wave velocity in material 1, and shear wave velocity in material 2, respectively.

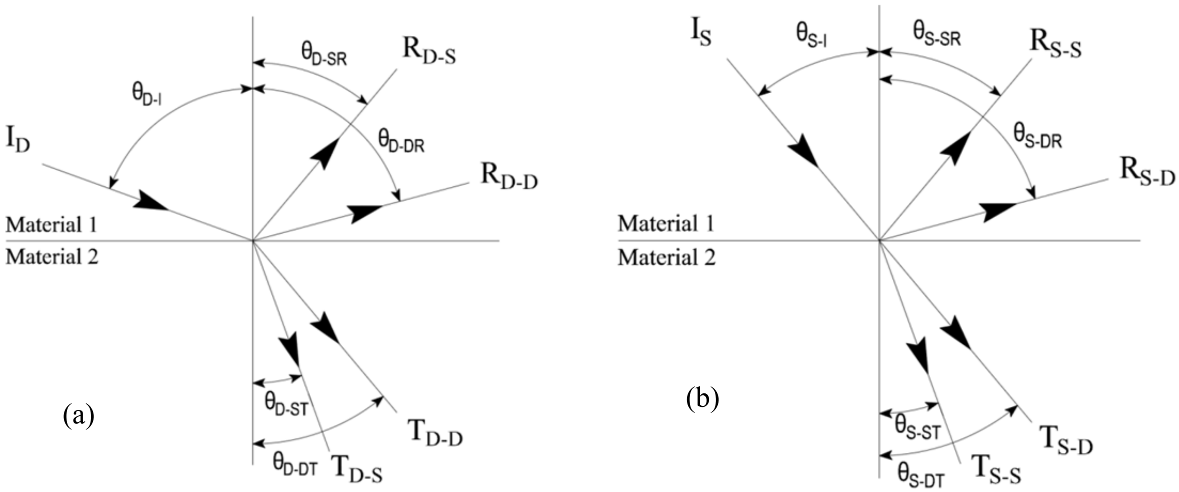

Figure 10-1 Reflection and transmission of waves at the interface of two solids, a) dilatational incident wave, b) shear incident wave

For a travelling stress wave, the displacement and stress continuity at the interface of two media has to be satisfied. The interface stress S_{xx} and S_{xy} in thin plates are given by:

$$S_{xx} = \lambda \frac{\partial u_y}{\partial y} + (\lambda + 2\mu) \frac{\partial u_x}{\partial x} \tag{10.3}$$

$$S_{xy} = \mu \left(\frac{\partial u_x}{\partial y} + \frac{\partial u_y}{\partial x} \right) \tag{10.4}$$

where λ and μ are Lame's parameters, and are given by $\lambda + 2\mu = \rho c_D^2$, and $\mu = \rho c_S^2$ with ρ representing the mass density of the medium. By enforcing displacement and stress continuity in thin plates at an interface, we have:

$$\begin{bmatrix} u_x^{(Mat2)} - u_x^{(Mat1)} \\ u_y^{(Mat2)} - u_y^{(Mat1)} \\ S_{xx}^{(Mat2)} - S_{xx}^{(Mat1)} \\ S_{xy}^{(Mat2)} - S_{xy}^{(Mat1)} \end{bmatrix} = \begin{bmatrix} 0 \\ 0 \\ 0 \\ 0 \end{bmatrix} \tag{10.5}$$

where $u_x^{(Mat1)}$ is the sum of displacement due to incident, transmitted, and reflected waves, and $u_x^{(Mat2)}$ is the sum of displacement due to transmitted, and reflected waves. The same description applies for $S_{xx}^{(Mat1)}$ and $S_{xx}^{(Mat2)}$. Expansion of Eq. (10.5) for incident dilatational wave leads to the following relationship:

$$
\begin{bmatrix}
-cos(\theta_{D-DR}) & -cos(\theta_{D-DT}) & sin(\theta_{D-SR}) & sin(\theta_{D-ST}) \\
-sin(\theta_{D-DR}) & sin(\theta_{D-DT}) & -cos(\theta_{D-SR}) & cos(\theta_{D-ST}) \\
-Z_{D1}\,cos(2\theta_{D-SR}) & Z_{D2}\,cos(2\theta_{D-ST}) & Z_{S1}\,sin(2\theta_{D-SR}) & -Z_{S2}\,sin(2\theta_{D-ST}) \\
-Z_{S1}\dfrac{c_{S1}}{c_{D1}}sin(2\theta_{D-DR}) & -Z_{S2}\dfrac{c_{S2}}{c_{D2}}sin(2\theta_{D-DT}) & -Z_{S1}\,cos(2\theta_{D-SR}) & -Z_{S2}\,cos(2\theta_{D-ST})
\end{bmatrix}
\begin{bmatrix} R_{D-D} \\ T_{D-D} \\ R_{D-S} \\ T_{D-S} \end{bmatrix}
= \begin{bmatrix} -\,cos(\theta_{D-I}) \\ sin(\theta_{D-I}) \\ Z_{D1}\,cos(2\theta_{D-SR}) \\ -Z_{S1}\dfrac{c_{S1}}{c_{D1}}sin(2\theta_{D-I}) \end{bmatrix} \tag{10.6}
$$

Similarly, the expansion of Eq. (10.5) for incident shear wave gives

$$
\begin{bmatrix}
-cos(\theta_{D-DR}) & -cos(\theta_{D-DT}) & sin(\theta_{D-SR}) & sin(\theta_{D-ST}) \\
-sin(\theta_{D-DR}) & sin(\theta_{D-DT}) & -cos(\theta_{D-SR}) & cos(\theta_{D-ST}) \\
-Z_{D1}\,cos(2\theta_{D-SR}) & Z_{D2}\,cos(2\theta_{D-ST}) & Z_{S1}\,sin(2\theta_{D-SR}) & -Z_{S2}\,sin(2\theta_{D-ST}) \\
-Z_{S1}\dfrac{c_{S1}}{c_{D1}}sin(2\theta_{D-DR}) & -Z_{S2}\dfrac{c_{S2}}{c_{D2}}sin(2\theta_{D-DT}) & -Z_{S1}\,cos(2\theta_{D-SR}) & -Z_{S2}\,cos(2\theta_{D-ST})
\end{bmatrix}
\begin{bmatrix} R_{S-D} \\ T_{S-D} \\ R_{S-S} \\ T_{S-S} \end{bmatrix}
= \begin{bmatrix} sin(\theta_{S-I}) \\ cos(\theta_{S-I}) \\ -Z_{S1}\,sin(2\theta_{S-I}) \\ -Z_{S1}\,cos(2\theta_{S-I}) \end{bmatrix} \tag{10.7}
$$

where Z_{D1}, Z_{D2}, Z_{S1}, and Z_{S2} are the dilatational impedance in material 1, dilatational impedance in material 2, shear impedance in material 1, and shear impedance in material 2, respectively.

The stress amplitude for reflected and transmitted dilatational and shear waves is plotted in Figure 10-2 and Figure 10-3 for incident dilatational and shear waves, respectively, for a particular Aluminum (AL)-High-density polyethylene (HDPE) bi-material interface. The material properties of AL and HDPE are given in Table 10-1. It should be noted that Eq. (10.6) and (10.7) are written for the displacement amplitudes; however in Figure 10-2 and Figure 10-3, the displacement amplitudes are converted to stress amplitudes using appropriate transformations. These figures show that for different incident wave angles, the ratio of shear and dilatational stress amplitude varies significantly. For incident shear wave, at an angle of 35°, the reflected dilatational wave becomes evanescent; however other waves will continue to propagate. Thus, for incident angles greater than 35°, Eq. (10.7) should be modified by removing the reflected dilatational wave, and enforcing displacement and stress continuity at the interface.

These results show that the incident angle has a noticeable effect in mitigating or amplifying the stress amplitudes. This means that the amplitude of the stress waves can be altered by converting the straight interface between two materials to a jagged path. This idea will be pursued in the remainder of this section for optimizing the interface profile of the layers in bi-layered rectangular plates with finite dimensions. It should be noted that the analytical solutions in this section are only applicable to semiinfinite media, and there is no closed form solution of this kind for finite structures. Accordingly, the FE numerical method is utilized for analyzing the proposed rectangular bi-layered plates.

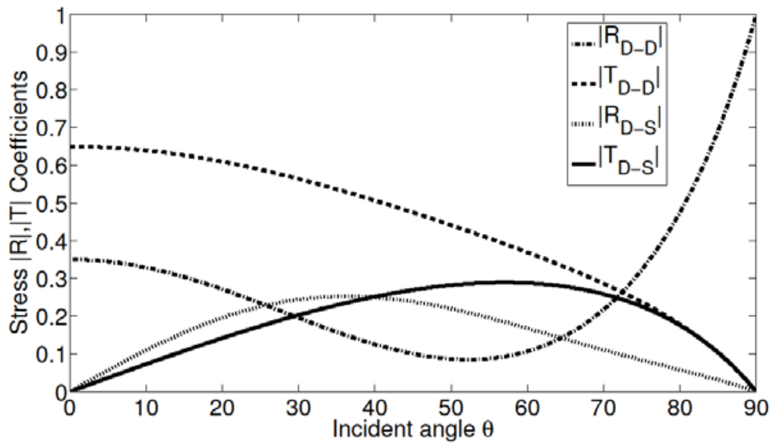

Figure 10-2 Reflection and transmission stress coefficients for incident dilatational wave on AL-HDPE interface for varying incident angle

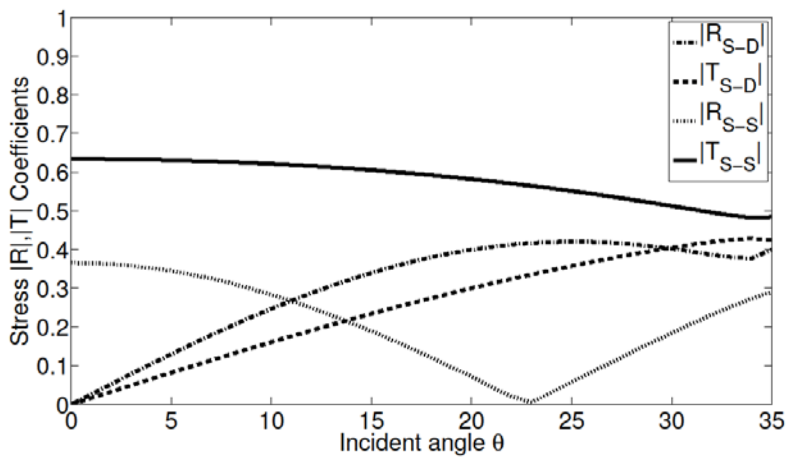

Figure 10-3 Reflection and transmission stress coefficients for incident shear wave on AL-HDPE interface for varying incident angle

10.3 Concept of interface profile optimization

In the previous section, it was observed that the angle of the incident pulse at the boundary of the two solid materials can change the characteristics of the reflected and transmitted waves significantly. Considering this fact, an optimization problem can be defined for minimizing the amplitude of the stress waves in a bi-layered plate by converting the interface profile between the two layers from a vertical straight line to a jagged shape. In this case, the angle of the incident wave at the intersection of the two media will no longer be zero (see Figure 10-1). Consequently, the stress waves will be scattered and a number of reflected and transmitted waves will be generated within the structure. By employing an appropriate optimization methodology, the profile of the jagged path can be optimized for the objective of stress wave attenuation at the clamped boundary of the bi-layered plate.

In order to introduce the concept of interface profile optimization, consider a general bi-layered plate shown in Figure 10-4. A transient dynamic load is applied to the left side of the plate (Line AF) and the plate is clamped at the right side (line JE). The top and bottom parts of the plate (lines FJ and AE) are traction-free boundaries. The horizontal and vertical dimensions of the plate are L_x and L_y, respectively, and the plate is divided into two parts: $ACHF$ and $CEJH$ with lengths L_1 and L_2, respectively. The objective of the problem is minimizing the maximum amplitude of the transient reaction force (on line AF), as it reaches the clamped boundary (line JE), by changing the interface profile between the two layers of the plate. To do so, an optimization zone (box) can be defined around the boundary of the two media, which can be divided into $n_x = n - 1$ and $n_y = m - 1$ segments in the horizontal and vertical directions, respectively, to generate an $n \times m$ grid, as shown in Figure 10-4. Thereafter, the optimization algorithm can select the points within the generated grid to develop a jagged or smooth interface between the two media. Without loss of generality, it is assumed that only one point can be selected by the optimization algorithm at each horizontal line (a number between 1 and n); therefore, the size of the solution space is n^m. The results of the optimization can be shown with an array of numbers. The length of this array is equal to the number of horizontal lines in the vertical direction (n_y), and each number within the array is bounded between 1 and the number of the vertical lines in the horizontal direction (n_x). To clarify further, an example is provided in Figure 10-5. In this example, the optimization zone is divided into 7 and 5 sections in the horizontal and vertical directions, respectively, which generates an 8×6 grid. Therefore, there are $n_y = 6$ horizontal lines in the optimization zone and each contains $n_x = 8$ points. This means that the optimization array is composed of 6 numbers, which can have a value between 1 and 8. For instance, the optimization array for the jagged boundary in Figure 10-5 is “3 8 1 4 5 2”.

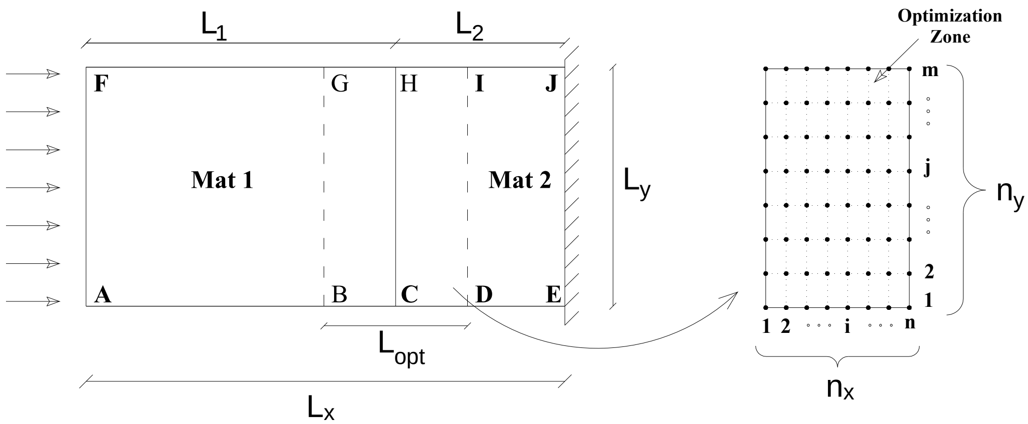

Figure 10-4 General bi-layered rectangular plate and its optimization zone

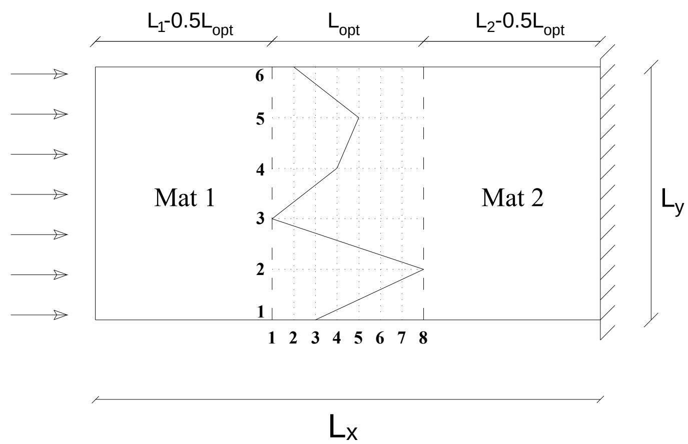

Figure 10-5 Example for the optimized interface between the two layers

10.4 Problem Definition

In the previous section, the concept of interface profile optimization for a bi-layered plate with jagged interface was introduced. This concept is utilized in this section to define a quantitative optimization problem for minimizing the amplitude of the stress waves in a bi-layered plate with finite dimensions.

Consider the bi-layered plates shown in Figure 10-6 with the horizontal and vertical dimensions of $L_x = 25.2\ cm$ and $L_y = 12.6\ cm$, respectively. These plates are divided into two parts with equal thickness of $0.5L_x = 12.6cm$, and the mid-section of the optimization zone is located at the mid-section of the plates. The thickness of the optimization zone (L_{opt}) is assumed to be $0.3L_x = 7.56cm$, $0.6L_x = 15.12cm$, and $0.9L_x = 22.68cm$ for the plates in Figure 10-6a, Figure 10-6b, and Figure 10-6c, respectively. The first and second layers of the plates are made of Aluminum (AL) and High-density polyethylene (HDPE), respectively. These materials are selected because of their significant impedance mismatch, which results in higher amount of wave scattering. According to wave propagation theories, the amplitude of the transmitted waves in the interface of two media mitigates as the wave passes from a high to a low impedance medium. Therefore, the AL layers in Figure 10-6 are placed on the left, before the HDPE layers. The mechanical properties of these materials are presented in Table 10-1. In this table, E, ρ, ν, c_D, c_S, and c_R represent Young's modulus, mass density, Poisson's ratio, dilatational wave velocity (for plane stress condition), shear wave velocity, and Rayleigh wave velocity, respectively, of the two materials. The velocity of the different types of waves can be found using the following formulas:

$$c_D = \sqrt{\frac{E}{\rho(1-\nu^2)}} \tag{10.8}$$

$$c_S = \sqrt{\frac{E}{2\rho(1+\nu)}} \tag{10.9}$$

$$c_R = \frac{0.87 + 1.12\nu}{1+\nu} c_S \tag{10.10}$$

The bi-layered plates are subjected to a transient half-sine loading with the duration of $T/2$, as shown in Figure 10-6. The ratio of the wavelength associated with this pulse to the total horizontal length of the structure is called the wavelength ratio and can be designated as:

$$R_\lambda = \frac{\lambda_{min}}{2L} \tag{10.11}$$

where λ_{min} is the associated wavelength, which is the product of the minimum wave speed within the structure (c_{min}) and the duration of a complete sine pulse T. The slowest wave in the plate structures is the Rayleigh wave; thus, for the problem at hand, c_{min} is equal to c_R of HDPE, which is $630\ m/s$.

Table 10-1 Mechanical properties of the plate materials

Material	E (GPa)	ρ (kg/m^3)	ν	c_D (m/s)	c_S (m/s)	c_R (m/s)
Aluminum	68.9	2700	0.33	5351	3097	2887
HDPE	1.2	950	0.42	1238	667	630

In order to investigate the effect of L_{opt} on the attenuation capacity of bi-layered plates, the structures in Figure 10-6 are subjected to a transient loading with a constant wavelength ratio of $R_\lambda = 0.05$, and their optimal interface profiles are then identified. It is observed that the structure with $L_{opt} = 0.3L_x$ (see Figure 10-6a) has higher attenuation capacity compared to the other structures (the details are presented later in section 10.8). Therefore, this structure is selected for studying the effect of other parameters such as the wavelength ratio of the transient loading and the grid dimensions.

The wave propagation behavior and attenuation capacity of any structure depends significantly on the duration (wavelength) of the transient loading. To examine this effect, the structure identified with $L_{opt} = 0.3L_x$ (Figure 10-6a) is subjected to four different wavelength ratios, i.e., $R_\lambda = 0.05, 0.1, 0.2,$ and 0.4. Considering the Rayleigh wave speed in HDPE ($c_R = 630\, m/s$), the duration of the half-sine pulses ($T/2$) for each wavelength ratio (R_λ) are calculated and presented in Table 10-2.

The objective of the defined optimization problem is to minimize the maximum amplitude of the total reaction force at any instant at the clamped boundary. To provide better insight, the reaction force history at the clamped boundary can be normalized by the amplitude of the applied force, and the optimization problem can be determined with the following formula:

$$\text{Objective function: Minimize } R_F \tag{10.12}$$

where, R_F represents the normalized force history at the boundary and can be found as:

$$R_F = max\left(\left|\frac{F_B}{F_L}\right|\right) \tag{10.13}$$

with F_B and F_L representing the force history at the clamped boundary and amplitude of applied transient loading, respectively.

Since the main purpose of this section is showing the effectiveness of interface profile optimization, the attenuation capacity of the optimized structures is determined by comparing the performance of these structures to bi-layered plates having a straight vertical layer interface. Therefore, the attenuation capacity of each optimal design is defined using the following formula:

$$Attenuation\ (\%) = \left(1 - \frac{(R_F)_J}{(R_F)_S}\right) \times 100 \tag{10.14}$$

where $(R_F)_J$ and $(R_F)_S$ denote the normalized force history Eq. (10.13) at the boundary of the bi-layered plates with jagged and straight vertical interface, respectively. It should be noted that for each optimal design, $(R_F)_S$ is found by analyzing a bi-layered plate with straight vertical interface that is subjected to a transient loading with similar duration used for the corresponding optimal design. All of the properties of these plates are similar to the structures in Figure 10-6, except the interface between the layers is a straight vertical line and the thickness of each layer (AL and HDPE layers) is $0.5 \times 25.2 = 12.6cm$.

In layered elastic systems, the number of reflections and transmissions of the stress waves increases as the analysis is performed for a longer duration of time. Therefore, one of the important factors in characterization of these systems is the duration of analysis. For practical problems, it is impossible to analyze the structures for infinite time and a stopping time should be selected based on the duration of the applied transient loading and the wave speed within the system. In this section, the duration of analysis (T_A) has been set to be 20 times the summation of the duration of the half-sine loading ($T/2$) and the maximum amount of time required for the slowest wave to reach the clamped boundary (t_{reach}). Therefore, T_A can be found using:

$$T_A = 20\left(\frac{T}{2} + t_{reach}\right) \tag{10.15}$$

$$t_{reach} = \frac{l_x}{C_{min}} \tag{10.16}$$

where l_x and C_{min} are the horizontal length and the slowest wave speed within the system. For the problem at hand, C_{min} is equal to the Rayleigh wave speed of HDPE. The duration of analysis (T_A) for different values of R_λ is presented in Table 10-2.

As mentioned in the previous section, the optimization zone can be divided into a grid defined by any integer number in the horizontal and vertical directions for generating the required interface for the geometry optimization. The optimization zones of the bi-layered plates in Figure 10-6a, Figure 10-6b, and Figure 10-6c are divided into 7,14, and 21 segments in the horizontal direction, respectively, while in the vertical direction, all of the structures are divided into 7 segments. Based on these divisions, the structures in Figure 10-6a, Figure 10-6b, and Figure 10-6c have 8×8, 15×8, and 22×8 grids, respectively.

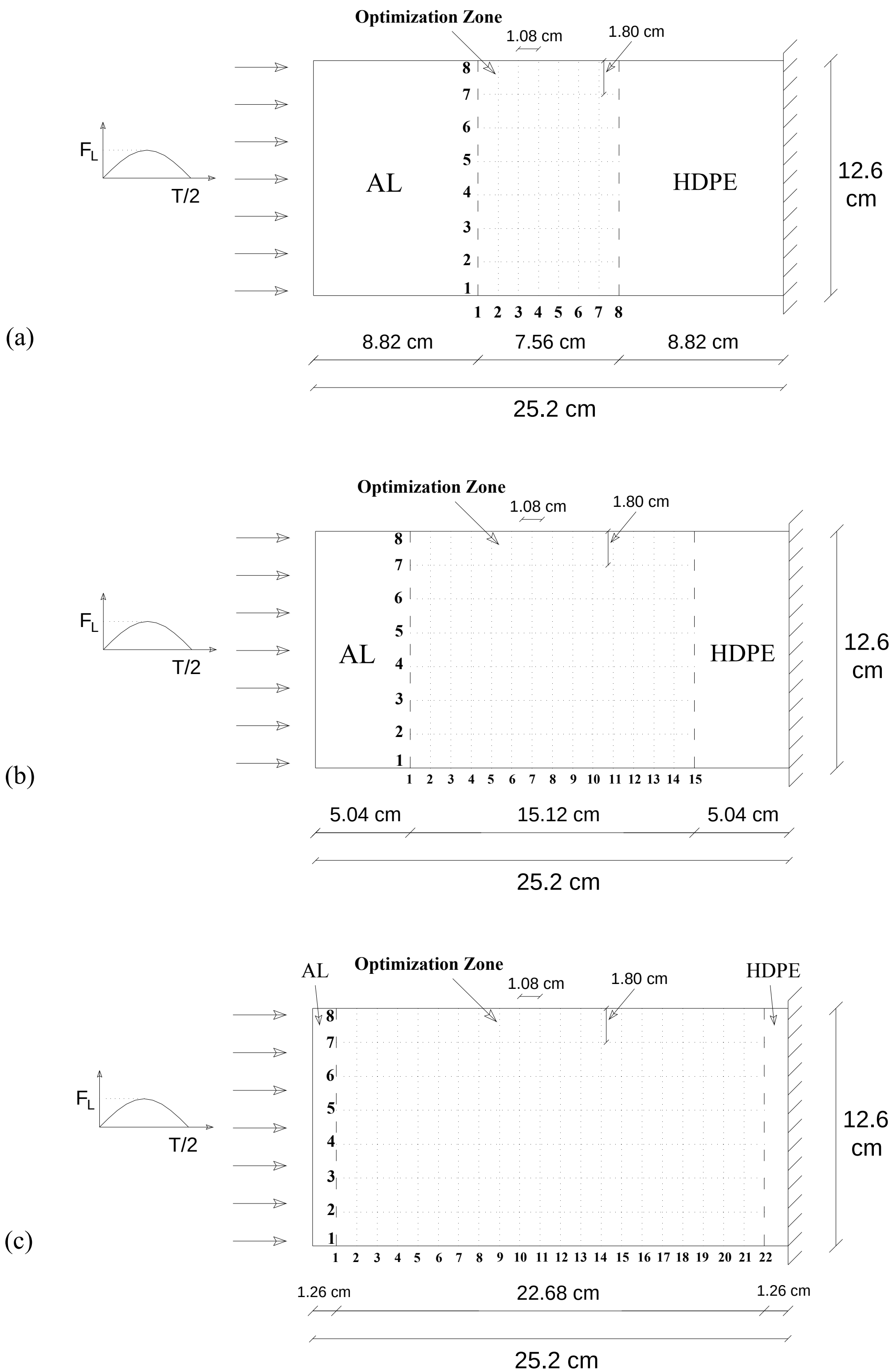

Figure 10-6 Bi-layered plates with a)$L_{opt} = 0.3L_x$, b) $L_{opt} = 0.6L_x$, c) $L_{opt} = 0.9L_x$

Table 10-2 Duration of half-sine loadings ($T/2$) and duration of analysis (T_A) for different values of wavelength ratios

R_λ	$T/2\ (sec)$	$T_A(sec)$
0.05	2.0E-05	8.4E-3
0.1	4.0E-05	8.8E-3
0.2	8.0E-05	9.6E-3
0.4	1.60E-04	1.12E-2

Considering the horizontal and vertical dimensions of the optimization zones, the width and height of each cell within the generated grids is 1.08cm and 1.80cm, respectively. It is assumed that the optimization method can select one point for each horizontal line of the grid. Therefore, the solution spaces for the structures with 8×8, 15×8, and 22×8 grids have $8^8 = 1.68E7$, $15^8 = 2.56E9$, and $22^8 = 5.49E10$ combinations, respectively.

In order to investigate the effect of grid dimensions, the optimization zone of the structure with $L_{opt} = 0.3L_x$ is divided into 1,3,5, and 7 cells in the horizontal and vertical directions to generate 2×2, 4×4, 6×6, and 8×8 grids as shown in Figure 10-7. The sensitivity of the attenuation capacity of the bi-layered plates with different grid sizes is discussed in Section 10.8.

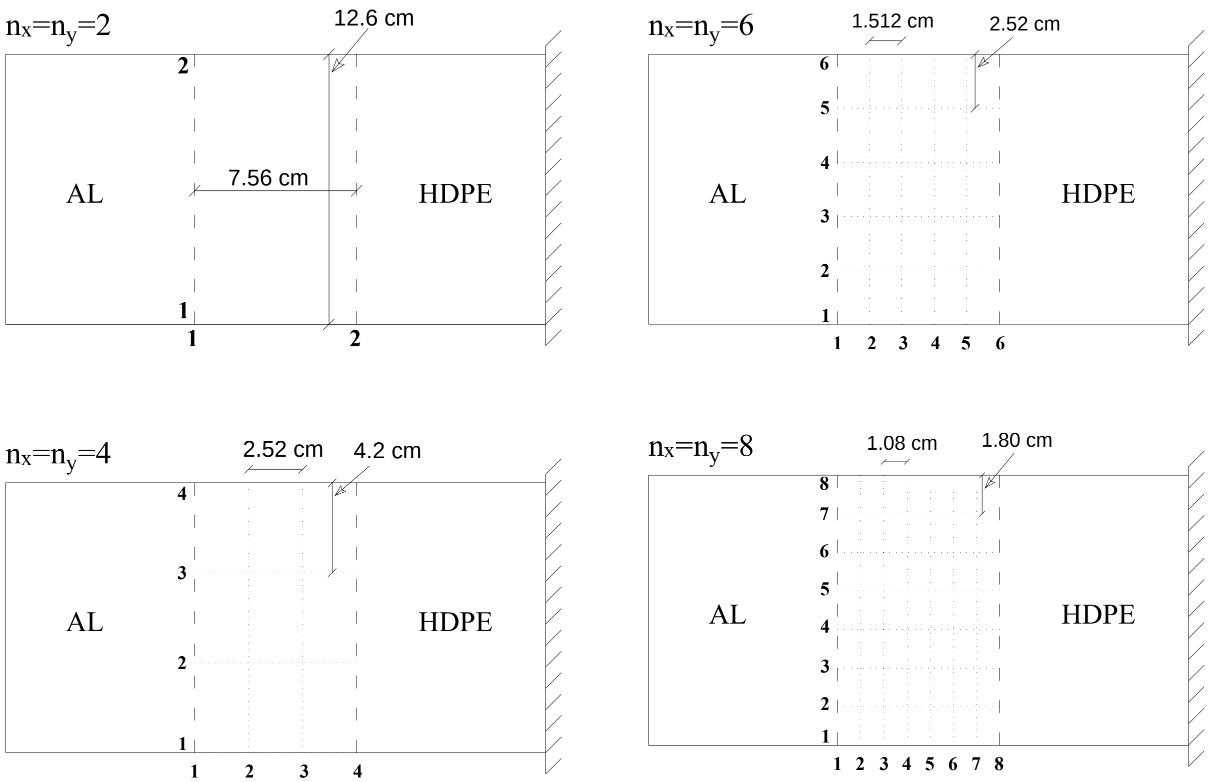

Figure 10-7 Bi-layered plates with $L_{opt} = 0.3L_x$ and $n_x = n_y = 2, 4, 6$ and 8

10.5 Optimization method

The solution space for the defined problems is very large, and it is obvious that an exhaustive search described earlier cannot be performed for finding the best solution. Therefore, an appropriate optimization procedure should be utilized for this purpose. Similar to the previous sections, GA is used for the geometry optimization of the potentially jagged interface.

As mentioned in section 10.2, there is no closed-form solution for the wave propagation behavior of finite bi-layered plates (with jagged interface profiles) subjected to transient dynamic loadings, and FE analysis is utilized for this purpose. In the following, FE modeling and the coupling of GA and FE are explained thoroughly.

10.6 FE modeling

The validity of using an FE method for wave propagation in plate structures is investigated by Moser, Jacobs et al. (1999). For an elastic system without damping, the matrix form of the equation of motion can be written as:

$$M\ddot{u} + Ku = P \tag{10.17}$$

where M and K represent the mass and stiffness matrices, respectively, and P is the applied dynamic force. The dynamic equilibrium equation, Eq. (10.17), can be solved using two general methods: Explicit and Implicit. Explicit dynamic analysis is used for the wave propagation analysis of the bi-layered plates, as this method is computationally efficient for dynamic modelling of the structures subjected to short dynamic loadings with an impulsive nature. The FE explicit analyses of the structures are performed using the commercial software Abaqus 6.12 (Simulia (2012)). Abaqus uses a central-difference time integration rule for explicit time integration of the equation of motion.

The accuracy of the wave propagation analysis using FE depends, significantly, on the temporal (time step) and spatial (element size) resolution of the FE model (Moser, Jacobs et al. (1999)). The explicit integration method is conditionally stable, and it is required that the time step of the integration be smaller than a critical value. For a system without damping, the critical time step can be found using (Bathe (1996)):

$$\Delta t < \Delta t_{cr} = \frac{T_n}{\pi} \tag{10.18}$$

where T_n is the smallest period of the FE assemblage. Generally, it is difficult to find the smallest period of the FE system and the following approximate formula is used for defining the value of the time step (Simulia (2012)):

$$\Delta t \approx \frac{\mathrm{L}_{min}}{c_D} \tag{10.19}$$

where L_{min} and c_D represent, respectively, the minimum length of the FE mesh and dilatational wave speed. The dilatational wave speed can be found using the Lame's constants and the mass density of the materials ($c_D = \sqrt{(\lambda + 2\mu)/\rho}$). Generally, a smaller time step than Eq. (10.19) is used in the explicit integration in order to assure the stability of the analysis. For example, Abaqus uses a time step within the following range for two-dimensional (2D) analysis (Simulia (2012)):

$$\frac{1}{\sqrt{2}}\frac{\mathrm{L}_{min}}{c_d} < \Delta t < \frac{\mathrm{L}_{min}}{c_d} \tag{10.20}$$

For the FE analysis of the bi-layered plates presented in this section, the time step is selected based on the element-by-element estimation of Abaqus. This method chooses the time step based on the smallest element characteristic length and the dilatational wave speed, as presented in Eq. (10.20). An interested reader is referred to Simulia (2012) for further information on the time step selection for explicit dynamic analysis.

In addition to the time step, special attention should be given to the element size of the FE mesh in order to obtain reliable results from the analysis. Generally, in wave propagation problems, the frequency of the applied loadings is high and thus their wavelength is small. In order to resolve the spatial features, the element size of the FE mesh should be small enough. According to Alleyne and Cawley (1991), it is required to have more than 10 nodes per wavelength of the applied loading. Moser, Jacobs et al. (1999) suggest the element mesh of the FE model be smaller than the following value:

$$l_e = \lambda_{min}/20 \tag{10.21}$$

where λ_{min} is the shortest wavelength within the system. The shortest wavelength can be found using Eq. (10.11). The minimum required dimensions of the elements (l_e) for the four different values of R_λ are presented in Table 10-3. Considering these values, the minimum size of the elements in the FE mesh of the bi-layered plates is chosen to be 1, 2, 4, and $8mm$ for $R_\lambda = 0.05, 0.1, 0.2,$ and 0.4, respectively.

It should be noted that the bi-layered plates in this section are modeled using a 3-node linear plane stress triangular element from the Abaqus element library (Element CPS3).

One of the important characteristics in FE analysis of the bi-layered plates is meshing of the FE model. Due to the existence of the potentially jagged interface, the meshing procedure is not straightforward, and the FE model should be partitioned appropriately. Based on the geometry of the jagged interface, the FE models are partitioned in a consistent way to produce appropriate mesh and all of the partitioning procedures are performed using a developed script, which is explained in the next section.

Table 10-3 Minimum element size of the mesh for different values of R_λ

R_λ	λ_{min} (m)	l_e (m)
0.05	0.0252	1.26E-3
0.1	0.0504	2.52E-3
0.2	0.1008	5.04E-3
0.4	0.2016	1.008E-2

10.7 Coupled GA-FE methodology

In order to minimize the amplitude of the stress waves in bi-layered plates, it is required to find the stress history at the boundary of the structures and evaluate its peak value within each run of the GA. Since the target of the problem is optimizing the geometry of the jagged interface between the boundaries, the features of the FE models change as the optimization procedure advances. Therefore, new FE models should be consistently generated within each run of GA, while more importantly retaining the objectivity of the meshing. This is done using the Abaqus Scripting Interface. Using this interface, a comprehensive Python script is written that is capable of building all of the features of the FE model without using the GUI. This script is implemented in the fitness function calculation of the GA procedure, and performs the following tasks in summary:

- Building the components of the FE model such as parts, materials, sections, and loading
- Estimating T_A and l_e using Eq. (10.15) and (10.21)
- Partitioning the FE model to generate an appropriate mesh
- Running the explicit dynamic FE analysis
- Extracting the stress history at the clamped boundary from the output database
- Calculating the fitness value using Eq. (10.13)

It should be noted that the optimization toolbox (version 6.2) of Matlab R2012a (MATLAB (2012) is used for solving the optimization problems presented herein. For each problem, the details of the GA runs are presented in the next section.

10.8 Results and discussion

In this section, the interface profiles of the structures in Figure 10-6 and Figure 10-7 are optimized using the developed GA-FE methodology and the results are presented for the effect of different parameters separately. The following parameters are investigated: length of the optimization zone (L_{opt}), grid dimensions, and wavelength ratio of the transient loading (R_λ).

10.8.1 Effect of the length of the optimization zone (L_{opt})

In order to investigate the effect of L_{opt}, the optimal designs of the bi-layered plates with $L_{opt} = 0.3, 0.6,$ and $0.9L_x$ are explored using the proposed GA-FE methodology. The dimensions of these structures and their optimization zones are shown in Figure 10-6. The grid dimensions of these plates are similar and all are subjected to a transient loading with the constant wavelength ratio of $R_\lambda = 0.05$. As the optimization algorithm can select one point for each horizontal line of the grid, the GA runs are performed with 8 integer variables with the lower and upper bounds of [1,8], [1,15], and [1,22] for the structures with $L_{opt} = 0.3, 0.6,$ and $0.9L_x$, respectively. For the plate with $L_{opt} = 0.3L_x$ (Figure 10-6a) the GA population size is set to be 100, while for the plates with $L_{opt} = 0.6$ and $0.9L_x$ (Figure 10-6b and Figure 10-6c), this value is assumed to be 200. The reason for selecting these values is that the solution space for each of the structures with $L_{opt} = 0.6$ and $0.9L_x$ is much larger than that of the structure with $L_{opt} = 0.3L_x$ (compare 15^8 and 22^8 with 8^8). For all of the optimal designs, the GA was run until the change in the average fitness value of the generations becomes less than a tolerance level, which is set at 1×10^{-6}. In order to assure the results of the GA optimization procedure, the problems are run several times and the results of the previous runs are used as the initial population for the next runs. This process is repeated until no further improvement is observed in the results.

The optimized vertical position strings (value of n_x at each n_y) and attenuation capacity for different values of L_{opt} are presented in Table 10-4 and the schematics of the optimal designs are depicted in Figure 10-8.

Table 10-4 Optimization string and attenuation capacity for different values of L_{opt}

L_{opt}	Optimization String	$(n_x)_{min}$	$(n_x)_{max}$	Attenuation (%)
0.3	7 1 8 7 4 2 1 1	1	8	58
0.6	5 3 6 5 11 11 5 10	3	11	56
0.9	12 13 14 12 10 8 4 10	4	14	53

The results of the optimization in Table 10-4 and Figure 10-8 show that the optimal interface profiles for the structures with $L_{opt} = 0.6$ and $0.9L_x$ have a narrow length compared to the length of the optimization zone (L_{opt}). For example, the difference between the minimum and maximum values of n_x for the structures with $L_{opt} = 0.6$ and $0.9L_x$ in Figure 10-8b and Figure 10-8c is $11 - 3 = 8$ and $14 - 4 = 10$, respectively. This means that the maximum horizontal length of the optimized interface profiles for the structures with $L_{opt} = 0.6$ and $0.9L_x$ is $8 \times 1.08 = 8.64cm\ (0.34L_x)$ and $10 \times 1.08 = 10.80cm\ (0.43L_x)$, respectively. These results show that by increasing L_{opt}, the optimal interface profiles do not occupy the whole length of the optimization zone. However, the optimal interface profile of the structure with $L_{opt} = 0.3L_x$ occupies the whole length of the optimization zone as shown in Figure 10-8a. In addition, according to Table 10-4 and Figure 10-8, the attenuation capacity of the structures does not increase for larger values of L_{opt}. This probably happens because the solution space for the structures with $L_{opt} = 0.6$ and $0.9L_x$ is extremely large (15^8 and 22^8). As mentioned above, to search the solution space further, the population size of the GA optimization for the plates with $L_{opt} = 0.6$ and $0.9L_x$ is set to be 200 (compare with 100 for $L_{opt} = 0.3$); however, the attenuation capacity is not increased. It is not practical to increase the population size of the GA further because of the extensive computational cost.

Based on these results, in the remainder of this section, the structure with $L_{opt} = 0.3L_x$ (see Figure 10-6a) is selected for investigating the effect of grid dimensions and wavelength ratio of the transient loading.

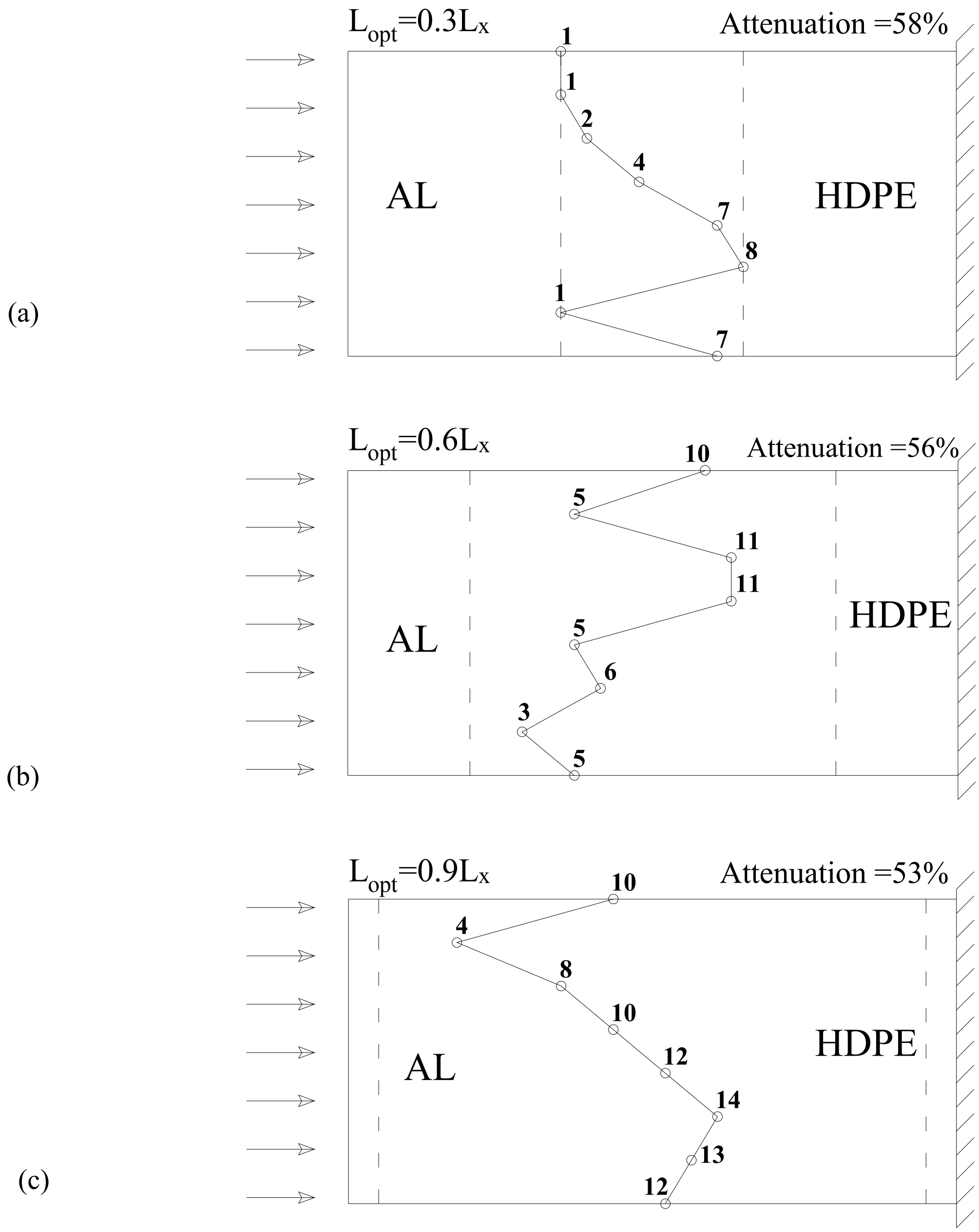

Figure 10-8 Optimal designs of the bi-layered plates in Figure 10-6 for $R_\lambda = 0.05$, a) $L_{opt} = 0.3L_x$, b) $L_{opt} = 0.6L_x$, c) $L_{opt} = 0.9L_x$

10.8.2 Effect of grid dimensions

To investigate the effect of grid dimensions, the optimal design of the structures in Figure 10-7 are found using the developed optimization methodology. The length of the optimization zone (L_{opt}) for all of the structures is $0.3L_x$ and the structures are subjected to a transient loading with $R_\lambda = 0.05$. It should be noted that GA is not used for the optimal design of the structures with $n_x = x_y = 2$ and 4 (see Figure 10-7) as the solution space has only $2^2 = 4$ and $4^4 = 256$ combinations, respectively. Therefore, simple exhaustive search is utilized for the optimization of these structures. However, the coupled GA-FE methodology is employed for finding the optimal design of the structures with $n_x = x_y = 6$ and 8. The details of the GA runs are exactly the same as the previous section and the population size is set to be 100.

The optimization string and attenuation capacity of the optimal design of the structures in Figure 10-7 are presented in Table 10-5 and the schematics of the optimal designs are depicted in Figure 10-9. The results show that the attenuation capacity of the bi-layered plates increases significantly when the number of grid points varies from 2 to 4 (compare 28% and 54% for these two cases, respectively). This phenomenon (increasing the attenuation capacity) is not observed by increasing the grid points from 4 to 6 and 6 to 8. Therefore, for the problem at hand, it is not efficient to generate a very fine grid to obtain higher attenuation capacity. Due to these facts, in the next section, the effect of wavelength ratio of the transient loading on the behavior of bi-layered plates will be investigated for a structure with $R_\lambda = 0.05$ and the grid dimensions of $1.08 \times 1.80\ cm^2$ (see the structure with $n_x = n_y = 8$ in Figure 10-6a or Figure 10-7).

Table 10-5 Optimization string and attenuation capacity for different values of $\mathbf{n_x}$ and $\mathbf{n_y}$

n_x and n_y	Optimization String	Attenuation (%)
2	1 2	28
4	3 4 1 1	54
6	1 1 2 6 5 4	55
8	7 1 8 7 4 2 1 1	58

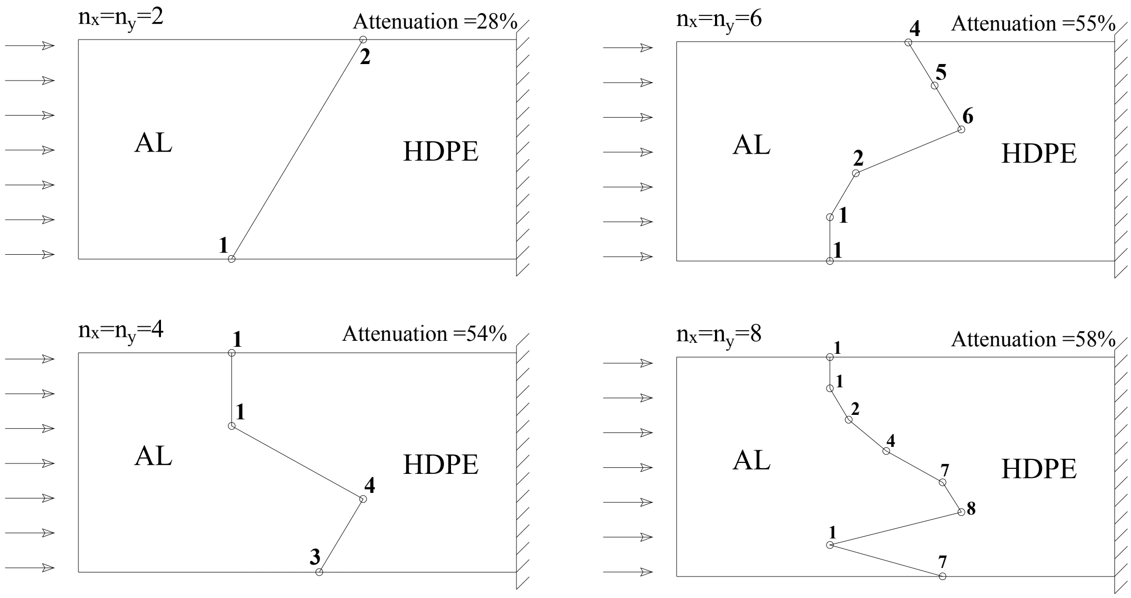

Figure 10-9 Optimal design of the bi-layered plates in Figure 10-7 for $R_\lambda = 0.05$

10.8.3 Effect of wavelength ratio (R_λ)

In order to investigate the effect of the wavelength ratio of the applied transient loading (R_λ), the structure in Figure 10-6a (with $L_{opt} = 0.3L_x$ *and* $n_x = n_y = 8$) is optimized for four different values of R_λ as indicated in Table 10-2. In the remainder of this section, the optimal designs for $R_\lambda = 0.05, 0.1, 0.2$ and 0.4 are identified as structures $A, B, C,$ and D, respectively. The GA runs are performed with 8 integer variables with the lower and upper bounds of $[1,8]$, and their population size is set to be 100. Other details of the GA runs are similar to the previous sections.

The optimized vertical position strings (value of n_x at each n_y) for different values of R_λ are presented in Table 10-6. The schematic of the optimal designs and the absolute value of the ratio of the force history at the boundary ($|F_B/F_L|$) of structures A, B, C, and D are presented in Figure 10-10, Figure 10-11, Figure 10-12, and Figure 10-13, respectively. In order to show the efficiency of the optimal designs, the stress history at the boundary of a similar bi-layered plate with a straight vertical interface is also depicted in these figures (with dotted lines).

Table 10-6 Optimization string and attenuation capacity of the structure in Figure 10-6a for different values of R_λ

R_λ	Structure	Optimization String	Attenuation (%)
0.05	A	7 1 8 7 4 2 1 1	58
0.1	B	5 5 8 5 2 1 1 1	36
0.2	C	3 4 4 2 7 7 6 8	28
0.4	D	5 5 8 4 2 1 1 1	15

The results of the optimization problems can be summarized as follows:

- The optimization string for $R_\lambda = 0.05$ (structure A - Figure 10-10) is "7 1 8 7 4 2 1 1", and the maximum amount of attenuation that can be obtained by this structure is 58%. Figure 10-10.b shows that the stress history at the boundary of the straight structure has a very large value at the beginning; however, there is no such peak in the stress history of the jagged structure, which results in a significant amount of attenuation.
- The optimization string for $R_\lambda = 0.1$ (structure B - Figure 10-11) is "5 5 8 5 2 1 1 1", and the maximum amount of attenuation that can be obtained by this structure is 36%. Figure 10-11.b shows that the peak values of the force history at the boundary of the straight structure are efficiently lessened by the jagged structure; however, the amount of attenuation at $R_\lambda = 0.1$ is less than at $R_\lambda = 0.05$.
- The optimization string for $R_\lambda = 0.2$ (structure C - Figure 10-12) is "3 4 4 2 7 7 6 8", and the maximum amount of attenuation that can be obtained by this structure is 28%. Again, the amount of attenuation at $R_\lambda = 0.2$ is decreased compared to $R_\lambda = 0.05$ (structure A) and 0.1 (structure B).
- The optimization string for $R_\lambda = 0.4$ (structure D - Figure 10-13) is "5 5 8 4 2 1 1 1" and the maximum amount of attenuation that can be obtained by this structure is only 15%. This structure is very similar to structure A, except the fourth number in the optimization string is 4 instead of 5. Compared to the other structures, it is obvious that the lowest amount of attenuation takes place at $R_\lambda = 0.4$.

These analyses show that the optimal interface profile depends, significantly, on the wavelength ratio (R_λ) of the applied loading. Moreover, the amount of attenuation decreases significantly by increasing R_λ. Considering the dimensions of the plate in Figure 10-6a, the minimum wavelength for structures A, B, C, and D is $0.1L, 0.2L, 0.4L$, and $0.8L$, respectively. Since the thickness of the optimization zone is $0.3L$, it can be concluded that higher amount of attenuation can be obtained if the optimization zone has larger length compared to the wavelength of the loading.

To explore the attenuation capacity of the optimal designs further, structures A, B, C, and D are subjected to transient loadings with various R_λ values and their corresponding attenuation capacity are presented in Table 10-7. Examining the results of this table, the attenuation-R_λ curve for each structure is plotted in Figure 10-14, and accordingly, the attenuation capacity of each structure can be explained as follows:

- Structure A has a very high attenuation capacity for $R_\lambda = 0.05$ (the wavelength for which it is optimized) and $R_\lambda = 0.1$; however, its performance is poor for larger R_λ values, especially for $R_\lambda = 0.4$. The minimum value of attenuation for this structure over the four cases is 2%, which occurs at $R_\lambda = 0.4$.
- Structures B and D have a very similar attenuation capacity, because their geometries are quite similar. The optimization capacities of these structures is very good for $R_\lambda = 0.2$ (it is only 1% less than the attenuation capacity of structure C). For $R_\lambda = 0.05$, the attenuation capacity of structures B and D is about 10% lower than that of structure A. The minimum values of attenuation over the four cases for structures B and D are 13% and 15%, respectively.
- Structure C provides a lower amount of attenuation for $R_\lambda = 0.05, 0.1$ and 0.4, and it is only efficient for $R_\lambda = 0.2$ (the wavelength for which it is optimized). The minimum attenuation over the four cases for this structure is 9%.

Based on these observations, either structure B or D is recommended for attenuating the intensity of the transient loadings with R_λ values between 0.05 and 0.4.

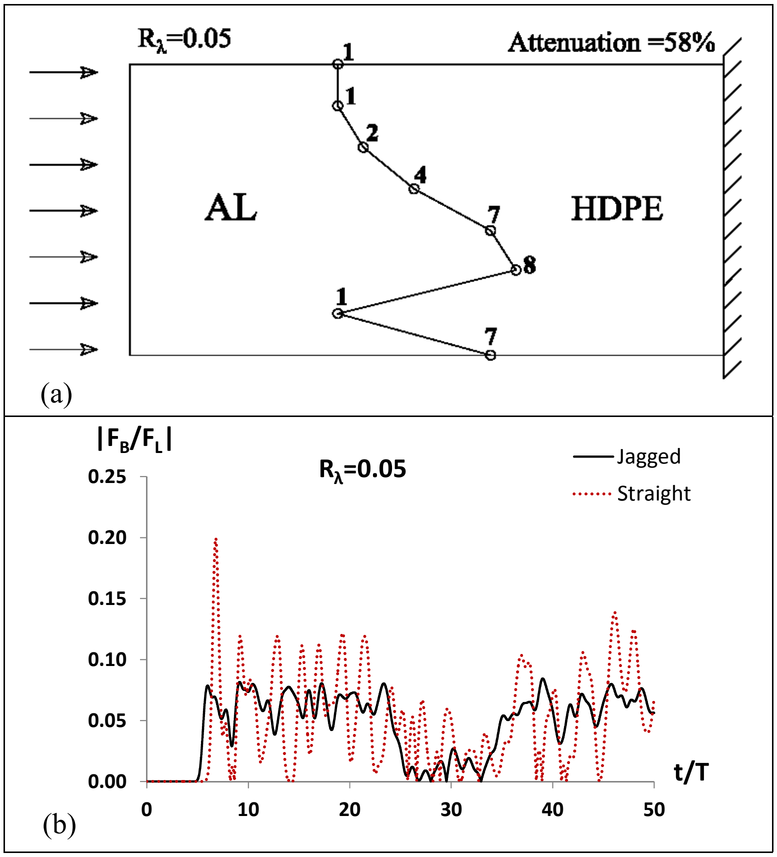

Figure 10-10 Structure *A*, a) schematic of the optimal design, b) force history at the boundary for $R_\lambda = 0.05$

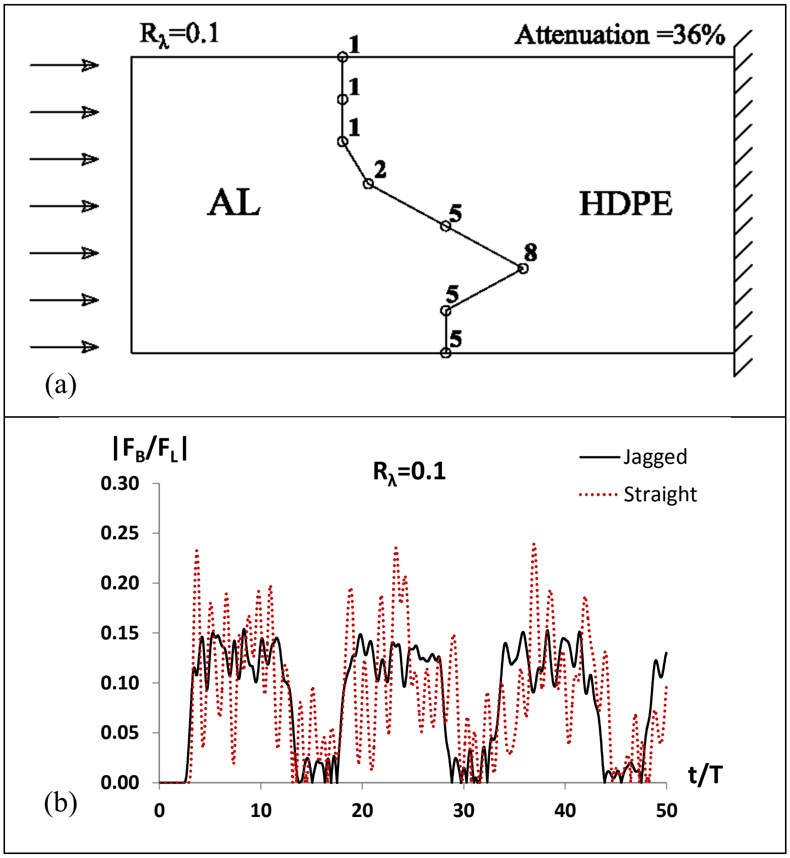

Figure 10-11 Structure *B*, a) schematic of the optimal design, b) force history at the boundary for $R_\lambda = 0.1$

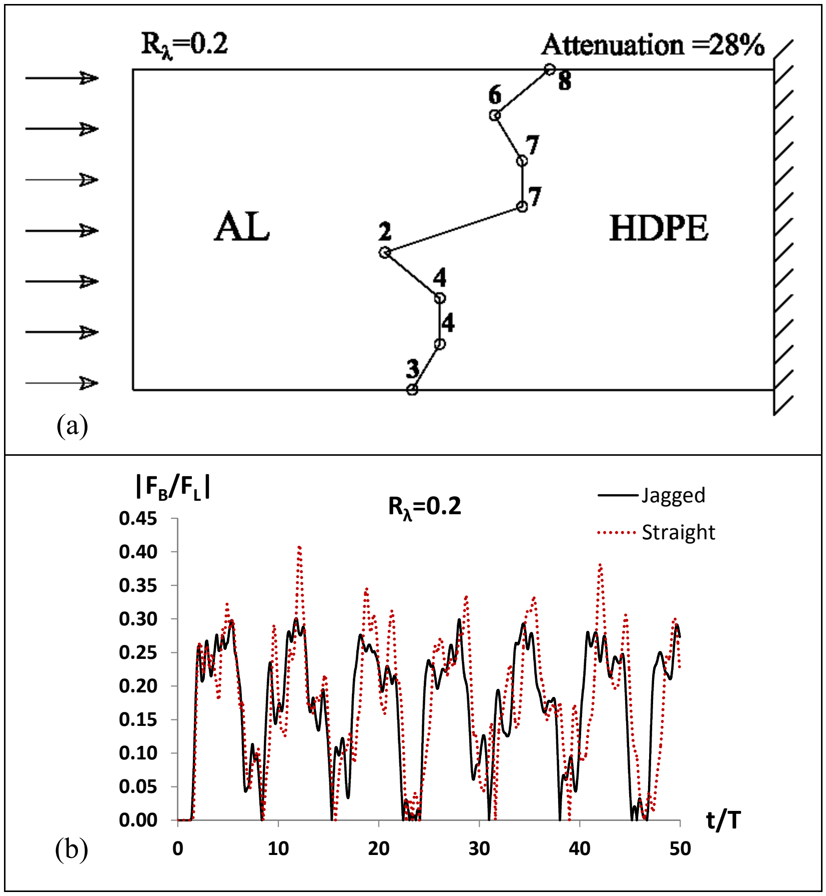

Figure 10-12 Structure C, a) schematic of the optimal design, b) force history at the boundary for $R_\lambda = 0.2$

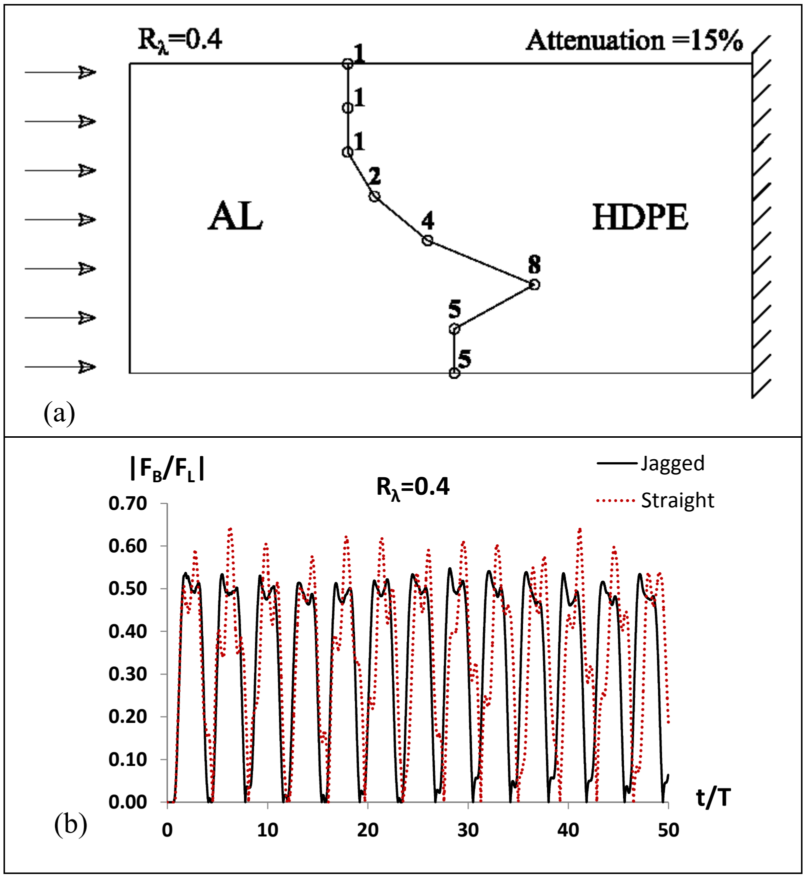

Figure 10-13 Structure *D*, a) schematic of the optimal design, b) force history at the boundary for $R_\lambda = 0.4$

Table 10-7 Amount of attenuation (%) in the optimized structures for different values of R_λ

R_λ	Structure			
	A	*B*	*C*	*D*
0.05	58	49	47	48
0.1	36	36	25	35
0.2	19	27	28	27
0.4	2	13	9	15

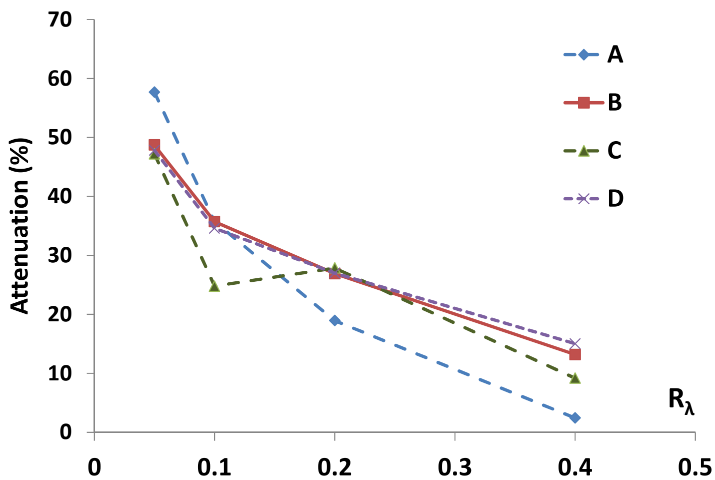

Figure 10-14 Attenuation-R_λ curve for the optimized structures

10.9 Summary

The stress wave attenuation in bi-layered rectangular plates with a potentially jagged interface is studied in this section. The structures are subjected to transient half-sine loading with various durations, and their interface profile is optimized for the objective of stress wave attenuation. A coupled GA-FE optimization methodology is developed for finding the optimal design of the interfaces.

The effect of different parameters such as the length of the optimization zone, the dimensions of the optimization grid, and the wavelength ratio of the applied transient loading is investigated. It is observed that the attenuation capacity of the bi-layered plates with jagged interface does not increase significantly by increasing the length of the optimization zone or by decreasing the dimensions of the grid cell (making a very fine optimization grid).

The results show that the interface profile has a significant effect in attenuating the stress waves, and the amount of attenuation depends directly on the associated wavelength of the applied transient loading. In addition, there is no unique interface profile for all of the transient loadings, and the optimal design of the interface varies for the loads with different wavelengths. The results also show that higher attenuation can be obtained if the associated wavelength of the applied load is small compared to the dimensions of the structure and the length of the optimization zone.

SECTION 11
SUMMARY, CONCLUSION, AND RECOMMENDATIONS FOR FUTURE RESEARCH

11.1 Summary

This report investigates the wave propagation characteristics of different types of discontinuities and proposes new efficient systems for mitigating impulsive loadings. The underlying concept explored in this report relies on the attenuation of stress waves in the systems associated with the reflection and transmission of waves at the discontinuities. Hence, with impetus to provide a better understanding of the attenuation capacity of the impulsive-loading mitigation strategies, the wave reflection and transmission in different types of materials and geometric discontinuities are investigated comprehensively.

The results obtained from these investigations are then utilized for designing new architectures for attenuating the stress waves generated from impulsive loadings. In order to design these architectures, the theoretical concepts from wave propagation analysis of the systems with discontinuities are combined with a heuristic optimization methodology, based on genetic algorithms (GA). In this work, GA is exploited for the optimal design of the stress wave attenuators because it avoids the difficulty of obtaining gradient information with respect to the design variables and is well-suited for the highly non-linear nature of the problems explored in this report.

Four types of stress wave attenuators are introduced in this report. These attenuators include: (i) layered collinear rod structures, (ii) layered diamond-shape beam structures, (iii) non-collinear beam structures, and (iv) porous plates. The layered stress wave attenuators have constant geometry while their material set-up is optimized during the design procedure. However, the non-collinear beam structures and porous plates are made of a single material, and the optimal design procedure seeks to find the best geometry of these systems for mitigating the effects of impulsive loadings. In addition to the proposed stress wave attenuators, the stress wave attenuation capacity of the bi-layered plates with jagged interface profile is also studied in the last section of this report. Similar to the approach used in non-collinear systems and porous plates, the material properties of the bi-layered plates remain unchanged during the design procedure; however, the profile of the interface between the two materials changes for the objective of stress wave attenuation.

The major contributions of this report can be summarized as follows:

- Study the effects of discontinuities in different structures such as rods, beams, and plates
- Derive reflection and transmission matrices for arbitrary "L" and "T" shaped Timoshenko beams
- Propose four types of stress wave attenuators
- Characterize the crucial parameters for designing the proposed stress wave attenuators
- Develop a heuristic optimal design procedure for finding the best material and geometry configurations of the proposed stress wave attenuators
- Explore the stress wave attenuation capacity of the proposed stress wave attenuators for the impulsive loadings with various frequency contents
- Explore the stress wave attenuation in bi-layered plates with jagged interface profile

11.2 Conclusion

The key conclusions of the study presented in this report are as follows:

- The reflection and transmission properties are very different for the various types of discontinuities in rods. Some discontinuities such as lumped mass and elastic boundaries can disperse the waves although the propagating signal is inherently non-dispersive, while some others such as stepped rods induce no dispersion.
- The reflection and transmission phenomena in Timoshenko beams are much more complex than in rods due to the dispersive nature of flexural waves, and reflection and transmission matrices are completely dependent on material properties, cross section geometry, and the frequency of loading.
- The required parameters for designing the layered stress wave attenuators include relative length of each layer, in-plane and out-of-plane dimensions, incident wave frequencies (wavelength), rigidity of the host structure, and impedance mismatch between different layers. It is observed that the dependence of the stress wave attenuator efficiency is a complex function of all parameters, and varies significantly in different ranges. The analyses reflect that impedance mismatch between different layers, incident wave frequencies (wavelength), and rigidity of the host structure are the most critical parameters in design.
- The developed optimization procedure is very effective for the optimal design of the proposed stress wave attenuators.
- The optimal design of the layered collinear and non-collinear stress wave attenuators are mainly composed of the materials with the highest and lowest impedance values, and the structures are usually optimized in a pattern in which the waves should pass from a high to low impedance material.

- Layered non-collinear stress wave attenuators have very high attenuation capacity in comparison to the collinear structures because of the existence of the flexural waves and the associated dispersion phenomenon.
- The single-layered non-collinear stress wave attenuators have a noticeable attenuation capacity especially for larger number of non-collinear parts within the structure.
- The general attenuation capacity of the porous plates is lower than the other types of the stress wave attenuators.
- The optimal design of the porous plates are usually composed of holes with the smallest and largest diameters, and the holes are usually arranged in a pattern in which the small holes are located close to the loading surface while the large holes are neighboring the fixed boundary. In addition, in majority of the optimal designs, the first and the last holes have the minimum and maximum diameters.
- In bi-layered plates, the interface profile has a significant effect in attenuating the stress waves, and the amount of attenuation depends directly on the wavelength associated with the applied impulsive loading. There is no unique interface profile for all of the impulsive loadings and the optimal design of the interface varies for the loads with different wavelengths.
- For all of the studied systems in this report, it is observed that the attenuation capacity increases for the impulsive loadings with high frequency values (short wavelength). This happens because the discontinuities within the systems can highly alter the characteristics of the stress pulses with short wavelengths.

11.3 Recommendations for Future Research

A list of recommendations for future research follows based on the results and findings of this report:

- Reflection and transmission matrices can be developed for discontinuities with viscous and plastic material properties.
- The major mechanism of stress wave attenuation in the layered systems in this report is stress wave scattering due to the impedance mismatch between the materials. A more comprehensive investigation can be performed by exploiting materials with viscous and plastic behaviors. The viscous and plastic behavior of materials can increase the attenuation capacity of the structures by adding the inelastic attenuation mechanism to the scattering attenuation.
- Generally, numerical analysis such as FE is utilized for shape optimization of continuous structures. In these problems, it is required that the FE model be modified during the optimization process. The

developed python scripts in this report can analyze the complex structural systems under various types of loading using FE method. These scripts can be easily modified during the optimization procedure; therefore, they can be coupled with various topology optimization techniques such as "ground structure method", "homogenization method", "Evolutionary structural optimization (ESO)", and "level set method (LSM)" for developing more efficient mitigating systems.

- The numerical and theoretical results obtained in this report can be verified using physical experimentation such as Split Hopkinson bar test.
- All of the investigated concepts in this report can be applied to the problems with the objective of stress wave amplification.

SECTION 12
REFERENCES

Alagappan, P., et al. (2014). "Wave propagation due to impact through layered polymer composites." *Composite Structures* **115**: 1-11.

Alleyne, D. and P. Cawley (1991). "A two-dimensional Fourier transform method for the measurement of propagating multimode signals." *The Journal of the Acoustical Society of America* **89**: 1159-1168.

Anfinsen, L. (1967). "Optimum design of layered elastic stress wave attenuators." *Journal of Applied Mechanics* **34**: 751-755.

Auld, B. A. (1973). "Acoustic fields and waves in solids", Рипол Классик.

Balling, R. J., et al. (2006). "Multiple optimum size/shape/topology designs for skeletal structures using a genetic algorithm." *Journal of Structural Engineering* **132**(7): 1158-1165.

Bathe, K.-J. (1996). "Finite element procedures." *Englewood Cliffs, N.J., Prentice Hall.*

Bel Hadj Ali, N., et al. (2009). "Multi-stage production cost optimization of semi-rigid steel frames using genetic algorithms." *Engineering Structures* **31**(11): 2766-2778.

Camp, C. V., et al. (2003). "Flexural design of reinforced concrete frames using a genetic algorithm." *Journal of Structural Engineering* **129**(1): 105-115.

Dargush, G. and R. Sant (2005). "Evolutionary aseismic design and retrofit of structures with passive energy dissipation." *Earthquake engineering & structural dynamics* **34**(13): 1601-1626.

Dede, T., et al. (2011). "Weight minimization of trusses with genetic algorithm." *Applied Soft Computing* **11**(2): 2565-2575.

Dorn, W. S., et al. (1964). "Automatic design of optimal structures." *Journal de Mecanique* **3**: 25-52.

Doyle, J. F. (1989). "Wave Propagation in Structures.", *Springer*.

El-Sabbagh, A., et al. (2008). "Topology optimization of periodic Mindlin plates." *Finite Elements in Analysis and Design* **44**(8): 439-449.

Goldberg, D. E. (1989). "Genetic Algorithms in Search, Optimization, and Machine Learning."

Hajela, P. and E. Lee (1995). "Genetic algorithms in truss topological optimization." *International journal of solids and structures* **32**(22): 3341-3357.

Holland, J. H. (1975). "Adaptation in natural and artificial systems: An introductory analysis with applications to biology, control, and artificial intelligence." *U Michigan Press.*

Jia, H., et al. (2011). "Evolutionary level set method for structural topology optimization." *Computers & Structures* **89**(5): 445-454.

Kirsch, U. (1989). "Optimal topologies of structures." *Applied Mechanics Reviews* **42**(8): 223-239.

Kociecki, M. and H. Adeli (2013). "Two-phase genetic algorithm for size optimization of free-form steel space-frame roof structures." *Journal of Constructional Steel Research* **90**: 283-296.

Konstanty, H. and F. Santosa (1995). "Optimal design of minimally reflective coatings." *Wave motion* **21**(3): 291-309.

Lavan, O. and G. F. Dargush (2009). "Multi-objective evolutionary seismic design with passive energy dissipation systems." *Journal of Earthquake Engineering* **13**(6): 758-790.

Lindholm, U. and K. Doshi (1965). "Wave propagation in an elastic nonhomogeneous bar of finite length." *Journal of Applied Mechanics* **32**: 135-142.

Luo, X., et al. (2009). "Analysis and optimal design of layered structures subjected to impulsive loading." *Computers & Structures* **87**(9): 543-551.

Luo, X., et al. (2011). "Optimal Design of Bundled Layered Elastic Stress Wave Attenuators." *Journal of Computing in Civil Engineering* **26**(3): 387-395.

Maiboroda, V., et al. (1992). "Wave attenuation in an elastic medium." *Journal of Soviet Mathematics* **60**(2): 1379-1382.

MATLAB (2012). "MATLAB R2012a and Optimization Toolbox 6.2." *Natick, Massachusetts, United States, The MathWorks, Inc.*

Mei, C. (2012). "Studying the effects of lumped end mass on vibrations of a Timoshenko beam using a wave-based approach." *Journal of Vibration and Control* **18**(5): 733-742.

Mei, C. and B. Mace (2005). "Wave reflection and transmission in Timoshenko beams and wave analysis of Timoshenko beam structures." *Journal of vibration and acoustics* **127**(4): 382-394.

Mitchell, M. (1998). "An Introduction to Genetic Algorithms (Complex Adaptive Systems)."

Moser, F., et al. (1999). "Modeling elastic wave propagation in waveguides with the finite element method." *Ndt & E International* **32**(4): 225-234.

Naik, N., et al. (2008). "Stress wave attenuation in ceramic plates." *Journal of Applied Physics* **103**(10): 103504.

Nha Chu, D., et al. (1997). "On various aspects of evolutionary structural optimization for problems with stiffness constraints." *Finite Elements in Analysis and Design* **24**(4): 197-212.

Osher, S. and J. A. Sethian (1988). "Fronts propagating with curvature-dependent speed: algorithms based on Hamilton-Jacobi formulations." *Journal of computational physics* **79**(1): 12-49.

Pandya, K. S., et al. (2012). "Stress wave attenuation in composites during ballistic impact." *Polymer Testing* **31**(2): 261-266.

Pezeshk, S., et al. (2000). "Design of nonlinear framed structures using genetic optimization." *Journal of Structural Engineering* **126**(3): 382-388.

Querin, O., et al. (1998). "Evolutionary structural optimisation (ESO) using a bidirectional algorithm." *Engineering Computations* **15**(8): 1031-1048.

Rafiee-Dehkharghani, R. (2014). "Stress wave scattering in solids for mitigating impulsive loadings." *Civil, Structural, and Environmental Engineering. Buffalo, University at Buffalo. Doctor of Philosphy*.

Rayleigh, L. (1926). "Theory of sound", 2, 161, London: Macmillan.

Rizzi, S. and J. Doyle (1992). "A spectral element approach to wave motion in layered solids." *Journal of vibration and acoustics* **114**(4): 569-577.

Sauren, A., et al. (1994). "One- and two-dimensional wave propagation in solids."

Shim, V. and K. Yap (1997). "Modelling impact deformation of foam-plate sandwich systems." *International journal of impact engineering* **19**(7): 615-636.

Simulia (2012). "Abaqus 6.12 documentation." *Dassault Systems SIMULIA Corporation*.

Singh, M. P. and L. M. Moreschi (2002). "Optimal placement of dampers for passive response control." *Earthquake engineering & structural dynamics* **31**(4): 955-976.

Sun, J., et al. (2010). "Optimization of concrete hollow brick using hybrid genetic algorithm combining with artificial neural networks." *International Journal of Heat and Mass Transfer* **53**(23): 5509-5518.

Suzuki, K. and N. Kikuchi (1991). "A homogenization method for shape and topology optimization." *Computer methods in applied mechanics and engineering* **93**(3): 291-318.

Thomson, W. T. (1950). "Transmission of elastic waves through a stratified solid medium." *Journal of Applied Physics* **21**(2): 89-93.

Timoshenko, S. P. (1921). "LXVI. On the correction for shear of the differential equation for transverse vibrations of prismatic bars." *The London, Edinburgh, and Dublin Philosophical Magazine and Journal of Science* **41**(245): 744-746.

Timoshenko, S. P. (1922). "X. On the transverse vibrations of bars of uniform cross-section." *The London, Edinburgh, and Dublin Philosophical Magazine and Journal of Science* **43**(253): 125-131.

Velo, A. P. and G. A. Gazonas (2003). "Optimal design of a two-layered elastic strip subjected to transient loading." *International journal of solids and structures* **40**(23): 6417-6428.

Wang, D., et al. (2000). "The wave annihilation technique and the design of nonreflective coatings." *SIAM Journal on Applied Mathematics* **60**(4): 1388-1424.

Wang, M. Y., et al. (2003). "A level set method for structural topology optimization." *Computer methods in applied mechanics and engineering* **192**(1): 227-246.

Xie, Y. and G. P. Steven (1993). "A simple evolutionary procedure for structural optimization." *Computers & Structures* **49**(5): 885-896.

Yang, X., et al. (1999). "Topology optimization for frequencies using an evolutionary method." *Journal of Structural Engineering* **125**(12): 1432-1438.

Yun, Y. M. and B. H. Kim (2005). "Optimum design of plane steel frame structures using second-order inelastic analysis and a genetic algorithm." *Journal of Structural Engineering* **131**(12): 1820-1831.

MCEER Technical Reports

MCEER publishes technical reports on a variety of subjects written by authors funded through MCEER. These reports are available from both MCEER Publications and the National Technical Information Service (NTIS). Requests for reports should be directed to MCEER Publications, MCEER, University at Buffalo, State University of New York, 133A Ketter Hall, Buffalo, New York 14260. Reports can also be requested through NTIS, P.O. Box 1425, Springfield, Virginia 22151. NTIS accession numbers are shown in parenthesis, if available.

NCEER-87-0001 "First-Year Program in Research, Education and Technology Transfer," 3/5/87, (PB88-134275, A04, MF-A01).

NCEER-87-0002 "Experimental Evaluation of Instantaneous Optimal Algorithms for Structural Control," by R.C. Lin, T.T. Soong and A.M. Reinhorn, 4/20/87, (PB88-134341, A04, MF-A01).

NCEER-87-0003 "Experimentation Using the Earthquake Simulation Facilities at University at Buffalo," by A.M. Reinhorn and R.L. Ketter, not available.

NCEER-87-0004 "The System Characteristics and Performance of a Shaking Table," by J.S. Hwang, K.C. Chang and G.C. Lee, 6/1/87, (PB88-134259, A03, MF-A01). This report is available only through NTIS (see address given above).

NCEER-87-0005 "A Finite Element Formulation for Nonlinear Viscoplastic Material Using a Q Model," by O. Gyebi and G. Dasgupta, 11/2/87, (PB88-213764, A08, MF-A01).

NCEER-87-0006 "Symbolic Manipulation Program (SMP) - Algebraic Codes for Two and Three Dimensional Finite Element Formulations," by X. Lee and G. Dasgupta, 11/9/87, (PB88-218522, A05, MF-A01).

NCEER-87-0007 "Instantaneous Optimal Control Laws for Tall Buildings Under Seismic Excitations," by J.N. Yang, A. Akbarpour and P. Ghaemmaghami, 6/10/87, (PB88-134333, A06, MF-A01). This report is only available through NTIS (see address given above).

NCEER-87-0008 "IDARC: Inelastic Damage Analysis of Reinforced Concrete Frame - Shear-Wall Structures," by Y.J. Park, A.M. Reinhorn and S.K. Kunnath, 7/20/87, (PB88-134325, A09, MF-A01). This report is only available through NTIS (see address given above).

NCEER-87-0009 "Liquefaction Potential for New York State: A Preliminary Report on Sites in Manhattan and Buffalo," by M. Budhu, V. Vijayakumar, R.F. Giese and L. Baumgras, 8/31/87, (PB88-163704, A03, MF-A01). This report is available only through NTIS (see address given above).

NCEER-87-0010 "Vertical and Torsional Vibration of Foundations in Inhomogeneous Media," by A.S. Veletsos and K.W. Dotson, 6/1/87, (PB88-134291, A03, MF-A01). This report is only available through NTIS (see address given above).

NCEER-87-0011 "Seismic Probabilistic Risk Assessment and Seismic Margins Studies for Nuclear Power Plants," by Howard H.M. Hwang, 6/15/87, (PB88-134267, A03, MF-A01). This report is only available through NTIS (see address given above).

NCEER-87-0012 "Parametric Studies of Frequency Response of Secondary Systems Under Ground-Acceleration Excitations," by Y. Yong and Y.K. Lin, 6/10/87, (PB88-134309, A03, MF-A01). This report is only available through NTIS (see address given above).

NCEER-87-0013 "Frequency Response of Secondary Systems Under Seismic Excitation," by J.A. HoLung, J. Cai and Y.K. Lin, 7/31/87, (PB88-134317, A05, MF-A01). This report is only available through NTIS (see address given above).

NCEER-87-0014 "Modelling Earthquake Ground Motions in Seismically Active Regions Using Parametric Time Series Methods," by G.W. Ellis and A.S. Cakmak, 8/25/87, (PB88-134283, A08, MF-A01). This report is only available through NTIS (see address given above).

NCEER-87-0015 "Detection and Assessment of Seismic Structural Damage," by E. DiPasquale and A.S. Cakmak, 8/25/87, (PB88-163712, A05, MF-A01). This report is only available through NTIS (see address given above).

NCEER-87-0016 "Pipeline Experiment at Parkfield, California," by J. Isenberg and E. Richardson, 9/15/87, (PB88-163720, A03, MF-A01). This report is available only through NTIS (see address given above).

NCEER-87-0017 "Digital Simulation of Seismic Ground Motion," by M. Shinozuka, G. Deodatis and T. Harada, 8/31/87, (PB88-155197, A04, MF-A01). This report is available only through NTIS (see address given above).

NCEER-87-0018 "Practical Considerations for Structural Control: System Uncertainty, System Time Delay and Truncation of Small Control Forces," J.N. Yang and A. Akbarpour, 8/10/87, (PB88-163738, A08, MF-A01). This report is only available through NTIS (see address given above).

NCEER-87-0019 "Modal Analysis of Nonclassically Damped Structural Systems Using Canonical Transformation," by J.N. Yang, S. Sarkani and F.X. Long, 9/27/87, (PB88-187851, A04, MF-A01).

NCEER-87-0020 "A Nonstationary Solution in Random Vibration Theory," by J.R. Red-Horse and P.D. Spanos, 11/3/87, (PB88-163746, A03, MF-A01).

NCEER-87-0021 "Horizontal Impedances for Radially Inhomogeneous Viscoelastic Soil Layers," by A.S. Veletsos and K.W. Dotson, 10/15/87, (PB88-150859, A04, MF-A01).

NCEER-87-0022 "Seismic Damage Assessment of Reinforced Concrete Members," by Y.S. Chung, C. Meyer and M. Shinozuka, 10/9/87, (PB88-150867, A05, MF-A01). This report is available only through NTIS (see address given above).

NCEER-87-0023 "Active Structural Control in Civil Engineering," by T.T. Soong, 11/11/87, (PB88-187778, A03, MF-A01).

NCEER-87-0024 "Vertical and Torsional Impedances for Radially Inhomogeneous Viscoelastic Soil Layers," by K.W. Dotson and A.S. Veletsos, 12/87, (PB88-187786, A03, MF-A01).

NCEER-87-0025 "Proceedings from the Symposium on Seismic Hazards, Ground Motions, Soil-Liquefaction and Engineering Practice in Eastern North America," October 20-22, 1987, edited by K.H. Jacob, 12/87, (PB88-188115, A23, MF-A01). This report is available only through NTIS (see address given above).

NCEER-87-0026 "Report on the Whittier-Narrows, California, Earthquake of October 1, 1987," by J. Pantelic and A. Reinhorn, 11/87, (PB88-187752, A03, MF-A01). This report is available only through NTIS (see address given above).

NCEER-87-0027 "Design of a Modular Program for Transient Nonlinear Analysis of Large 3-D Building Structures," by S. Srivastav and J.F. Abel, 12/30/87, (PB88-187950, A05, MF-A01). This report is only available through NTIS (see address given above).

NCEER-87-0028 "Second-Year Program in Research, Education and Technology Transfer," 3/8/88, (PB88-219480, A04, MF-A01).

NCEER-88-0001 "Workshop on Seismic Computer Analysis and Design of Buildings With Interactive Graphics," by W. McGuire, J.F. Abel and C.H. Conley, 1/18/88, (PB88-187760, A03, MF-A01). This report is only available through NTIS (see address given above).

NCEER-88-0002 "Optimal Control of Nonlinear Flexible Structures," by J.N. Yang, F.X. Long and D. Wong, 1/22/88, (PB88-213772, A06, MF-A01).

NCEER-88-0003 "Substructuring Techniques in the Time Domain for Primary-Secondary Structural Systems," by G.D. Manolis and G. Juhn, 2/10/88, (PB88-213780, A04, MF-A01).

NCEER-88-0004 "Iterative Seismic Analysis of Primary-Secondary Systems," by A. Singhal, L.D. Lutes and P.D. Spanos, 2/23/88, (PB88-213798, A04, MF-A01).

NCEER-88-0005 "Stochastic Finite Element Expansion for Random Media," by P.D. Spanos and R. Ghanem, 3/14/88, (PB88-213806, A03, MF-A01).

NCEER-88-0006 "Combining Structural Optimization and Structural Control," by F.Y. Cheng and C.P. Pantelides, 1/10/88, (PB88-213814, A05, MF-A01).

NCEER-88-0007 "Seismic Performance Assessment of Code-Designed Structures," by H.H-M. Hwang, J-W. Jaw and H-J. Shau, 3/20/88, (PB88-219423, A04, MF-A01). This report is only available through NTIS (see address given above).

NCEER-88-0008 "Reliability Analysis of Code-Designed Structures Under Natural Hazards," by H.H-M. Hwang, H. Ushiba and M. Shinozuka, 2/29/88, (PB88-229471, A07, MF-A01). This report is only available through NTIS (see address given above).

NCEER-88-0009 "Seismic Fragility Analysis of Shear Wall Structures," by J-W Jaw and H.H-M. Hwang, 4/30/88, (PB89-102867, A04, MF-A01).

NCEER-88-0010 "Base Isolation of a Multi-Story Building Under a Harmonic Ground Motion - A Comparison of Performances of Various Systems," by F-G Fan, G. Ahmadi and I.G. Tadjbakhsh, 5/18/88, (PB89-122238, A06, MF-A01). This report is only available through NTIS (see address given above).

NCEER-88-0011 "Seismic Floor Response Spectra for a Combined System by Green's Functions," by F.M. Lavelle, L.A. Bergman and P.D. Spanos, 5/1/88, (PB89-102875, A03, MF-A01).

NCEER-88-0012 "A New Solution Technique for Randomly Excited Hysteretic Structures," by G.Q. Cai and Y.K. Lin, 5/16/88, (PB89-102883, A03, MF-A01).

NCEER-88-0013 "A Study of Radiation Damping and Soil-Structure Interaction Effects in the Centrifuge," by K. Weissman, supervised by J.H. Prevost, 5/24/88, (PB89-144703, A06, MF-A01).

NCEER-88-0014 "Parameter Identification and Implementation of a Kinematic Plasticity Model for Frictional Soils," by J.H. Prevost and D.V. Griffiths, not available.

NCEER-88-0015 "Two- and Three- Dimensional Dynamic Finite Element Analyses of the Long Valley Dam," by D.V. Griffiths and J.H. Prevost, 6/17/88, (PB89-144711, A04, MF-A01).

NCEER-88-0016 "Damage Assessment of Reinforced Concrete Structures in Eastern United States," by A.M. Reinhorn, M.J. Seidel, S.K. Kunnath and Y.J. Park, 6/15/88, (PB89-122220, A04, MF-A01). This report is only available through NTIS (see address given above).

NCEER-88-0017 "Dynamic Compliance of Vertically Loaded Strip Foundations in Multilayered Viscoelastic Soils," by S. Ahmad and A.S.M. Israil, 6/17/88, (PB89-102891, A04, MF-A01).

NCEER-88-0018 "An Experimental Study of Seismic Structural Response With Added Viscoelastic Dampers," by R.C. Lin, Z. Liang, T.T. Soong and R.H. Zhang, 6/30/88, (PB89-122212, A05, MF-A01). This report is available only through NTIS (see address given above).

NCEER-88-0019 "Experimental Investigation of Primary - Secondary System Interaction," by G.D. Manolis, G. Juhn and A.M. Reinhorn, 5/27/88, (PB89-122204, A04, MF-A01).

NCEER-88-0020 "A Response Spectrum Approach For Analysis of Nonclassically Damped Structures," by J.N. Yang, S. Sarkani and F.X. Long, 4/22/88, (PB89-102909, A04, MF-A01).

NCEER-88-0021 "Seismic Interaction of Structures and Soils: Stochastic Approach," by A.S. Veletsos and A.M. Prasad, 7/21/88, (PB89-122196, A04, MF-A01). This report is only available through NTIS (see address given above).

NCEER-88-0022 "Identification of the Serviceability Limit State and Detection of Seismic Structural Damage," by E. DiPasquale and A.S. Cakmak, 6/15/88, (PB89-122188, A05, MF-A01). This report is available only through NTIS (see address given above).

NCEER-88-0023 "Multi-Hazard Risk Analysis: Case of a Simple Offshore Structure," by B.K. Bhartia and E.H. Vanmarcke, 7/21/88, (PB89-145213, A05, MF-A01).

NCEER-88-0024 "Automated Seismic Design of Reinforced Concrete Buildings," by Y.S. Chung, C. Meyer and M. Shinozuka, 7/5/88, (PB89-122170, A06, MF-A01). This report is available only through NTIS (see address given above).

NCEER-88-0025 "Experimental Study of Active Control of MDOF Structures Under Seismic Excitations," by L.L. Chung, R.C. Lin, T.T. Soong and A.M. Reinhorn, 7/10/88, (PB89-122600, A04, MF-A01).

NCEER-88-0026 "Earthquake Simulation Tests of a Low-Rise Metal Structure," by J.S. Hwang, K.C. Chang, G.C. Lee and R.L. Ketter, 8/1/88, (PB89-102917, A04, MF-A01).

NCEER-88-0027 "Systems Study of Urban Response and Reconstruction Due to Catastrophic Earthquakes," by F. Kozin and H.K. Zhou, 9/22/88, (PB90-162348, A04, MF-A01).

NCEER-88-0028 "Seismic Fragility Analysis of Plane Frame Structures," by H.H-M. Hwang and Y.K. Low, 7/31/88, (PB89-131445, A06, MF-A01).

NCEER-88-0029 "Response Analysis of Stochastic Structures," by A. Kardara, C. Bucher and M. Shinozuka, 9/22/88, (PB89-174429, A04, MF-A01).

NCEER-88-0030 "Nonnormal Accelerations Due to Yielding in a Primary Structure," by D.C.K. Chen and L.D. Lutes, 9/19/88, (PB89-131437, A04, MF-A01).

NCEER-88-0031 "Design Approaches for Soil-Structure Interaction," by A.S. Veletsos, A.M. Prasad and Y. Tang, 12/30/88, (PB89-174437, A03, MF-A01). This report is available only through NTIS (see address given above).

NCEER-88-0032 "A Re-evaluation of Design Spectra for Seismic Damage Control," by C.J. Turkstra and A.G. Tallin, 11/7/88, (PB89-145221, A05, MF-A01).

NCEER-88-0033 "The Behavior and Design of Noncontact Lap Splices Subjected to Repeated Inelastic Tensile Loading," by V.E. Sagan, P. Gergely and R.N. White, 12/8/88, (PB89-163737, A08, MF-A01).

NCEER-88-0034 "Seismic Response of Pile Foundations," by S.M. Mamoon, P.K. Banerjee and S. Ahmad, 11/1/88, (PB89-145239, A04, MF-A01).

NCEER-88-0035 "Modeling of R/C Building Structures With Flexible Floor Diaphragms (IDARC2)," by A.M. Reinhorn, S.K. Kunnath and N. Panahshahi, 9/7/88, (PB89-207153, A07, MF-A01).

NCEER-88-0036 "Solution of the Dam-Reservoir Interaction Problem Using a Combination of FEM, BEM with Particular Integrals, Modal Analysis, and Substructuring," by C-S. Tsai, G.C. Lee and R.L. Ketter, 12/31/88, (PB89-207146, A04, MF-A01).

NCEER-88-0037 "Optimal Placement of Actuators for Structural Control," by F.Y. Cheng and C.P. Pantelides, 8/15/88, (PB89-162846, A05, MF-A01).

NCEER-88-0038 "Teflon Bearings in Aseismic Base Isolation: Experimental Studies and Mathematical Modeling," by A. Mokha, M.C. Constantinou and A.M. Reinhorn, 12/5/88, (PB89-218457, A10, MF-A01). This report is available only through NTIS (see address given above).

NCEER-88-0039 "Seismic Behavior of Flat Slab High-Rise Buildings in the New York City Area," by P. Weidlinger and M. Ettouney, 10/15/88, (PB90-145681, A04, MF-A01).

NCEER-88-0040 "Evaluation of the Earthquake Resistance of Existing Buildings in New York City," by P. Weidlinger and M. Ettouney, 10/15/88, not available.

NCEER-88-0041 "Small-Scale Modeling Techniques for Reinforced Concrete Structures Subjected to Seismic Loads," by W. Kim, A. El-Attar and R.N. White, 11/22/88, (PB89-189625, A05, MF-A01).

NCEER-88-0042 "Modeling Strong Ground Motion from Multiple Event Earthquakes," by G.W. Ellis and A.S. Cakmak, 10/15/88, (PB89-174445, A03, MF-A01).

NCEER-88-0043 "Nonstationary Models of Seismic Ground Acceleration," by M. Grigoriu, S.E. Ruiz and E. Rosenblueth, 7/15/88, (PB89-189617, A04, MF-A01).

NCEER-88-0044 "SARCF User's Guide: Seismic Analysis of Reinforced Concrete Frames," by Y.S. Chung, C. Meyer and M. Shinozuka, 11/9/88, (PB89-174452, A08, MF-A01).

NCEER-88-0045 "First Expert Panel Meeting on Disaster Research and Planning," edited by J. Pantelic and J. Stoyle, 9/15/88, (PB89-174460, A05, MF-A01).

NCEER-88-0046 "Preliminary Studies of the Effect of Degrading Infill Walls on the Nonlinear Seismic Response of Steel Frames," by C.Z. Chrysostomou, P. Gergely and J.F. Abel, 12/19/88, (PB89-208383, A05, MF-A01).

NCEER-88-0047 "Reinforced Concrete Frame Component Testing Facility - Design, Construction, Instrumentation and Operation," by S.P. Pessiki, C. Conley, T. Bond, P. Gergely and R.N. White, 12/16/88, (PB89-174478, A04, MF-A01).

NCEER-89-0001 "Effects of Protective Cushion and Soil Compliancy on the Response of Equipment Within a Seismically Excited Building," by J.A. HoLung, 2/16/89, (PB89-207179, A04, MF-A01).

NCEER-89-0002 "Statistical Evaluation of Response Modification Factors for Reinforced Concrete Structures," by H.H-M. Hwang and J-W. Jaw, 2/17/89, (PB89-207187, A05, MF-A01).

NCEER-89-0003 "Hysteretic Columns Under Random Excitation," by G-Q. Cai and Y.K. Lin, 1/9/89, (PB89-196513, A03, MF-A01).

NCEER-89-0004 "Experimental Study of `Elephant Foot Bulge' Instability of Thin-Walled Metal Tanks," by Z-H. Jia and R.L. Ketter, 2/22/89, (PB89-207195, A03, MF-A01).

NCEER-89-0005 "Experiment on Performance of Buried Pipelines Across San Andreas Fault," by J. Isenberg, E. Richardson and T.D. O'Rourke, 3/10/89, (PB89-218440, A04, MF-A01). This report is available only through NTIS (see address given above).

NCEER-89-0006 "A Knowledge-Based Approach to Structural Design of Earthquake-Resistant Buildings," by M. Subramani, P. Gergely, C.H. Conley, J.F. Abel and A.H. Zaghw, 1/15/89, (PB89-218465, A06, MF-A01).

NCEER-89-0007 "Liquefaction Hazards and Their Effects on Buried Pipelines," by T.D. O'Rourke and P.A. Lane, 2/1/89, (PB89-218481, A09, MF-A01).

NCEER-89-0008 "Fundamentals of System Identification in Structural Dynamics," by H. Imai, C-B. Yun, O. Maruyama and M. Shinozuka, 1/26/89, (PB89-207211, A04, MF-A01).

NCEER-89-0009 "Effects of the 1985 Michoacan Earthquake on Water Systems and Other Buried Lifelines in Mexico," by A.G. Ayala and M.J. O'Rourke, 3/8/89, (PB89-207229, A06, MF-A01).

NCEER-89-R010 "NCEER Bibliography of Earthquake Education Materials," by K.E.K. Ross, Second Revision, 9/1/89, (PB90-125352, A05, MF-A01). This report is replaced by NCEER-92-0018.

NCEER-89-0011 "Inelastic Three-Dimensional Response Analysis of Reinforced Concrete Building Structures (IDARC-3D), Part I - Modeling," by S.K. Kunnath and A.M. Reinhorn, 4/17/89, (PB90-114612, A07, MF-A01). This report is available only through NTIS (see address given above).

NCEER-89-0012 "Recommended Modifications to ATC-14," by C.D. Poland and J.O. Malley, 4/12/89, (PB90-108648, A15, MF-A01).

NCEER-89-0013 "Repair and Strengthening of Beam-to-Column Connections Subjected to Earthquake Loading," by M. Corazao and A.J. Durrani, 2/28/89, (PB90-109885, A06, MF-A01).

NCEER-89-0014 "Program EXKAL2 for Identification of Structural Dynamic Systems," by O. Maruyama, C-B. Yun, M. Hoshiya and M. Shinozuka, 5/19/89, (PB90-109877, A09, MF-A01).

NCEER-89-0015 "Response of Frames With Bolted Semi-Rigid Connections, Part I - Experimental Study and Analytical Predictions," by P.J. DiCorso, A.M. Reinhorn, J.R. Dickerson, J.B. Radziminski and W.L. Harper, 6/1/89, not available.

NCEER-89-0016 "ARMA Monte Carlo Simulation in Probabilistic Structural Analysis," by P.D. Spanos and M.P. Mignolet, 7/10/89, (PB90-109893, A03, MF-A01).

NCEER-89-P017 "Preliminary Proceedings from the Conference on Disaster Preparedness - The Place of Earthquake Education in Our Schools," Edited by K.E.K. Ross, 6/23/89, (PB90-108606, A03, MF-A01).

NCEER-89-0017 "Proceedings from the Conference on Disaster Preparedness - The Place of Earthquake Education in Our Schools," Edited by K.E.K. Ross, 12/31/89, (PB90-207895, A012, MF-A02). This report is available only through NTIS (see address given above).

NCEER-89-0018 "Multidimensional Models of Hysteretic Material Behavior for Vibration Analysis of Shape Memory Energy Absorbing Devices, by E.J. Graesser and F.A. Cozzarelli, 6/7/89, (PB90-164146, A04, MF-A01).

NCEER-89-0019 "Nonlinear Dynamic Analysis of Three-Dimensional Base Isolated Structures (3D-BASIS)," by S. Nagarajaiah, A.M. Reinhorn and M.C. Constantinou, 8/3/89, (PB90-161936, A06, MF-A01). This report has been replaced by NCEER-93-0011.

NCEER-89-0020 "Structural Control Considering Time-Rate of Control Forces and Control Rate Constraints," by F.Y. Cheng and C.P. Pantelides, 8/3/89, (PB90-120445, A04, MF-A01).

NCEER-89-0021 "Subsurface Conditions of Memphis and Shelby County," by K.W. Ng, T-S. Chang and H-H.M. Hwang, 7/26/89, (PB90-120437, A03, MF-A01).

NCEER-89-0022 "Seismic Wave Propagation Effects on Straight Jointed Buried Pipelines," by K. Elhmadi and M.J. O'Rourke, 8/24/89, (PB90-162322, A10, MF-A02).

NCEER-89-0023 "Workshop on Serviceability Analysis of Water Delivery Systems," edited by M. Grigoriu, 3/6/89, (PB90-127424, A03, MF-A01).

NCEER-89-0024 "Shaking Table Study of a 1/5 Scale Steel Frame Composed of Tapered Members," by K.C. Chang, J.S. Hwang and G.C. Lee, 9/18/89, (PB90-160169, A04, MF-A01).

NCEER-89-0025 "DYNA1D: A Computer Program for Nonlinear Seismic Site Response Analysis - Technical Documentation," by Jean H. Prevost, 9/14/89, (PB90-161944, A07, MF-A01). This report is available only through NTIS (see address given above).

NCEER-89-0026 "1:4 Scale Model Studies of Active Tendon Systems and Active Mass Dampers for Aseismic Protection," by A.M. Reinhorn, T.T. Soong, R.C. Lin, Y.P. Yang, Y. Fukao, H. Abe and M. Nakai, 9/15/89, (PB90-173246, A10, MF-A02). This report is available only through NTIS (see address given above).

NCEER-89-0027 "Scattering of Waves by Inclusions in a Nonhomogeneous Elastic Half Space Solved by Boundary Element Methods," by P.K. Hadley, A. Askar and A.S. Cakmak, 6/15/89, (PB90-145699, A07, MF-A01).

NCEER-89-0028 "Statistical Evaluation of Deflection Amplification Factors for Reinforced Concrete Structures," by H.H.M. Hwang, J-W. Jaw and A.L. Ch'ng, 8/31/89, (PB90-164633, A05, MF-A01).

NCEER-89-0029 "Bedrock Accelerations in Memphis Area Due to Large New Madrid Earthquakes," by H.H.M. Hwang, C.H.S. Chen and G. Yu, 11/7/89, (PB90-162330, A04, MF-A01).

NCEER-89-0030 "Seismic Behavior and Response Sensitivity of Secondary Structural Systems," by Y.Q. Chen and T.T. Soong, 10/23/89, (PB90-164658, A08, MF-A01).

NCEER-89-0031 "Random Vibration and Reliability Analysis of Primary-Secondary Structural Systems," by Y. Ibrahim, M. Grigoriu and T.T. Soong, 11/10/89, (PB90-161951, A04, MF-A01).

NCEER-89-0032 "Proceedings from the Second U.S. - Japan Workshop on Liquefaction, Large Ground Deformation and Their Effects on Lifelines, September 26-29, 1989," Edited by T.D. O'Rourke and M. Hamada, 12/1/89, (PB90-209388, A22, MF-A03).

NCEER-89-0033 "Deterministic Model for Seismic Damage Evaluation of Reinforced Concrete Structures," by J.M. Bracci, A.M. Reinhorn, J.B. Mander and S.K. Kunnath, 9/27/89, (PB91-108803, A06, MF-A01).

NCEER-89-0034 "On the Relation Between Local and Global Damage Indices," by E. DiPasquale and A.S. Cakmak, 8/15/89, (PB90-173865, A05, MF-A01).

NCEER-89-0035 "Cyclic Undrained Behavior of Nonplastic and Low Plasticity Silts," by A.J. Walker and H.E. Stewart, 7/26/89, (PB90-183518, A10, MF-A01).

NCEER-89-0036 "Liquefaction Potential of Surficial Deposits in the City of Buffalo, New York," by M. Budhu, R. Giese and L. Baumgrass, 1/17/89, (PB90-208455, A04, MF-A01).

NCEER-89-0037 "A Deterministic Assessment of Effects of Ground Motion Incoherence," by A.S. Veletsos and Y. Tang, 7/15/89, (PB90-164294, A03, MF-A01).

NCEER-89-0038 "Workshop on Ground Motion Parameters for Seismic Hazard Mapping," July 17-18, 1989, edited by R.V. Whitman, 12/1/89, (PB90-173923, A04, MF-A01).

NCEER-89-0039 "Seismic Effects on Elevated Transit Lines of the New York City Transit Authority," by C.J. Costantino, C.A. Miller and E. Heymsfield, 12/26/89, (PB90-207887, A06, MF-A01).

NCEER-89-0040 "Centrifugal Modeling of Dynamic Soil-Structure Interaction," by K. Weissman, Supervised by J.H. Prevost, 5/10/89, (PB90-207879, A07, MF-A01).

NCEER-89-0041 "Linearized Identification of Buildings With Cores for Seismic Vulnerability Assessment," by I-K. Ho and A.E. Aktan, 11/1/89, (PB90-251943, A07, MF-A01).

NCEER-90-0001 "Geotechnical and Lifeline Aspects of the October 17, 1989 Loma Prieta Earthquake in San Francisco," by T.D. O'Rourke, H.E. Stewart, F.T. Blackburn and T.S. Dickerman, 1/90, (PB90-208596, A05, MF-A01).

NCEER-90-0002 "Nonnormal Secondary Response Due to Yielding in a Primary Structure," by D.C.K. Chen and L.D. Lutes, 2/28/90, (PB90-251976, A07, MF-A01).

NCEER-90-0003 "Earthquake Education Materials for Grades K-12," by K.E.K. Ross, 4/16/90, (PB91-251984, A05, MF-A05). This report has been replaced by NCEER-92-0018.

NCEER-90-0004 "Catalog of Strong Motion Stations in Eastern North America," by R.W. Busby, 4/3/90, (PB90-251984, A05, MF-A01).

NCEER-90-0005 "NCEER Strong-Motion Data Base: A User Manual for the GeoBase Release (Version 1.0 for the Sun3)," by P. Friberg and K. Jacob, 3/31/90 (PB90-258062, A04, MF-A01).

NCEER-90-0006 "Seismic Hazard Along a Crude Oil Pipeline in the Event of an 1811-1812 Type New Madrid Earthquake," by H.H.M. Hwang and C-H.S. Chen, 4/16/90, (PB90-258054, A04, MF-A01).

NCEER-90-0007 "Site-Specific Response Spectra for Memphis Sheahan Pumping Station," by H.H.M. Hwang and C.S. Lee, 5/15/90, (PB91-108811, A05, MF-A01).

NCEER-90-0008 "Pilot Study on Seismic Vulnerability of Crude Oil Transmission Systems," by T. Ariman, R. Dobry, M. Grigoriu, F. Kozin, M. O'Rourke, T. O'Rourke and M. Shinozuka, 5/25/90, (PB91-108837, A06, MF-A01).

NCEER-90-0009 "A Program to Generate Site Dependent Time Histories: EQGEN," by G.W. Ellis, M. Srinivasan and A.S. Cakmak, 1/30/90, (PB91-108829, A04, MF-A01).

NCEER-90-0010 "Active Isolation for Seismic Protection of Operating Rooms," by M.E. Talbott, Supervised by M. Shinozuka, 6/8/9, (PB91-110205, A05, MF-A01).

NCEER-90-0011 "Program LINEARID for Identification of Linear Structural Dynamic Systems," by C-B. Yun and M. Shinozuka, 6/25/90, (PB91-110312, A08, MF-A01).

NCEER-90-0012 "Two-Dimensional Two-Phase Elasto-Plastic Seismic Response of Earth Dams," by A.N. Yiagos, Supervised by J.H. Prevost, 6/20/90, (PB91-110197, A13, MF-A02).

NCEER-90-0013 "Secondary Systems in Base-Isolated Structures: Experimental Investigation, Stochastic Response and Stochastic Sensitivity," by G.D. Manolis, G. Juhn, M.C. Constantinou and A.M. Reinhorn, 7/1/90, (PB91-110320, A08, MF-A01).

NCEER-90-0014 "Seismic Behavior of Lightly-Reinforced Concrete Column and Beam-Column Joint Details," by S.P. Pessiki, C.H. Conley, P. Gergely and R.N. White, 8/22/90, (PB91-108795, A11, MF-A02).

NCEER-90-0015 "Two Hybrid Control Systems for Building Structures Under Strong Earthquakes," by J.N. Yang and A. Danielians, 6/29/90, (PB91-125393, A04, MF-A01).

NCEER-90-0016 "Instantaneous Optimal Control with Acceleration and Velocity Feedback," by J.N. Yang and Z. Li, 6/29/90, (PB91-125401, A03, MF-A01).

NCEER-90-0017 "Reconnaissance Report on the Northern Iran Earthquake of June 21, 1990," by M. Mehrain, 10/4/90, (PB91-125377, A03, MF-A01).

NCEER-90-0018 "Evaluation of Liquefaction Potential in Memphis and Shelby County," by T.S. Chang, P.S. Tang, C.S. Lee and H. Hwang, 8/10/90, (PB91-125427, A09, MF-A01).

NCEER-90-0019 "Experimental and Analytical Study of a Combined Sliding Disc Bearing and Helical Steel Spring Isolation System," by M.C. Constantinou, A.S. Mokha and A.M. Reinhorn, 10/4/90, (PB91-125385, A06, MF-A01). This report is available only through NTIS (see address given above).

NCEER-90-0020 "Experimental Study and Analytical Prediction of Earthquake Response of a Sliding Isolation System with a Spherical Surface," by A.S. Mokha, M.C. Constantinou and A.M. Reinhorn, 10/11/90, (PB91-125419, A05, MF-A01).

NCEER-90-0021 "Dynamic Interaction Factors for Floating Pile Groups," by G. Gazetas, K. Fan, A. Kaynia and E. Kausel, 9/10/90, (PB91-170381, A05, MF-A01).

NCEER-90-0022 "Evaluation of Seismic Damage Indices for Reinforced Concrete Structures," by S. Rodriguez-Gomez and A.S. Cakmak, 9/30/90, PB91-171322, A06, MF-A01).

NCEER-90-0023 "Study of Site Response at a Selected Memphis Site," by H. Desai, S. Ahmad, E.S. Gazetas and M.R. Oh, 10/11/90, (PB91-196857, A03, MF-A01).

NCEER-90-0024 "A User's Guide to Strongmo: Version 1.0 of NCEER's Strong-Motion Data Access Tool for PCs and Terminals," by P.A. Friberg and C.A.T. Susch, 11/15/90, (PB91-171272, A03, MF-A01).

NCEER-90-0025 "A Three-Dimensional Analytical Study of Spatial Variability of Seismic Ground Motions," by L-L. Hong and A.H.-S. Ang, 10/30/90, (PB91-170399, A09, MF-A01).

NCEER-90-0026 "MUMOID User's Guide - A Program for the Identification of Modal Parameters," by S. Rodriguez-Gomez and E. DiPasquale, 9/30/90, (PB91-171298, A04, MF-A01).

NCEER-90-0027 "SARCF-II User's Guide - Seismic Analysis of Reinforced Concrete Frames," by S. Rodriguez-Gomez, Y.S. Chung and C. Meyer, 9/30/90, (PB91-171280, A05, MF-A01).

NCEER-90-0028 "Viscous Dampers: Testing, Modeling and Application in Vibration and Seismic Isolation," by N. Makris and M.C. Constantinou, 12/20/90 (PB91-190561, A06, MF-A01).

NCEER-90-0029 "Soil Effects on Earthquake Ground Motions in the Memphis Area," by H. Hwang, C.S. Lee, K.W. Ng and T.S. Chang, 8/2/90, (PB91-190751, A05, MF-A01).

NCEER-91-0001 "Proceedings from the Third Japan-U.S. Workshop on Earthquake Resistant Design of Lifeline Facilities and Countermeasures for Soil Liquefaction, December 17-19, 1990," edited by T.D. O'Rourke and M. Hamada, 2/1/91, (PB91-179259, A99, MF-A04).

NCEER-91-0002 "Physical Space Solutions of Non-Proportionally Damped Systems," by M. Tong, Z. Liang and G.C. Lee, 1/15/91, (PB91-179242, A04, MF-A01).

NCEER-91-0003 "Seismic Response of Single Piles and Pile Groups," by K. Fan and G. Gazetas, 1/10/91, (PB92-174994, A04, MF-A01).

NCEER-91-0004 "Damping of Structures: Part 1 - Theory of Complex Damping," by Z. Liang and G. Lee, 10/10/91, (PB92-197235, A12, MF-A03).

NCEER-91-0005 "3D-BASIS - Nonlinear Dynamic Analysis of Three Dimensional Base Isolated Structures: Part II," by S. Nagarajaiah, A.M. Reinhorn and M.C. Constantinou, 2/28/91, (PB91-190553, A07, MF-A01). This report has been replaced by NCEER-93-0011.

NCEER-91-0006 "A Multidimensional Hysteretic Model for Plasticity Deforming Metals in Energy Absorbing Devices," by E.J. Graesser and F.A. Cozzarelli, 4/9/91, (PB92-108364, A04, MF-A01).

NCEER-91-0007 "A Framework for Customizable Knowledge-Based Expert Systems with an Application to a KBES for Evaluating the Seismic Resistance of Existing Buildings," by E.G. Ibarra-Anaya and S.J. Fenves, 4/9/91, (PB91-210930, A08, MF-A01).

NCEER-91-0008 "Nonlinear Analysis of Steel Frames with Semi-Rigid Connections Using the Capacity Spectrum Method," by G.G. Deierlein, S-H. Hsieh, Y-J. Shen and J.F. Abel, 7/2/91, (PB92-113828, A05, MF-A01).

NCEER-91-0009 "Earthquake Education Materials for Grades K-12," by K.E.K. Ross, 4/30/91, (PB91-212142, A06, MF-A01). This report has been replaced by NCEER-92-0018.

NCEER-91-0010 "Phase Wave Velocities and Displacement Phase Differences in a Harmonically Oscillating Pile," by N. Makris and G. Gazetas, 7/8/91, (PB92-108356, A04, MF-A01).

NCEER-91-0011 "Dynamic Characteristics of a Full-Size Five-Story Steel Structure and a 2/5 Scale Model," by K.C. Chang, G.C. Yao, G.C. Lee, D.S. Hao and Y.C. Yeh," 7/2/91, (PB93-116648, A06, MF-A02).

NCEER-91-0012 "Seismic Response of a 2/5 Scale Steel Structure with Added Viscoelastic Dampers," by K.C. Chang, T.T. Soong, S-T. Oh and M.L. Lai, 5/17/91, (PB92-110816, A05, MF-A01).

NCEER-91-0013 "Earthquake Response of Retaining Walls; Full-Scale Testing and Computational Modeling," by S. Alampalli and A-W.M. Elgamal, 6/20/91, not available.

NCEER-91-0014 "3D-BASIS-M: Nonlinear Dynamic Analysis of Multiple Building Base Isolated Structures," by P.C. Tsopelas, S. Nagarajaiah, M.C. Constantinou and A.M. Reinhorn, 5/28/91, (PB92-113885, A09, MF-A02).

NCEER-91-0015 "Evaluation of SEAOC Design Requirements for Sliding Isolated Structures," by D. Theodossiou and M.C. Constantinou, 6/10/91, (PB92-114602, A11, MF-A03).

NCEER-91-0016 "Closed-Loop Modal Testing of a 27-Story Reinforced Concrete Flat Plate-Core Building," by H.R. Somaprasad, T. Toksoy, H. Yoshiyuki and A.E. Aktan, 7/15/91, (PB92-129980, A07, MF-A02).

NCEER-91-0017 "Shake Table Test of a 1/6 Scale Two-Story Lightly Reinforced Concrete Building," by A.G. El-Attar, R.N. White and P. Gergely, 2/28/91, (PB92-222447, A06, MF-A02).

NCEER-91-0018 "Shake Table Test of a 1/8 Scale Three-Story Lightly Reinforced Concrete Building," by A.G. El-Attar, R.N. White and P. Gergely, 2/28/91, (PB93-116630, A08, MF-A02).

NCEER-91-0019 "Transfer Functions for Rigid Rectangular Foundations," by A.S. Veletsos, A.M. Prasad and W.H. Wu, 7/31/91, not available.

NCEER-91-0020 "Hybrid Control of Seismic-Excited Nonlinear and Inelastic Structural Systems," by J.N. Yang, Z. Li and A. Danielians, 8/1/91, (PB92-143171, A06, MF-A02).

NCEER-91-0021 "The NCEER-91 Earthquake Catalog: Improved Intensity-Based Magnitudes and Recurrence Relations for U.S. Earthquakes East of New Madrid," by L. Seeber and J.G. Armbruster, 8/28/91, (PB92-176742, A06, MF-A02).

NCEER-91-0022 "Proceedings from the Implementation of Earthquake Planning and Education in Schools: The Need for Change - The Roles of the Changemakers," by K.E.K. Ross and F. Winslow, 7/23/91, (PB92-129998, A12, MF-A03).

NCEER-91-0023 "A Study of Reliability-Based Criteria for Seismic Design of Reinforced Concrete Frame Buildings," by H.H.M. Hwang and H-M. Hsu, 8/10/91, (PB92-140235, A09, MF-A02).

NCEER-91-0024 "Experimental Verification of a Number of Structural System Identification Algorithms," by R.G. Ghanem, H. Gavin and M. Shinozuka, 9/18/91, (PB92-176577, A18, MF-A04).

NCEER-91-0025 "Probabilistic Evaluation of Liquefaction Potential," by H.H.M. Hwang and C.S. Lee," 11/25/91, (PB92-143429, A05, MF-A01).

NCEER-91-0026 "Instantaneous Optimal Control for Linear, Nonlinear and Hysteretic Structures - Stable Controllers," by J.N. Yang and Z. Li, 11/15/91, (PB92-163807, A04, MF-A01).

NCEER-91-0027 "Experimental and Theoretical Study of a Sliding Isolation System for Bridges," by M.C. Constantinou, A. Kartoum, A.M. Reinhorn and P. Bradford, 11/15/91, (PB92-176973, A10, MF-A03).

NCEER-92-0001 "Case Studies of Liquefaction and Lifeline Performance During Past Earthquakes, Volume 1: Japanese Case Studies," Edited by M. Hamada and T. O'Rourke, 2/17/92, (PB92-197243, A18, MF-A04).

NCEER-92-0002 "Case Studies of Liquefaction and Lifeline Performance During Past Earthquakes, Volume 2: United States Case Studies," Edited by T. O'Rourke and M. Hamada, 2/17/92, (PB92-197250, A20, MF-A04).

NCEER-92-0003 "Issues in Earthquake Education," Edited by K. Ross, 2/3/92, (PB92-222389, A07, MF-A02).

NCEER-92-0004 "Proceedings from the First U.S. - Japan Workshop on Earthquake Protective Systems for Bridges," Edited by I.G. Buckle, 2/4/92, (PB94-142239, A99, MF-A06).

NCEER-92-0005 "Seismic Ground Motion from a Haskell-Type Source in a Multiple-Layered Half-Space," A.P. Theoharis, G. Deodatis and M. Shinozuka, 1/2/92, not available.

NCEER-92-0006 "Proceedings from the Site Effects Workshop," Edited by R. Whitman, 2/29/92, (PB92-197201, A04, MF-A01).

NCEER-92-0007 "Engineering Evaluation of Permanent Ground Deformations Due to Seismically-Induced Liquefaction," by M.H. Baziar, R. Dobry and A-W.M. Elgamal, 3/24/92, (PB92-222421, A13, MF-A03).

NCEER-92-0008 "A Procedure for the Seismic Evaluation of Buildings in the Central and Eastern United States," by C.D. Poland and J.O. Malley, 4/2/92, (PB92-222439, A20, MF-A04).

NCEER-92-0009 "Experimental and Analytical Study of a Hybrid Isolation System Using Friction Controllable Sliding Bearings," by M.Q. Feng, S. Fujii and M. Shinozuka, 5/15/92, (PB93-150282, A06, MF-A02).

NCEER-92-0010 "Seismic Resistance of Slab-Column Connections in Existing Non-Ductile Flat-Plate Buildings," by A.J. Durrani and Y. Du, 5/18/92, (PB93-116812, A06, MF-A02).

NCEER-92-0011 "The Hysteretic and Dynamic Behavior of Brick Masonry Walls Upgraded by Ferrocement Coatings Under Cyclic Loading and Strong Simulated Ground Motion," by H. Lee and S.P. Prawel, 5/11/92, not available.

NCEER-92-0012 "Study of Wire Rope Systems for Seismic Protection of Equipment in Buildings," by G.F. Demetriades, M.C. Constantinou and A.M. Reinhorn, 5/20/92, (PB93-116655, A08, MF-A02).

NCEER-92-0013 "Shape Memory Structural Dampers: Material Properties, Design and Seismic Testing," by P.R. Witting and F.A. Cozzarelli, 5/26/92, (PB93-116663, A05, MF-A01).

NCEER-92-0014 "Longitudinal Permanent Ground Deformation Effects on Buried Continuous Pipelines," by M.J. O'Rourke, and C. Nordberg, 6/15/92, (PB93-116671, A08, MF-A02).

NCEER-92-0015 "A Simulation Method for Stationary Gaussian Random Functions Based on the Sampling Theorem," by M. Grigoriu and S. Balopoulou, 6/11/92, (PB93-127496, A05, MF-A01).

NCEER-92-0016 "Gravity-Load-Designed Reinforced Concrete Buildings: Seismic Evaluation of Existing Construction and Detailing Strategies for Improved Seismic Resistance," by G.W. Hoffmann, S.K. Kunnath, A.M. Reinhorn and J.B. Mander, 7/15/92, (PB94-142007, A08, MF-A02).

NCEER-92-0017 "Observations on Water System and Pipeline Performance in the Limón Area of Costa Rica Due to the April 22, 1991 Earthquake," by M. O'Rourke and D. Ballantyne, 6/30/92, (PB93-126811, A06, MF-A02).

NCEER-92-0018 "Fourth Edition of Earthquake Education Materials for Grades K-12," Edited by K.E.K. Ross, 8/10/92, (PB93-114023, A07, MF-A02).

NCEER-92-0019 "Proceedings from the Fourth Japan-U.S. Workshop on Earthquake Resistant Design of Lifeline Facilities and Countermeasures for Soil Liquefaction," Edited by M. Hamada and T.D. O'Rourke, 8/12/92, (PB93-163939, A99, MF-E11).

NCEER-92-0020 "Active Bracing System: A Full Scale Implementation of Active Control," by A.M. Reinhorn, T.T. Soong, R.C. Lin, M.A. Riley, Y.P. Wang, S. Aizawa and M. Higashino, 8/14/92, (PB93-127512, A06, MF-A02).

NCEER-92-0021 "Empirical Analysis of Horizontal Ground Displacement Generated by Liquefaction-Induced Lateral Spreads," by S.F. Bartlett and T.L. Youd, 8/17/92, (PB93-188241, A06, MF-A02).

NCEER-92-0022 "IDARC Version 3.0: Inelastic Damage Analysis of Reinforced Concrete Structures," by S.K. Kunnath, A.M. Reinhorn and R.F. Lobo, 8/31/92, (PB93-227502, A07, MF-A02).

NCEER-92-0023 "A Semi-Empirical Analysis of Strong-Motion Peaks in Terms of Seismic Source, Propagation Path and Local Site Conditions, by M. Kamiyama, M.J. O'Rourke and R. Flores-Berrones, 9/9/92, (PB93-150266, A08, MF-A02).

NCEER-92-0024 "Seismic Behavior of Reinforced Concrete Frame Structures with Nonductile Details, Part I: Summary of Experimental Findings of Full Scale Beam-Column Joint Tests," by A. Beres, R.N. White and P. Gergely, 9/30/92, (PB93-227783, A05, MF-A01).

NCEER-92-0025 "Experimental Results of Repaired and Retrofitted Beam-Column Joint Tests in Lightly Reinforced Concrete Frame Buildings," by A. Beres, S. El-Borgi, R.N. White and P. Gergely, 10/29/92, (PB93-227791, A05, MF-A01).

NCEER-92-0026 "A Generalization of Optimal Control Theory: Linear and Nonlinear Structures," by J.N. Yang, Z. Li and S. Vongchavalitkul, 11/2/92, (PB93-188621, A05, MF-A01).

NCEER-92-0027 "Seismic Resistance of Reinforced Concrete Frame Structures Designed Only for Gravity Loads: Part I - Design and Properties of a One-Third Scale Model Structure," by J.M. Bracci, A.M. Reinhorn and J.B. Mander, 12/1/92, (PB94-104502, A08, MF-A02).

NCEER-92-0028 "Seismic Resistance of Reinforced Concrete Frame Structures Designed Only for Gravity Loads: Part II - Experimental Performance of Subassemblages," by L.E. Aycardi, J.B. Mander and A.M. Reinhorn, 12/1/92, (PB94-104510, A08, MF-A02).

NCEER-92-0029 "Seismic Resistance of Reinforced Concrete Frame Structures Designed Only for Gravity Loads: Part III - Experimental Performance and Analytical Study of a Structural Model," by J.M. Bracci, A.M. Reinhorn and J.B. Mander, 12/1/92, (PB93-227528, A09, MF-A01).

NCEER-92-0030 "Evaluation of Seismic Retrofit of Reinforced Concrete Frame Structures: Part I - Experimental Performance of Retrofitted Subassemblages," by D. Choudhuri, J.B. Mander and A.M. Reinhorn, 12/8/92, (PB93-198307, A07, MF-A02).

NCEER-92-0031 "Evaluation of Seismic Retrofit of Reinforced Concrete Frame Structures: Part II - Experimental Performance and Analytical Study of a Retrofitted Structural Model," by J.M. Bracci, A.M. Reinhorn and J.B. Mander, 12/8/92, (PB93-198315, A09, MF-A03).

NCEER-92-0032 "Experimental and Analytical Investigation of Seismic Response of Structures with Supplemental Fluid Viscous Dampers," by M.C. Constantinou and M.D. Symans, 12/21/92, (PB93-191435, A10, MF-A03). This report is available only through NTIS (see address given above).

NCEER-92-0033 "Reconnaissance Report on the Cairo, Egypt Earthquake of October 12, 1992," by M. Khater, 12/23/92, (PB93-188621, A03, MF-A01).

NCEER-92-0034 "Low-Level Dynamic Characteristics of Four Tall Flat-Plate Buildings in New York City," by H. Gavin, S. Yuan, J. Grossman, E. Pekelis and K. Jacob, 12/28/92, (PB93-188217, A07, MF-A02).

NCEER-93-0001 "An Experimental Study on the Seismic Performance of Brick-Infilled Steel Frames With and Without Retrofit," by J.B. Mander, B. Nair, K. Wojtkowski and J. Ma, 1/29/93, (PB93-227510, A07, MF-A02).

NCEER-93-0002 "Social Accounting for Disaster Preparedness and Recovery Planning," by S. Cole, E. Pantoja and V. Razak, 2/22/93, (PB94-142114, A12, MF-A03).

NCEER-93-0003 "Assessment of 1991 NEHRP Provisions for Nonstructural Components and Recommended Revisions," by T.T. Soong, G. Chen, Z. Wu, R-H. Zhang and M. Grigoriu, 3/1/93, (PB93-188639, A06, MF-A02).

NCEER-93-0004 "Evaluation of Static and Response Spectrum Analysis Procedures of SEAOC/UBC for Seismic Isolated Structures," by C.W. Winters and M.C. Constantinou, 3/23/93, (PB93-198299, A10, MF-A03).

NCEER-93-0005 "Earthquakes in the Northeast - Are We Ignoring the Hazard? A Workshop on Earthquake Science and Safety for Educators," edited by K.E.K. Ross, 4/2/93, (PB94-103066, A09, MF-A02).

NCEER-93-0006 "Inelastic Response of Reinforced Concrete Structures with Viscoelastic Braces," by R.F. Lobo, J.M. Bracci, K.L. Shen, A.M. Reinhorn and T.T. Soong, 4/5/93, (PB93-227486, A05, MF-A02).

NCEER-93-0007 "Seismic Testing of Installation Methods for Computers and Data Processing Equipment," by K. Kosar, T.T. Soong, K.L. Shen, J.A. HoLung and Y.K. Lin, 4/12/93, (PB93-198299, A07, MF-A02).

NCEER-93-0008 "Retrofit of Reinforced Concrete Frames Using Added Dampers," by A. Reinhorn, M. Constantinou and C. Li, not available.

NCEER-93-0009 "Seismic Behavior and Design Guidelines for Steel Frame Structures with Added Viscoelastic Dampers," by K.C. Chang, M.L. Lai, T.T. Soong, D.S. Hao and Y.C. Yeh, 5/1/93, (PB94-141959, A07, MF-A02).

NCEER-93-0010 "Seismic Performance of Shear-Critical Reinforced Concrete Bridge Piers," by J.B. Mander, S.M. Waheed, M.T.A. Chaudhary and S.S. Chen, 5/12/93, (PB93-227494, A08, MF-A02).

NCEER-93-0011 "3D-BASIS-TABS: Computer Program for Nonlinear Dynamic Analysis of Three Dimensional Base Isolated Structures," by S. Nagarajaiah, C. Li, A.M. Reinhorn and M.C. Constantinou, 8/2/93, (PB94-141819, A09, MF-A02).

NCEER-93-0012 "Effects of Hydrocarbon Spills from an Oil Pipeline Break on Ground Water," by O.J. Helweg and H.H.M. Hwang, 8/3/93, (PB94-141942, A06, MF-A02).

NCEER-93-0013 "Simplified Procedures for Seismic Design of Nonstructural Components and Assessment of Current Code Provisions," by M.P. Singh, L.E. Suarez, E.E. Matheu and G.O. Maldonado, 8/4/93, (PB94-141827, A09, MF-A02).

NCEER-93-0014 "An Energy Approach to Seismic Analysis and Design of Secondary Systems," by G. Chen and T.T. Soong, 8/6/93, (PB94-142767, A11, MF-A03).

NCEER-93-0015 "Proceedings from School Sites: Becoming Prepared for Earthquakes - Commemorating the Third Anniversary of the Loma Prieta Earthquake," Edited by F.E. Winslow and K.E.K. Ross, 8/16/93, (PB94-154275, A16, MF-A02).

NCEER-93-0016 "Reconnaissance Report of Damage to Historic Monuments in Cairo, Egypt Following the October 12, 1992 Dahshur Earthquake," by D. Sykora, D. Look, G. Croci, E. Karaesmen and E. Karaesmen, 8/19/93, (PB94-142221, A08, MF-A02).

NCEER-93-0017 "The Island of Guam Earthquake of August 8, 1993," by S.W. Swan and S.K. Harris, 9/30/93, (PB94-141843, A04, MF-A01).

NCEER-93-0018 "Engineering Aspects of the October 12, 1992 Egyptian Earthquake," by A.W. Elgamal, M. Amer, K. Adalier and A. Abul-Fadl, 10/7/93, (PB94-141983, A05, MF-A01).

NCEER-93-0019 "Development of an Earthquake Motion Simulator and its Application in Dynamic Centrifuge Testing," by I. Krstelj, Supervised by J.H. Prevost, 10/23/93, (PB94-181773, A-10, MF-A03).

NCEER-93-0020 "NCEER-Taisei Corporation Research Program on Sliding Seismic Isolation Systems for Bridges: Experimental and Analytical Study of a Friction Pendulum System (FPS)," by M.C. Constantinou, P. Tsopelas, Y-S. Kim and S. Okamoto, 11/1/93, (PB94-142775, A08, MF-A02).

NCEER-93-0021 "Finite Element Modeling of Elastomeric Seismic Isolation Bearings," by L.J. Billings, Supervised by R. Shepherd, 11/8/93, not available.

NCEER-93-0022 "Seismic Vulnerability of Equipment in Critical Facilities: Life-Safety and Operational Consequences," by K. Porter, G.S. Johnson, M.M. Zadeh, C. Scawthorn and S. Eder, 11/24/93, (PB94-181765, A16, MF-A03).

NCEER-93-0023 "Hokkaido Nansei-oki, Japan Earthquake of July 12, 1993, by P.I. Yanev and C.R. Scawthorn, 12/23/93, (PB94-181500, A07, MF-A01).

NCEER-94-0001 "An Evaluation of Seismic Serviceability of Water Supply Networks with Application to the San Francisco Auxiliary Water Supply System," by I. Markov, Supervised by M. Grigoriu and T. O'Rourke, 1/21/94, (PB94-204013, A07, MF-A02).

NCEER-94-0002 "NCEER-Taisei Corporation Research Program on Sliding Seismic Isolation Systems for Bridges: Experimental and Analytical Study of Systems Consisting of Sliding Bearings, Rubber Restoring Force Devices and Fluid Dampers," Volumes I and II, by P. Tsopelas, S. Okamoto, M.C. Constantinou, D. Ozaki and S. Fujii, 2/4/94, (PB94-181740, A09, MF-A02 and PB94-181757, A12, MF-A03).

NCEER-94-0003 "A Markov Model for Local and Global Damage Indices in Seismic Analysis," by S. Rahman and M. Grigoriu, 2/18/94, (PB94-206000, A12, MF-A03).

NCEER-94-0004 "Proceedings from the NCEER Workshop on Seismic Response of Masonry Infills," edited by D.P. Abrams, 3/1/94, (PB94-180783, A07, MF-A02).

NCEER-94-0005 "The Northridge, California Earthquake of January 17, 1994: General Reconnaissance Report," edited by J.D. Goltz, 3/11/94, (PB94-193943, A10, MF-A03).

NCEER-94-0006 "Seismic Energy Based Fatigue Damage Analysis of Bridge Columns: Part I - Evaluation of Seismic Capacity," by G.A. Chang and J.B. Mander, 3/14/94, (PB94-219185, A11, MF-A03).

NCEER-94-0007 "Seismic Isolation of Multi-Story Frame Structures Using Spherical Sliding Isolation Systems," by T.M. Al-Hussaini, V.A. Zayas and M.C. Constantinou, 3/17/94, (PB94-193745, A09, MF-A02).

NCEER-94-0008 "The Northridge, California Earthquake of January 17, 1994: Performance of Highway Bridges," edited by I.G. Buckle, 3/24/94, (PB94-193851, A06, MF-A02).

NCEER-94-0009 "Proceedings of the Third U.S.-Japan Workshop on Earthquake Protective Systems for Bridges," edited by I.G. Buckle and I. Friedland, 3/31/94, (PB94-195815, A99, MF-A06).

NCEER-94-0010 "3D-BASIS-ME: Computer Program for Nonlinear Dynamic Analysis of Seismically Isolated Single and Multiple Structures and Liquid Storage Tanks," by P.C. Tsopelas, M.C. Constantinou and A.M. Reinhorn, 4/12/94, (PB94-204922, A09, MF-A02).

NCEER-94-0011 "The Northridge, California Earthquake of January 17, 1994: Performance of Gas Transmission Pipelines," by T.D. O'Rourke and M.C. Palmer, 5/16/94, (PB94-204989, A05, MF-A01).

NCEER-94-0012 "Feasibility Study of Replacement Procedures and Earthquake Performance Related to Gas Transmission Pipelines," by T.D. O'Rourke and M.C. Palmer, 5/25/94, (PB94-206638, A09, MF-A02).

NCEER-94-0013 "Seismic Energy Based Fatigue Damage Analysis of Bridge Columns: Part II - Evaluation of Seismic Demand," by G.A. Chang and J.B. Mander, 6/1/94, (PB95-18106, A08, MF-A02).

NCEER-94-0014 "NCEER-Taisei Corporation Research Program on Sliding Seismic Isolation Systems for Bridges: Experimental and Analytical Study of a System Consisting of Sliding Bearings and Fluid Restoring Force/Damping Devices," by P. Tsopelas and M.C. Constantinou, 6/13/94, (PB94-219144, A10, MF-A03).

NCEER-94-0015 "Generation of Hazard-Consistent Fragility Curves for Seismic Loss Estimation Studies," by H. Hwang and J-R. Huo, 6/14/94, (PB95-181996, A09, MF-A02).

NCEER-94-0016 "Seismic Study of Building Frames with Added Energy-Absorbing Devices," by W.S. Pong, C.S. Tsai and G.C. Lee, 6/20/94, (PB94-219136, A10, A03).

NCEER-94-0017 "Sliding Mode Control for Seismic-Excited Linear and Nonlinear Civil Engineering Structures," by J. Yang, J. Wu, A. Agrawal and Z. Li, 6/21/94, (PB95-138483, A06, MF-A02).

NCEER-94-0018 "3D-BASIS-TABS Version 2.0: Computer Program for Nonlinear Dynamic Analysis of Three Dimensional Base Isolated Structures," by A.M. Reinhorn, S. Nagarajaiah, M.C. Constantinou, P. Tsopelas and R. Li, 6/22/94, (PB95-182176, A08, MF-A02).

NCEER-94-0019 "Proceedings of the International Workshop on Civil Infrastructure Systems: Application of Intelligent Systems and Advanced Materials on Bridge Systems," Edited by G.C. Lee and K.C. Chang, 7/18/94, (PB95-252474, A20, MF-A04).

NCEER-94-0020 "Study of Seismic Isolation Systems for Computer Floors," by V. Lambrou and M.C. Constantinou, 7/19/94, (PB95-138533, A10, MF-A03).

NCEER-94-0021 "Proceedings of the U.S.-Italian Workshop on Guidelines for Seismic Evaluation and Rehabilitation of Unreinforced Masonry Buildings," Edited by D.P. Abrams and G.M. Calvi, 7/20/94, (PB95-138749, A13, MF-A03).

NCEER-94-0022 "NCEER-Taisei Corporation Research Program on Sliding Seismic Isolation Systems for Bridges: Experimental and Analytical Study of a System Consisting of Lubricated PTFE Sliding Bearings and Mild Steel Dampers," by P. Tsopelas and M.C. Constantinou, 7/22/94, (PB95-182184, A08, MF-A02).

NCEER-94-0023 “Development of Reliability-Based Design Criteria for Buildings Under Seismic Load,” by Y.K. Wen, H. Hwang and M. Shinozuka, 8/1/94, (PB95-211934, A08, MF-A02).

NCEER-94-0024 “Experimental Verification of Acceleration Feedback Control Strategies for an Active Tendon System,” by S.J. Dyke, B.F. Spencer, Jr., P. Quast, M.K. Sain, D.C. Kaspari, Jr. and T.T. Soong, 8/29/94, (PB95-212320, A05, MF-A01).

NCEER-94-0025 “Seismic Retrofitting Manual for Highway Bridges,” Edited by I.G. Buckle and I.F. Friedland, published by the Federal Highway Administration (PB95-212676, A15, MF-A03).

NCEER-94-0026 “Proceedings from the Fifth U.S.-Japan Workshop on Earthquake Resistant Design of Lifeline Facilities and Countermeasures Against Soil Liquefaction,” Edited by T.D. O’Rourke and M. Hamada, 11/7/94, (PB95-220802, A99, MF-E08).

NCEER-95-0001 "Experimental and Analytical Investigation of Seismic Retrofit of Structures with Supplemental Damping: Part 1 - Fluid Viscous Damping Devices," by A.M. Reinhorn, C. Li and M.C. Constantinou, 1/3/95, (PB95-266599, A09, MF-A02).

NCEER-95-0002 "Experimental and Analytical Study of Low-Cycle Fatigue Behavior of Semi-Rigid Top-And-Seat Angle Connections," by G. Pekcan, J.B. Mander and S.S. Chen, 1/5/95, (PB95-220042, A07, MF-A02).

NCEER-95-0003 "NCEER-ATC Joint Study on Fragility of Buildings," by T. Anagnos, C. Rojahn and A.S. Kiremidjian, 1/20/95, (PB95-220026, A06, MF-A02).

NCEER-95-0004 "Nonlinear Control Algorithms for Peak Response Reduction," by Z. Wu, T.T. Soong, V. Gattulli and R.C. Lin, 2/16/95, (PB95-220349, A05, MF-A01).

NCEER-95-0005 "Pipeline Replacement Feasibility Study: A Methodology for Minimizing Seismic and Corrosion Risks to Underground Natural Gas Pipelines," by R.T. Eguchi, H.A. Seligson and D.G. Honegger, 3/2/95, (PB95-252326, A06, MF-A02).

NCEER-95-0006 "Evaluation of Seismic Performance of an 11-Story Frame Building During the 1994 Northridge Earthquake," by F. Naeim, R. DiSulio, K. Benuska, A. Reinhorn and C. Li, not available.

NCEER-95-0007 "Prioritization of Bridges for Seismic Retrofitting," by N. Basöz and A.S. Kiremidjian, 4/24/95, (PB95-252300, A08, MF-A02).

NCEER-95-0008 "Method for Developing Motion Damage Relationships for Reinforced Concrete Frames," by A. Singhal and A.S. Kiremidjian, 5/11/95, (PB95-266607, A06, MF-A02).

NCEER-95-0009 "Experimental and Analytical Investigation of Seismic Retrofit of Structures with Supplemental Damping: Part II - Friction Devices," by C. Li and A.M. Reinhorn, 7/6/95, (PB96-128087, A11, MF-A03).

NCEER-95-0010 "Experimental Performance and Analytical Study of a Non-Ductile Reinforced Concrete Frame Structure Retrofitted with Elastomeric Spring Dampers," by G. Pekcan, J.B. Mander and S.S. Chen, 7/14/95, (PB96-137161, A08, MF-A02).

NCEER-95-0011 "Development and Experimental Study of Semi-Active Fluid Damping Devices for Seismic Protection of Structures," by M.D. Symans and M.C. Constantinou, 8/3/95, (PB96-136940, A23, MF-A04).

NCEER-95-0012 "Real-Time Structural Parameter Modification (RSPM): Development of Innervated Structures," by Z. Liang, M. Tong and G.C. Lee, 4/11/95, (PB96-137153, A06, MF-A01).

NCEER-95-0013 "Experimental and Analytical Investigation of Seismic Retrofit of Structures with Supplemental Damping: Part III - Viscous Damping Walls," by A.M. Reinhorn and C. Li, 10/1/95, (PB96-176409, A11, MF-A03).

NCEER-95-0014 "Seismic Fragility Analysis of Equipment and Structures in a Memphis Electric Substation," by J-R. Huo and H.H.M. Hwang, 8/10/95, (PB96-128087, A09, MF-A02).

NCEER-95-0015 "The Hanshin-Awaji Earthquake of January 17, 1995: Performance of Lifelines," Edited by M. Shinozuka, 11/3/95, (PB96-176383, A15, MF-A03).

NCEER-95-0016 "Highway Culvert Performance During Earthquakes," by T.L. Youd and C.J. Beckman, available as NCEER-96-0015.

NCEER-95-0017 "The Hanshin-Awaji Earthquake of January 17, 1995: Performance of Highway Bridges," Edited by I.G. Buckle, 12/1/95, not available.

NCEER-95-0018 "Modeling of Masonry Infill Panels for Structural Analysis," by A.M. Reinhorn, A. Madan, R.E. Valles, Y. Reichmann and J.B. Mander, 12/8/95, (PB97-110886, MF-A01, A06).

NCEER-95-0019 "Optimal Polynomial Control for Linear and Nonlinear Structures," by A.K. Agrawal and J.N. Yang, 12/11/95, (PB96-168737, A07, MF-A02).

NCEER-95-0020 "Retrofit of Non-Ductile Reinforced Concrete Frames Using Friction Dampers," by R.S. Rao, P. Gergely and R.N. White, 12/22/95, (PB97-133508, A10, MF-A02).

NCEER-95-0021 "Parametric Results for Seismic Response of Pile-Supported Bridge Bents," by G. Mylonakis, A. Nikolaou and G. Gazetas, 12/22/95, (PB97-100242, A12, MF-A03).

NCEER-95-0022 "Kinematic Bending Moments in Seismically Stressed Piles," by A. Nikolaou, G. Mylonakis and G. Gazetas, 12/23/95, (PB97-113914, MF-A03, A13).

NCEER-96-0001 "Dynamic Response of Unreinforced Masonry Buildings with Flexible Diaphragms," by A.C. Costley and D.P. Abrams," 10/10/96, (PB97-133573, MF-A03, A15).

NCEER-96-0002 "State of the Art Review: Foundations and Retaining Structures," by I. Po Lam, not available.

NCEER-96-0003 "Ductility of Rectangular Reinforced Concrete Bridge Columns with Moderate Confinement," by N. Wehbe, M. Saiidi, D. Sanders and B. Douglas, 11/7/96, (PB97-133557, A06, MF-A02).

NCEER-96-0004 "Proceedings of the Long-Span Bridge Seismic Research Workshop," edited by I.G. Buckle and I.M. Friedland, not available.

NCEER-96-0005 "Establish Representative Pier Types for Comprehensive Study: Eastern United States," by J. Kulicki and Z. Prucz, 5/28/96, (PB98-119217, A07, MF-A02).

NCEER-96-0006 "Establish Representative Pier Types for Comprehensive Study: Western United States," by R. Imbsen, R.A. Schamber and T.A. Osterkamp, 5/28/96, (PB98-118607, A07, MF-A02).

NCEER-96-0007 "Nonlinear Control Techniques for Dynamical Systems with Uncertain Parameters," by R.G. Ghanem and M.I. Bujakov, 5/27/96, (PB97-100259, A17, MF-A03).

NCEER-96-0008 "Seismic Evaluation of a 30-Year Old Non-Ductile Highway Bridge Pier and Its Retrofit," by J.B. Mander, B. Mahmoodzadegan, S. Bhadra and S.S. Chen, 5/31/96, (PB97-110902, MF-A03, A10).

NCEER-96-0009 "Seismic Performance of a Model Reinforced Concrete Bridge Pier Before and After Retrofit," by J.B. Mander, J.H. Kim and C.A. Ligozio, 5/31/96, (PB97-110910, MF-A02, A10).

NCEER-96-0010 "IDARC2D Version 4.0: A Computer Program for the Inelastic Damage Analysis of Buildings," by R.E. Valles, A.M. Reinhorn, S.K. Kunnath, C. Li and A. Madan, 6/3/96, (PB97-100234, A17, MF-A03).

NCEER-96-0011 "Estimation of the Economic Impact of Multiple Lifeline Disruption: Memphis Light, Gas and Water Division Case Study," by S.E. Chang, H.A. Seligson and R.T. Eguchi, 8/16/96, (PB97-133490, A11, MF-A03).

NCEER-96-0012 "Proceedings from the Sixth Japan-U.S. Workshop on Earthquake Resistant Design of Lifeline Facilities and Countermeasures Against Soil Liquefaction, Edited by M. Hamada and T. O'Rourke, 9/11/96, (PB97-133581, A99, MF-A06).

NCEER-96-0013 "Chemical Hazards, Mitigation and Preparedness in Areas of High Seismic Risk: A Methodology for Estimating the Risk of Post-Earthquake Hazardous Materials Release," by H.A. Seligson, R.T. Eguchi, K.J. Tierney and K. Richmond, 11/7/96, (PB97-133565, MF-A02, A08).

NCEER-96-0014 "Response of Steel Bridge Bearings to Reversed Cyclic Loading," by J.B. Mander, D-K. Kim, S.S. Chen and G.J. Premus, 11/13/96, (PB97-140735, A12, MF-A03).

NCEER-96-0015 "Highway Culvert Performance During Past Earthquakes," by T.L. Youd and C.J. Beckman, 11/25/96, (PB97-133532, A06, MF-A01).

NCEER-97-0001 "Evaluation, Prevention and Mitigation of Pounding Effects in Building Structures," by R.E. Valles and A.M. Reinhorn, 2/20/97, (PB97-159552, A14, MF-A03).

NCEER-97-0002 "Seismic Design Criteria for Bridges and Other Highway Structures," by C. Rojahn, R. Mayes, D.G. Anderson, J. Clark, J.H. Hom, R.V. Nutt and M.J. O'Rourke, 4/30/97, (PB97-194658, A06, MF-A03).

NCEER-97-0003 "Proceedings of the U.S.-Italian Workshop on Seismic Evaluation and Retrofit," Edited by D.P. Abrams and G.M. Calvi, 3/19/97, (PB97-194666, A13, MF-A03).

NCEER-97-0004 "Investigation of Seismic Response of Buildings with Linear and Nonlinear Fluid Viscous Dampers," by A.A. Seleemah and M.C. Constantinou, 5/21/97, (PB98-109002, A15, MF-A03).

NCEER-97-0005 "Proceedings of the Workshop on Earthquake Engineering Frontiers in Transportation Facilities," edited by G.C. Lee and I.M. Friedland, 8/29/97, (PB98-128911, A25, MR-A04).

NCEER-97-0006 "Cumulative Seismic Damage of Reinforced Concrete Bridge Piers," by S.K. Kunnath, A. El-Bahy, A. Taylor and W. Stone, 9/2/97, (PB98-108814, A11, MF-A03).

NCEER-97-0007 "Structural Details to Accommodate Seismic Movements of Highway Bridges and Retaining Walls," by R.A. Imbsen, R.A. Schamber, E. Thorkildsen, A. Kartoum, B.T. Martin, T.N. Rosser and J.M. Kulicki, 9/3/97, (PB98-108996, A09, MF-A02).

NCEER-97-0008 "A Method for Earthquake Motion-Damage Relationships with Application to Reinforced Concrete Frames," by A. Singhal and A.S. Kiremidjian, 9/10/97, (PB98-108988, A13, MF-A03).

NCEER-97-0009 "Seismic Analysis and Design of Bridge Abutments Considering Sliding and Rotation," by K. Fishman and R. Richards, Jr., 9/15/97, (PB98-108897, A06, MF-A02).

NCEER-97-0010 "Proceedings of the FHWA/NCEER Workshop on the National Representation of Seismic Ground Motion for New and Existing Highway Facilities," edited by I.M. Friedland, M.S. Power and R.L. Mayes, 9/22/97, (PB98-128903, A21, MF-A04).

NCEER-97-0011 "Seismic Analysis for Design or Retrofit of Gravity Bridge Abutments," by K.L. Fishman, R. Richards, Jr. and R.C. Divito, 10/2/97, (PB98-128937, A08, MF-A02).

NCEER-97-0012 "Evaluation of Simplified Methods of Analysis for Yielding Structures," by P. Tsopelas, M.C. Constantinou, C.A. Kircher and A.S. Whittaker, 10/31/97, (PB98-128929, A10, MF-A03).

NCEER-97-0013 "Seismic Design of Bridge Columns Based on Control and Repairability of Damage," by C-T. Cheng and J.B. Mander, 12/8/97, (PB98-144249, A11, MF-A03).

NCEER-97-0014 "Seismic Resistance of Bridge Piers Based on Damage Avoidance Design," by J.B. Mander and C-T. Cheng, 12/10/97, (PB98-144223, A09, MF-A02).

NCEER-97-0015 "Seismic Response of Nominally Symmetric Systems with Strength Uncertainty," by S. Balopoulou and M. Grigoriu, 12/23/97, (PB98-153422, A11, MF-A03).

NCEER-97-0016 "Evaluation of Seismic Retrofit Methods for Reinforced Concrete Bridge Columns," by T.J. Wipf, F.W. Klaiber and F.M. Russo, 12/28/97, (PB98-144215, A12, MF-A03).

NCEER-97-0017 "Seismic Fragility of Existing Conventional Reinforced Concrete Highway Bridges," by C.L. Mullen and A.S. Cakmak, 12/30/97, (PB98-153406, A08, MF-A02).

NCEER-97-0018 "Loss Asssessment of Memphis Buildings," edited by D.P. Abrams and M. Shinozuka, 12/31/97, (PB98-144231, A13, MF-A03).

NCEER-97-0019 "Seismic Evaluation of Frames with Infill Walls Using Quasi-static Experiments," by K.M. Mosalam, R.N. White and P. Gergely, 12/31/97, (PB98-153455, A07, MF-A02).

NCEER-97-0020 "Seismic Evaluation of Frames with Infill Walls Using Pseudo-dynamic Experiments," by K.M. Mosalam, R.N. White and P. Gergely, 12/31/97, (PB98-153430, A07, MF-A02).

NCEER-97-0021 "Computational Strategies for Frames with Infill Walls: Discrete and Smeared Crack Analyses and Seismic Fragility," by K.M. Mosalam, R.N. White and P. Gergely, 12/31/97, (PB98-153414, A10, MF-A02).

NCEER-97-0022 "Proceedings of the NCEER Workshop on Evaluation of Liquefaction Resistance of Soils," edited by T.L. Youd and I.M. Idriss, 12/31/97, (PB98-155617, A15, MF-A03).

MCEER-98-0001 "Extraction of Nonlinear Hysteretic Properties of Seismically Isolated Bridges from Quick-Release Field Tests," by Q. Chen, B.M. Douglas, E.M. Maragakis and I.G. Buckle, 5/26/98, (PB99-118838, A06, MF-A01).

MCEER-98-0002 "Methodologies for Evaluating the Importance of Highway Bridges," by A. Thomas, S. Eshenaur and J. Kulicki, 5/29/98, (PB99-118846, A10, MF-A02).

MCEER-98-0003 "Capacity Design of Bridge Piers and the Analysis of Overstrength," by J.B. Mander, A. Dutta and P. Goel, 6/1/98, (PB99-118853, A09, MF-A02).

MCEER-98-0004 "Evaluation of Bridge Damage Data from the Loma Prieta and Northridge, California Earthquakes," by N. Basoz and A. Kiremidjian, 6/2/98, (PB99-118861, A15, MF-A03).

MCEER-98-0005 "Screening Guide for Rapid Assessment of Liquefaction Hazard at Highway Bridge Sites," by T. L. Youd, 6/16/98, (PB99-118879, A06, not available on microfiche).

MCEER-98-0006 "Structural Steel and Steel/Concrete Interface Details for Bridges," by P. Ritchie, N. Kauhl and J. Kulicki, 7/13/98, (PB99-118945, A06, MF-A01).

MCEER-98-0007 "Capacity Design and Fatigue Analysis of Confined Concrete Columns," by A. Dutta and J.B. Mander, 7/14/98, (PB99-118960, A14, MF-A03).

MCEER-98-0008 "Proceedings of the Workshop on Performance Criteria for Telecommunication Services Under Earthquake Conditions," edited by A.J. Schiff, 7/15/98, (PB99-118952, A08, MF-A02).

MCEER-98-0009 "Fatigue Analysis of Unconfined Concrete Columns," by J.B. Mander, A. Dutta and J.H. Kim, 9/12/98, (PB99-123655, A10, MF-A02).

MCEER-98-0010 "Centrifuge Modeling of Cyclic Lateral Response of Pile-Cap Systems and Seat-Type Abutments in Dry Sands," by A.D. Gadre and R. Dobry, 10/2/98, (PB99-123606, A13, MF-A03).

MCEER-98-0011 "IDARC-BRIDGE: A Computational Platform for Seismic Damage Assessment of Bridge Structures," by A.M. Reinhorn, V. Simeonov, G. Mylonakis and Y. Reichman, 10/2/98, (PB99-162919, A15, MF-A03).

MCEER-98-0012 "Experimental Investigation of the Dynamic Response of Two Bridges Before and After Retrofitting with Elastomeric Bearings," by D.A. Wendichansky, S.S. Chen and J.B. Mander, 10/2/98, (PB99-162927, A15, MF-A03).

MCEER-98-0013 "Design Procedures for Hinge Restrainers and Hinge Sear Width for Multiple-Frame Bridges," by R. Des Roches and G.L. Fenves, 11/3/98, (PB99-140477, A13, MF-A03).

MCEER-98-0014 "Response Modification Factors for Seismically Isolated Bridges," by M.C. Constantinou and J.K. Quarshie, 11/3/98, (PB99-140485, A14, MF-A03).

MCEER-98-0015 "Proceedings of the U.S.-Italy Workshop on Seismic Protective Systems for Bridges," edited by I.M. Friedland and M.C. Constantinou, 11/3/98, (PB2000-101711, A22, MF-A04).

MCEER-98-0016 "Appropriate Seismic Reliability for Critical Equipment Systems: Recommendations Based on Regional Analysis of Financial and Life Loss," by K. Porter, C. Scawthorn, C. Taylor and N. Blais, 11/10/98, (PB99-157265, A08, MF-A02).

MCEER-98-0017 "Proceedings of the U.S. Japan Joint Seminar on Civil Infrastructure Systems Research," edited by M. Shinozuka and A. Rose, 11/12/98, (PB99-156713, A16, MF-A03).

MCEER-98-0018 "Modeling of Pile Footings and Drilled Shafts for Seismic Design," by I. PoLam, M. Kapuskar and D. Chaudhuri, 12/21/98, (PB99-157257, A09, MF-A02).

MCEER-99-0001 "Seismic Evaluation of a Masonry Infilled Reinforced Concrete Frame by Pseudodynamic Testing," by S.G. Buonopane and R.N. White, 2/16/99, (PB99-162851, A09, MF-A02).

MCEER-99-0002 "Response History Analysis of Structures with Seismic Isolation and Energy Dissipation Systems: Verification Examples for Program SAP2000," by J. Scheller and M.C. Constantinou, 2/22/99, (PB99-162869, A08, MF-A02).

MCEER-99-0003 "Experimental Study on the Seismic Design and Retrofit of Bridge Columns Including Axial Load Effects," by A. Dutta, T. Kokorina and J.B. Mander, 2/22/99, (PB99-162877, A09, MF-A02).

MCEER-99-0004 "Experimental Study of Bridge Elastomeric and Other Isolation and Energy Dissipation Systems with Emphasis on Uplift Prevention and High Velocity Near-source Seismic Excitation," by A. Kasalanati and M. C. Constantinou, 2/26/99, (PB99-162885, A12, MF-A03).

MCEER-99-0005 "Truss Modeling of Reinforced Concrete Shear-flexure Behavior," by J.H. Kim and J.B. Mander, 3/8/99, (PB99-163693, A12, MF-A03).

MCEER-99-0006 "Experimental Investigation and Computational Modeling of Seismic Response of a 1:4 Scale Model Steel Structure with a Load Balancing Supplemental Damping System," by G. Pekcan, J.B. Mander and S.S. Chen, 4/2/99, (PB99-162893, A11, MF-A03).

MCEER-99-0007 "Effect of Vertical Ground Motions on the Structural Response of Highway Bridges," by M.R. Button, C.J. Cronin and R.L. Mayes, 4/10/99, (PB2000-101411, A10, MF-A03).

MCEER-99-0008 "Seismic Reliability Assessment of Critical Facilities: A Handbook, Supporting Documentation, and Model Code Provisions," by G.S. Johnson, R.E. Sheppard, M.D. Quilici, S.J. Eder and C.R. Scawthorn, 4/12/99, (PB2000-101701, A18, MF-A04).

MCEER-99-0009 "Impact Assessment of Selected MCEER Highway Project Research on the Seismic Design of Highway Structures," by C. Rojahn, R. Mayes, D.G. Anderson, J.H. Clark, D'Appolonia Engineering, S. Gloyd and R.V. Nutt, 4/14/99, (PB99-162901, A10, MF-A02).

MCEER-99-0010 "Site Factors and Site Categories in Seismic Codes," by R. Dobry, R. Ramos and M.S. Power, 7/19/99, (PB2000-101705, A08, MF-A02).

MCEER-99-0011 "Restrainer Design Procedures for Multi-Span Simply-Supported Bridges," by M.J. Randall, M. Saiidi, E. Maragakis and T. Isakovic, 7/20/99, (PB2000-101702, A10, MF-A02).

MCEER-99-0012 "Property Modification Factors for Seismic Isolation Bearings," by M.C. Constantinou, P. Tsopelas, A. Kasalanati and E. Wolff, 7/20/99, (PB2000-103387, A11, MF-A03).

MCEER-99-0013 "Critical Seismic Issues for Existing Steel Bridges," by P. Ritchie, N. Kauhl and J. Kulicki, 7/20/99, (PB2000-101697, A09, MF-A02).

MCEER-99-0014 "Nonstructural Damage Database," by A. Kao, T.T. Soong and A. Vender, 7/24/99, (PB2000-101407, A06, MF-A01).

MCEER-99-0015 "Guide to Remedial Measures for Liquefaction Mitigation at Existing Highway Bridge Sites," by H.G. Cooke and J. K. Mitchell, 7/26/99, (PB2000-101703, A11, MF-A03).

MCEER-99-0016 "Proceedings of the MCEER Workshop on Ground Motion Methodologies for the Eastern United States," edited by N. Abrahamson and A. Becker, 8/11/99, (PB2000-103385, A07, MF-A02).

MCEER-99-0017 "Quindío, Colombia Earthquake of January 25, 1999: Reconnaissance Report," by A.P. Asfura and P.J. Flores, 10/4/99, (PB2000-106893, A06, MF-A01).

MCEER-99-0018 "Hysteretic Models for Cyclic Behavior of Deteriorating Inelastic Structures," by M.V. Sivaselvan and A.M. Reinhorn, 11/5/99, (PB2000-103386, A08, MF-A02).

MCEER-99-0019 "Proceedings of the 7^{th} U.S.- Japan Workshop on Earthquake Resistant Design of Lifeline Facilities and Countermeasures Against Soil Liquefaction," edited by T.D. O'Rourke, J.P. Bardet and M. Hamada, 11/19/99, (PB2000-103354, A99, MF-A06).

MCEER-99-0020 "Development of Measurement Capability for Micro-Vibration Evaluations with Application to Chip Fabrication Facilities," by G.C. Lee, Z. Liang, J.W. Song, J.D. Shen and W.C. Liu, 12/1/99, (PB2000-105993, A08, MF-A02).

MCEER-99-0021 "Design and Retrofit Methodology for Building Structures with Supplemental Energy Dissipating Systems," by G. Pekcan, J.B. Mander and S.S. Chen, 12/31/99, (PB2000-105994, A11, MF-A03).

MCEER-00-0001 "The Marmara, Turkey Earthquake of August 17, 1999: Reconnaissance Report," edited by C. Scawthorn; with major contributions by M. Bruneau, R. Eguchi, T. Holzer, G. Johnson, J. Mander, J. Mitchell, W. Mitchell, A. Papageorgiou, C. Scaethorn, and G. Webb, 3/23/00, (PB2000-106200, A11, MF-A03).

MCEER-00-0002 "Proceedings of the MCEER Workshop for Seismic Hazard Mitigation of Health Care Facilities," edited by G.C. Lee, M. Ettouney, M. Grigoriu, J. Hauer and J. Nigg, 3/29/00, (PB2000-106892, A08, MF-A02).

MCEER-00-0003 "The Chi-Chi, Taiwan Earthquake of September 21, 1999: Reconnaissance Report," edited by G.C. Lee and C.H. Loh, with major contributions by G.C. Lee, M. Bruneau, I.G. Buckle, S.E. Chang, P.J. Flores, T.D. O'Rourke, M. Shinozuka, T.T. Soong, C-H. Loh, K-C. Chang, Z-J. Chen, J-S. Hwang, M-L. Lin, G-Y. Liu, K-C. Tsai, G.C. Yao and C-L. Yen, 4/30/00, (PB2001-100980, A10, MF-A02).

MCEER-00-0004 "Seismic Retrofit of End-Sway Frames of Steel Deck-Truss Bridges with a Supplemental Tendon System: Experimental and Analytical Investigation," by G. Pekcan, J.B. Mander and S.S. Chen, 7/1/00, (PB2001-100982, A10, MF-A02).

MCEER-00-0005 "Sliding Fragility of Unrestrained Equipment in Critical Facilities," by W.H. Chong and T.T. Soong, 7/5/00, (PB2001-100983, A08, MF-A02).

MCEER-00-0006 "Seismic Response of Reinforced Concrete Bridge Pier Walls in the Weak Direction," by N. Abo-Shadi, M. Saiidi and D. Sanders, 7/17/00, (PB2001-100981, A17, MF-A03).

MCEER-00-0007 "Low-Cycle Fatigue Behavior of Longitudinal Reinforcement in Reinforced Concrete Bridge Columns," by J. Brown and S.K. Kunnath, 7/23/00, (PB2001-104392, A08, MF-A02).

MCEER-00-0008 "Soil Structure Interaction of Bridges for Seismic Analysis," I. PoLam and H. Law, 9/25/00, (PB2001-105397, A08, MF-A02).

MCEER-00-0009 "Proceedings of the First MCEER Workshop on Mitigation of Earthquake Disaster by Advanced Technologies (MEDAT-1), edited by M. Shinozuka, D.J. Inman and T.D. O'Rourke, 11/10/00, (PB2001-105399, A14, MF-A03).

MCEER-00-0010 "Development and Evaluation of Simplified Procedures for Analysis and Design of Buildings with Passive Energy Dissipation Systems, Revision 01," by O.M. Ramirez, M.C. Constantinou, C.A. Kircher, A.S. Whittaker, M.W. Johnson, J.D. Gomez and C. Chrysostomou, 11/16/01, (PB2001-105523, A23, MF-A04).

MCEER-00-0011 "Dynamic Soil-Foundation-Structure Interaction Analyses of Large Caissons," by C-Y. Chang, C-M. Mok, Z-L. Wang, R. Settgast, F. Waggoner, M.A. Ketchum, H.M. Gonnermann and C-C. Chin, 12/30/00, (PB2001-104373, A07, MF-A02).

MCEER-00-0012 "Experimental Evaluation of Seismic Performance of Bridge Restrainers," by A.G. Vlassis, E.M. Maragakis and M. Saiid Saiidi, 12/30/00, (PB2001-104354, A09, MF-A02).

MCEER-00-0013 "Effect of Spatial Variation of Ground Motion on Highway Structures," by M. Shinozuka, V. Saxena and G. Deodatis, 12/31/00, (PB2001-108755, A13, MF-A03).

MCEER-00-0014 "A Risk-Based Methodology for Assessing the Seismic Performance of Highway Systems," by S.D. Werner, C.E. Taylor, J.E. Moore, II, J.S. Walton and S. Cho, 12/31/00, (PB2001-108756, A14, MF-A03).

MCEER-01-0001 "Experimental Investigation of P-Delta Effects to Collapse During Earthquakes," by D. Vian and M. Bruneau, 6/25/01, (PB2002-100534, A17, MF-A03).

MCEER-01-0002 "Proceedings of the Second MCEER Workshop on Mitigation of Earthquake Disaster by Advanced Technologies (MEDAT-2)," edited by M. Bruneau and D.J. Inman, 7/23/01, (PB2002-100434, A16, MF-A03).

MCEER-01-0003 "Sensitivity Analysis of Dynamic Systems Subjected to Seismic Loads," by C. Roth and M. Grigoriu, 9/18/01, (PB2003-100884, A12, MF-A03).

MCEER-01-0004 "Overcoming Obstacles to Implementing Earthquake Hazard Mitigation Policies: Stage 1 Report," by D.J. Alesch and W.J. Petak, 12/17/01, (PB2002-107949, A07, MF-A02).

MCEER-01-0005 "Updating Real-Time Earthquake Loss Estimates: Methods, Problems and Insights," by C.E. Taylor, S.E. Chang and R.T. Eguchi, 12/17/01, (PB2002-107948, A05, MF-A01).

MCEER-01-0006 "Experimental Investigation and Retrofit of Steel Pile Foundations and Pile Bents Under Cyclic Lateral Loadings," by A. Shama, J. Mander, B. Blabac and S. Chen, 12/31/01, (PB2002-107950, A13, MF-A03).

MCEER-02-0001 "Assessment of Performance of Bolu Viaduct in the 1999 Duzce Earthquake in Turkey" by P.C. Roussis, M.C. Constantinou, M. Erdik, E. Durukal and M. Dicleli, 5/8/02, (PB2003-100883, A08, MF-A02).

MCEER-02-0002 "Seismic Behavior of Rail Counterweight Systems of Elevators in Buildings," by M.P. Singh, Rildova and L.E. Suarez, 5/27/02. (PB2003-100882, A11, MF-A03).

MCEER-02-0003 "Development of Analysis and Design Procedures for Spread Footings," by G. Mylonakis, G. Gazetas, S. Nikolaou and A. Chauncey, 10/02/02, (PB2004-101636, A13, MF-A03, CD-A13).

MCEER-02-0004 "Bare-Earth Algorithms for Use with SAR and LIDAR Digital Elevation Models," by C.K. Huyck, R.T. Eguchi and B. Houshmand, 10/16/02, (PB2004-101637, A07, CD-A07).

MCEER-02-0005 "Review of Energy Dissipation of Compression Members in Concentrically Braced Frames," by K.Lee and M. Bruneau, 10/18/02, (PB2004-101638, A10, CD-A10).

MCEER-03-0001 "Experimental Investigation of Light-Gauge Steel Plate Shear Walls for the Seismic Retrofit of Buildings" by J. Berman and M. Bruneau, 5/2/03, (PB2004-101622, A10, MF-A03, CD-A10).

MCEER-03-0002 "Statistical Analysis of Fragility Curves," by M. Shinozuka, M.Q. Feng, H. Kim, T. Uzawa and T. Ueda, 6/16/03, (PB2004-101849, A09, CD-A09).

MCEER-03-0003 "Proceedings of the Eighth U.S.-Japan Workshop on Earthquake Resistant Design f Lifeline Facilities and Countermeasures Against Liquefaction," edited by M. Hamada, J.P. Bardet and T.D. O'Rourke, 6/30/03, (PB2004-104386, A99, CD-A99).

MCEER-03-0004 "Proceedings of the PRC-US Workshop on Seismic Analysis and Design of Special Bridges," edited by L.C. Fan and G.C. Lee, 7/15/03, (PB2004-104387, A14, CD-A14).

MCEER-03-0005 "Urban Disaster Recovery: A Framework and Simulation Model," by S.B. Miles and S.E. Chang, 7/25/03, (PB2004-104388, A07, CD-A07).

MCEER-03-0006 "Behavior of Underground Piping Joints Due to Static and Dynamic Loading," by R.D. Meis, M. Maragakis and R. Siddharthan, 11/17/03, (PB2005-102194, A13, MF-A03, CD-A00).

MCEER-04-0001 "Experimental Study of Seismic Isolation Systems with Emphasis on Secondary System Response and Verification of Accuracy of Dynamic Response History Analysis Methods," by E. Wolff and M. Constantinou, 1/16/04 (PB2005-102195, A99, MF-E08, CD-A00).

MCEER-04-0002 "Tension, Compression and Cyclic Testing of Engineered Cementitious Composite Materials," by K. Kesner and S.L. Billington, 3/1/04, (PB2005-102196, A08, CD-A08).

MCEER-04-0003 "Cyclic Testing of Braces Laterally Restrained by Steel Studs to Enhance Performance During Earthquakes," by O.C. Celik, J.W. Berman and M. Bruneau, 3/16/04, (PB2005-102197, A13, MF-A03, CD-A00).

MCEER-04-0004 "Methodologies for Post Earthquake Building Damage Detection Using SAR and Optical Remote Sensing: Application to the August 17, 1999 Marmara, Turkey Earthquake," by C.K. Huyck, B.J. Adams, S. Cho, R.T. Eguchi, B. Mansouri and B. Houshmand, 6/15/04, (PB2005-104888, A10, CD-A00).

MCEER-04-0005 "Nonlinear Structural Analysis Towards Collapse Simulation: A Dynamical Systems Approach," by M.V. Sivaselvan and A.M. Reinhorn, 6/16/04, (PB2005-104889, A11, MF-A03, CD-A00).

MCEER-04-0006 "Proceedings of the Second PRC-US Workshop on Seismic Analysis and Design of Special Bridges," edited by G.C. Lee and L.C. Fan, 6/25/04, (PB2005-104890, A16, CD-A00).

MCEER-04-0007 "Seismic Vulnerability Evaluation of Axially Loaded Steel Built-up Laced Members," by K. Lee and M. Bruneau, 6/30/04, (PB2005-104891, A16, CD-A00).

MCEER-04-0008 "Evaluation of Accuracy of Simplified Methods of Analysis and Design of Buildings with Damping Systems for Near-Fault and for Soft-Soil Seismic Motions," by E.A. Pavlou and M.C. Constantinou, 8/16/04, (PB2005-104892, A08, MF-A02, CD-A00).

MCEER-04-0009 "Assessment of Geotechnical Issues in Acute Care Facilities in California," by M. Lew, T.D. O'Rourke, R. Dobry and M. Koch, 9/15/04, (PB2005-104893, A08, CD-A00).

MCEER-04-0010 "Scissor-Jack-Damper Energy Dissipation System," by A.N. Sigaher-Boyle and M.C. Constantinou, 12/1/04 (PB2005-108221).

MCEER-04-0011 "Seismic Retrofit of Bridge Steel Truss Piers Using a Controlled Rocking Approach," by M. Pollino and M. Bruneau, 12/20/04 (PB2006-105795).

MCEER-05-0001 "Experimental and Analytical Studies of Structures Seismically Isolated with an Uplift-Restraint Isolation System," by P.C. Roussis and M.C. Constantinou, 1/10/05 (PB2005-108222).

MCEER-05-0002 "A Versatile Experimentation Model for Study of Structures Near Collapse Applied to Seismic Evaluation of Irregular Structures," by D. Kusumastuti, A.M. Reinhorn and A. Rutenberg, 3/31/05 (PB2006-101523).

MCEER-05-0003 "Proceedings of the Third PRC-US Workshop on Seismic Analysis and Design of Special Bridges," edited by L.C. Fan and G.C. Lee, 4/20/05, (PB2006-105796).

MCEER-05-0004 "Approaches for the Seismic Retrofit of Braced Steel Bridge Piers and Proof-of-Concept Testing of an Eccentrically Braced Frame with Tubular Link," by J.W. Berman and M. Bruneau, 4/21/05 (PB2006-101524).

MCEER-05-0005 "Simulation of Strong Ground Motions for Seismic Fragility Evaluation of Nonstructural Components in Hospitals," by A. Wanitkorkul and A. Filiatrault, 5/26/05 (PB2006-500027).

MCEER-05-0006 "Seismic Safety in California Hospitals: Assessing an Attempt to Accelerate the Replacement or Seismic Retrofit of Older Hospital Facilities," by D.J. Alesch, L.A. Arendt and W.J. Petak, 6/6/05 (PB2006-105794).

MCEER-05-0007 "Development of Seismic Strengthening and Retrofit Strategies for Critical Facilities Using Engineered Cementitious Composite Materials," by K. Kesner and S.L. Billington, 8/29/05 (PB2006-111701).

MCEER-05-0008 "Experimental and Analytical Studies of Base Isolation Systems for Seismic Protection of Power Transformers," by N. Murota, M.Q. Feng and G-Y. Liu, 9/30/05 (PB2006-111702).

MCEER-05-0009 "3D-BASIS-ME-MB: Computer Program for Nonlinear Dynamic Analysis of Seismically Isolated Structures," by P.C. Tsopelas, P.C. Roussis, M.C. Constantinou, R. Buchanan and A.M. Reinhorn, 10/3/05 (PB2006-111703).

MCEER-05-0010 "Steel Plate Shear Walls for Seismic Design and Retrofit of Building Structures," by D. Vian and M. Bruneau, 12/15/05 (PB2006-111704).

MCEER-05-0011 "The Performance-Based Design Paradigm," by M.J. Astrella and A. Whittaker, 12/15/05 (PB2006-111705).

MCEER-06-0001 "Seismic Fragility of Suspended Ceiling Systems," H. Badillo-Almaraz, A.S. Whittaker, A.M. Reinhorn and G.P. Cimellaro, 2/4/06 (PB2006-111706).

MCEER-06-0002 "Multi-Dimensional Fragility of Structures," by G.P. Cimellaro, A.M. Reinhorn and M. Bruneau, 3/1/06 (PB2007-106974, A09, MF-A02, CD A00).

MCEER-06-0003 "Built-Up Shear Links as Energy Dissipators for Seismic Protection of Bridges," by P. Dusicka, A.M. Itani and I.G. Buckle, 3/15/06 (PB2006-111708).

MCEER-06-0004 "Analytical Investigation of the Structural Fuse Concept," by R.E. Vargas and M. Bruneau, 3/16/06 (PB2006-111709).

MCEER-06-0005 "Experimental Investigation of the Structural Fuse Concept," by R.E. Vargas and M. Bruneau, 3/17/06 (PB2006-111710).

MCEER-06-0006 "Further Development of Tubular Eccentrically Braced Frame Links for the Seismic Retrofit of Braced Steel Truss Bridge Piers," by J.W. Berman and M. Bruneau, 3/27/06 (PB2007-105147).

MCEER-06-0007 "REDARS Validation Report," by S. Cho, C.K. Huyck, S. Ghosh and R.T. Eguchi, 8/8/06 (PB2007-106983).

MCEER-06-0008 "Review of Current NDE Technologies for Post-Earthquake Assessment of Retrofitted Bridge Columns," by J.W. Song, Z. Liang and G.C. Lee, 8/21/06 (PB2007-106984).

MCEER-06-0009 "Liquefaction Remediation in Silty Soils Using Dynamic Compaction and Stone Columns," by S. Thevanayagam, G.R. Martin, R. Nashed, T. Shenthan, T. Kanagalingam and N. Ecemis, 8/28/06 (PB2007-106985).

MCEER-06-0010 "Conceptual Design and Experimental Investigation of Polymer Matrix Composite Infill Panels for Seismic Retrofitting," by W. Jung, M. Chiewanichakorn and A.J. Aref, 9/21/06 (PB2007-106986).

MCEER-06-0011 "A Study of the Coupled Horizontal-Vertical Behavior of Elastomeric and Lead-Rubber Seismic Isolation Bearings," by G.P. Warn and A.S. Whittaker, 9/22/06 (PB2007-108679).

MCEER-06-0012 "Proceedings of the Fourth PRC-US Workshop on Seismic Analysis and Design of Special Bridges: Advancing Bridge Technologies in Research, Design, Construction and Preservation," Edited by L.C. Fan, G.C. Lee and L. Ziang, 10/12/06 (PB2007-109042).

MCEER-06-0013 "Cyclic Response and Low Cycle Fatigue Characteristics of Plate Steels," by P. Dusicka, A.M. Itani and I.G. Buckle, 11/1/06 06 (PB2007-106987).

MCEER-06-0014 "Proceedings of the Second US-Taiwan Bridge Engineering Workshop," edited by W.P. Yen, J. Shen, J-Y. Chen and M. Wang, 11/15/06 (PB2008-500041).

MCEER-06-0015 "User Manual and Technical Documentation for the REDARS™ Import Wizard," by S. Cho, S. Ghosh, C.K. Huyck and S.D. Werner, 11/30/06 (PB2007-114766).

MCEER-06-0016 "Hazard Mitigation Strategy and Monitoring Technologies for Urban and Infrastructure Public Buildings: Proceedings of the China-US Workshops," edited by X.Y. Zhou, A.L. Zhang, G.C. Lee and M. Tong, 12/12/06 (PB2008-500018).

MCEER-07-0001 "Static and Kinetic Coefficients of Friction for Rigid Blocks," by C. Kafali, S. Fathali, M. Grigoriu and A.S. Whittaker, 3/20/07 (PB2007-114767).

MCEER-07-0002 "Hazard Mitigation Investment Decision Making: Organizational Response to Legislative Mandate," by L.A. Arendt, D.J. Alesch and W.J. Petak, 4/9/07 (PB2007-114768).

MCEER-07-0003 "Seismic Behavior of Bidirectional-Resistant Ductile End Diaphragms with Unbonded Braces in Straight or Skewed Steel Bridges," by O. Celik and M. Bruneau, 4/11/07 (PB2008-105141).

MCEER-07-0004 "Modeling Pile Behavior in Large Pile Groups Under Lateral Loading," by A.M. Dodds and G.R. Martin, 4/16/07(PB2008-105142).

MCEER-07-0005 "Experimental Investigation of Blast Performance of Seismically Resistant Concrete-Filled Steel Tube Bridge Piers," by S. Fujikura, M. Bruneau and D. Lopez-Garcia, 4/20/07 (PB2008-105143).

MCEER-07-0006 "Seismic Analysis of Conventional and Isolated Liquefied Natural Gas Tanks Using Mechanical Analogs," by I.P. Christovasilis and A.S. Whittaker, 5/1/07, not available.

MCEER-07-0007 "Experimental Seismic Performance Evaluation of Isolation/Restraint Systems for Mechanical Equipment – Part 1: Heavy Equipment Study," by S. Fathali and A. Filiatrault, 6/6/07 (PB2008-105144).

MCEER-07-0008 "Seismic Vulnerability of Timber Bridges and Timber Substructures," by A.A. Sharma, J.B. Mander, I.M. Friedland and D.R. Allicock, 6/7/07 (PB2008-105145).

MCEER-07-0009 "Experimental and Analytical Study of the XY-Friction Pendulum (XY-FP) Bearing for Bridge Applications," by C.C. Marin-Artieda, A.S. Whittaker and M.C. Constantinou, 6/7/07 (PB2008-105191).

MCEER-07-0010 "Proceedings of the PRC-US Earthquake Engineering Forum for Young Researchers," Edited by G.C. Lee and X.Z. Qi, 6/8/07 (PB2008-500058).

MCEER-07-0011 "Design Recommendations for Perforated Steel Plate Shear Walls," by R. Purba and M. Bruneau, 6/18/07, (PB2008-105192).

MCEER-07-0012 "Performance of Seismic Isolation Hardware Under Service and Seismic Loading," by M.C. Constantinou, A.S. Whittaker, Y. Kalpakidis, D.M. Fenz and G.P. Warn, 8/27/07, (PB2008-105193).

MCEER-07-0013 "Experimental Evaluation of the Seismic Performance of Hospital Piping Subassemblies," by E.R. Goodwin, E. Maragakis and A.M. Itani, 9/4/07, (PB2008-105194).

MCEER-07-0014 "A Simulation Model of Urban Disaster Recovery and Resilience: Implementation for the 1994 Northridge Earthquake," by S. Miles and S.E. Chang, 9/7/07, (PB2008-106426).

MCEER-07-0015 "Statistical and Mechanistic Fragility Analysis of Concrete Bridges," by M. Shinozuka, S. Banerjee and S-H. Kim, 9/10/07, (PB2008-106427).

MCEER-07-0016 "Three-Dimensional Modeling of Inelastic Buckling in Frame Structures," by M. Schachter and AM. Reinhorn, 9/13/07, (PB2008-108125).

MCEER-07-0017 "Modeling of Seismic Wave Scattering on Pile Groups and Caissons," by I. Po Lam, H. Law and C.T. Yang, 9/17/07 (PB2008-108150).

MCEER-07-0018 "Bridge Foundations: Modeling Large Pile Groups and Caissons for Seismic Design," by I. Po Lam, H. Law and G.R. Martin (Coordinating Author), 12/1/07 (PB2008-111190).

MCEER-07-0019 "Principles and Performance of Roller Seismic Isolation Bearings for Highway Bridges," by G.C. Lee, Y.C. Ou, Z. Liang, T.C. Niu and J. Song, 12/10/07 (PB2009-110466).

MCEER-07-0020 "Centrifuge Modeling of Permeability and Pinning Reinforcement Effects on Pile Response to Lateral Spreading," by L.L Gonzalez-Lagos, T. Abdoun and R. Dobry, 12/10/07 (PB2008-111191).

MCEER-07-0021 "Damage to the Highway System from the Pisco, Perú Earthquake of August 15, 2007," by J.S. O'Connor, L. Mesa and M. Nykamp, 12/10/07, (PB2008-108126).

MCEER-07-0022 "Experimental Seismic Performance Evaluation of Isolation/Restraint Systems for Mechanical Equipment – Part 2: Light Equipment Study," by S. Fathali and A. Filiatrault, 12/13/07 (PB2008-111192).

MCEER-07-0023 "Fragility Considerations in Highway Bridge Design," by M. Shinozuka, S. Banerjee and S.H. Kim, 12/14/07 (PB2008-111193).

MCEER-07-0024 "Performance Estimates for Seismically Isolated Bridges," by G.P. Warn and A.S. Whittaker, 12/30/07 (PB2008-112230).

MCEER-08-0001 "Seismic Performance of Steel Girder Bridge Superstructures with Conventional Cross Frames," by L.P. Carden, A.M. Itani and I.G. Buckle, 1/7/08, (PB2008-112231).

MCEER-08-0002 "Seismic Performance of Steel Girder Bridge Superstructures with Ductile End Cross Frames with Seismic Isolators," by L.P. Carden, A.M. Itani and I.G. Buckle, 1/7/08 (PB2008-112232).

MCEER-08-0003 "Analytical and Experimental Investigation of a Controlled Rocking Approach for Seismic Protection of Bridge Steel Truss Piers," by M. Pollino and M. Bruneau, 1/21/08 (PB2008-112233).

MCEER-08-0004 "Linking Lifeline Infrastructure Performance and Community Disaster Resilience: Models and Multi-Stakeholder Processes," by S.E. Chang, C. Pasion, K. Tatebe and R. Ahmad, 3/3/08 (PB2008-112234).

MCEER-08-0005 "Modal Analysis of Generally Damped Linear Structures Subjected to Seismic Excitations," by J. Song, Y-L. Chu, Z. Liang and G.C. Lee, 3/4/08 (PB2009-102311).

MCEER-08-0006 "System Performance Under Multi-Hazard Environments," by C. Kafali and M. Grigoriu, 3/4/08 (PB2008-112235).

MCEER-08-0007 "Mechanical Behavior of Multi-Spherical Sliding Bearings," by D.M. Fenz and M.C. Constantinou, 3/6/08 (PB2008-112236).

MCEER-08-0008 "Post-Earthquake Restoration of the Los Angeles Water Supply System," by T.H.P. Tabucchi and R.A. Davidson, 3/7/08 (PB2008-112237).

MCEER-08-0009 "Fragility Analysis of Water Supply Systems," by A. Jacobson and M. Grigoriu, 3/10/08 (PB2009-105545).

MCEER-08-0010 "Experimental Investigation of Full-Scale Two-Story Steel Plate Shear Walls with Reduced Beam Section Connections," by B. Qu, M. Bruneau, C-H. Lin and K-C. Tsai, 3/17/08 (PB2009-106368).

MCEER-08-0011 "Seismic Evaluation and Rehabilitation of Critical Components of Electrical Power Systems," S. Ersoy, B. Feizi, A. Ashrafi and M. Ala Saadeghvaziri, 3/17/08 (PB2009-105546).

MCEER-08-0012 "Seismic Behavior and Design of Boundary Frame Members of Steel Plate Shear Walls," by B. Qu and M. Bruneau, 4/26/08 . (PB2009-106744).

MCEER-08-0013 "Development and Appraisal of a Numerical Cyclic Loading Protocol for Quantifying Building System Performance," by A. Filiatrault, A. Wanitkorkul and M. Constantinou, 4/27/08 (PB2009-107906).

MCEER-08-0014 "Structural and Nonstructural Earthquake Design: The Challenge of Integrating Specialty Areas in Designing Complex, Critical Facilities," by W.J. Petak and D.J. Alesch, 4/30/08 (PB2009-107907).

MCEER-08-0015 "Seismic Performance Evaluation of Water Systems," by Y. Wang and T.D. O'Rourke, 5/5/08 (PB2009-107908).

MCEER-08-0016 "Seismic Response Modeling of Water Supply Systems," by P. Shi and T.D. O'Rourke, 5/5/08 (PB2009-107910).

MCEER-08-0017 "Numerical and Experimental Studies of Self-Centering Post-Tensioned Steel Frames," by D. Wang and A. Filiatrault, 5/12/08 (PB2009-110479).

MCEER-08-0018 "Development, Implementation and Verification of Dynamic Analysis Models for Multi-Spherical Sliding Bearings," by D.M. Fenz and M.C. Constantinou, 8/15/08 (PB2009-107911).

MCEER-08-0019 "Performance Assessment of Conventional and Base Isolated Nuclear Power Plants for Earthquake Blast Loadings," by Y.N. Huang, A.S. Whittaker and N. Luco, 10/28/08 (PB2009-107912).

MCEER-08-0020 “Remote Sensing for Resilient Multi-Hazard Disaster Response – Volume I: Introduction to Damage Assessment Methodologies,” by B.J. Adams and R.T. Eguchi, 11/17/08 (PB2010-102695).

MCEER-08-0021 “Remote Sensing for Resilient Multi-Hazard Disaster Response – Volume II: Counting the Number of Collapsed Buildings Using an Object-Oriented Analysis: Case Study of the 2003 Bam Earthquake,” by L. Gusella, C.K. Huyck and B.J. Adams, 11/17/08 (PB2010-100925).

MCEER-08-0022 “Remote Sensing for Resilient Multi-Hazard Disaster Response – Volume III: Multi-Sensor Image Fusion Techniques for Robust Neighborhood-Scale Urban Damage Assessment,” by B.J. Adams and A. McMillan, 11/17/08 (PB2010-100926).

MCEER-08-0023 “Remote Sensing for Resilient Multi-Hazard Disaster Response – Volume IV: A Study of Multi-Temporal and Multi-Resolution SAR Imagery for Post-Katrina Flood Monitoring in New Orleans,” by A. McMillan, J.G. Morley, B.J. Adams and S. Chesworth, 11/17/08 (PB2010-100927).

MCEER-08-0024 “Remote Sensing for Resilient Multi-Hazard Disaster Response – Volume V: Integration of Remote Sensing Imagery and VIEWS^{TM} Field Data for Post-Hurricane Charley Building Damage Assessment,” by J.A. Womble, K. Mehta and B.J. Adams, 11/17/08 (PB2009-115532).

MCEER-08-0025 “Building Inventory Compilation for Disaster Management: Application of Remote Sensing and Statistical Modeling,” by P. Sarabandi, A.S. Kiremidjian, R.T. Eguchi and B. J. Adams, 11/20/08 (PB2009-110484).

MCEER-08-0026 “New Experimental Capabilities and Loading Protocols for Seismic Qualification and Fragility Assessment of Nonstructural Systems,” by R. Retamales, G. Mosqueda, A. Filiatrault and A. Reinhorn, 11/24/08 (PB2009-110485).

MCEER-08-0027 “Effects of Heating and Load History on the Behavior of Lead-Rubber Bearings,” by I.V. Kalpakidis and M.C. Constantinou, 12/1/08 (PB2009-115533).

MCEER-08-0028 “Experimental and Analytical Investigation of Blast Performance of Seismically Resistant Bridge Piers,” by S.Fujikura and M. Bruneau, 12/8/08 (PB2009-115534).

MCEER-08-0029 “Evolutionary Methodology for Aseismic Decision Support,” by Y. Hu and G. Dargush, 12/15/08.

MCEER-08-0030 “Development of a Steel Plate Shear Wall Bridge Pier System Conceived from a Multi-Hazard Perspective,” by D. Keller and M. Bruneau, 12/19/08 (PB2010-102696).

MCEER-09-0001 “Modal Analysis of Arbitrarily Damped Three-Dimensional Linear Structures Subjected to Seismic Excitations,” by Y.L. Chu, J. Song and G.C. Lee, 1/31/09 (PB2010-100922).

MCEER-09-0002 “Air-Blast Effects on Structural Shapes,” by G. Ballantyne, A.S. Whittaker, A.J. Aref and G.F. Dargush, 2/2/09 (PB2010-102697).

MCEER-09-0003 “Water Supply Performance During Earthquakes and Extreme Events,” by A.L. Bonneau and T.D. O’Rourke, 2/16/09 (PB2010-100923).

MCEER-09-0004 “Generalized Linear (Mixed) Models of Post-Earthquake Ignitions,” by R.A. Davidson, 7/20/09 (PB2010-102698).

MCEER-09-0005 “Seismic Testing of a Full-Scale Two-Story Light-Frame Wood Building: NEESWood Benchmark Test,” by I.P. Christovasilis, A. Filiatrault and A. Wanitkorkul, 7/22/09 (PB2012-102401).

MCEER-09-0006 “IDARC2D Version 7.0: A Program for the Inelastic Damage Analysis of Structures,” by A.M. Reinhorn, H. Roh, M. Sivaselvan, S.K. Kunnath, R.E. Valles, A. Madan, C. Li, R. Lobo and Y.J. Park, 7/28/09 (PB2010-103199).

MCEER-09-0007 “Enhancements to Hospital Resiliency: Improving Emergency Planning for and Response to Hurricanes,” by D.B. Hess and L.A. Arendt, 7/30/09 (PB2010-100924).

MCEER-09-0008 "Assessment of Base-Isolated Nuclear Structures for Design and Beyond-Design Basis Earthquake Shaking," by Y.N. Huang, A.S. Whittaker, R.P. Kennedy and R.L. Mayes, 8/20/09 (PB2010-102699).

MCEER-09-0009 "Quantification of Disaster Resilience of Health Care Facilities," by G.P. Cimellaro, C. Fumo, A.M Reinhorn and M. Bruneau, 9/14/09 (PB2010-105384).

MCEER-09-0010 "Performance-Based Assessment and Design of Squat Reinforced Concrete Shear Walls," by C.K. Gulec and A.S. Whittaker, 9/15/09 (PB2010-102700).

MCEER-09-0011 "Proceedings of the Fourth US-Taiwan Bridge Engineering Workshop," edited by W.P. Yen, J.J. Shen, T.M. Lee and R.B. Zheng, 10/27/09 (PB2010-500009).

MCEER-09-0012 "Proceedings of the Special International Workshop on Seismic Connection Details for Segmental Bridge Construction," edited by W. Phillip Yen and George C. Lee, 12/21/09 (PB2012-102402).

MCEER-10-0001 "Direct Displacement Procedure for Performance-Based Seismic Design of Multistory Woodframe Structures," by W. Pang and D. Rosowsky, 4/26/10 (PB2012-102403).

MCEER-10-0002 "Simplified Direct Displacement Design of Six-Story NEESWood Capstone Building and Pre-Test Seismic Performance Assessment," by W. Pang, D. Rosowsky, J. van de Lindt and S. Pei, 5/28/10 (PB2012-102404).

MCEER-10-0003 "Integration of Seismic Protection Systems in Performance-Based Seismic Design of Woodframed Structures," by J.K. Shinde and M.D. Symans, 6/18/10 (PB2012-102405).

MCEER-10-0004 "Modeling and Seismic Evaluation of Nonstructural Components: Testing Frame for Experimental Evaluation of Suspended Ceiling Systems," by A.M. Reinhorn, K.P. Ryu and G. Maddaloni, 6/30/10 (PB2012-102406).

MCEER-10-0005 "Analytical Development and Experimental Validation of a Structural-Fuse Bridge Pier Concept," by S. El-Bahey and M. Bruneau, 10/1/10 (PB2012-102407).

MCEER-10-0006 "A Framework for Defining and Measuring Resilience at the Community Scale: The PEOPLES Resilience Framework," by C.S. Renschler, A.E. Frazier, L.A. Arendt, G.P. Cimellaro, A.M. Reinhorn and M. Bruneau, 10/8/10 (PB2012-102408).

MCEER-10-0007 "Impact of Horizontal Boundary Elements Design on Seismic Behavior of Steel Plate Shear Walls," by R. Purba and M. Bruneau, 11/14/10 (PB2012-102409).

MCEER-10-0008 "Seismic Testing of a Full-Scale Mid-Rise Building: The NEESWood Capstone Test," by S. Pei, J.W. van de Lindt, S.E. Pryor, H. Shimizu, H. Isoda and D.R. Rammer, 12/1/10 (PB2012-102410).

MCEER-10-0009 "Modeling the Effects of Detonations of High Explosives to Inform Blast-Resistant Design," by P. Sherkar, A.S. Whittaker and A.J. Aref, 12/1/10 (PB2012-102411).

MCEER-10-0010 "L'Aquila Earthquake of April 6, 2009 in Italy: Rebuilding a Resilient City to Withstand Multiple Hazards," by G.P. Cimellaro, I.P. Christovasilis, A.M. Reinhorn, A. De Stefano and T. Kirova, 12/29/10.

MCEER-11-0001 "Numerical and Experimental Investigation of the Seismic Response of Light-Frame Wood Structures," by I.P. Christovasilis and A. Filiatrault, 8/8/11 (PB2012-102412).

MCEER-11-0002 "Seismic Design and Analysis of a Precast Segmental Concrete Bridge Model," by M. Anagnostopoulou, A. Filiatrault and A. Aref, 9/15/11.

MCEER-11-0003 'Proceedings of the Workshop on Improving Earthquake Response of Substation Equipment," Edited by A.M. Reinhorn, 9/19/11 (PB2012-102413).

MCEER-11-0004 "LRFD-Based Analysis and Design Procedures for Bridge Bearings and Seismic Isolators," by M.C. Constantinou, I. Kalpakidis, A. Filiatrault and R.A. Ecker Lay, 9/26/11.

MCEER-11-0005 "Experimental Seismic Evaluation, Model Parameterization, and Effects of Cold-Formed Steel-Framed Gypsum Partition Walls on the Seismic Performance of an Essential Facility," by R. Davies, R. Retamales, G. Mosqueda and A. Filiatrault, 10/12/11.

MCEER-11-0006 "Modeling and Seismic Performance Evaluation of High Voltage Transformers and Bushings," by A.M. Reinhorn, K. Oikonomou, H. Roh, A. Schiff and L. Kempner, Jr., 10/3/11.

MCEER-11-0007 "Extreme Load Combinations: A Survey of State Bridge Engineers," by G.C. Lee, Z. Liang, J.J. Shen and J.S. O'Connor, 10/14/11.

MCEER-12-0001 "Simplified Analysis Procedures in Support of Performance Based Seismic Design," by Y.N. Huang and A.S. Whittaker.

MCEER-12-0002 "Seismic Protection of Electrical Transformer Bushing Systems by Stiffening Techniques," by M. Koliou, A. Filiatrault, A.M. Reinhorn and N. Oliveto, 6/1/12.

MCEER-12-0003 "Post-Earthquake Bridge Inspection Guidelines," by J.S. O'Connor and S. Alampalli, 6/8/12.

MCEER-12-0004 "Integrated Design Methodology for Isolated Floor Systems in Single-Degree-of-Freedom Structural Fuse Systems," by S. Cui, M. Bruneau and M.C. Constantinou, 6/13/12.

MCEER-12-0005 "Characterizing the Rotational Components of Earthquake Ground Motion," by D. Basu, A.S. Whittaker and M.C. Constantinou, 6/15/12.

MCEER-12-0006 "Bayesian Fragility for Nonstructural Systems," by C.H. Lee and M.D. Grigoriu, 9/12/12.

MCEER-12-0007 "A Numerical Model for Capturing the In-Plane Seismic Response of Interior Metal Stud Partition Walls," by R.L. Wood and T.C. Hutchinson, 9/12/12.

MCEER-12-0008 "Assessment of Floor Accelerations in Yielding Buildings," by J.D. Wieser, G. Pekcan, A.E. Zaghi, A.M. Itani and E. Maragakis, 10/5/12.

MCEER-13-0001 "Experimental Seismic Study of Pressurized Fire Sprinkler Piping Systems," by Y. Tian, A. Filiatrault and G. Mosqueda, 4/8/13.

MCEER-13-0002 "Enhancing Resource Coordination for Multi-Modal Evacuation Planning," by D.B. Hess, B.W. Conley and C.M. Farrell, 2/8/13.

MCEER-13-0003 "Seismic Response of Base Isolated Buildings Considering Pounding to Moat Walls," by A. Masroor and G. Mosqueda, 2/26/13.

MCEER-13-0004 "Seismic Response Control of Structures Using a Novel Adaptive Passive Negative Stiffness Device," by D.T.R. Pasala, A.A. Sarlis, S. Nagarajaiah, A.M. Reinhorn, M.C. Constantinou and D.P. Taylor, 6/10/13.

MCEER-13-0005 "Negative Stiffness Device for Seismic Protection of Structures," by A.A. Sarlis, D.T.R. Pasala, M.C. Constantinou, A.M. Reinhorn, S. Nagarajaiah and D.P. Taylor, 6/12/13.

MCEER-13-0006 "Emilia Earthquake of May 20, 2012 in Northern Italy: Rebuilding a Resilient Community to Withstand Multiple Hazards," by G.P. Cimellaro, M. Chiriatti, A.M. Reinhorn and L. Tirca, June 30, 2013.

MCEER-13-0007 "Precast Concrete Segmental Components and Systems for Accelerated Bridge Construction in Seismic Regions," by A.J. Aref, G.C. Lee, Y.C. Ou and P. Sideris, with contributions from K.C. Chang, S. Chen, A. Filiatrault and Y. Zhou, June 13, 2013.

MCEER-13-0008 "A Study of U.S. Bridge Failures (1980-2012)," by G.C. Lee, S.B. Mohan, C. Huang and B.N. Fard, June 15, 2013.

MCEER-13-0009 "Development of a Database Framework for Modeling Damaged Bridges," by G.C. Lee, J.C. Qi and C. Huang, June 16, 2013.

MCEER-13-0010 "Model of Triple Friction Pendulum Bearing for General Geometric and Frictional Parameters and for Uplift Conditions," by A.A. Sarlis and M.C. Constantinou, July 1, 2013.

MCEER-13-0011 "Shake Table Testing of Triple Friction Pendulum Isolators under Extreme Conditions," by A.A. Sarlis, M.C. Constantinou and A.M. Reinhorn, July 2, 2013.

MCEER-13-0012 "Theoretical Framework for the Development of MH-LRFD," by G.C. Lee (coordinating author), H.A Capers, Jr., C. Huang, J.M. Kulicki, Z. Liang, T. Murphy, J.J.D. Shen, M. Shinozuka and P.W.H. Yen, July 31, 2013.

MCEER-13-0013 "Seismic Protection of Highway Bridges with Negative Stiffness Devices," by N.K.A. Attary, M.D. Symans, S. Nagarajaiah, A.M. Reinhorn, M.C. Constantinou, A.A. Sarlis, D.T.R. Pasala, and D.P. Taylor, September 3, 2014.

MCEER-14-0001 "Simplified Seismic Collapse Capacity-Based Evaluation and Design of Frame Buildings with and without Supplemental Damping Systems," by M. Hamidia, A. Filiatrault, and A. Aref, May 19, 2014.

MCEER-14-0002 "Comprehensive Analytical Seismic Fragility of Fire Sprinkler Piping Systems," by Siavash Soroushian, Emmanuel "Manos" Maragakis, Arash E. Zaghi, Alicia Echevarria, Yuan Tian and Andre Filiatrault, August 26, 2014.

MCEER-14-0003 "Hybrid Simulation of the Seismic Response of a Steel Moment Frame Building Structure through Collapse," by M. Del Carpio Ramos, G. Mosqueda and D.G. Lignos, October 30, 2014.

MCEER-14-0004 "Blast and Seismic Resistant Concrete-Filled Double Skin Tubes and Modified Steel Jacketed Bridge Columns," by P.P. Fouche and M. Bruneau, June 30, 2015.

MCEER-14-0005 "Seismic Performance of Steel Plate Shear Walls Considering Various Design Approaches," by R. Purba and M. Bruneau, October 31, 2014.

MCEER-14-0006 "Air-Blast Effects on Civil Structures," by Jinwon Shin, Andrew S. Whittaker, Amjad J. Aref and David Cormie, October 30, 2014.

MCEER-14-0007 "Seismic Performance Evaluation of Precast Girders with Field-Cast Ultra High Performance Concrete (UHPC) Connections," by G.C. Lee, C. Huang, J. Song, and J. S. O'Connor, July 31, 2014.

MCEER-14-0008 "Post-Earthquake Fire Resistance of Ductile Concrete-Filled Double-Skin Tube Columns," by Reza Imani, Gilberto Mosqueda and Michel Bruneau, December 1, 2014.

MCEER-14-0009 "Cyclic Inelastic Behavior of Concrete Filled Sandwich Panel Walls Subjected to In-Plane Flexure," by Y. Alzeni and M. Bruneau, December 19, 2014.

MCEER-14-0010 "Analytical and Experimental Investigation of Self-Centering Steel Plate Shear Walls," by D.M. Dowden and M. Bruneau, December 19, 2014.

MCEER-15-0001 "Seismic Analysis of Multi-story Unreinforced Masonry Buildings with Flexible Diaphragms," by J. Aleman, G. Mosqueda and A.S. Whittaker, June 12, 2015.

MCEER-15-0002 "Site Response, Soil-Structure Interaction and Structure-Soil-Structure Interaction for Performance Assessment of Buildings and Nuclear Structures," by C. Bolisetti and A.S. Whittaker, June 15, 2015.

MCEER-15-0003 "Stress Wave Attenuation in Solids for Mitigating Impulsive Loadings," by R. Rafiee-Dehkharghani, A.J. Aref and G. Dargush, August 15, 2015..

.

MCEER
EARTHQUAKE ENGINEERING TO EXTREME EVENTS
University at Buffalo, The State University of New York
133A Ketter Hall ▪ Buffalo, New York 14260-4300
Phone: (716) 645-3391 ▪ Fax: (716) 645-3399
Email: *mceer@buffalo.edu* ▪ Web: ***http://mceer.buffalo.edu***
University at Buffalo *The State University of New York*

ISSN 1520-295X